# ULTRASOUND CONTRAST AGENTS FOR IMAGING AND THERAPY

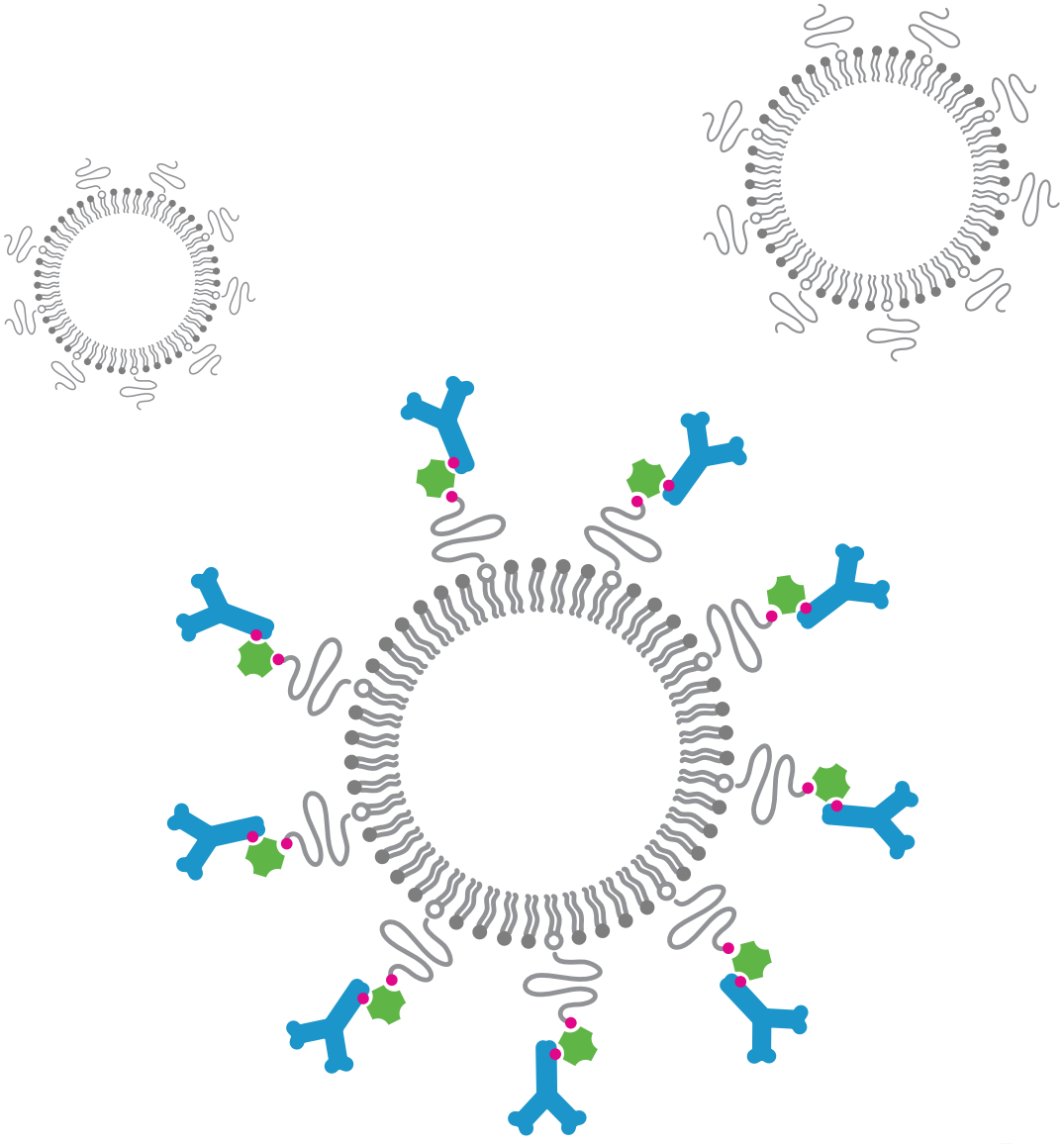

Tom van Rooij

# Ultrasound Contrast Agents for Imaging and Therapy

Echocontrastmiddelen voor beeldvorming en therapie

Tom van Rooij

## COLOPHON

ISBN: 9789462335165
Cover design: Flip Vossen & Tom van Rooij
Printed by: Gildeprint, Enschede, the Netherlands



For a printed version please contact:
Secretary Biomedical Engineering (January 2017: room Ee 2302)
Erasmus MC
P.O. Box 2040
3000 CA Rotterdam
the Netherlands

# Ultrasound Contrast Agents for Imaging and Therapy

Echocontrastmiddelen voor beeldvorming en therapie

# Thesis

to obtain the degree of Doctor from the
Erasmus University Rotterdam
by command of the
rector magnificus

Prof. dr. H.A.P. Pols

and in accordance with the decision of the Doctorate Board

The public defence shall be held on

Wednesday 18th of January 2017 at 13.30 hours

by

**Tom van Rooij**

born in Eindhoven

Erasmus University Rotterdam

**DOCTORAL COMMITTEE:**

| | |
|---|---|
| **Promoters:** | Prof. dr. ir. N. de Jong |
| | Prof. dr. ir. A.F.W. van der Steen |
| **Other members:** | Prof. dr. C. Ince |
| | Prof. dr. A.M. Versluis |
| | Prof. dr. E. Stride |
| **Co-promoter:** | Dr. K. Kooiman |


This thesis is part of NanoNextNL, a micro and nanotechnology innovation consortium of the Government of the Netherlands and 130 partners from academia and industry. More information can be found on www.nanonextnl.nl.

The research described in this thesis has been carried out at the Department of Biomedical Engineering, Thorax Center, Erasmus MC in Rotterdam.

Financial support by the Dutch Heart Foundation and the Dutch Kidney Foundation for the publication of this thesis is gratefully acknowledged.

# VOORWOORD

Waarom bellen en ultrageluid? Met een achtergrond in MRI en klinische chemie is dit niet de meest voor de hand liggende keuze. Aan de andere kant zag ik hierin een mooie combinatie van biologie, wat scheikunde en een beeldvormende techniek waar tevens een toekomst in zit qua therapeutische mogelijkheden. Vanwege de samenstelling van de afdeling gaf dit onderzoek me ook de kans om zelf te kiezen hoe technisch of biologisch ik het onderzoek in wilde vullen. Ik heb meer geleerd dan ik vooraf had kunnen bedenken, zoals cellen kweken, werken met proefdieren en het in recordtempo schrijven van artikelen. De meeste voldoening haal ik uit de wetenschap dat ik patiënten kan helpen en ik ben er dan ook trots op dat de studie naar acuut nierfalen al een jaar na de preklinische fase naar de intensive care wordt gebracht. Ik ben erg blij en opgelucht dat ik nu dit boekje afgeleverd heb en ben trots op het resultaat van vier jaar (hard) werken. Waarschijnlijk zul je na het lezen van dit voorwoord meteen doorbladeren naar het dankwoord om te kijken of je genoemd wordt, maar neem ook even de tijd om de rest te bekijken. Het zou jammer zijn als ik alles voor niets heb geschreven…

*Tom, december 2016*

**Financial support for the printing of this thesis was kindly provided by:**

Bracco Suisse SA

Erasmus MC

FUJIFILM VisualSonics, Inc

Lipoid GmbH

Oldelft Ultrasound

Olympus Nederland B.V.

TraskBritt

# Contents

Chapter 1

# Introduction

## 1.1. ULTRASOUND

Sound is omnipresent: some sounds we can hear, others we cannot hear. Whether we can hear a certain sound depends on its frequency. A young and healthy human ear can pick up sound with frequencies between 20 and 20,000 Hz [1]. Sound close to 20 Hz has long sound waves and a low pitch; think of the bass in music, whereas the higher spectrum has short sound waves and a high pitch, such as the sound of a flying mosquito. Sound at frequencies higher than the ones we can hear is referred to as ultrasound. Although we are not able to hear those sounds, they have been proven to be very valuable to us in naval applications (sonar) and in the hospital. The first application of medical ultrasound (Dutch: echografie of echo) dates back to 1942. In that year Karl Dussik performed an ultrasound transmission scan with a transmit transducer on one side of the head of a patient, and a receive transducer on the other side. This was also the first scientific publication on medical ultrasonics. A few years later, in 1947, George D. Ludwig used ultrasound to locate gallstones and John Julian Wild used it to detect breast masses [2]. Since these early introductions of medical ultrasound, it is now mostly known from applications in obstetrics and gynecology to visualize the unborn child (Fig. 1.1).

The principle of ultrasound imaging is the detection of reflected sound waves (the echoes). Because different tissues reflect ultrasound differently, an image can be reconstructed. Ultrasound imaging is therefore very useful for real-time imaging of tissue, but one of the drawbacks is that it is not capable of visualizing blood.

**Fig. 1.1.** Ultrasound image of 27-weeks old fetus (www.echowonder.nl)

## 1.2. ULTRASOUND CONTRAST AGENTS

In 1968, Raymond Gramiak and Pravin M. Shah administered saline intravenously to a patient during an ultrasound examination of the aortic root [3]. Surprisingly, the injection of saline enabled them to visualize the blood; this was caused by the mini air bubbles that were present in the saline or that were caused by the saline injection [3]. We now know that this result was caused by the fact that gas bubbles are very efficient reflectors of sound, due to their compression and expansion in response to the incident ultrasound wave [4]. This property of gas bubbles has been exploited for over forty years for the development of ultrasound contrast agents (UCAs). Air bubbles, such as those present in agitated saline, dissolve within tens of milliseconds in blood [5], which limits their use as contrast agent for ultrasound imaging. Over the years, several types of UCAs have been developed to increase

the lifetime of the gas bubbles after injection in the blood stream. In 1994, the first commercially available contrast agent Albunex (Molecular Biosystems, San Diego, CA, USA) was marketed; air bubbles coated with human albumin, an abundant blood protein, to increase their stability [6]. To further increase the lifetime of these so called microbubbles of 1-10 µm in diameter [7-10], the air in the core was replaced by heavier gasses with lower diffusion coefficients in blood. The inert gasses that are currently used in commercially available ultrasound contrast agents are $SF_6$ in SonoVue/Lumason (Bracco Imaging, Milan, Italy) [7, 8], $C_3F_8$ in Definity (Lantheus Medical Imaging, North Billerica, MA, USA) [9] and in Optison (GE Healthcare AS, Oslo, Norway), and $C_4F_{10}$ in Sonazoid (Daiichi Sankyo, GE Healthcare, Tokyo, Japan) [11].

The newest generation of UCAs also contains $C_4F_{10}$ (e.g. VEGFR2-targeted BR55, Bracco Imaging) and is currently still in the phase of clinical trials to assess their safety before approval by the regulating agencies as the Food and Drug Administration (FDA) for the USA and the European Medicines Evaluation Agency (EMEA) for Europe. Using $C_4F_{10}$ as the gas core has improved microbubble stability, but next to the gas core the coating could also be optimized to increase stability. Albumin results in a relatively thick and rigid shell [5], which limits oscillation of the gas bubble. Other coatings such as lipids or polymers were therefore introduced and are currently still used [12-18]. Lipids have the great advantage that they result in relatively large oscillation amplitudes [18-20], whereas polymers can increase the payload for hydrophobic drugs in their core [14]. However, polymer contrast agents have stiffer shells that need to be cracked in order to let the gas escape or the oil to be vaporized to provide sufficient contrast [13, 14, 21]. Both lipids and polymers have the advantage that they offer more options to tune the shell properties, which in addition opens up opportunities for functionalization and targeting of the microbubbles.

## 1.3. CONTRAST-ENHANCED ULTRASOUND IMAGING AND THERAPY

Contrast-enhanced ultrasound (CEUS) is currently used to aid diagnosis in several organs, such as heart, liver, breast, kidney, and prostate, but also to detect neovessels [22-27]. Next to enhanced visualization of the blood for diagnostic purposes, microbubbles can also be functionalized by conjugating ligands to their surface to target specific biomarkers of a disease or a disease process [28-30]. These targeted microbubbles can be used for a wide range of pre-clinical applications including diagnosis, molecular imaging, monitoring of drug treatment, and therapy [30-32]. For therapies involving drug delivery, one can exploit an interesting property of oscillating microbubbles. Due to the microbubble vibration it can 'massage' a cell and create permanent or transient pores in the cell membrane [33-37]. The formation of these pores is called sonoporation, which can be used to locally enhance the delivery of drugs or to locally induce cell death [38, 39]. Although the exact mechanism

remains unknown, it has been shown that the acoustic settings and microbubble behavior mainly determine whether cells are sonoporated or not [35, 40, 41].

Although the acoustic behavior of microbubbles has been experimentally studied in detail for the last decade, our understanding is still far from complete. Modeling of single microbubbles oscillating in an ultrasound field aids in this understanding and can complement experimental findings. In 1917, Lord Rayleigh derived an equation to describe the behavior of a single oscillating air bubble [42], which has later been modified by Plesset to the now known Rayleigh-Plesset equation [43]. This equation has been applied by many researchers to describe the behavior of microbubbles that are freely-floating or are located close to a membrane [5, 44]. Recently, a model has been introduced by Lajoinie et al. that applies the Rayleigh-Plesset equation in two dimensions in a spherical coordinate system, in order to solve the equation for each axisymmetric line segment [15]. This is the first model that predicts the oscillation of functionalized microbubbles that are bound to a membrane.

Most of the previously described models [5, 15, 44] approximate the true microbubble oscillation quite accurately and can therefore be used to determine shell properties from experimental data, such as damping, elasticity, and viscosity. However, some relations are still not completely clear. Although we know that the microbubble size is inversely related to their resonance frequency [45], i.e., the ultrasound frequency at which the highest response can be measured, the shell and gas core of the microbubble also contribute to their acoustic response [19]. Each commercially available or in-house produced UCA is composed of different gas cores and coating compositions, but the exact relation between the microbubble composition and their acoustic responses remains unknown.

Most UCAs consist of microbubbles with a lipid-based shell. Various combinations of lipids have been shown to result in different distributions over the microbubble shell; some combinations distribute uniformly over the shell, while others form ordered domains or microstructures [46-49]. Some of these microbubbles have long contrast persistence *in vivo* and provide good contrast, while others provide only limited or no contrast at all [50]. A possible reason for these differences is the variation in shell composition. Surprisingly, the relation between shell composition and the acoustic properties of single microbubbles has never been thoroughly studied and remains so far unknown. Because only a single or a few targeted microbubbles can adhere to the biomarker of interest, complete understanding of single microbubble behavior is crucial for molecular imaging and local drug delivery applications. The aim of this thesis is to unravel the relation between shell properties and the acoustic response of single microbubbles. Next, the most stable and acoustically best performing UCAs are also investigated *in vitro* for therapeutic applications by means of sonoporation, and for *in vivo* diagnostic imaging applications.

## 1.4. OUTLINE OF THIS THESIS

A graphical overview of the work described in this thesis is provided in Fig. 1.2. In **Chapter 2** we give an overview of the current use of targeted microbubbles for ultrasound molecular imaging and drug delivery. We describe the preparation of targeted microbubbles in terms of coating materials and methods to attach ligands to the shell for specific biomarkers that can be successfully targeted. Next, techniques to assess shell and acoustic properties of targeted microbubbles are discussed and possible approaches are provided for discriminating targeted microbubbles that have adhered to a biomarker from those that have not. Finally, the current status of ultrasound molecular imaging and drug delivery is discussed.

For imaging of superficial organs and preclinical imaging of small animals such as mice and rats, high-frequency CEUS imaging is mostly used. Clinical examinations are usually performed at lower frequencies, so the commercially available UCAs have been optimized for low frequency applications. At high frequencies, UCAs that consist of smaller microbubbles have higher resonance frequencies and therefore respond better. In **Chapter 3** we focus on designing, producing, and characterizing twelve different UCAs for high-frequency applications. We vary shell compositions and use two production methods: sonication and mechanical agitation, both with their own advantages and disadvantages.

Two out of these twelve microbubble compositions are functionalized and studied in more detail in **Chapter 4** in terms of their shell microstructure and binding characteristics. To study the lipid shell at the molecular level super-resolution microscopy is required. The relation between the determined shell microstructures and the acoustic properties is characterized in **Chapter 5**. To stimulate a microbubble, frequencies above 1 MHz [51] are usually applied. This means that it oscillates at least one million times per second. To fully capture these oscillations ultra-high-speed optical cameras are required; we therefore used our Brandaris 128 camera [52] to study microbubble behavior.

Next to the microbubbles we describe in the previous chapters, one can also use other types of UCAs. In collaboration with the University of Cincinnati (Cincinnati, OH, USA) we studied echogenic liposomes (**Chapter 6**). These echogenic liposomes consist of a multi-layer of lipids encapsulating a gas and an aqueous phase [53], that have the potential to locally deliver bioactive gasses such as oxygen [54], deliver drugs to dissolve blood clots (sonothrombolysis) [55], or to enhance radiation and cytostatic cancer therapies. In this chapter we develop a generic model to determine the shell and acoustic properties of echogenic liposomes on measurements acquired by the Brandaris 128 camera.

Since the ultra-high-speed Brandaris 128 camera only visualizes the gas core of the microbubbles, it cannot be used to directly study the shell. This requires an ultra-high-speed camera that can caputre real-time movement of fluorescently labeled lipids in the shell of oscillating microbubbles (**Chapter 7**). The camera that was recently build by the University

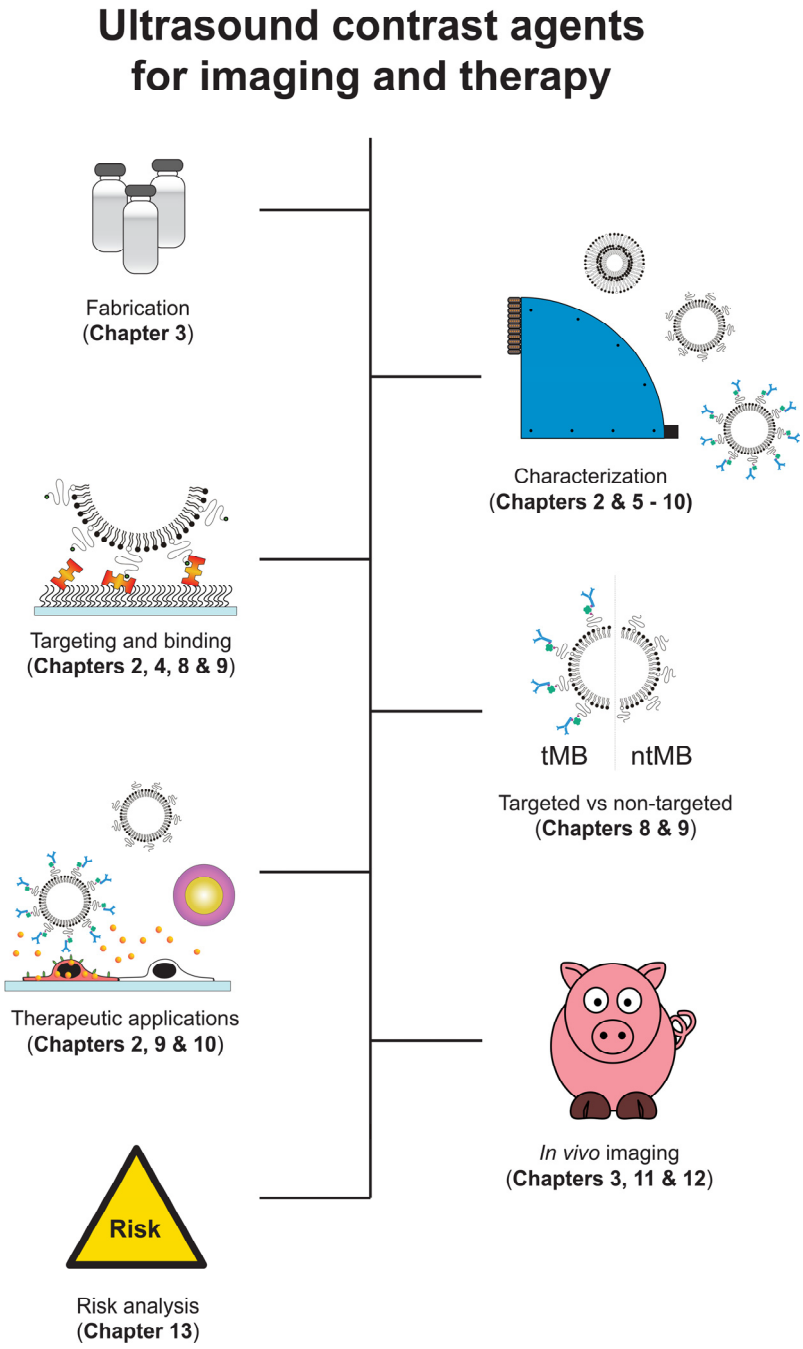


**Fig. 1.2.** Graphical guide through this thesis.

of Pittsburgh Medical Center (UPMC Cam, Pittsburgh, PN, USA) [56] meets these requirements and is used to visualize fluorescently labeled microbubbles to assess whether the lipid behavior in the shell can be related to their acoustic behavior.

In **Chapter 8** the acoustic properties of the same type of microbubbles as in **Chapters 4 and 5** are studied to identify parameters that can be used to acoustically discriminate microbubbles that had bound to a model biomarker from those that had not. The aim is to increase the specificity of ultrasound molecular imaging and reduce examination times.

To study the therapeutic effects of microbubbles and ultrasound, experiments on cells (*in vitro*) or in living animals (*in vivo*) are required. Using bright field ultra-high-speed imaging in combination with fluorescence imaging, both the microbubble oscillation can be captured and its effect on cells can be studied *in vitro*. **Chapter 9** investigates the influence of targeting and the effects that various acoustic settings have on the oscillation and displacement of microbubbles and how this affects the viability of human endothelial cells. Similar types of experiments were performed in **Chapter 10** on laser-activated polymer-coated microcapsules. This research is performed in collaboration with the University of Twente (Enschede, the Netherlands). The polymer microcapsules are a very different class of contrast agents, because the polymer is mixed with a light-absorbing dye and encapsulates oil instead of gas [15, 57]. Upon irradiation with a laser, the oil core evaporates and forms a gas bubble [58]. The formation of these gas bubbles generates an ultrasound signal that may be used for imaging [58] or can induce sonoporation and local cell death.

The *in vivo* imaging studies described in this thesis focus on acute kidney injury (AKI); an acute and rapid decrease in kidney function, typically within hours or days [59]. AKI is a frequent complication in patients admitted to the intensive care unit (ICU) and is associated with adverse outcomes including increased length of hospital and ICU stay, development of chronic kidney disease, and increased short- and long-term mortality risk [60]. About 2 in 100 hospitalized patients develop AKI, and for patients that are admitted to the ICU this number increases to more than 50% [59-61]. This is a very serious and costly clinical problem that we believe could be tackled by using CEUS to speed up diagnosis and to monitor therapy. We focus on two of the main causes of AKI: loss of blood volume (hemorrhage-induced hypovolemic shock, **Chapter 11**) and a whole-body infection which results in septic shock [59] (**Chapter 12**).

**Chapter 13** covers the risks associated with ultrasound contrast agent injection and CEUS measurements from the cellular level to their applications for diagnosis in clinical practice. In the final chapter (**Chapter 14**) the content of this thesis is discussed and possible directions for further research in the field of ultrasound contrast agents for imaging and therapy are provided.

Chapter **2**

# Targeted ultrasound contrast agents for ultrasound molecular imaging and therapy

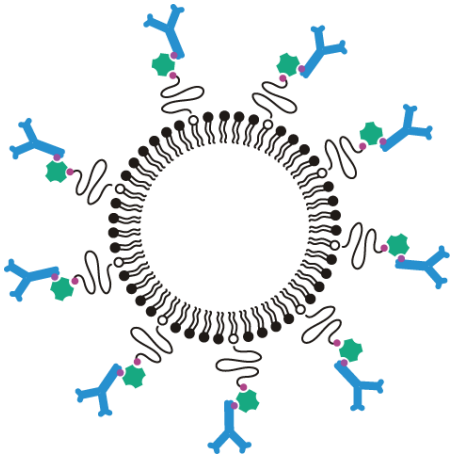

Tom van Rooij*, Verya Daeichin*, Ilya Skachkov, Nico de Jong, Klazina Kooiman
(* both first authors contributed equally)

*International Journal of Hyperthermia*, 31:2, 90–106 (2015)

## 2.1. ABSTRACT

Ultrasound contrast agents (UCAs) are used routinely in the clinic to enhance contrast in ultrasonography. More recently, UCAs have been functionalized by conjugating ligands to their surface to target specific biomarkers of a disease or a disease process. These targeted UCAs (tUCAs) are used for a wide range of pre-clinical applications including diagnosis, monitoring of drug treatment, and therapy. In this review, recent achievements with tUCA in the field of molecular imaging, evaluation of therapy, drug delivery, and therapeutic applications are discussed. We present the different coating materials and aspects that have to be considered when manufacturing tUCAs. Next to tUCA design and the choice of ligands for specific biomarkers, additional techniques are discussed that are applied to improve binding of the tUCAs to their target and to quantify the strength of this bond. As imaging techniques rely on the specific behavior of tUCAs in an ultrasound field, it is crucial to understand the characteristics of both free and adhered tUCAs. To image and quantify the adhered tUCAs, the state-of-the-art techniques used for ultrasound molecular imaging and quantification are presented. This review concludes with the potential of tUCAs for drug delivery and therapeutic applications.

## 2.2. INTRODUCTION

Ultrasound contrast agents (UCAs) consist of gas bubbles that are typically stabilized by an albumin, lipid or polymer shell. For over three decades, UCA have been clinically used to enhance ultrasound (US) imaging in different fields, such as cardiology and radiology [62, 63]. Targeted UCAs (tUCAs) differ from clinically approved UCAs by the decoration of their shell with targeting ligands [17]. Due to their typical size (~1-10 µm) UCAs are confined to the blood pool only [64, 65]. This makes tUCAs ideal agents to adhere to intravascular biomarkers expressed on endothelial cells, to target for instance cancer and cardiovascular disease, as covered in this review. Because of the large compressibility of the gas core of the microbubbles (MBs), they create nonlinear backscatter and reflection in an US field, allowing for differentiation between the highly echogenic agent and surrounding tissues and fluids [28, 45]. Recently, smaller tUCAs have been synthesized which allow them to extravasate out of leaky vasculature offering opportunities for new applications [66, 67].

This review focuses on tUCAs for ultrasound molecular imaging (UMI) and therapy. Manufacturing and functionalizing tUCAs will be covered, including targeting novel biomarkers. The binding and acoustic properties of bound tUCAs will be evaluated, as these properties are important for both UMI and therapy. The current state-of-the-art clinical and preclinical molecular imaging techniques and quantification methods are discussed. tUCA-mediated drug and gene delivery is a relatively new field as the first proof of concept was reported in 2011 [35]. The progress since then will be presented.

## 2.3. TARGETING AND BINDING OF tUCAs

To compose tUCAs several aspects have to be accounted for. A choice for the coating has to be made, the biomarkers that are upregulated in the disease of interest have to be identified, and a suitable targeting ligand has to be found. This targeting ligand has to be attached to the contrast agent and the binding properties of the tUCA have to be evaluated.

### Coating materials

The commercially available UCAs have different coating materials to reduce the surface tension and gas diffusion out of the UCAs, thereby increasing their lifetime. These are: albumin (Albunex, Cardiosphere, Optison), galactose (Echovist, Levovist), lipids (Definity, Imagent, Levovist, Lumason, MicroMarker, Sonazoid, SonoVue, Targestar), or polymers (Acusphere, Sonovist) [68, 69]. The main advantage of lipid-coated bubbles is that different mixtures can be easily formulated and modified [69]. Very recently, super-resolution fluorescence microscopy revealed that the main lipid in the coating (1,2-distearoyl-*sn*-glycero-3-phosphocholine (DSPC) or 1,2-dipalmitoyl-*sn*-glycero-3-phosphocholine (DPPC)) influences the ligand distribution on the shell [70] and it was also shown that the difference in ligand distribution also changes the acoustical properties [71]. This offers opportunities for designing UCAs with very specific and known properties. Most lipid-coated UCAs have a brush of polyethylene glycol (PEG) incorporated in their shell to prevent close contact between neighboring bubbles to inhibit their fusion and to shield them from the immune system [69]. But although this is generally accepted as a method to increase UCA lifetime, the necessity of incorporating PEG for tUCAs has been questioned [72]. This study indicated that small peptides either conjugated to the lipid directly or via a PEG-spacer (~10 monomers), might hinder access of the ligand to the target receptors when short PEG brushes (molecular weight of 350 kDa; i.e. 8 monomers) are part of the coating. Even when the MBs were prepared without a PEG brush in their coating, the introduction of a PEG spacer between the ligand and the lipid seemed to reduce binding. Their hypothesis is that the flexibility of the spacer possibly enabled the peptide to loop back onto the bubble surface. According to Marsh et al. [73] this is indeed what happens: due to their choice of incorporating relatively short PEG chains in the coating, the PEG chains will be in the mushroom regime and therefore assume a random configuration. If they would have used similar concentrations of PEG with longer chains, such as PEG(2000) containing 45 monomers, these chains would be in the brush state: a more stretched and less random configuration [73]. The random configuration of the PEG chain in the study of Myrset et al. [72] could thus shield the ligand, whilst a brush configuration may have been advantageous.

Polymer tUCAs have a stiffer and thicker coating than lipid-coated bubbles, and the main acoustic difference is their echogenicity: usually a polymer bubble is destructed and the free

gas bubble is detected, whereas a lipid-coated bubble can be used for non-destructive imaging [45]. Combinations of different shell materials have also been reported; Ottoboni et al. [74] used microcapsules with a cross-linked albumin outer layer and a poly-(DL-lactide) inner layer. The advantage of the two different layers is the possibility to tweak the acoustic performance via the inner polymer layer in terms of their stiffness and thickness, and to change the biological activity via the protein outer layer.

*In vivo*, the adsorption of serum proteins on the shell (opsonization) is a major challenge in the design of UCA, as it might inhibit binding of the tUCA to its target. Lipid-coated MBs based on phosphatidylcholine (PC)—especially pure DSPC—have lower serum protein adsorption, higher stability in serum, and lower uptake by the reticuloendothelial system (RES) than negatively charged phospholipids, such as phosphatidylserine (PS) [72]. Another problem caused by opsonization is its triggering capacity for phagocytosis. As targeting ligands typically present nucleophilic groups (e.g., hydroxyl or amino) this could trigger complement C3/C3b activation to promote phagocytosis and decrease the tUCA circulation time. This can be partly overcome by using longer PEG chains that are in the brush state [73] to shield the ligands for complement activation ("overbrushing") and thus reduce immunogenicity [75]. Unnikrishnan and Klibanov [69] on the other hand, state that complement activation aids MB adherence in the microvasculature. Although PEGylation of UCAs might decrease the circulation time, it does reduce immunogenicity and thus seems to be desirable.

**Attaching ligands**

The ligand that makes the tUCA functional is typically a peptide, protein, polymer, antibody, nanobody or aptamer [68, 76-78] (Fig. 2.1A). A reactive moiety suitable for conjugation with the ligand of interest needs to be attached to the tUCA shell, of which biotin (noncovalent), or covalent coupling via a carboxylate group, thiol, or maleimide are most common [69, 79] (Fig. 2.1A3). Covalent coupling does not require foreign proteins such as streptavidin, so the chances of immune response in a clinical setting are low [80]. A carboxyl group incorporated in the tUCA shell can be activated with carbodiimide, forming an active ester that reacts with the protein amino group, forming an amide bond. However, proteins possess multiple lysine residues, so coupling via amide bonds is random and may therefore interfere with ligand-receptor interaction. As an alternative, a maleimide on the shell is coupled to a thiol group on the ligand (or vice versa), forming a thioether. The advantage of maleimide-thiol coupling is oriented coupling: a ligand protein possessing a single thiol then has a single point attachment to the bubble shell. This retains the affinity of the ligand to its target [69]. A new class of ligands are camelid-derived single-domain antibody-fragments (~15 kDa) called nanobodies, that do not induce an immune response in humans [77].

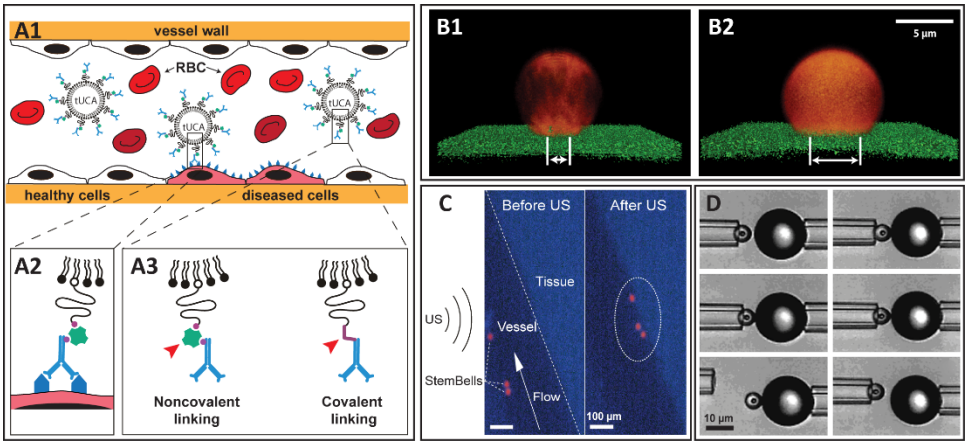


**Fig. 2.1.** Targeting and binding of tUCAs. **(A)** tUCAs targeted to their specific biomarker via an antibody (the antibody is used as an example and can be replaced by other ligands, as mentioned in the text). **(A1)** shows both free and adhered tUCAs in a blood vessel (RBC = red blood cell). **(A2)** shows a detailed representation of a ligand that is coupled to the lipid shell via biotin-streptavidin bridging, where the ligand adheres to the biomarker. The red arrows in A3 point to an example of a non-covalent linker (i.e. biotin-streptavidin bridging) and a covalent linker. **(B)** A lipid-coated MB with a shell based on DSPC (**B1**) or DPPC (**B2**), where the DSPC-based MB has a smaller binding area (indicated by white arrow) and a more spherical shape than the DPPC-based MB (reprinted (adapted) from Kooiman et al. [70], with permission from John Wiley and Sons). **(C)** StemBells before the application of US (left panel) are pushed towards the vessel wall due to acoustic radiation force (right panel) (reprinted (adapted) from Kokhuis et al. [81] with permission from John Wiley and Sons). **(D)** A MB attached to a glass bead via two micropipettes. The force needed to separate them is used to measure the binding force (reprinted (adapted) with permission from Kim et al. [82]. © 2014 American Chemical Society).

### Biomarkers and targeting strategies

tUCAs can be decorated with ligands against various diseases. As typical UCAs are confined to the vascular tree [65], the most commonly targeted biological processes are angiogenesis, inflammation, and thrombosis. With the introduction of smaller tUCAs that can extravasate, apoptosis can also be targeted [83].

*Angiogenesis*

Generally, tumors can be targeted by means of biomarkers for angiogenesis: $\alpha_v\beta_3$ integrin, vascular endothelial growth factor (VEGF), vascular endothelial growth factor receptor 2 (VEGFR2), endoglin (CD105) [68, 76, 84, 85], or a combination hereof [86]. Cyclic RGD is a clinically translatable ligand that was confirmed to adhere to endothelial cells expressing $\alpha_v\beta_3$. In addition, the bubbles conjugated to cRGD had sufficient residence time to attach to the integrin and were specific for $\alpha_v\beta_3$-expressing cells [87]. Another strategy to target $\alpha_v\beta_3$ used the clinically approved contrast agent Sonazoid. The PS incorporated in the UCA

coating was conjugated to lactaderin. This is analogous to the process of phagocytosis: apoptotic cells externalize PS allowing lactaderin to bind to PS to promote binding to the integrins on the surface of phagocytic cells [88]. Since adherence of the MBs functionalized with lactadherin to human umbilical vein endothelial cells (HUVEC) under flow was higher than for bare MBs, this complex has potential to be translated to the clinic for targeting angiogenesis.

For VEGFR2 targeting the lipid-coated BR55 bubble (Bracco Diagnostics) is most promising for translation to the clinic for which a heterodimer peptide is directly conjugated to the PEGylated lipid [84]. Recently, a phase 0 clinical trial with this agent for prostate cancer was successfully conducted [89].

*Inflammation*

Inflammation plays a role in several diseases, such as atherosclerosis, and transient ischemia [90-93]. Specific inflammation markers that have been used for tUCAs are intracellular adhesion molecule 1 (ICAM-1), vascular cell adhesion molecule 1 (VCAM-1), E-selectin, and P-selectin [74, 76, 94, 95]. MBs targeted to VCAM-1 can be used to discriminate the severity of inflammatory burden in mice with various degrees of atherosclerosis [90]. This suggests that assessment of early inflammation in plaques is feasible. However, the same study showed that MB attachment to endothelial cells exposed to high wall shear stresses was very low (*in vitro*). This did improve with short interruptions of the high shear rate, as is the case with a pulsatile blood flow. Since the adhesion molecules ICAM-1 and VCAM-1 mediate the firmer adhesion of the leukocytes to the endothelium, and E-selectin and P-selectin promote the initial attachment and rolling of leukocytes [76], targeting both selectin and adhesion molecules can potentially improve initial binding and increase the binding strength.

*Thrombosis*

Targeting of thrombi is mainly focused on the glycoprotein IIb-IIIa (GPIIb-IIIa or CD41/CD61) expressed by activated platelets in the thrombus [66, 68, 76, 96]. This glycoprotein mediates platelet-aggregation and is the most abundant receptor on the platelet surface [96]. Using Targestar-SA (Targeson Inc., San Diego, CA, USA) conjugated with anti-GPIIb/IIIa single-chain antibodies, these bubbles bound specifically to activated platelets *in vitro*. This may allow for real-time *in vivo* molecular imaging of acute arterial thrombosis and monitoring of pharmacological thrombolysis. Next to antibodies, it has been shown that cRGD can also be used to target GPIIb-IIIa. Although this ligand is generally known as a marker for angiogenesis, cRGD was shown to be specific for GPIIb-IIIa (also known as integrin $\alpha_{iib}\beta_3$) as well [97]. cRGD was conjugated to the MBs via thiol-maleimide coupling and binding to GPIIb-IIIa was evaluated *in vitro* in the presence of plasma and under wall shear stresses up to 8 dynes/cm$^2$ [66]—a value representative for the human aorta

averaged over the heart cycle [98]. Several studies have demonstrated that cRGD exhibits an ~30× higher binding efficiency than linear RGD, and indeed significantly more cRGD bubbles adhered up to the highest shear rate *in vitro* and in the larger arteries of mice [66].

Nakatsuka et al. [78] recently introduced a new concept using MBs that are only acoustically active at thrombin levels associated with clot formation. The targeting moiety of these bubbles was a thrombin aptamer crosslinking strand (TACS). Crosslinking limits the nonlinear signal generation of the MB due to the immobilization of the lipids in the shell. Upon decrosslinking the polymer-DNA strands completely displace from the TACS, allowing the MB to oscillate freely, enhancing their nonlinear response. The MBs consisted of DSPC, DPPA (1,2-dipalmitoyl-*sn*-glycero-3-phosphate), and 1,2-distearoyl-*sn*-glycero-3-phosphoethanolamine-poly(acrylic acid)-TACS (DSPE-PAA-TACS). When the bubbles are in contact with thrombin in the thrombus, this protein binds to the aptamer, which results in decrosslinking. The *in vitro* onset of decrosslinking was about 20 nM thrombin. Since *in vivo* clot formation starts with a concentration of ~25 nM thrombin this offers opportunities to detect small clots at an early stage [78]. This has been shown *in vivo* using similar MBs, but with different amounts of DSPE-PEG(5000) added to the mixture [99]. Small amounts of PEG were found to improve stability, while higher concentrations did not contribute significantly to stability. Indeed, it was also shown that these aptamer MBs enhanced US signal in the vicinity of clots.

**Novel targeting strategies**

The last few years molecular imaging using MBs has emerged and multiple novel targets have been proposed and investigated. Prostate cancer is difficult to diagnose noninvasively, and common practice is routine clinical testing in the laboratory to determine the level of prostate-specific antigen in the blood. However, this test lacks sensitivity and specificity [100]. The prostate-specific membrane antigen (PSMA) has higher expression levels in prostate cancer epithelial tissue than in normal prostate tissue and benign prostatic hyperplasia [101], and is therefore very promising for UMI and staging of prostate cancer as shown *in vitro* [102]. Next to prostate cancer, other types of cancers have been successfully targeted *in vivo* using tUCA: 1) tumor vessels of angiosarcoma that were targeted via secreted frizzled related protein 2 (SFRP2) using DSPC:PEG(2000)-PE bubbles [103]; 2) ovarian cancer tumor vasculature that expresses CD276 with Target-Ready MicroMarker conjugated to anti-CD276 [104]; and 3) the neovasculature of pancreatic ductal adenocarcinoma targeted to thymocyte differentiation antigen 1 (Thy1 or CD90) using anti-Thy1 MBs [105]. The latter two are specific endothelial markers for human cancer types, which are a challenge to investigate in a preclinical setting. The group of Willmann [104, 105] therefore developed a mouse model that expresses human vascular biomarkers by transfecting mouse endothelial cells with the human biomarker of interest and implanting these together with the tumor cells of interest.

In a preclinical setting Targestar-B was targeted to epidermal growth factor receptor (EGFR) and CD147 expressed in head and neck squamous cell carcinoma, where using the dual targeting was reported as most promising [106]. Although E-selectin is not a novel target, its upregulation due to inflammation can also be used to monitor tumor progression and metastasis. E-selectin can therefore be used as a new targeting strategy for early screening for tumors with metastatic potential [85]. Next to novel targeting strategies for tumors, ischemia-reperfusion after myocardial infarction was targeted to matrix metalloproteinase-2 (MMP-2) using polymer-shelled microcapsules. Apoptosis is another recently studied target, typically targeted to PS. Annexin V is known to specifically bind to PS [107] and was used for apoptosis imaging in breast cancer cells using nanobubbles [83].

**Techniques to enhance binding**

Binding of tUCAs to target biomarkers under *in vivo* conditions is a key factor for successful application of molecular imaging for diagnosis and therapy (Fig. 2.1A). Methods to enhance binding of targeted MBs (tMBs) generally depend on adjustments in the coating of the tMBs and/or applying acoustic radiation force to push the tMBs to the target cells. Deflating the tMBs to increase the shell surface area [95], conjugating two [108] or three [109] different ligands to the coating, or optimizing the length of the ligand linker [110] are among those studies optimizing the tMBs for an enhanced binding effect. Also, the probability of successful binding may be increased by homogenizing the ligand distribution on the MB shell [70], but needs further investigation. In addition, larger tMBs have a higher binding force because of their larger binding area. Nevertheless, the shear forces induced by the blood flow experienced by larger tMBs are higher than those experienced by smaller tMBs: this increases the risk of detachment of larger tMBs from their targets. In a numerical study, the optimal tMB size for enhanced binding (assuming they keep their spherical shape) is suggested to be in the range of 2–4 μm in diameter [111]. In a very recent study, super-resolution microscopy was used to compare tMBs based on DSPC or DPPC in terms of ligand distribution, binding area, and their shape upon binding (Fig. 2.1B) [70]. This study shows that DSPC tMBs keep their spherical shapes after binding (Fig. 2.1B1) and have significantly smaller binding areas than DPPC tMBs, which had a dome-shape after binding (Fig. 2.1B2). Magnetic MBs have also been developed to enhance the targeting in UMI and therapy [112-114]. Magnetic targeting uses an externally applied magnetic field, typically applied using a permanent magnet, to control the location of magnetically responsive MBs. Various magnetic MB preparations and applications have been published by Stride et al. in 2009 and 2012 [113, 115]. For instance, the gas core of the MB can be surrounded by a ferrofluid and stabilized by an outer coating of L-α-PC. Such a magnetic MB could increase the dwell time of tMBs in a target volume, whilst specificity could be provided by biochemical targeting [115].

In addition to the tMB shell modifications, acoustic radiation force [116] can be used to push the MBs against the vessel wall to further improve the targeting rate of the MBs [117-120]. This technique was also successfully used to improve the delivery of stem cells to the vessel wall which can be used for the repair of damaged tissue (Fig. 2.1C) by developing echogenic complexes by conjugating tMBs to stem cells (StemBells) [81].

**Measuring binding force**

To evaluate the efficacy and strength of tUCAs, a measurement system capable of assessing the strength of various binding configurations is necessary. Several *in vitro* methods have been proposed. Kim et al. [82] used a micromanipulation technique to adhere a single tMB to an individual glass bead using two separate pipets (Fig. 2.1D). The pressure applied by the bead pipet was incrementally increased until the MB detached from the bead. Using this method, the binding force was measured as a function of composition and structure of the lipid shell and the receptor-ligand pair in a controlled *in vitro* environment. For instance, the detachment force for the biotin-PEG-avidin system was measured to be in the order of 100 nN assuming the contact area of the MBs and the coated surface to be around 10 $\mu m^2$. In another study, atomic force microscopy (AFM) was used for assessing the adhesive interactions of tMBs with their target cells *in vitro* [121]. They used in-house developed lipid-shelled tMBs conjugated to the CD31 antibody using biotin-avidin bridging for adhesion to Sk-Hep1 hepatic endothelial cells and measured single distributions of the binding forces with a median of 93 pN. Controlled shear flow has also shown potential for monitoring the binding force of MBs targeted to P-selectin *in vitro* [122]. In this experiment attachment and detachment of tMBs to P-selectin immobilized on a culture dish was investigated in a parallel-plate flow chamber by increasing shear stress at intervals of 30 seconds. The accumulation rate first increased with shear stress, reached a maximum at ~0.6 $dyn/cm^2$ and then decreased. Half-maximal detachment was reached at 34 $dyn/cm^2$. These results suggest that accumulation and retention of tMBs are possible under physiologic flow conditions [98]. Another approach for measuring binding force is the effect of secondary Bjerknes forces on tMBs, which was studied using a high-speed camera [123, 124]. The secondary Bjerknes force is an averaged net force that neighboring MBs experience due to their oscillations in an ultrasound field. The direction of the force depends on the phase difference between the MB oscillations and the oscillating pressure gradient [44]. Kokhuis et al. [123] observed that bound tMBs deform in the direction of their neighboring MB when they were subjected to secondary Bjerknes forces. If low-intensity ultrasound is applied, the deformation induces an elastic restoring force, causing the MBs to recoil back to their equilibrium position. For higher acoustic pressures, the secondary Bjerknes force can break the bond between the tMB and the surface. Using this technique, the binding force between a single biotinylated MB and an avidin-coated surface was measured to be between 0.9 and 2 nN. In addition, the optical observation of the event suggests that lipid

anchors are pulled out of the MBs shell, rather than destruction of the strong bond between biotin and avidin [123].

## 2.4. CHARACTERIZATION OF tUCAs

Non-targeted MBs for contrast-enhanced imaging, such as SonoVue and Definity, have been thoroughly characterized in terms of their acoustic behavior in an US field [125-128]. These studies mainly focused on bulk measurements, as regular contrast-enhanced US imaging is also performed in vessels containing high concentrations of microbubbles. However, for imaging of tMBs where only very few adhered MBs may be in the imaging field, the response of only a single MB or a cluster of MBs has to be detected [129]. The response of a single MB in an US field is therefore of high interest to aid enhancement of the backscattered signal to improve imaging. A first step is to determine the MB properties after attaching a targeting ligand to it. The next step is the characterization of tMBs adhered to their molecular targets, and comparing this to the response of non-adhered tMBs to find parameters to distinguish them from each other.

**Functionalized lipid-coated MBs**

Only a few studies used functionalized MBs to determine the effect of functionalization on the MB properties; in particular their elasticity using either atomic force microscopy (AFM) or high-speed optical imaging. Using AFM, an elasticity was found that was almost 30× higher for streptavidin-functionalized bubbles than for bare lipid-coated bubbles (710±41 vs 25±1.4 mN/m; DPPC:PE-biotin, 90:10 mol%) [130]. Recently, the same group performed AFM studies on bubbles with a $C_3F_8$ core and a lipid-coating of DPPC:DSPE-PEG(2000)-biotin or DPPC:DOPE-biotin (1,2-dioleoyl-*sn*-glycero-3-phosphoethanolamine-biotin) in a 90:10 ratio [131]. Both types were functionalized with streptavidin and bubbles with diameters between 3 and 4 µm were deformed up to 20% of their original size, whereas non-functionalized bubbles were deformed up to 50%. Here, streptavidin functionalization increased the elasticity to 26.9±1.4 mN/m for the PEGylated bubbles, but PEGylation itself was also found to increase the elasticity (17.7±0.7 vs 10.7±0.5 mN/m). However, the increase in elasticity between PEGylated and non-PEGylated MBs might actually be a consequence of the different lipids that were used for both bubble types: DSPE or DOPE as it has recently been shown that the main lipid of non-targeted biotinylated MBs changes the distribution of the lipids in the shell and its shell properties [70, 71]. The authors do not explain the large difference in stiffness values between both studies [130, 131]. Indeed, there does not seem to be a straightforward explanation. The preparation method is identical, but although the biotinylated lipids are different this cannot explain such a large difference. The major difference between both studies is the PEGylation [131], but this was found to increase the stiffness, and contradicts with their results.

To study the influence of functionalization on several MB properties, we functionalized identical biotinylated MBs—with either DSPC or DPPC as the main coating lipid [70]—with streptavidin via avidin-biotin bridging [132]. These unbound bubbles were investigated at frequencies between 1 and 4 MHz at a pressure of 50 kPa and their vibrational response was recorded by optical ultrahigh-speed imaging [20, 71]. For DSPC and DPPC-based bubbles the acoustic stability increased after functionalization, although their shrinkage remained significant (Table I). The resonance frequencies of functionalized and non-functionalized DSPC MBs were similar, whereas those of DPPC MBs were higher for the functionalized ones. The number of MBs responsive at the subharmonic (SH) frequency was slightly lower for functionalized DSPC bubbles than for non-functionalized DSPC bubbles. For DPPC there was no change after functionalization. At the second harmonic frequency the functionalized and non-functionalized DSPC bubbles behaved similar, whereas after functionalization hardly any DPPC bubbles responded. The viscoelastic shell properties of both functionalized and non-functionalized MBs were estimated [20, 71] using the Marmottant model [19]. The shell elasticity for DSPC slightly increased after functionalization, whereas for DPPC the elasticity increased almost fourfold. The shell damping and viscosity, on the other hand, did not change after functionalization.

**Table 1.** Characteristics of streptavidin-functionalized and non-functionalized DSPC and DPPC bubbles

| Type | Strept-avidin | # MBs | Stability (%)* | Responding at SH (%) | Responding at second harmonic frequency (%) | Elasticity (N/m) | Viscosity ($\times 10^{-8}$ kg/s)* |
|---|---|---|---|---|---|---|---|
| DSPC | No§ | 15 | 95.9 (3.5) | 27 | 67 | 0.17 ± 0.06 | 1.2 (0.9) |
| | Yes | 12 | 99.1 (2.8) | 17 | 75 | 0.23 ± 0.06 | 1.0 (0.5) |
| DPPC | No§ | 14 | 90.3 (8.2) | 67 | 17 | 0.06 ± 0.08 | 1.0 (0.3) |
| | Yes | 6 | 94.4 (4.3) | 71 | 79 | 0.21 ± 0.08 | 1.8 (0.6) |

* Median (interquartile range, IQR)

§ Data adapted from van Rooij et al. (14)

A critical side note regarding the elasticity estimated for the functionalized DPPC MBs is the narrow size distribution that did not cover the same range as the DSPC bubbles (DPPC: 4.8-6.2 μm; DSPC: 3.1-7.3 μm). However, our results clearly show an increase of the resonance frequency and thus of the elasticity, which corresponds with the results obtained using AFM [130, 131]. The increase in elasticity after functionalization is believed to be due to the presence of crystallization of streptavidin around the lipid shell forming a stiffer external layer [131] as also observed on streptavidin-functionalized giant unilamellar phospholipid vesicles [133, 134]. This is also consistent with the increased stability: a stiffer and thicker shell better prevents gas escape [135]. The above mentioned studies all found differences between streptavidin-functionalized MBs and non-functionalized MBs. In contrast, Overvelde et al. [136] concluded that the frequency of maximum response and the

maximum amplitude of oscillation of functionalized bubbles (BG-6438, Bracco Imaging S.p.A., Milan, Italy) and non-functionalized bubbles (BG-6437, Bracco) did not seem to change.

Although streptavidin-biotin binding is a useful tool to gain insights into the effects of coupling of relatively large and heavy ligands to MBs *in vitro*, it can never be used clinically due to strong immune responses [80]. Therefore, alternatives for *in vivo* targeting have to be considered, such as peptides, polymers, or antibodies, as discussed in the Targeting and binding section. Peptides consist of a few amino acids (~100-200 Da) [137] and the RGD-peptide used typically for targeting has a molecular mass of ~380 Da. Since functionalizing bubbles with a small, low molecular mass ligand such as biotin (~250 Da) has hardly any effect on the MB response, it is expected that functionalization of MBs with a peptide has also minimal effect. Polymers are regularly used in MB designs to increase circulation times and to function as a stealth mechanism, mostly in the form of a PEG-lipid [138]. Abou-Saleh et al. [131] only mentioned a slight increase in elasticity upon PEGylation, but it is not known whether addition of a polymer changes other properties. Streptavidin-functionalization, on the other hand, has a significant effect on MB response. Since antibodies (~150 kDa) are more than 2× heavier than streptavidin (~60 kDa) an even larger effect, especially on the elasticity and resonance frequency, is expected. In addition, coupling an antibody covalently to a lipid could also induce cross-linking of the lipids as there are usually several reactive groups on an antibody.

**Discriminating free from adhered MBs**

The next step after functionalization of MBs is studying their behavior when they have bound to their molecular target. Moreover, the differences in acoustical signals between free and adhered bubbles are the key feature to facilitate discrimination.

Some of the non-functionalized biotinylated bubble types described in the previous section [70, 71, 129] were used to target an avidin-coated cellulose capillary using acoustic radiation force to promote binding [139]. Optical imaging was used to confirm bubble adhesion and high-speed optical imaging was used to visualize the oscillations [140]. The adherent MBs oscillated symmetrically in the plane parallel to the wall (similar to a free-floating MB) and asymmetrically in the plane normal to the wall. The side of the MB near the boundary expanded and contracted to a lesser extent than the side away from the boundary. The normalized radial expansion was larger for adherent bubbles in both imaging planes. When the transmission pressure was increased from 240 to 450 kPa, the center of the microbubble began to collapse toward the fixed boundary, producing a jet. At even higher pressures (650 kPa) fragmentation was observed in the plane parallel to the boundary, where the remaining fragments expanded and contracted, and were displaced along the wall away from the ultrasound source [139]. This can be advantageous for drug delivery applications when the drug is incorporated in or attached to the shell of the MB.

The response at the fundamental frequency was larger for adherent bubbles than for free bubbles [140], the responses at the SH frequency were similar, and the second harmonic component also increased [139]. At increasing pressures the signals at the third and fourth harmonic frequency were also higher for adhered MBs. One of the underlying causes of the higher fundamental (and maybe also harmonic) signals of adherent bubbles could be due to the small diameter of the bubbles (<< acoustical wavelength) and the nearly uniform spatial distribution of free bubbles, resulting in incoherent echo summation and a small backscattered intensity from each sample volume. Alternatively, a layer of tUCA adherent to the inside of a vessel wall reflects US coherently, resulting in a large reflection of the fundamental component. Secondly, the adherent bubbles formed aggregates, which increase the coupling between adjacent bubbles and thus their effective scattering cross section [140].

In addition to adhered and free floating microbubbles, Overvelde et al. [136] studied bubbles close to an OptiCell wall, using ultrahigh-speed imaging. For non-functionalized bubbles close to the wall the amplitudes at the frequency of maximum response were lower than for free-floating non-functionalized MBs. However, the OptiCell wall was not blocked for unspecific binding, hence these bubbles probably also adhered to the wall and cannot be considered as non-adherent. The observation that still holds is the 50% lower frequency of maximum response for adherent functionalized MBs than for functionalized and non-functionalized MBs in the unbounded fluid (150 μm away from the wall). The lower frequency of maximum response for bubbles bound to the OptiCell wall might be due to an increase in damping due to the coupling of the bubble and the wall.

Besides optical interrogation of bubbles, acoustical measurements have been used to characterize tMBs. Prior to the acoustical measurements, the biotinylated bubbles were sized by optical microscopy and subsequently injected in a capillary with or without streptavidin-coating [141]. Scattering of non-biotinylated bubbles and biotinylated bubbles at the fundamental frequency (2 MHz) was similar, whether or not the capillary was coated. The second harmonic resonance radius of an adherent MB was higher than that of a non-adherent targeted bubble, i.e. the second harmonic resonance frequency was higher. The reason that a difference between biotinylated and non-biotinylated bubbles was not found might be just a size or mass effect of the functionalization ligand. Not only is biotin (~250 Da) much smaller than streptavidin (~60 kDa), but one streptavidin molecule can bind up to four biotin molecules [138] that could form a protein layer around the shell, as suggested by others [131, 134]. The effect of biotinylation on the resonance frequency might therefore be only minimal.

The most recent study that compared free with bound MBs focused on the SH response frequencies at 11 and 25 MHz [142]. The rationale behind applying higher frequencies is imaging in a preclinical setting, but also in a clinical setting for the assessment of atherosclerosis in the carotid or for superficial tumors these high frequencies are needed.

This study used the commercially available Target-Ready MicroMarker (lipid-coated and streptavidin functionalized) which had stronger SH activity for larger bubbles when insonified at 11 MHz, i.e. the SH resonance frequency decreased upon binding. At 25 MHz the difference was smaller between free and bound MBs, but the amplitude of the adhered bubbles was 20% higher. In general, the pressure thresholds for SHs were lower at 11 MHz than at 25 MHz. Bound bubbles disrupted at lower pressure thresholds than unbound, especially at 11 MHz. At this frequency mainly compression-only behavior was observed for both bound and unbound MBs, whereas at 25 MHz the oscillations were expansion-dominated. Although differences in SH resonance were present, no shift in the fundamental resonance frequency was observed. This study also aimed to find a strategy to enhance the SH signal for imaging. Optimal pulse-inversion techniques require the same phase (0 radian phase shift) of the responses induced by both transmit pulses. Consequently, due to complete constructive interference (much like an opposite phase of $\pi$ radian is desirable between fundamental echoes to ensure complete destructive interference) this would yield the maximal SH amplitude. At 11 MHz the SH emissions were consistently half a wavelength ($\pi/2$ radian) out of phase and at 25 MHz it varied more, but a similar trend was observed. This suggests that with the incorporation of a phase-shifting strategy; SH signal amplitudes from pulse-inversion techniques can be increased to 60% to enhance imaging.
Interestingly, the before mentioned studies show an opposite effect on the resonance frequency upon binding of the MBs. For streptavidin-functionalized MBs in an OptiCell insonified at pressures between 2 and 4 MHz, the resonance frequency decreased [136], while for biotinylated MBs in a streptavidin-coated capillary insonified at 2 and 3.5 MHz the resonance frequency increased [141]. At higher frequencies streptavidin-coated bubbles at 11 MHz showed an increase in resonance frequency, while they showed a decrease at 25 MHz [142]. A potential explanation for the observed opposing trends may be frequency-dependent boundary effects, for example caused by frequency-dependent boundary stiffness [142]. Nevertheless, these contradictions show that much is still unknown concerning the effects of binding on the bubble response. As this is the key factor for acoustical differentiation between bound and unbound MBs, single MB studies are needed for reliable determination of the bubble properties. Especially *in vivo* studies could aid the understanding of MB behavior in a clinically-translatable environment.

**Other types of targeted tUCAs**

Next to the lipid-coated MBs described above, the characteristics of other types of tUCAs such as polymer and nanobubbles have been studied. Schmidt et al. [143] used poly(l-lactic acid) (PLA) capsules that bonded to a neutravidin-adsorbed polystyrene surface (similar to an OptiCell wall). In this study the microcapsules adhered to the surface under flow conditions with wall shear stresses between 0.2 dyn/cm$^2$ and 1.5 dyn/cm$^2$. The capsules first slowed down before binding and were easier to detach at higher shear stresses and higher

acoustic pressures. At the highest pressure of 291 kPa an appreciable fraction of the capsules also ruptured and released their gas content.

Recently, polyvinylalcohol (PVA) capsules gained specific interest due to their chemical versatility that enables functionalization with different ligands, for instance hyaluronic acid for the targeting of tumor cells and tissues [144]. The properties of the air-filled PVA capsules were compared to other polymer-coated capsules and commercially available bubbles with lipid and protein coatings [145]. At very high pressures up to 2.344 MPa (mechanical index (MI) = 1.58) the shell's shear modulus was estimated to be 3.7 MPa. Assuming a shell thickness of 0.5 μm [145] this corresponds to an elasticity parameter of 5.6 N/m: an order of magnitude higher than for lipid-coated bubbles [20, 127, 128]. The *in vitro* capsule concentration necessary to obtain the same signal was similar to Albunex, 5 to 10-fold lower than for SonoVue and Definity and even 35-fold lower than for Optison. Using the same concentrations for SonoVue and PVA bubbles the second and higher harmonic signals for PVA were up to 10 dB higher.

Sub-micron sized nanobubbles (~200 nm) may potentially extravasate by passing the capillary barrier to reach cells at the tumor cell target site [66]. This property makes them promising for targeted molecular imaging and drug delivery in tumors. Due to the higher permeability of tumor vasculature—enhanced permeability and retention (EPR) effect—nanobubbles are more likely to accumulate in tumors, known as passive targeting. The stability of the lipid-Pluronic nanobubbles was higher than that of Definity (*in vitro*). In mice, the lipid-Pluronic nanobubbles were imaged using contrast harmonic imaging at 8 MHz and their contrast in the tumor was higher than for Definity. This was ascribed to the possible extravasation of the nanobubbles, which retains them in the tumor and thus increased the signal.

## 2.5. ULTRASOUND MOLECULAR IMAGING

UMI that uses tUCAs is a multidisciplinary technology applicable for both diagnosis, monitoring of lesion formation, and therapy evaluation.

### Contrast-specific imaging techniques

MBs generate higher harmonics, SHs and ultraharmonics of the excitation frequency [146-151]. Upon excitation by multi-frequency bursts, MBs can also act as nonlinear mixers of the excitation frequencies and produce cross-products [152-154]. Conventional nonlinear imaging techniques, at lower frequencies (< 15 MHz), focus mainly on detection of higher harmonics [155-159]. The need for high resolution UMI in small animal applications has pushed the frequencies used in preclinical imaging to above 15 MHz [160]. At these frequencies similar nonlinear techniques have been implemented [161-165]. However, performance of these imaging methods is degraded because the excitation frequency is

much higher than the resonance frequency of the MBs, attenuation is higher, and far-wall artifacts are a big challenge to overcome [166-170]. Therefore, improved imaging methods have been extensively studied, such as improved harmonic imaging methods [171-173], chirp coded excitation alone [174, 175] or combined with pulse inversion [176, 177]. Among the nonlinear components of the MB response the SH signal has drawn much attention lately, due to its MB specificity and artifact-free characteristics. Moreover, SH response of the MB has shown its potential for selectively imaging bound tMBs [142, 178]. The SH signal is strongly dependent on the applied acoustic pressures, the ambient pressure variations [147, 179-183], and the envelope of the excitation signal [184-188]. The SH signal is also less attenuated than the ultraharmonic and higher harmonics, and therefore a more suitable choice for high frequency applications. Next to the different strategies to improve the sensitivity of MB detection, adjusting the MBs is another approach to gain sensitivity. It has been shown that UMI of sorted 3 µm MBs results in an approximately 20 times higher video intensity than for unsorted populations [189]. This size lies within the optimal tMB size distribution for enhanced binding, as shown numerically [111]. This can significantly maximize the sensitivity to small numbers of MBs for UMI.

Selective imaging of true bound tMBs from free flowing unbound ones is another challenge that is extensively studied [190-194]. The most common approach for imaging and quantification of tMBs is to wait for a few minutes (2 [195] to 20 minutes [196]) so most of the circulating MBs have been taken up by the lungs and liver (i.e. RES system), or have been dissolved. This time also allows the tMBs to accumulate at the site of their targets. Then low power nondestructive pulses are applied to image the tMBs, followed by a high power disruptive pulse (flash) to eliminate the MBs within the imaging plane which is again followed by low power pulses to image the residual circulating MBs (Fig. 2.2A). The intensity difference before and after the flash corresponds to the amount of bound tMBs and is a measure for the biomarker concentration [197-200], as shown in Fig. 2.2A. In such methods the quantification of bound tMBs strongly depends on the injected dose, imaging system gain, and local perfusion [190]. In addition, the influence of inhaled gasses in the anesthetic protocols influences the MBs longevity [201-204]. These studies confirmed longer circulation times of in-house lipid-shell decafluorobutane-filled UCAs and commercially available UCAs such as Definity® and Albunex® when animals breathe medical air instead of pure oxygen as the carrier gas for the isoflurane anesthetic. This is perhaps due to a reduced ventilation/perfusion mismatch and classical diffusion between the blood gasses and the gas inside the MBs (e. g. perfluorobutane), in which nitrogen plays a role by increasing the volume of the MBs and diluting other gas species in the MBs gas core [204].

The presence of tissue motion can compromise quantification, as well as high concentrations of freely recirculating MBs after the waiting period. Several methods for selectively imaging the bound tMBs in real time have been proposed: utilizing an image-push-image sequence [190]; transmission at a low frequency and reception at a high

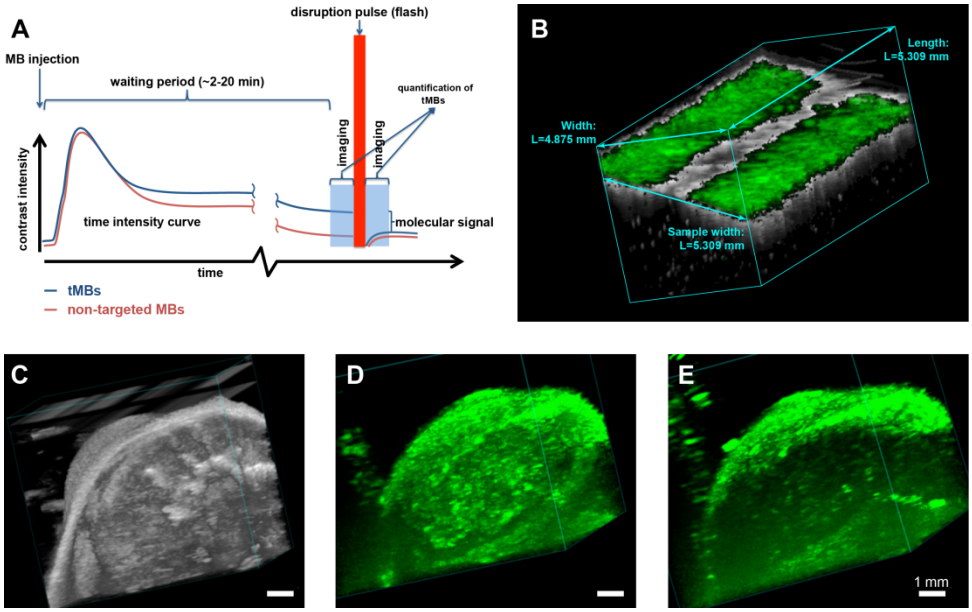


**Fig. 2.2.** Ultrasound molecular imaging. **(A)** Timeline of the imaging protocol and schematic representation of a typical time intensity curve in the region of interest (e.g. tumor). **(B)** B-mode (grey) overlaid with non-linear contrast mode (green) US imaging in 3D to detect the $\alpha_v\beta_3$ expression via $\alpha_v\beta_3$-tMBs (MicroMarker) adhered to the SVEC cells (SV40-transformed murine endothelial cell line), which were cultured in an OptiCell. The band in the middle of the figure in which there is no green signal present shows the destruction of the tMBs with the flash burst. **(C–E)** 3D micro-UMI using VEGFR-2 Target-Ready MicroMarker on a subcutaneous human hepatocellular carcinoma tumor which was developed by injection of HuH7 cells in male nude NMRI mice. All animal work was approved by the regulatory authority of Erasmus MC and performed in compliance with the Dutch government regulation guidelines. **(C)** 3D B-mode US render of the tumor. **(D)** 3D render of contrast images 10 min after bound tMBs within the entire volume of the tumor. **(E)** 3D render of contrast images 10 min after injecting the control MBs. Lack of signals within the tumor indicates no attachment of control MBs to the VEGFR-2 receptors. For **(B–E)**, imaging was performed with a Vevo 2100 US imaging system and MS250 probe at 18 MHz. The probe was moved with increments of 32 mm using a step motor (VisualSonics).

frequency [191]; using the SH response of the MBs and interframe filtering [192]; and using singular value spectra properties [193]. However, none of the proposed methods have yet been applied *in vivo*. Only Pysz et al. developed a quantification method based on dwell time MB signal measurements, which was tested *in vivo* in well vascularized tumors in mice [205]. However, in this *in vivo* model where attachment of tMBs is significant, the classical way of quantification also performs well. Thus, the performance of the method developedby Pysz et al. in applications with very few tMBs in the presence of circulating MBs remains unclear. Daeichin et al. have developed an off-line quantification method for the detection of biomarker concentrations *in vivo* in cases with a high number of bound

MBs, as well as only very few bound MBs [206]. This method benefits from motion compensation and individual contrast spot detection, and is capable of distinguishing bound MBs from unbound MBs based on their displacement. Such a quantification method can be applied in studies performed with different imaging settings because it is less sensitive to imaging parameters.

***In vivo* molecular imaging**

As discussed previously, the diagnostic focus of UMI is mainly on inflammation, thrombosis and angiogenesis. Assessment of angiogenesis is perhaps the application where UMI is used the most [86, 90-93, 207-212]. For evaluating tumor growth noninvasively, successful *in vivo* quantification of the expression levels of the angiogenetic biomarkers $\alpha_v\beta_3$ integrin, endoglin, and VEGFR2, which vary during tumor growth in subcutaneous cancer xenografts, have been reported [211]. Recently, an UMI study using MBs targeted to $\alpha_v\beta_3$ in an ovarian cancer model in hens [213], suggested that the detection of ovarian tumor–associated angiogenic microvessels improved when using UMI. For assessing the efficacy of cell-based therapies, UMI has been used to image a genetically engineered cell-surface marker on endothelial progenitor cells to track the fate of these progenitor cells after their delivery into vascular engraftment *in vivo* within Matrigel plugs [214]. Next to the basic research that is performed using UMI, numerous studies are putting a step forward by investigating the possibilities of clinically translatable targeted MBs. In humans, the first phase 0 clinical trial for prostate cancer UMI was presented recently using BR55, a VEGFR2-tUCA [89]. Although it was only a safety study it was reported that 12 out of 14 lesions (proven by histology) could be detected with UMI. Bachawal et al. [215] used BR55 in transgenic mice with breast cancer and ductal carcinoma. UMI allowed for highly accurate detection of both breast cancer and ductal carcinoma in situ and this can be a promising clinical approach for early breast cancer detection. In addition, BR55 has shown its potential for early detection of liver dysplasia in transgenic mice [216].

UMI has also been used to noninvasively assess the effects of anti-inflammatory treatment on endothelial inflammation in early atherosclerosis in genetically modified mice [217, 218]. UMI has also proven its ability to detect biomarkers of early response to chemotherapy in several cancer types by MBs targeted to single biomarker expressions (VEGFR2, $\alpha_V\beta_3$, endoglin, Annexin V, or VEGF-VEGFR complex) [83, 210, 219-221] and MBs targeted to two or more of these biomarker expressions [195]. Impressively, studies have shown that UMI using $\alpha_v\beta_3$-tMBs is a consistent method that can classify a tumor as a responder or a non-responder as early as two days after treatment [222, 223]. To establish the link to clinical oncology Flisikowska et al. [224] have suggested the use of larger animal cancer models with more similarities to humans, such as genetically modified pigs. They proposed programs to generate gene-targeted pigs with mutations in tumor suppressor genes and proto-oncogenes that replicate key lesions responsible for a variety of human

cancers. Whilst tumor models in large animals are challenging, cardiovascular disease can more easily be modeled. A study on miniswines suffering from atherosclerosis showed that an improved endothelial permeability through ultrasound-activated nitric oxide loaded echogenic immunoliposomes, can facilitate the delivery of anti-ICAM-1 conjugated echogenic immunoliposomes to inflammatory components in the arterial wall. This approach therefore has the potential to improve UMI of atheroma [225]. Next to pigs, the expression of P-selectin and VCAM-1 expression in the carotid of nonhuman primates has also been recently assessed with UMI. This study showed that endothelial cell adhesion molecule expression in large arteries could be an early event that coincides with diet-induced obesity and insulin resistance in nonhuman primates [226]. In another recent study on nonhuman primates with myocardial ischemia, UMI showed to be both safe and effective for imaging recent myocardial ischemia. Lipid-coated MBs were functionalized with dimeric recombinant human P-selectin glycoprotein ligand-1, a recombinant ligand appropriate for humans were used [227]. The study suggests that UMI can be useful for detecting recent ischemia in patients with chest pain, even in the absence of necrosis [227].

**Three dimensional UMI**

It is challenging to image the same plane repeatedly in 2D UMI serial studies and small misalignments can already introduce a substantial error. tMBs are attached to their targets and are therefore stationary in UMI applications where tissue motion is absent. This thus opens up opportunities for three dimensional (3D) UMI using 2D probes, by mechanically moving the ultrasound probe over the target of interest. This is illustrated in Fig. 2.2 where 3D UMI is performed with VEGFR2 Target-Ready MicroMarker (FUJIFILM VisualSonics, Inc., Toronto, Ontario, Canada) on subcutaneous human hepatocellular carcinoma tumor in a mouse.

Feasibility of 3D UMI has also been proven by other groups. Streeter at al. [196] performed 3D UMI of tumors expressing $\alpha_v\beta_3$ integrin by mechanically stepping the transducer across the tumor in 800 μm increments. In another study, it was shown that multiple injections of tMBs did not block sufficient binding sites to bias molecular imaging data in serial studies [228], which is an important finding. Using the clinically promising BR55 agent, 3D UMI was shown to be very well suited in depicting the angiogenic activity in very small breast lesions, suggesting its potential for detecting and characterizing these lesions in a very early stages [229]. Combining the effort to selectively image bound tMBs and 3D UMI, Hu et al. [230] used a broadband single pulse imaging sequence (transmitting at low frequencies and receiving at high frequencies) that is faster than the multi-pulse methods. Then, this method was combined with interframe filtering to selectively image targeted MBs without waiting for clearance of unbound MBs, thereby reducing acquisition time from 10 to 2 minutes. Their results suggest a feasible method for 3D UMI that is faster than current multi-pulse strategies.

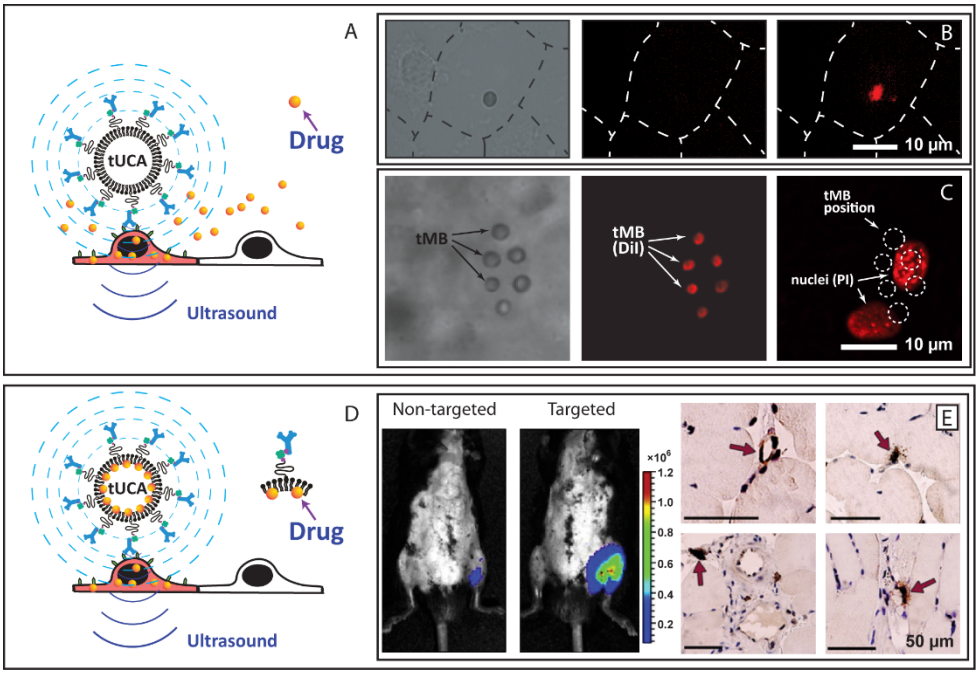


**Fig. 2.3.** US and targeted microbubble mediated drug delivery. **(A)** Schematic of co-administration of the drug together with tUCAs. **(B)** Propidium iodide (PI) uptake in endothelial cells *in vitro* induced by vibrating CD31-tUCAs; dashed lines indicate cell borders. Left panel: bright field before US; middle panel: fluorescence before US; right panel: fluorescence after US showing PI uptake (reprinted (adapted) from Kooiman et al. [10]. © 2014, with permission from Elsevier). **(C)** PI uptake in endothelial cells *in vivo* induced by vibrating $\alpha_v\beta_3$-tUCAs. Left panel: bright field before US showing a cluster of six tUCAs; middle panel: fluorescence before US showing the DiI-labelled tUCAs; right panel: fluorescence after US showing PI uptake (© 2014 IEEE. Reprinted, with permission, from Skachkov et al. [183]). **(D)** Delivery of the drug when it is attached to or incorporated in the tUCA shell. **(E)** P-selectin-tUCAs are five times more efficient than non-targeted UCAs for gene delivery *in vivo* in a hind limb ischaemia skeletal muscle model. Validation of luciferase reporter plasmid transfection in rats using bioluminescence (left two panels) and imunohistochemistry (right four panels; arrows point to plasmid transfection in endothelial and perivascular cells; reprinted (adapted) from Xie et al. [186], © 2014, with permission from Elsevier).

## 2.6. tUCAs AS THERANOSTICS

### Enhanced drug delivery

In combination with ultrasound, UCAs are known to enhance drug delivery. Despite the fact that the mechanism behind this enhancement is not well known, vibrating MBs can stimulate drug uptake through cell membrane pore formation, a process also known as sonoporation, opening of intercellular junctions, or endocytosis [36, 45]. Whilst UCA-mediated drug delivery has been studied since 1997 [231], tUCA-mediated drug delivery is

relatively new. In 2011, Kooiman et al. were the first to show that CD31-tUCAs could sonoporate primary endothelial cells *in vitro* [35]. Cell membrane permeability (Fig. 2.3B) was already induced at acoustic pressures as low as 80-200 kPa (1 MHz, 6×10 cycle bursts), indicated by uptake of the co-administered model drug propidium iodide (PI). Since then, several other studies reported tUCAs for drug delivery by either co-administrating the drug with the tUCAs or loading the drug in/on the tUCAs. Another co-administration *in vitro* study using PI showed that sonoporation of cancer cells by $\alpha_v\beta_6$-tUCAs was higher with chirp pulses from 3-7 MHz than with chirp pulses between 1.3 and 3.1 MHz or single frequency insonification at 2.2 or 5 MHz (110 kPa, 10 µs burst, pulse repetition frequency (PRF) 1 kHz, 2 min treatment) [232]. This can be explained by the fact that chirp pulses cover a broader range of resonance frequencies, as MBs with various sizes have different resonance frequencies; chirp pulses are therefore more efficient than single frequency pulses. In the chicken embryo model (*in vivo*), a single sine-wave burst (1 MHz, 1000 cycles at 150 or 200 kPa) was sufficient for vascular PI uptake using $\alpha_v\beta_3$-tUCA as shown in Fig. 2.3C [233].

tUCAs can also be loaded with genetic drugs (plasmid DNA, siRNA, mRNA) or drugs for local gene/drug delivery. Philips et al. [234] used VCAM-1-tUCAs loaded with plasmid DNA to transfect smooth muscle cells with the model gene green fluorescent protein (GFP) *in vitro* at 1 MHz (200-300 kPa, PRF 100 Hz, ~5 sec per cell) and at 1.5 MHz (200 kPa, PRF 8 kHz, ~5 s per cell). In another study ovarian cancer cells were transfected with wild-type p53 tumor suppressor gene using Luteinizing Hormone-Releasing Hormone analog (LHRHa)-tUCA to induce apoptosis (1 MHz, 0.5 W/cm$^2$, 30 s treatment) [235]. Two studies [236, 237] showed that tUCAs loaded with luciferase plasmid can transfect vasculature *in vivo*. Xie et al. [236] used P-selectin tUCAs in a hindlimb ischemia skeletal muscle model (see Fig. 2.3E; 1.6 MHz, 0.6-1.8 MPa, Power Doppler, pulsing interval 5 s, PRF 2.5 kHz for 10 min), whereas Tlaxca et al. [237] used mucosal addressin cell adhesion molecule-1 or VCAM-1-tUCA in a model for Crohn's disease (1 MHz, 5 W/cm$^2$, 25% duty cycle for 5 min).

Two types of drugs loaded in tUCAs have been reported for cancer treatment. Paclitaxel loaded into tUCAs induced tumor cell apoptosis *in vitro* in ovarian cancer cells (LHRHa-tUCAs, 0.3 MHz, 0.5 W/cm$^2$, 30 sec treatment) [238] and breast cancer cells (LyP-1-tUCA, 1 MHz, 4 W/cm$^2$, 50% duty cycle, 2 min. treatment) [239] as well as *in vivo* (LHRHa-tUCAs, 0.3 MHz, 1 W/cm$^2$, 50% duty cycle, 3 min treatment) [240]. *In vivo*, the tUCAs were administered intraperitoneally allowing the tUCAs to adhere to the ovarian cancer cells. The other anti-cancer drug loaded into VEGFR2-tUCAs was BCNU (1,3-bis(2-chloroethyl)-1-nitrosourea) for the treatment of glioma brain tumors *in vitro* (1 MHz, 0.5 MPa, 10,000 cycles, PRF 5 Hz for 1 min treatment at 2 sites) and *in vivo* (1 MHz, 0.7 MPa, 10 ms burst, 5% duty cycle, PRF 5 Hz, 1 min treatment at 2 sites), where *in vivo* the tUCAs were also used to open the blood brain barrier [241].

**tUCAs versus non-tUCAs for enhanced drug delivery**

Strikingly, when tUCAs for drug delivery are directly compared with their non-targeted UCA counterparts, tUCAs are more efficient both *in vitro* [232, 234, 235, 238, 239] (up to 7.7-fold higher [239]) and *in vivo* [236, 237, 240, 241] (up to 5-fold higher [236]), irrelevant whether the drug was co-administered with the tUCAs or whether the drug was loaded on/in the tUCAs. Although the reasons for this higher efficiency have not yet been investigated, several could be possible. Possibly the main reason could be that tUCAs vibrate against the cells directly as they are bound to the cells, which may result in a more efficient transfer of acoustic energy, especially because sonoporation was only reported in cells adjacent to vibrating microbubbles for non-tUCAs [37, 242]. The acoustic behavior of the tUCAs itself could also explain this difference, as *in vitro* studies have shown that tUCAs are acoustically more stable, vibrate with a larger amplitude at the fundamental frequency, fragment in the plane parallel to the boundary and have a different resonance frequency (see characterization of tUCAs section). Microbubble clustering could also be a phenomenon contributing to the higher efficiency of tUCAs, as a cluster of bubbles is known to behave as one large bubble, which is also associated with a shift in their resonance frequency [243]. This is substantiated by the chicken embryo study in which clusters of 10 to16 tMBs had a 16-fold higher sonoporation efficacy than single tMBs [233].

A disadvantage of using tUCAs for drug delivery was reported by Hu et al. [244] who showed that insonified $\alpha_v\beta_3$-tUCAs temporarily decreased blood flow within the insonified area after application of a 5 MHz, 2 or 4 MPa color-Doppler destruction pulse (6-cycle pulse length, PRF 124 Hz, 900 ms duration). Although such high frequency and pressure pulses are not typically used for drug delivery, temporarily reducing the blood flow could be advantageous to keep the delivered drug in the treated area. The reduced blood flow could also reduce tumor size by itself as has been reported for non-tUCA [245].

With tUCAs now also being used for drug delivery, the terms ultrasound-mediated targeted drug delivery or ultrasound and microbubble targeted drug delivery (UMTD) have become confusing. UMTD is used for drug delivery using non-targeted UCA where "targeted" refers to the local application of the ultrasound itself. We therefore suggest banning the UMTD term and use ultrasound and microbubble mediated drug delivery (UMMD) for non-targeted UCAs and ultrasound and targeted microbubble mediated drug delivery (UtMMD) for tUCAs instead.

## 2.7. OUTLOOK AND CONCLUSIONS

Recent studies on larger human-like animals such as pigs and nonhuman primates, as well as the first phase 0 clinical trial for prostate cancer with the VEGFR2 tUCA BR55 show the capability of clinical UMI in the near future. Recent insights in shell coating properties of tUCAs, new strategies for targeting, and the development of nanoscale tUCAs will open up a new range of opportunities and will broaden the spectrum of diseases that can be targeted.

Intrinsic properties of the tUCAs, such as deformability due to low elasticity could be used as an advantage to improve binding. This underlines the necessity of single tMB investigation to further understand their properties. Upon binding, opposite effects on the resonance frequency are reported, which also reflects a change in harmonic frequencies. The increase in their SH amplitude upon binding could potentially be utilized for selective imaging of adhered tMBs, which could speed up the UMI and increase its specificity. Obviously, 3D imaging is desired for UMI applications, either by mechanically moving a two dimensional probe or using a volumetric 3D probe.

By using tUCAs as local drug delivery systems, intracellular drug uptake can be enhanced several fold in comparison to non-tUCAs. tUCAs able to carry and deliver a high payload are needed, as is the elucidation of the mechanism by which tUCA stimulate drug uptake. A novel therapeutic use of tUCAs for cancer treatment could be the functionalization with kinase inhibitors. These molecules have a high affinity for cancer cell receptors and are already approved or in clinical trials as anticancer drugs, such as gefitinib (EGFR), sunitinib (FLT-1), Bevacizumab (VEGF) [246]. Bound kinase inhibitor-tUCAs could therefore facilitate both UMI and act as inhibitor activators for apoptosis. With BR55 now undergoing regulatory approval for clinical use, this will hopefully pave the way for other tUCA with other targets as well. However, for every new tUCA or drug-loaded tUCA regulatory approval will be needed before clinical use.

tUCAs can also be used as theranostic agent without the addition of a drug or gene, but in combination with high intensity focused ultrasound (HIFU) techniques instead. These techniques utilize high-energy focused ultrasound to locally increase the temperature at the focal point for ablation of tumors. UCAs, as synergists, have become a research topic to improve the efficiency of HIFU treatment [247, 248]. In this field, a folate-tUCA (phase transition nanoemulsion) has shown great potential to enhance HIFU ablation of ovarian cancer *in vivo* [249].

In conclusion, adding to the wide applications of UMI for diagnosis, the therapeutic benefits of this technology also play a major role in its popularity. Detection of diseased cells using tUCAs combined with local drug delivery, sonoporation, and HIFU are good examples of the applications and the potential of UMI for therapy.

**Acknowledgements**

This research is partly supported by the Center for Translational Molecular Medicine and the Dutch Heart Foundation (PARISk), and by NanoNextNL, a micro and nanotechnology consortium of the Government of the Netherlands and 130 partners. This work is also part of the research program Veni, which is financed by the Netherlands Organisation for Scientific Research (NWO) (KK).

Chapter 3

# Microbubble composition and preparation for high-frequency contrast-enhanced ultrasound imaging: in vitro and in vivo evaluation

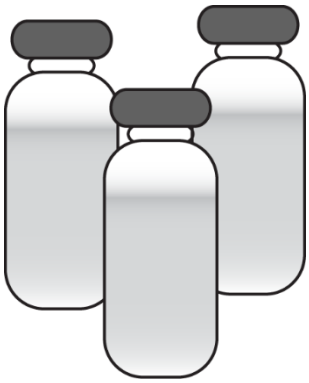

Verya Daeichin, Tom van Rooij, Ilya Skachkov, Bulent Ergin, Patricia A.C. Specht, Alexandre Lima, Can Ince, Johan G. Bosch, Antonius F.W. van der Steen, Nico de Jong, Klazina Kooiman

*IEEE Transactions on Ultrasound Ferroelectrics and Frequency Control* (2016) – *Submitted*

## 3.1. ABSTRACT

Although high-frequency ultrasound imaging is gaining attention in various applications, hardly any ultrasound contrast agents (UCAs) dedicated to such frequencies (>15 MHz) are available for contrast-enhanced ultrasound imaging (CEUS). Moreover, the composition of the limited commercially available UCAs for high-frequency CEUS (hfCEUS) is largely unknown, while shell properties have been shown to be an important factor for their performance. The aim of our study was to produce UCAs in-house for hfCEUS. Twelve different UCA formulations A-L were made by either sonication or mechanical agitation. The gas core consisted of $C_4F_{10}$ and the main coating lipid was either DSPC (A-F formulation) or DPPC (G-L formulation). Mechanical agitation resulted in UCAs with smaller microbubbles (number weighted mean diameter ~1 μm) than sonication (number weighted mean diameter ~2 μm). UCA formulations with similar size distributions but different main lipid component, showed that the DPPC-based UCA formulations had higher nonlinear responses at both the fundamental and subharmonic frequencies *in vitro* for hfCEUS using the Vevo 2100 high-frequency preclinical scanner (FUJIFILM VisualSonics Inc.). In addition, UCA formulations F (DSPC-based) and L (DPPC-based) that were made by mechanical agitation performed similar *in vitro* to the commercially available Target-Ready MicroMarker (FUJIFILM VisualSonics Inc.). UCA formulation F also performed similar to Target-Ready MicroMarker *in vivo* in pigs with similar mean contrast intensity within the kidney (n=7), but formulation L did not. This is likely due to the lower stability of formulation L *in vivo*. Our study shows that DSPC-based microbubbles produced by mechanical agitation resulted in small microbubbles with high nonlinear responses suitable for hfCEUS imaging.

## 3.2. INTRODUCTION

Ultrasound imaging at high frequencies (≥ 15 MHz) enables high resolution imaging at the price of lower penetration depth, making this technique highly suitable for imaging of small animals [160] and superficial organs in large animals (e.g. skin [250]) and humans (e.g. eye [251] and skin tumors [252]). Alternatively, an endoscopic (e.g. transrectal [253]) or intravascular probe [254] could be used if the organ of interest lies deeper within the body.

Contrast-enhanced ultrasound imaging (CEUS) allows assessment of blood flow to improve diagnosis and monitor therapy. For CEUS, intravenously injected ultrasound contrast agents (UCAs) are needed that consist of gas-coated microbubbles dispersed in saline [17, 63, 255]. Examples of preclinical high-frequency CEUS (hfCEUS) are tumor angiogenesis imaging [45] and cerebral microvascular hemodynamics assessment in rats [256]. Microbubbles are effective UCAs with a strong resonance structure and inherently nonlinear behavior in response to a time varying pressure field [45, 256]. These nonlinear oscillations can be present at the subharmonic (SH), fundamental, ultra-harmonic, and higher harmonic frequency. The nonlinear signals generated by the microbubbles are

utilized in imaging techniques to separate the UCA signal from that of the surrounding tissue [161].

Methods based on the detection of higher harmonics are hindered by artifacts when the excitation frequency is high (≥ 15 MHz), such as nonlinear propagation artifacts [166, 184]. In addition to those artifacts, higher harmonics undergo dramatic attenuation because of their high frequencies, which limits the penetration depth. Nonlinear fundamental contrast imaging is the most common approach for nonlinear hfCEUS imaging [161]. The nonlinear fundamental component suffers less from attenuation, but nonlinear propagation is still a drawback. SH imaging, on the other hand, is free from such artifacts, is less attenuated, and neither generated during propagation in tissue nor scattered by tissue [257]. A SH signal can be achieved with minimum amplitude excitation if the driving frequency is twice the resonance frequency of the microbubbles [178, 258]. To increase the sensitivity of hfCEUS both the imaging techniques and the UCA design need to be optimized.

The performance of UCAs highly depends on the resonance behavior of a microbubble, which is inversely related to its diameter [44, 178]. Therefore, UCAs with smaller microbubbles can improve the sensitivity of hfCEUS imaging. Next to size, microbubble shell properties have been shown to be an important factor for their performance, mainly in the generation of SH [259, 260]. The lipid composition of the microbubble shell in the commercially available UCAs for hfCEUS is only known for Definity [9], but unknown for MicroMarker [261] and Targestar P-HF [163]. For high-frequency ultrasound molecular imaging, functionalizing the microbubbles is required to target them to the biomarker of interest [262]. Although Target-Ready MicroMarker provides streptavidin linkage [164], no UCA is commercially available to provide covalent coupling of the ligand to the microbubble shell, limiting flexibility in choice of ligands. In-house produced UCAs could overcome these disadvantages.

Based on a preliminary experiment we conducted before [263], the aim of our study was to produce lipid-coated UCAs in-house with high nonlinear response for hfCEUS. Based on microbubble size a resonance frequency can be predicted [44], but the actual response still depends on the shell microstructure, as we previously showed for the main lipids used in commercially available UCAs [8, 9]: 1,2-distearoyl-sn-glycero-3-phosphocholine (DSPC) or 1,2-dipalmitoyl-sn-glycero-3-phosphocholine (DPPC) [260]. We therefore studied twelve different UCA types with the aim to produce microbubbles with a size similar to Definity [9] and MicroMarker [261]. UCAs were either produced by sonication, i.e. the most common UCA production method [264], or mechanical agitation, i.e. the method by which Definity is prepared [9]. In addition, we compared the UCA compositions we [70] and others [16, 265] have used throughout the years, and quantitatively evaluated the performance of the in-house produced UCAs to Target-Ready MicroMarker *in vitro* and *in vivo* with hfCEUS using the most commonly used high-frequency ultrasound imaging platform (Vevo 2100, FUJIFILM VisualSonics Inc. Toronto, ON, Canada).

## 3.3. MATERIALS AND METHODS

### Ultrasound contrast agent preparation

All UCAs were produced in phosphate-buffered saline (PBS; Invitrogen, Groningen, the Netherlands) as the aqueous medium. UCAs were either produced by probe sonication at 20 kHz with a Sonicator Ultrasonic Processor XL2020 at setting 10 (Heat Systems, Farmingdale, NY, USA) as previously described [70, 129] for 60, 90 or 120 s or by mechanical agitation for 45 s using a Vial Shaker (Bristol-Myers Squibb Medical Imaging, Inc., North Billerica, MA, USA). UCAs with a $C_4F_{10}$ (F2 Chemicals, Preston, UK) gas core and different phospholipid coating formulations (see Table 3.1) were made. The main phospholipid component for all UCA formulations was either 1,2-distearoyl-*sn*-glycero-3-phosphocholine (DSPC; P6517), purchased from Sigma-Aldrich, Zwijndrecht, the Netherlands (formulations A-F), or 1,2-dipalmitoyl-*sn*-glycero-3-phosphocholine (DPPC; 850355), purchased from Avanti Polar Lipids, Alabaster, AL, USA (formulations G-L). The other coating components were polyoxyethylene (40) stearate (PEG-40 stearate; P3440; Sigma-Aldrich), 1,2-distearoyl-*sn*-glycero-3-phosphoethanolamine-N-carboxy(polyethylene glycol) (DSPE-PEG(2000); 880125; Avanti Polar Lipids), and 1,2-distearoyl-*sn*-glycero-3-phosphoethanolamine-N-biotinyl(polyethylene glycol) (DSPE-PEG(2000)-biotin; 880129; Avanti Polar Lipids).

**Table 3.1.**
Production of microbubbles: composition of microbubble phospholipid coating, other coating components, additives, and method of production; MB = microbubble

| UCA ID | Main coating component (mol%) | | Other coating components (mol%) | | | Glycerol (v/v %) | Propylene glycol (v/v %) | Method of MB production (time) | |
|---|---|---|---|---|---|---|---|---|---|
| | DSPC | DPPC | PEG-40 stearate | DSPE-PEG(2000) | DSPE-PEG(2000) biotin | | | Sonication (s) | Vial shaker (s) |
| A | 59.4 | - | 35.7 | 4.1 | 0.8 | - | - | 60 | - |
| B | 59.4 | - | 35.7 | 4.1 | 0.8 | - | - | 90 | - |
| C | 59.4 | - | 35.7 | 4.1 | 0.8 | - | - | 120 | - |
| D | 59.4 | - | 35.7 | 4.1 | 0.8 | - | - | - | 45 |
| E | 92.4 | - | - | 6.4 | 1.2 | 5 | 5 | - | 45 |
| F | 92.4 | - | - | 6.4 | 1.2 | 10 | 20 | - | 45 |
| G | - | 59.4 | 35.7 | 4.1 | 0.8 | - | - | 60 | - |
| H | - | 59.4 | 35.7 | 4.1 | 0.8 | - | - | 90 | - |
| I | - | 59.4 | 35.7 | 4.1 | 0.8 | - | - | 120 | - |
| J | - | 59.4 | 35.7 | 4.1 | 0.8 | - | - | - | 45 |
| K | - | 92.4 | - | 6.4 | 1.2 | 5 | 5 | - | 45 |
| L | - | 92.4 | - | 6.4 | 1.2 | 10 | 20 | - | 45 |

Coating formulations A-D and G-J were identical to our previously produced UCAs made by sonication for 10 s (number weighted mean ~4 µm) [29]. The UCAs made by vial shaking either contained no glycerol and no propylene glycol (formulation D and J) as reported by Sirsi et al. [266] and Moran et al. [267] or contained 5% v/v glycerol (818709, Merck Millipore, Merck, Amsterdam, the Netherlands) and 5% v/v propylene glycol (82280, Sigma-Aldrich) (formulation E and K) as reported by Segers et al. [31] or 10% v/v glycerol and 20% v/v propylene glycol (formulation F and L) as reported by Geers et al. [265]. Our UCA formulations E, F, K, and L only contained two different lipids, which is typical for in-house produced UCAs made by vial shaking [47, 265, 268, 269]. We chose DSPE-PEG(2000) in addition to the main lipid DSPC or DPPC because this lipid can be utilized for targeting, whereas the PEG-40-stearate cannot [262]. The molar ratio of DSPC or DPPC to (DSPE-PEG(2000) + DSPE-PEG(2000)-biotin) was kept identical to UCA formulations A-D and G-J.

UCAs produced by sonication (formulation A-C, G-I) were put in 5 mL glass serum bottles (223738; Wheaton, Millville, NJ, USA), topped with $C_4F_{10}$ gas and closed with a rubber stopper (Z166065; Sigma-Aldrich) and aluminum cap (224193-01; Wheaton). Before the experiments, UCAs made by sonication were washed three times by centrifugation at 400 *g* for 1 min (Heraeus Biofuge, Thermo Scientific, Etten-Leur, the Netherlands) to remove the excess lipids. For the vial shaking method, 1 mL of the solution (lipid concentration 0.4 mg/mL for formulations D-F, J-L) was pipetted in a 2 mL glass screw top vial (5182-0714; Agilent Technologies, Santa Clara, CA, USA), topped with $C_4F_{10}$ gas and closed with a screw cap (5182-0717; Agilent Technologies).

Target-Ready MicroMarker UCA was prepared from the ready kit (FUJIFILM VisualSonics Inc.) according to the manufacturer's instructions: the lyophilisate cake was reconstituted with 1 mL of 0.9% sodium chloride solution. The microbubbles in this UCA consist of a phospholipid shell encapsulating a $C_4F_{10}/N_2$ gas core [261]. All UCAs were produced or reconstituted not more than a few hours before the experiments. Size distributions of the UCAs were measured using a Coulter Counter (Multisizer 3, Beckman Coulter, Mijdrecht, the Netherlands). A 20 µm aperture tube was used, allowing quantification of particle diameters between 0.4 and 12 µm using a linear spacing between the 256 channels. Measurements were repeated three times for each UCA to obtain the mean microbubble diameter, size distribution, and concentration. Polydispersity of the UCAs was calculated by assessing the SPAN, which illustrates the width of the distribution, by using (d90%–d10%)/d50% where d10, d50 and d90 are the microbubble number weighted diameters below which 10, 50, and 90% of the cumulative amount of number weighted microbubbles is found. Data are presented with standard deviations (SD).

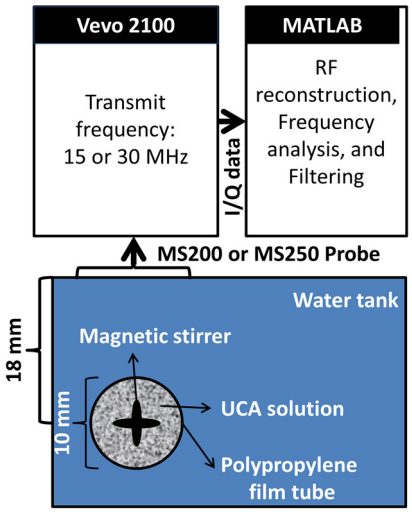


**Fig. 3.1.** Experimental setup for the *in vitro* characterization of the UCA.

### *In vitro* hfCEUS imaging and quantification

A schematic of our experimental setup is depicted in Fig. 3.1. The 10 mm diameter thin shell cylindrical tube, made of polypropylene film backing and coated with a water based acrylic adhesive having a total thickness of 52 µm (tesa® 4024 PV 2), was mounted in a water tank with its center at the focus (18 mm) of the imaging probe. The tube was filled with 15 mL air-saturated PBS. UCA dilutions were pipetted in the tube and mixed gently using a magnetic stirrer in order to have a homogeneous suspension. For the first B-mode scan, the UCA concentration was $5\times10^4$ microbubbles/mL. Next, the effect of the UCA concentration on SH imaging was tested for selected UCAs using two concentrations: $8\times10^6$ and $4\times10^5$ microbubbles/mL, hereafter referred to as high and low concentration, respectively. All measurements were conducted within 10 minutes after pipetting the UCA suspensions into the tube. For each new UCA or dilution, the tube was washed with distilled air-saturated water, filled with air-saturated PBS, and placed in the same location in the water tank.

We used a high-frequency pre-clinical ultrasound scanner operated at 15 or 30 MHz, with two linear array transducers (MS200 probe (15 MHz) and MS250 probe (30 MHz), FUJIFILM VisualSonics Inc.). The wide beam-width setting was chosen in order to have a low, more uniform transmit pressure over depth in the tube [161]. To study the scattering properties of all twelve UCA formulations, the MS200 probe was used at 15 MHz transmit frequency at 1% transmit power and 1 cycle pulse duration in B-mode. On the selected UCA formulations (C, I, F, L, and Target-Ready MicroMarker) SH imaging was performed with the MS250 probe. This probe has a center frequency of 22.5 MHz and a -6 dB two-way bandwidth of 70% (15 -

30 MHz) [161], therefore suitable for SH imaging if transmitting at 30 MHz. The selection of the SH imaging parameters such as transmit frequency (30 MHz), power (10% corresponding to a peak to peak pressure of ~200 kPa), pulse sequence (pulse inversion [161]) and length (20 cycles for better separation of the SH component in the frequency domain) were based on a previous study in which these parameters were optimized for SH imaging [257]. The focus of the MS250 probe was set at 18 mm.

For all experiments, radiofrequency (RF) signals were reconstructed from I/Q samples and further post-processed off-line using MATLAB (The MathWorks, Natick, MA, USA). Three regions of interest (ROI) were selected within the tube containing the UCA: ROI 1 was centered at 15 mm; ROI 2 at 18 mm (focal point); and ROI 3 at 21 mm. Two hundred RF lines were averaged in the frequency domain for analysis of UCA responses at the fundamental (15 or 30 MHz) and SH (15 MHz) frequencies within each ROI.

RF data were digitally band-pass filtered around SH frequencies in the frequency domain, with a fifth-order Butterworth filter. The -6 dB frequency cut-off for the SH filter was chosen from 13 to 17 MHz. One should note that, in our analyses, the signals at the fundamental frequency (30 MHz) correspond to the nonlinear behavior of the UCAs at that frequency and not the linear backscattered signal. This is because the analyses were performed on the RF signals reconstructed from the pulse inversion sequence, which removes the linear components of the backscattered signal at the fundamental frequency [270].

***In vivo* hfCEUS imaging and quantification**

The animal protocol was approved by the animal ethics committee of the Erasmus MC (EMC3379 142-14-01) and conducted in strict accordance to the National Guidelines for Animal Care and Handling. After overnight fasting with free access to water, the female pigs (crossbred Landrace × Yorkshire, 3-4 months of age) of approximately 30 kg (n = 4) were pre-medicated with an intramuscular injection of Tiletamine (5 mg/kg), Zolazepam (5 mg/kg) (Zoletil, both Virbac Laboratories, Carros, France) and xylazine (2,25 mg/kg) (Sedazine® 2%, AST Farma BV Oudewater, the Netherlands). Anesthesia was maintained with a combination of intravenous infusion of midazolam (1.5 mg/kg/h, Actavis, New Jersey, USA.), ketamine (5 mg/kg/h, Alfasan, Woerden, the Netherlands), sufentanil (4 µg/kg/h, Sufenta Fort, Janssen Pharmaceuticals Ltd. USA), and rocuronium bromide (4 mg/kg/h, Fresenius Kabi, Germany) through an ear vein cannula. The animals were ventilated through an endotracheal tube (7.0 Fr), placed in the trachea via midline cervical tracheostomy in a volume controlled mode (Servo 300, Siemens-Elema, Solna, Sweden) with fraction of inspired oxygen of 0.40, a frequency to achieve normocapnia, and a positive end-expiratory pressure of 5 cm $H_2O$. Surgery via the right flank was performed to expose the right kidney. hfCEUS imaging was performed by manually injecting a 1 mL UCA bolus in the jugular vein followed by a 10 mL 0.9% sodium chloride flush. The performance of selected in-house

produced UCA formulations (F and L) was compared to that of Target-Ready MicroMarker. The order in which they were injected was random. The nonlinear hfCEUS measurements were recorded using the Vevo 2100 equipped with an MS250 transducer (18 MHz transmit frequency, 10 frames per second, 10% power, ~400 kPa (MI < 0.1)). The Vevo 2100 uses the amplitude modulation pulse sequence in the nonlinear contrast imaging mode which mainly detects the nonlinear fundamental component of the UCA [161]. Immediately after injection of the UCA into the catheter, the ventilation of the animal was paused to minimize movement due to breathing. After 25-30 s the measurement had been completed and the ventilation was turned on again. Cine loops of side-by-side B-mode and nonlinear contrast mode images were stored as lossless DICOM images for further offline analysis using MATLAB. First, correction for tissue motion in the imaging plane was applied as described previously [271, 272]. Briefly, the motion pattern of tissue in the field of view was extracted from the B-mode images and applied to the contrast mode images to correct for the motion in the field of view. Three regions of interest (ROI) were chosen for every DICOM recording at a depth of 0.5-5 mm, 5-9 mm, and 9-13.5 mm. For each ROI, all pixel intensities were summed and normalized to the area of the ROI. The intensity in each frame was obtained to construct a time-intensity curve (TIC) and the frames with the maximum intensity were detected and the mean intensity and standard deviation of this frame and the five frames before and after this frame were calculated. In addition, alternative ROIs were chosen to compare contrast enhancement in the artery with that in the microcirculation where no clear vascularity was visible. The ratio between the intensities in these ROIs was used to quantify the ability to discriminate the blood vessels from the peripheral enhancement.

#### Statistics

The ratios for the arteries and microvasculature of Target-Ready MicroMarker and UCA formulation F were tested for significance using paired-samples Student's *t*-tests, after first ensuring that the data was normally distributed using Shapiro-Wilk normality tests. A p-value < 0.05 was regarded as indicating significance.

## 3.4. RESULTS

#### Ultrasound contrast agent preparation

After production, all UCA formulations appeared white as shown in Fig. 3.2 a and b, indicating that UCAs could be produced with all twelve formulations. UCA formulations D and J were least white. In addition, both these formulations had the smallest layer of microbubbles at the top of the aqueous solution in the vial after leaving the vials on the bench for 2 h (Fig. 3.2 c and d), suggesting a lower amount of microbubbles in these formulations.

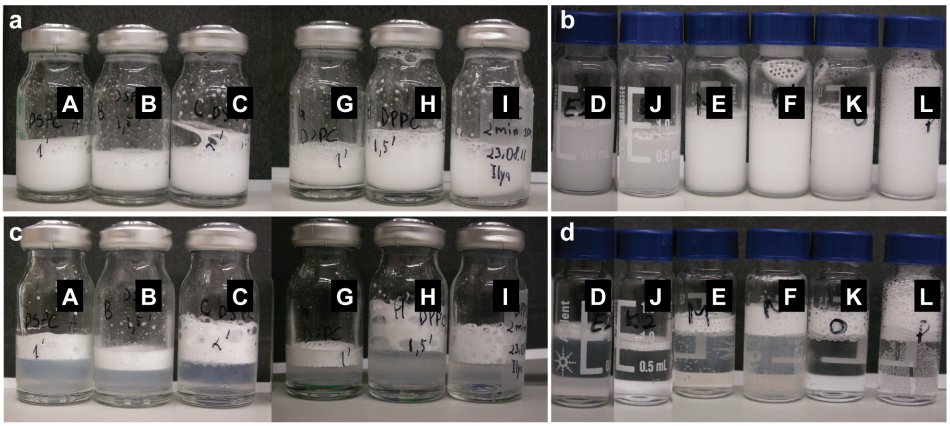


**Fig. 3.2.** Photos of UCA formulations A-L after production when gently redispersed **(a** and **b)** and after standing on bench for 2 h **(c** and **d).** Formulations A-C and G-I **(a** and **c)** were made by sonication while formulations D-F and J-L **(b** and **d)** were made by vial shaking.

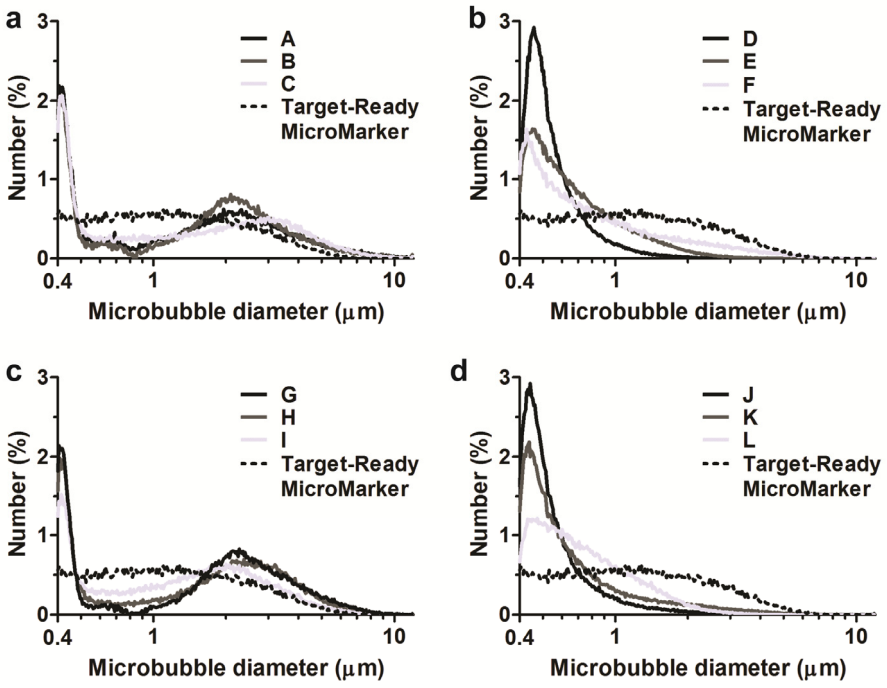


**Fig. 3.3**. Number weighted size distributions of **(a)** DSPC-based UCAs made by sonication (UCA type A, B, C); **(b)** DSPC-based UCAs made by vial shaking (UCA type D, E, F); **(c)** DPPC-based UCAs made by sonication (UCA type G, H, I); and **(d)** DPPC-based UCAs made by vial shaking (UCA type J, K, L) all compared with Target-Ready MicroMarker.

The number weighted size distribution of UCA formulations A-L and Target-Ready MicroMarker are shown in Fig. 3.3; the volume weighted size distribution is shown in Fig. 3.4. None of the A-L type UCA formulations had a number weighted mean diameter, volume weighted mean diameter, or size distribution identical to that of Target-Ready MicroMarker. UCA formulations A-C and G-I made by sonication (Fig. 3.3a and 3.3c) contained higher amounts of large microbubbles than Target-Ready MicroMarker. All the UCAs produced by sonication had two distinct peaks in their size distribution (0.4-0.5 µm and 2-3 µm). Longer sonication times did not alter the mean number weighted diameter much, as shown in Table 3.2. The volume weighted diameter decreased upon longer sonication times, while the concentration of microbubbles increased. UCA formulations D-F and J-L made by vial shaking resulted in smaller microbubbles (Fig. 3.3b and 3.3d; Table 3.2) than when microbubbles were made by sonication. DSPC or DPPC as main coating resulted in microbubbles of similar mean number weighted diameters for both UCA production methods (Table 3.2). The highest microbubble concentration was found in UCA formulation E. Microbubbles with the smallest mean number weighted diameter were found in UCA

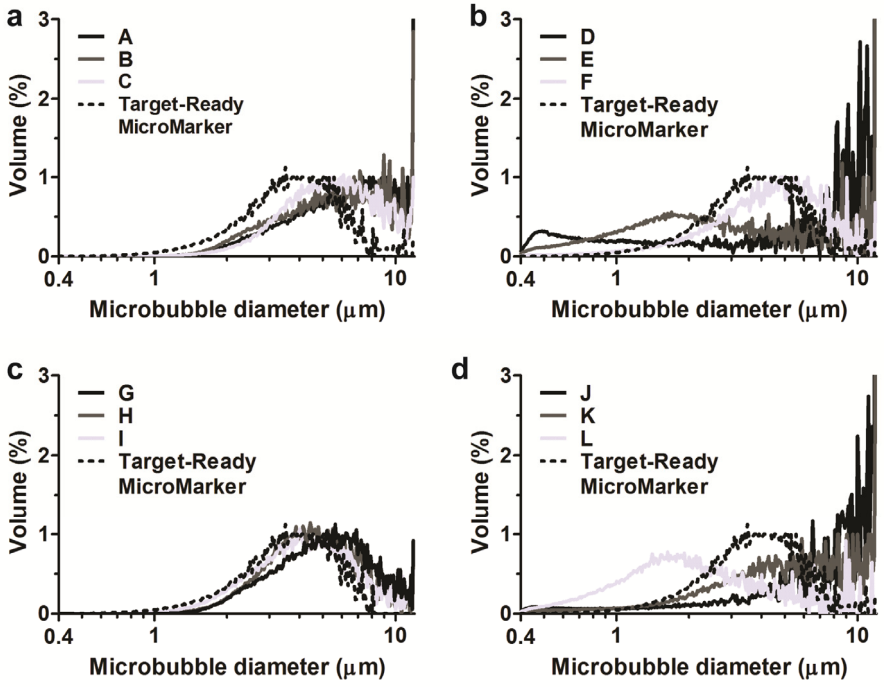


**Fig. 3.4**. Volume weighted size distributions of **(a)** DSPC-based UCAs made by sonication (UCA type A, B, C); **(b)** DSPC-based UCAs made by vial shaking (UCA type D, E, F); **(c)** DPPC-based UCAs made by sonication (UCA type G, H, I); and **(d)** DPPC-based UCAs made by vial shaking (UCA type J, K, L) all compared with Target-Ready MicroMarker.

formulation D and J while this was UCA formulation L for microbubbles with the smallest mean volume weighted diameter, all of which were produced by vial shaking. The highest mean number weighted diameters were found in formulation B and H and the highest volume weighted diameter was found in UCA formulation J. The UCA formulation with the smallest SPAN was formulation D while formulation F had the largest SPAN.

**Table 3.2**. UCA formulations: mean ± SD microbubble concentration, size, and SPAN.

| UCA ID | Concentration ($10^9$ per mL) | Number weighted diameter (μm) | Volume weighted diameter (μm) | SPAN |
|---|---|---|---|---|
| A | 1.9 | 1.9 | 6.4 | 2.3 |
| B | 1.6 | 2.0 | 5.9 | 1.9 |
| C | 2.3 | 1.9 | 5.7 | 2.7 |
| D | 6.9 | 0.6 | 5.6 | 0.7 |
| E | 16.7 | 0.8 | 3.4 | 1.4 |
| F | 7.0 | 1.1 | 4.6 | 2.6 |
| G | 2.5 | 2.1 | 5.4 | 1.9 |
| H | 1.9 | 2.0 | 4.8 | 1.9 |
| I | 3.0 | 1.7 | 4.6 | 2.1 |
| J | 1.2 | 0.6 | 7.5 | 1.0 |
| K | 4.7 | 0.8 | 5.8 | 1.9 |
| L | 10.0 | 0.9 | 2.8 | 1.4 |
| Target-Ready MicroMarker | 1.0 | 1.5 | 4.0 | 2.2 |

***In vitro* hfCEUS**

As shown in Fig. 3.5, different ultrasound scattering intensities of UCA formulations A-L were observed at 15 MHz *in vitro*. The error bars in Fig. 3.5 represent the variation in B-mode signal intensity within the ROI (the entire cross-section of the cylindrical tube containing the UCA). For both the DSPC-based and DPPC-based UCA formulations, microbubbles with larger mean diameters resulted in slightly higher intensities. In addition, UCAs produced by sonication which had similar mean number weighted diameters, also showed similar signal intensity in the B-mode scan (A, B, C and G, H, I in Fig. 3.5. UCA formulation F had the highest signal of the DSPC-based UCAs made by vial shaking, while this was formulation K for the DPPC-based UCAs. However, a large standard deviation was observed for formulation K, due to a non-uniform signal throughout the tube. Two UCA formulations produced by sonication and two produced by vial shaking were selected for further studies. Based on the results so far, UCA formulations C and I were selected out of the sonication produced UCAs as they contained the highest concentration of microbubbles. For the vial shaking produced

UCAs, formulations F and L were selected because they gave the highest ultrasound signal in B-mode with the smallest standard deviation.

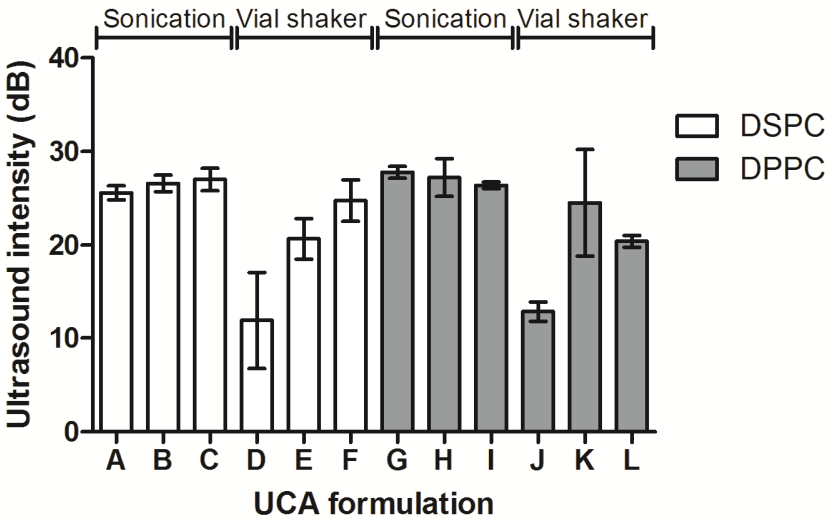


**Fig. 3.5.** Ultrasound intensities (dB) at 15 MHz for UCA formulations A-L. Intensities obtained from the PBS control were subtracted from the intensities obtained from the UCA formulations. A-F type UCAs had DSPC as the main coating lipid, while this was DPPC for G-L type UCAs.

Images of UCA formulations C, F, I, and L, and Target-Ready MicroMarker at high and low concentrations, filtered around their SH frequency (15 MHz), and the corresponding frequency spectra for the three ROIs are presented in Fig. 3.6. At high UCA concentration, attenuation was dominant for formulations C, I, and L. This attenuation effect is also reflected in the corresponding spectra of these UCAs, where the amplitude of the spectra at the SH frequency drops about 10 dB for the deeper ROIs with respect to the highest SH amplitude. Target-Ready MicroMarker and UCA formulation F at high concentration had the highest and most homogeneous SH response throughout the three ROIs. At low UCA concentration, the attenuation effect was less pronounced. The SH amplitude of Target-Ready MicroMarker dropped about 11 dB when UCA concentration was reduced by a factor of 20. The SH amplitude of UCA formulation I at such low concentration was 10 dB higher than that for Target-Ready MicroMarker and was homogeneous throughout the UCA area.

In all the corresponding spectra of the UCA signals in both high and low concentration, the amplitude of the nonlinear fundamental signal was maximal at the focus of the transducer, where the acoustic energy was at its maximum (ROI 2). At high concentrations, Target-Ready MicroMarker showed the highest nonlinear response at the fundamental

frequency. However at low concentration, all our in-house produced UCAs had higher nonlinear responses at the fundamental frequency than Target-Ready MicroMarker. The attenuation effect was similar for the SH response and the nonlinear fundamental response. UCA formulations C, I, and L showed higher attenuation than Target-Ready MicroMarker and UCA formulation F.

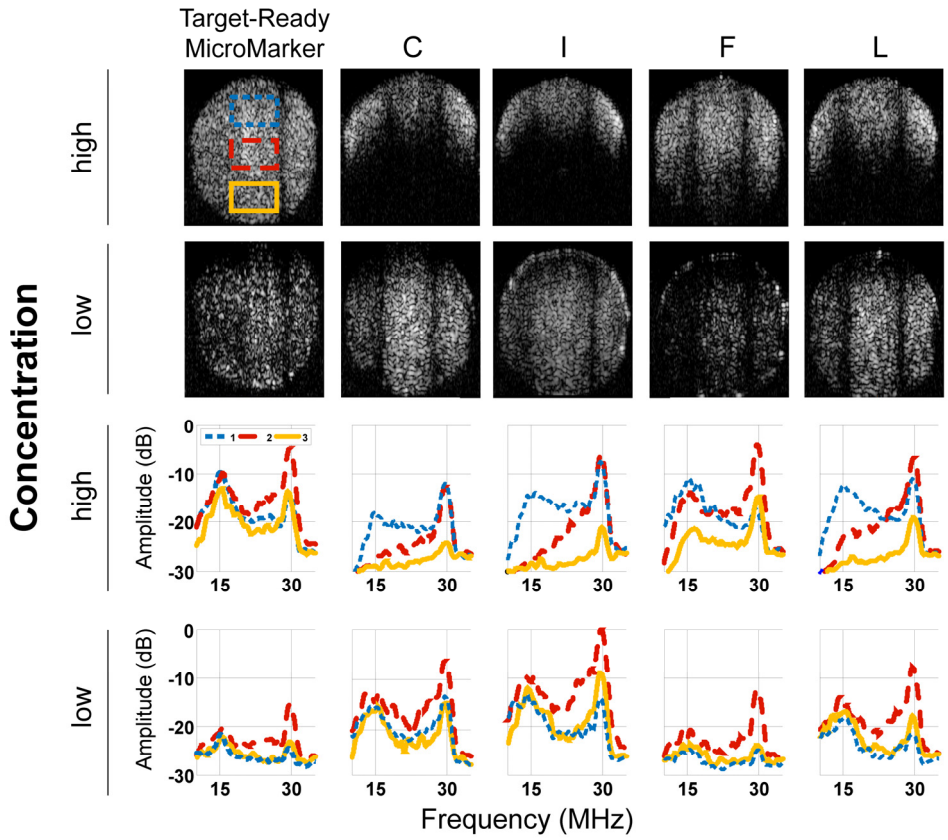


**Fig. 3.6.** *In vitro* subharmonic images of Target-Ready MicroMarker and formulation C, I, F, and L at high ($8.0\times10^6$ microbubbles/mL) and low ($4.0\times10^5$ microbubbles/mL) concentrations (top panel) and the corresponding spectra of each region of interest at three depths for each image (bottom panel).

### *In vivo* hfCEUS

Of the four formulations that were studied *in vitro* for their SH and nonlinear fundamental response, the two best performing UCA formulations were selected for *in vivo* hfCEUS studies: F and L. This decision was based on the fact that both the acoustic signal and microbubble size distribution resembled Target-Ready MicroMarker the closest. Fig. 3.7

shows the result of the comparison between Target-Ready MicroMarker and UCA formulations F and L in the same animal (n = 1).

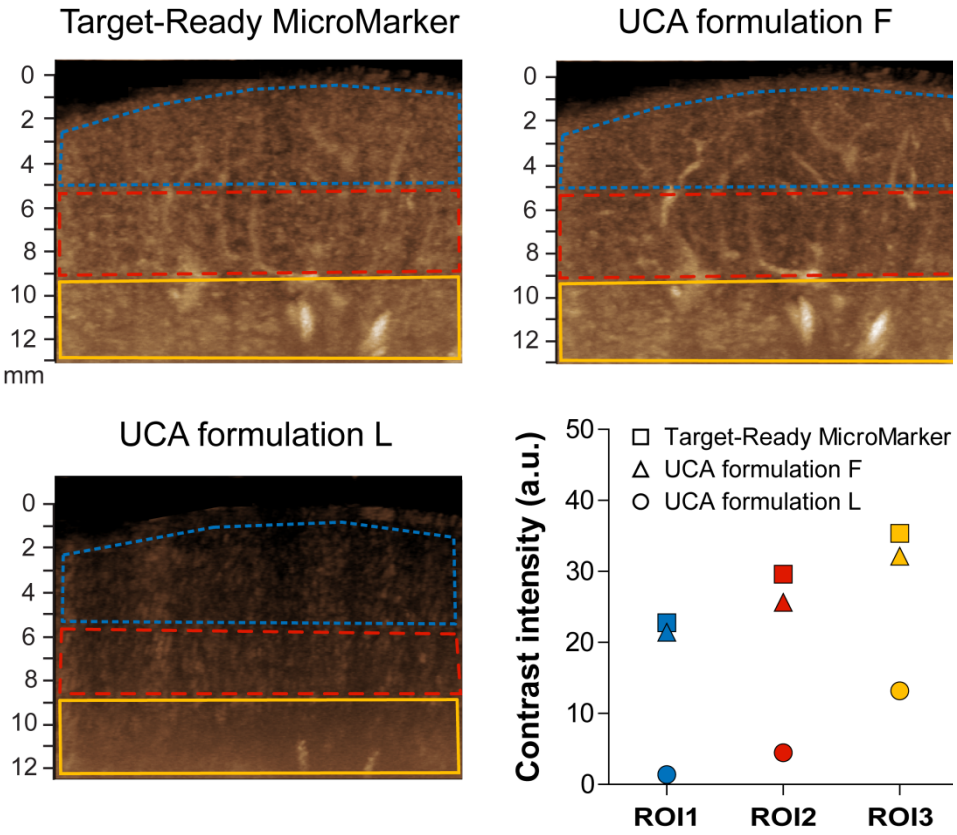


**Fig. 3.7.** Examples of *in vivo* hfCEUS measurements of Target-Ready MicroMarker and formulations F and L in the kidney of the same animal. The maximum intensity projection is shown. The bottom graph shows the quantification of intensities in the three different ROIs of which the colors correspond to those in the maximum intensity projections.

For each recording, three ROIs were drawn: in the focal region (blue), in the middle of the field of view (red), and the bottom of the field of view (yellow). The mean ± SD intensity in each ROI is shown in the bottom panel of Fig. 3.7 for all three UCAs. hfCEUS images revealed slightly lower overall intensities for UCA formulation F than for Target-Ready MicroMarker. Formulation L on the other hand, revealed only two larger vessels in ROI 3, while hardly any intensity increase was observed outside these vessels or in ROI 1 and ROI 2. Because contrast enhancement of UCA formulation L was negligible, only Target-Ready MicroMarker and UCA formulation F were further evaluated. The TICs corresponding to the

example in Fig. 3.7 for Target-Ready MicroMarker (grey) and UCA formulation F (black) show very similar behavior between both UCAs in all three ROIs (Fig. 3.8).

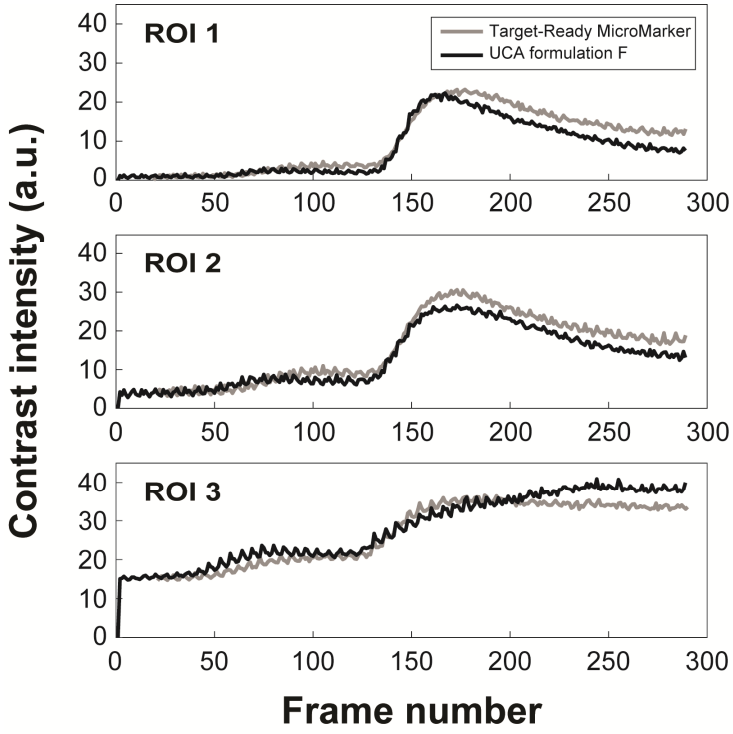


**Fig. 3.8.** Time-intensity curves (TICs) of Target-Ready MicroMarker (grey) and UCA formulation F (black) for the different ROIs as shown in Fig. 3.7. The TICs correspond to the same injections as the example shown in Fig. 3.7.

The experiments comparing Target-Ready MicroMarker and formulation F (n = 7 in total) confirmed the observation that the total contrast enhancement of Target-Ready MicroMarker was higher, although the difference was lower in ROI 3 (Fig. 3.9).

This implies lower attenuation for UCA formulation F than for Target-Ready MicroMarker. Since UCA formulation F seemed to better visualize the larger vessels and Target-Ready MicroMarker resulted in more enhancement in the microvasculature (see Fig. 3.7), we quantified the ratio between enhancement in the arteries and the microvasculature for all injections. The symbols that are used in Fig. 3.9 correspond to those in Fig. 3.10, and quantification of the example in Fig. 3.7 (▽) shows better discrimination of the artery from the microvasculature for UCA formulation F. Although this example showed

a clear difference, overall the differences between Target-Ready MicroMarker and UCA formulation F were not significant ($p > 0.05$).

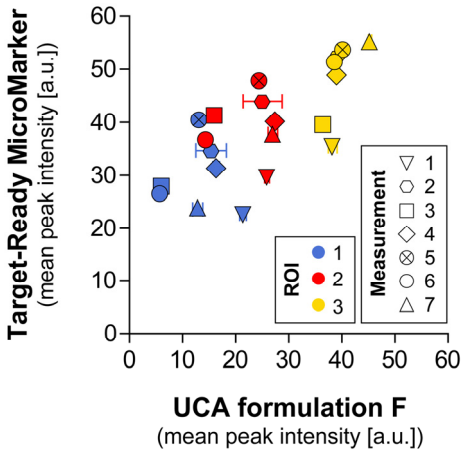


**Fig. 3.9.** Complete comparison of Target-Ready MicroMarker and UCA formulation F. The markers indicate the mean peak intensity of each measurement, the bars the corresponding standard deviation (n = 7). The symbols indicate the data obtained from the same paired injection where ▽ indicates the example shown in Fig. 3.7 (measurement 1, animal a). Measurement 2 was performed in animal b and measurements 3-7 in animal c.

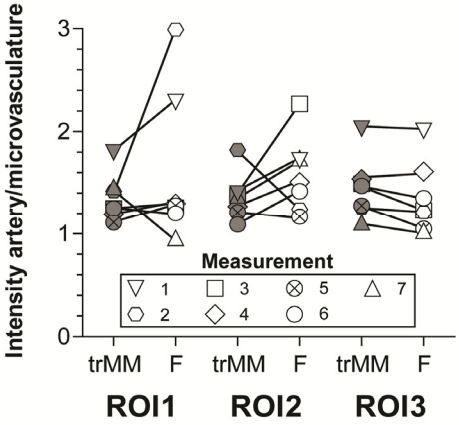


**Fig. 3.10.** Comparison of the ratios of contrast enhancement in the arteries and the microvasculature between Target-Ready MicroMarker (grey) and UCA formulation F (white). The symbols, identical to the symbols in Fig. 3.9, indicate the data obtained from the same paired injection where ▽ indicates the example shown in Fig. 3.7 (measurement 1, animal a). Measurement 2 was performed in animal b and measurements 3-7 in animal c. The lines connect the paired injections (injected in random order). Differences between the two UCAs were not significant.

We also verified the reproducibility of UCA formulation F by repetitive injection in the same animal (n = 3) and found similar intensities in ROI 1 and ROI 3 between the first and second injection (Fig. 3.11). In ROI 2 the second injection was 17% lower than the first injection. The third injection was 39% lower than the first injection in ROI 1, 31% lower in ROI 2, and only 11% lower in ROI 3. We verified that the baseline values before the start of each measurement were comparable. Reproducibility for Target-Ready MicroMarker was not studied.

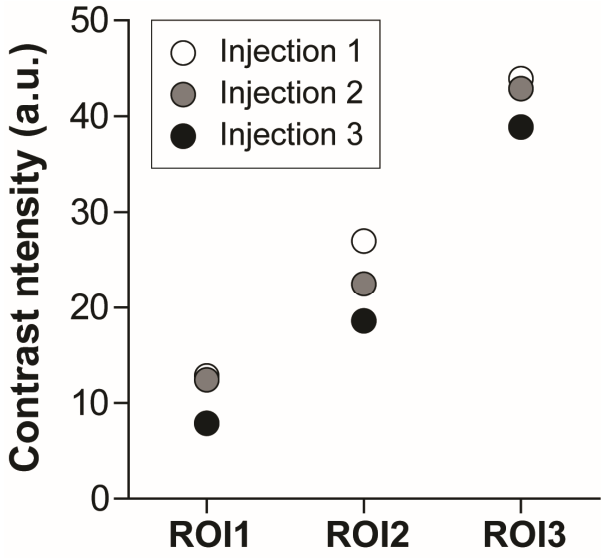


**Fig. 3.11.** Repeated injections (n = 3) of UCA formulation F in the same animal. For each injection contrast enhancement decreased.

## 3.5. DISCUSSION

In this study we showed that one of our in-house produced UCAs for hfCEUS resembled the performance of the commercially available Target-Ready MicroMarker both *in vitro* and *in vivo*. The best performing UCA was produced by 45 s vial shaking and consisted of 92.4% DSPC, 7.6% DSPE-PEG(2000), in an aqueous solution of 70% PBS, 10% glycerol, and 20% propylene glycol with a $C_4F_{10}$ gas core.

### Ultrasound contrast agent preparation

In our study, microbubble diameters were larger for sonication produced UCAs than when microbubbles were produced by vial shaking, which is in line with what Sirsi et al. [266] found for their in-house produced UCAs with a coating of DSPC and PEG-40 stearate (9:1 molar ratio) and $C_4F_{10}$ gas core. In contrast, Moran et al. [267] reported similar number weighted mean diameters of ~0.5 μm for their in-house produced UCAs by sonication and vial shaking. Their nitrogen-filled microbubbles had a coating of dipalmitoyl phosphatidylethanolamine (DPPE), phosphatidylcholine, dipalmitoyl phosphatidyl-DL-glycerol, and cholesterol. The contrasting findings in microbubble diameters between the two production methods, i.e., sonication and vial shaking, suggest that the microbubble composition and gas core may also play a role in the size of the produced microbubbles. On

the other hand, different probe-sonication devices were used in these studies (Sonicator Ultrasonic Processor XL2020 in our study; Branson Ultrasonics Model 250A by Sirsi et al. [266, 273]; Soniprep 150 by Moran et al. [267]) which could have given different ultrasonic power outputs thereby influencing the microbubble size distribution [264].

We previously reported [70] that 10 s sonication for the same UCA formulations as A-C (DSPC-based) and G-I (DPPC-based) resulted in microbubbles with a mean number weighted diameter of 4.2 and 3.9 μm respectively. Although sonication for 60 s resulted in smaller microbubbles (~2 μm in mean number weighted diameter; see Table 3.2), the number weighted mean diameter was similar after 60, 90 or 120 s sonication. This was also observed by Moran et al. [267] who reported that the number weighted mean diameter of ~0.5 μm did not change when the sonication time was varied between 30, 60, 90, or 300 s for their lipid-coated microbubbles (coating composition see above). However, the number weighted size distribution of our UCAs produced by sonication had two peaks (0.4-0.5 μm and 2-3 μm; Fig. 3.3). A longer sonication time seemed to produce lower amounts of large microbubbles (> 2 μm) and more microbubbles in between the peaks (0.5-2 μm). This result is confirmed with the changes in the volume weighted mean diameters which decreased with increasing sonication time. In addition, microbubble concentrations increased for longer sonication times. It is likely that more microbubbles can be produced during longer sonication times because excess unincorporated lipids are always present when microbubbles are made by sonication [138]. The increase in the concentration and the changes in the size distribution of the UCA suggest that longer sonication times can break up bigger microbubbles into smaller ones.

Our in-house produced UCA formulations D and J were made by vial shaking in the absence of glycerol and propylene glycol, just as Sirsi et al. [266] and Moran et al. [267] did. On the other hand, glycerol and propylene glycol are often added to increase the fluid viscosity when making UCAs in-house by vial shaking [47, 265, 268, 269] and are also present in the clinically approved Definity [9]. When the concentrations of glycerol and propylene glycol were increased from 0%/0% to 5%/5% and 10%/20% v/v, we found varying results on microbubble size and concentration. For the DPPC-based UCAs (formulations J, K, and L) increasing the concentration of glycerol and propylene glycol increased the microbubble concentration and the number weighted mean diameter. For the DSPC-based UCAs (formulations D, E and F), the number weighted mean diameter followed the same trend. The concentration of the microbubbles, on the other hand, first increased with 5%/5% glycerol and propylene glycol and decreased for the highest concentration. In addition, UCA formulations F and L were more stable after 2 h than those without glycerol and propylene glycol. This suggests that glycerol and propylene glycol can play a role not only in increasing the concentration of the microbubbles, but also on the stability of the produced microbubbles. This increased stability of UCA formulations F and L was also observed in the increased intensity in the *in vitro* B-mode images of these UCAs.

***In vitro* hfCEUS**

In an *in vitro* setup, mimicking a practical imaging condition, we showed that both the shell microstructure of microbubbles as well as their size distribution have a considerable impact on their nonlinear behavior both at the SH and fundamental frequencies. All our homemade UCAs showed high nonlinear behavior when excited at 30 MHz, which was comparable to the commercially available Target-Ready MicroMarker. Such high nonlinear response at both the SH and fundamental frequencies can be attributed to the small sizes of all studied microbubbles. The larger microbubbles in formulations C and I (2-3 µm) accounted for more attenuation at high concentrations. This hypothesis is confirmed by the lower attenuation of the smaller microbubbles in UCAs F and L, while the nonlinear responses remained high. The attenuation effect was more pronounced for the SH component than the nonlinear responses at the fundamental frequency. This is perhaps due to the threshold behavior of SH oscillations [184]. The microbubbles at the lower part of the focal zone may not have been excited with sufficiently high pressures to undergo SH oscillation. However, when the concentration was 20× lower, the SH response of these larger microbubbles became stronger and more homogeneous throughout the sample.

Comparison of UCA formulations C and I with similar size distributions but different main lipid component, showed that the DPPC-based UCA formulation I showed higher nonlinear responses at both the fundamental and SH frequencies. At low concentration, the response of UCA formulation I at the fundamental and SH frequency was 6 and 3 dB higher, respectively, than for the DSPC-based UCA formulation C. This higher SH response has also been reported by van Rooij et al. [260] utilizing optical single microbubble spectroscopy in the range of 1-4 MHz.

The small size of Target-Ready MicroMarker microbubbles seems to play an important role in its nonlinear behavior, particularly for the SH response at high-frequency excitation. The majority of the microbubbles have a diameter below 1.5 µm, corresponding to a resonance frequency around and higher than 15 MHz [274, 275]. It is conventionally thought that SH generation is achieved most readily (i.e., at lowest pressure threshold) when microbubbles are excited at twice their resonance frequency [258]. This means that for the majority of the Target-Ready MicroMarker microbubbles, the 30 MHz excitation used in this study is around twice their resonance frequency. Indeed, high amplitude SH response of Target-Ready MicroMarker UCA has previously been reported by Helfield et al. [259], although they studied individual microbubbles in an acoustical setup. Another reason for the high SH behavior of the UCAs we observed may be the rectangular shape of the excitation used in the Vevo 2100 scanner. It has been reported that rectangular-shaped excitations generate a self-demodulation signal which enhances the SH response of microbubbles [184, 257]. Our *in vitro* results show that Target-Ready MicroMarker is also producing a strong nonlinear response at the fundamental frequency. This characteristic is

already being utilized in the Vevo 2100 scanner as the default nonlinear contrast mode with amplitude modulation pulse sequence to improve the contrast to tissue ratio in hfCEUS.

It has been shown before that smaller microbubbles provide higher contrast for hfCEUS imaging. Goertz et al. reported that the decantation technique to isolate smaller Definity microbubbles can be employed to produce an attenuation pattern that appears more favorable for hfCEUS [276]. Also Moran et al. [267] have shown that decreasing the mean diameter of the lipid-based sonication UCAs significantly increased the mean backscattering power at 40 MHz. In another study, Peyman et al. [277] showed that the majority of the signal measured using the VisualSonics Vevo 770 (40 MHz) in the mixed microbubble/nanobubble population was attributable to the nanobubbles, with a much lower proportion of the signal coming from microbubbles. Our results are in agreement with these studies.

We showed that at 30 MHz transmit frequency and at low UCA concentration, DPPC-based UCAs behaved more nonlinearly than those based on DSPC. At higher concentration, smaller microbubbles (Target-Ready MicroMarker and UCA formulation F) produced the most homogeneous SH responses. For UCA formulations C and I we previously observed differences in lipid distribution [70]. The DPPC lipid has a lower elastic compressibility modulus than DSPC [278, 279], which may be related to SH behavior as our DPPC-based UCAs showed more SH behavior than our DSPC-based UCAs, as reported before for single microbubbles [260]. Unfortunately, the coating composition of Target-Ready MicroMarker is unknown, so we do not know how our homemade UCAs resemble the composition of Target-Ready MicroMarker.

***In vivo* hfCEUS**

We studied UCA formulations F and L *in vivo* and found that the overall performance of UCA formulation F was similar to that of Target-Ready MicroMarker. UCA formulation L, on the other hand, resulted in hardly any contrast enhancement despite the fact that both in-house produced UCAs had similar number-weighted mean diameters and the concentration of microbubbles was even higher for UCA formulation L. The most important difference between the two UCAs is their composition and the associated differences between DSPC as main component (formulation F) and DPPC (formulation L) in terms of microstructure [48, 70, 280, 281] and acoustic behavior *in vitro* [260]. Using an Acuson Sequoia 512 in nonlinear imaging mode at 7 MHz (15L8 transducer) the *in vitro* half-life of DPPC-based UCAs (DPPC:DSPE-PEG5000, 9:1, in-house produced by vial shaking) was 10× lower than for those based on DSPC, whereas the half-life was better *in vivo*, but still 5× lower than for DSPC-based UCAs [50]. Although these and our in-house produced DPPC-based UCAs did not perform well *in vivo*, the commercially available and clinically approved UCA Definity that is also DPPC-based [9] has been shown to provide good contrast enhancement in pigs [282]

and humans [283, 284]. It has to be noted that the other components of Definity are DPPA and DPPE-mPEG5000 [9], which can alter the acoustic properties and stability.

Other research groups have also characterized their own in-house produced UCAs for hfCEUS, but either characterized them acoustically *in vitro* [18, 259, 260, 277, 285, 286] and/or imaged them *in vivo* [266, 277], instead of imaging them in both situations. Although acoustic characterization of single microbubbles provides insights in microbubble behavior, imaging of microbubbles *in vitro* in a controlled and simplified setup is essential before translation towards complex *in vivo* applications. Neither *in vivo* studies compared their in-house produced UCAs to a commercially available UCA as a reference. Peyman et al. [277] imaged their microbubbles (DPPC:DSPE-PEG(2000), 4:1, microfluidic production) in the mouse aorta at 40 MHz in fundamental mode using the Vevo 770, which resulted in hardly any contrast enhancement. Simultaneously with their microbubbles they also produced nanobubbles (~200 nm diameter), which provided 3× higher contrast peak intensities. Sirsi et al. [266] isolated microbubbles (DSPC:PEG-40-stearate, 9:1 molar ratio, both sonication and vial shaking) of distinct size populations (1-2, 2-4, 6-8 μm) and determined their acoustic impact directly *in vivo* in the mouse kidney using 40-MHz fundamental mode imaging using the Vevo 770. Surprisingly, they report that the smaller microbubbles (1-2 μm) resulted in higher attenuation and less echogenicity than the larger microbubbles (6-8 μm). One reason for these contradictory results could be the differences in microbubble shell composition in these studies. Also, in the study conducted by Sirsi et al., the targets were the small capillaries in the mouse kidney while Peyman et al. quantified the UCA contrast in the mouse aorta which is a much larger vessel. Both the concentration of the microbubbles in the ROI and the differences in ambient pressures in kidney capillaries and the aorta could have played a role in these contradictory findings.

The TICs of UCA formulation F and Target-Ready MicroMarker were very similar, but slightly higher peaks and longer contrast persistence were found for Target-Ready MicroMarker. The prolonged contrast enhancement is likely due to the higher acoustic stability of Target-Ready MicroMarker. These microbubbles not only contain a lipid shell, but are also covered by streptavidin which has been shown to increase the stiffness and therefore reduce acoustic dissolution *in vitro* [262]. The higher contrast peak intensity for Target-Ready MicroMarker was shown to be present for all injections, but the difference with UCA formulation F was smaller in the deeper cortex. This may result from the higher concentration of formulation F microbubbles that was injected and appeared in the large vessels in the deeper cortex. The differences in concentration between Target-Ready MicroMarker and UCA formulation F influenced the interpretation of our results. We concluded that the performance between both UCAs was comparable, but it has to be taken into account that an injection of 1 mL UCA formulation F contained ~7× more microbubbles than 1 mL of Target-Ready MicroMarker. However, both concentrations are the same order of magnitude as the commercially available ones, since a typical human dose

of Definity contains $4.2\times10^9$ microbubbles [9] and a typical dose of SonoVue/Lumason varies between $3.0\times10^8$ and $1.1\times10^9$ microbubbles [8]. In addition, the concentration of microbubbles between batches of Target-Ready MicroMarker that were used in our experiments varied between $2.6\times10^8$ and $1.3\times10^9$ microbubbles/mL (n = 5). These concentrations were assessed by us and are in line with what others have reported, namely $8.4\times10^8$ [164], $9.2\times10^8$ [162], and $1.9\times10^9$ [287]. The batch to batch variability in microbubble concentration for our UCA formulation F ranged from $2.1\times10^9$ to $5.5\times10^9$ microbubbles/mL (n = 5 batches) and was therefore narrower than for Target-Ready MicroMarker. The variation in the mean microbubble diameter (both number and volume weighted) were similar for Target-Ready MicroMarker and our in-house produced UCA formulation F. The number weighted mean diameter for Target-Ready MicroMarker was 1.8 ± 0.4, the volume-weighted mean diameter was 4.6 ± 0.8 while this was 1.2 ± 0.1 and 5.6 ± 1.0 for our in-house produced F type UCA (both n = 5 batches). The variability in microbubble size and concentration can be caused by vial handling, even within manufacturer's recommended procedures, as has been suggested by Goertz et al. [276].

Repeated bolus injections of UCA formulation F in the same animal resulted in significantly less enhancement for the third injection. Others have reported differences between consecutive injections in cats [288] and mice [289, 290]. In the kidney and spleen of healthy cats, the second bolus injection of SonoVue resulted in higher peak intensities [288]. Dizeux et al. [290] reported that the maximum intensity (peak enhancement) was constant for four consecutive injections in the healthy renal murine cortex, but increased from the second to the fourth injection in renal tumor tissue. In contrast, Rix et al. [289] reported constant peak enhancement in murine liver tumors and decreasing peak enhancement with consecutive injections in the healthy liver. We can only conclude that variability in consecutive injections is a known issue for CEUS and differs between organisms and organs.

**Limitations**

The main limitation of using in-house produced UCAs is that it can be challenging to produce them under Good Manufacturing Practice conditions [291]. For example, batch to batch reproducibility may be an issue, as is sterility. However, for terminal preclinical experiments as in our study, the UCAs do not have to be sterile. For longitudinal preclinical experiments, there are options for sterilization of lipid formulations [292, 293]. In our *in vivo* experiments we used nonlinear fundamental imaging at 18 MHz with amplitude modulation instead of SH imaging with pulse inversion at 30 MHz as used *in vitro*. Although SH imaging is free from nonlinear propagation artifacts, nonlinear fundamental imaging with amplitude modulation provides higher contrast to tissue ratio with Vevo 2100 [257].

## 3.6. CONCLUSION

Our results suggest that our UCA formulation F performs equally well as Target-Ready MicroMarker in hfCEUS imaging. This study shows that small UCAs having high nonlinear responses for hfCEUS can be produced by mechanical agitation, a shell composition of 92.4% DSPC, 6.4% DSPE-PEG(2000) and 1.2% DSPE-PEG(2000)-biotin encapsulating a $C_4F_{10}$ gas core, in a PBS-based liquid with 10% glycerol and 20% propylene glycol.

**Acknowledgements**

The authors greatly thank all colleagues who made the experiments possible for their help and support, especially Y. Ince from the Department of Translational Physiology, Academic Medical Center, Amsterdam, the Netherlands and the Dept. of Intensive Care Adults, Erasmus MC, Rotterdam, the Netherlands; and M. Sorelli from the Dept. of Intensive Care Adults, Erasmus MC, Rotterdam, the Netherlands and the Department of Information Engineering, University of Florence, Florence, Italy.

Chapter 4

# DSPC or DPPC as main shell component influences ligand distribution and binding area of lipid-coated targeted microbubbles

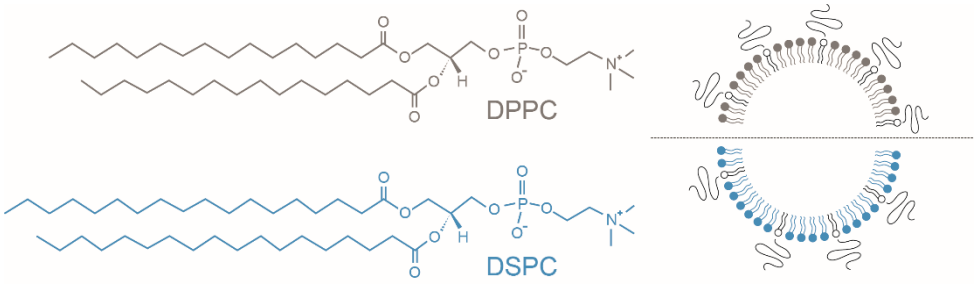


Klazina Kooiman, Tom J.A. Kokhuis, Tom van Rooij, Ilya Skachkov, Alex Nigg, Johannes G. Bosch, Antonius F.W. van der Steen, Wiggert A. van Cappellen, Nico de Jong

*European Journal of Lipid Science and Technology*, 116:9, 1217–1227 (2014)

## 4.1. ABSTRACT

Ultrasound contrast agents (UCA) consist of gas-filled coated microbubbles with diameters of 1-10 µm. Targeted UCA can bind to biomarkers associated with disease through coating-incorporated ligands, making ultrasound molecular imaging possible. The aim of our research was to compare the ligand distribution, binding area, and bound microbubble shape of 1,2-distearoyl-*sn*-glycero-3-phosphocholine (DSPC) based and 1,2-dipalmitoyl-*sn*-glycero-3-phosphocholine (DPPC) based lipid-coated microbubbles using super-resolution microscopy. Ligand distribution was studied by conjugating the fluorescent streptavidin Oregon Green 488 to the biotinylated microbubbles. An inhomogeneous streptavidin distribution was found when DSPC was the main coating lipid. When DSPC was replaced by DPPC, a more homogeneous streptavidin distribution was observed. Binding area of targeted microbubbles was studied using biotinylated microbubbles bound to a streptavidin-coated surface. DSPC microbubbles had a significantly smaller binding area than DPPC microbubbles. Whereas the bound DSPC microbubbles remained spherical, the DPPC microbubbles were dome-shaped. This study reveals that lipid-coated microbubbles differ in ligand distribution, binding area, and bound microbubble shape solely on the basis of their main lipid component.

## 4.2. INTRODUCTION

Ultrasound imaging is a widely used non-invasive diagnostic imaging modality. In the 1990s the first ultrasound contrast agents (UCA) became available for clinical use [64, 294]. UCA consist of a fluid comprised of coated gas microbubbles with diameters between 1 and 10 µm. Upon intravenous administration, UCA stay within the vascular tree as they are too large to extravasate [64, 65]. Initially, UCA were mainly used to improve diagnostic ultrasound imaging, such as enhancing the contrast for the detection of the heart wall border. Current applications also include detailed analysis of blood volume and flow in cardiology and radiology, for example to detect myocardium perfusion defects and tumors [32, 62, 65, 295]. Recent research has also shown the potential of UCA for therapeutic applications such as drug delivery and molecular imaging [296-298].

The UCA shell improves the lifetime of the microbubbles after intravenous administration. Current clinically available UCA are comprised of a lipid monolayer or albumin coating with a gas core composed of a high molecular weight inert gas, for example perfluorobutane ($C_4F_{10}$) [5, 299]. Ligands can be conjugated to the UCA shell, resulting in targeted or functionalized microbubbles, making ultrasound molecular imaging possible. Molecular imaging is an emerging field and aims to image molecular changes associated with diseases by imaging biological processes in living systems at the cellular and molecular level. Preclinically, ultrasound molecular imaging has shown its potential for inflammation, ischemia-reperfusion injury, angiogenesis, and thrombi [297, 298]. Recently,

the successful first human phase 0 clinical trial for prostate cancer was presented [89], using a lipid coated microbubble targeted to vascular endothelial growth factor receptor 2 (VEGFR2).

For ultrasound molecular imaging, two steps are important: 1) binding of the targeted microbubble to the biomarker, and 2) imaging of the bound targeted microbubble using ultrasound. Several groups have focused on increasing binding of targeted microbubbles by applying acoustic radiation force to push the bubbles to the biomarkers on the vessel wall [300], deflating the microbubble which results in excess shell surface area [95], conjugating two [108] or three [109] different ligands to the coating, or varying ligand linker length [110]. Studies have not focused on the distribution of the ligand on the microbubble coating, even though Borden et al reported an heterogeneous ligand distribution, where the ligand was located in fine lines between domains [47]. However, this was reported for a microbubble ~20 μm in size, which is not a clinically relevant size. It is not thoroughly investigated whether ligand distributions are also heterogeneous for microbubbles of clinically relevant sizes or for different lipid coating compositions. A homogeneous ligand distribution could be more advantageous than a heterogeneous ligand distribution due to an increased probability of a successful binding event, especially in large vessels with high blood flow [301].

Research is ongoing to distinguish bound from unbound targeted microbubbles using ultrasound [136, 140, 302], and to determine the binding force of bound targeted microbubbles [82, 121, 123]. Larger targeted microbubbles have a larger binding area and therefore a higher binding force as more bonds can be formed. At the same time, the shear forces on the bound microbubble as a result of blood flow will also be higher for larger microbubbles, and thus persistence after binding will be lower for larger microbubbles. Modeling has predicted the optimal targeted microbubble size for binding to be 2 – 4 μm in diameter [111]. However, the shape of the bound microbubble was assumed spherical, but it is not known if targeted microbubbles remain spherical upon binding.

The aim of our research was to compare the ligand distribution, binding area, and bound microbubble shape of 1,2-distearoyl-*sn*-glycero-3-phosphocholine (DSPC) based and 1,2-dipalmitoyl-*sn*-glycero-3-phosphocholine (DPPC) based lipid-coated targeted microbubbles using high-resolution microscopy. The DSPC microbubble, which we previously used in a drug delivery study [35], resembles the clinically approved UCA SonoVue in coating composition (coating composition: polyethylene glycol (PEG(4000); Molecular weight (MW) 4000), DSPC, and 1,2-dihexadecanoyl-*sn*-glycero-3-phospho-(1'-*rac*-glycerol) (DPPG) [7]). The DPPC based microbubbles resemble the clinically approved UCA Definity (coating composition: DPPC, 1,2-dihexadecanoyl-*sn*-glycero-3-phosphate (DPPA), and 1,2-dipalmitoyl-*sn*-glycero-3-phosphoethanolamine(polyethylene glycol) (DPPE-PEG(5000); Molecular weight 5000) [9]).

## 4.3. MATERIALS AND METHODS

### Materials

DPPC, 1,2-distearoyl-*sn*-glycero-3-phosphoethanolamine-N-carboxy(polyethylene glycol) (DSPE-PEG(2000); MW 2000), 1,2-distearoyl-*sn*-glycero-3-phosphoethanolamine-N-biotinyl(polyethylene glycol) (DSPE-PEG(2000)-biotin; MW 2000) were purchased from Avanti Polar Lipids, USA. DSPC, polyoxyethylene (40) stearate (PEG-40 stearate) were obtained from Sigma. Perfluorobutane ($C_4F_{10}$) was purchased from Linde Gas Benelux. Streptavidin Oregon Green 488, streptavidin Oregon Green 514, 1,1'-dioctadecyl-3,3,3',3'-tetramethylindodicarbocyanine perchlorate (DiD), 100 nm yellow-green fluorescent beads were obtained from Molecular Probes (F8803), Life Technologies. PD-10 desalting columns were purchased from GE Healthcare Bio-Sciences. Custom polycarboxylate hydrogel-coated (1.5 micron) quartz glasses (30 mm in diameter, 0.22 mm thickness), amine coupling kit (containing EDC·HCl, activation buffer, borate elution buffer, and quenching buffer) were purchased from XanTec bioanalytics GmbH, Germany.

### Preparation of microbubbles

Biotinylated lipid coated microbubbles (composition in mol%: DSPC or DPPC 59.4; PEG-40 stearate 35.7; DSPE-PEG(2000) 4.1, DSPE-PEG(2000)-biotin 0.8) with a $C_4F_{10}$ gas core were made by sonication for 10 seconds using the method described by Klibanov et al [129]. DSPC microbubbles refer to the microbubbles with DSPC as main coating component, DPPC microbubbles to those with DPPC as main coating component.

### Microbubble size distribution

Microbubble size distributions were measured on a Coulter Counter Multisizer 3 (n = 3) (Beckman Coulter, Mijdrecht, the Netherlands). A 50 μm aperture tube was used, allowing quantification between 1 and 30 μm using a linear spacing between the 256 channels. Polydispersity of the samples was assessed by the SPAN, defined as (d90%-d10%)/d50% where d90%, d10% and d50% are the microbubble diameters below which 90, 10, and 50% of the cumulative amount of microbubbles is found.

### Ligand distribution within microbubble coating

*Ligand conjugation*

The ligand fluorescent streptavidin Oregon Green 488 was conjugated to the biotinylated microbubbles as described by Lindner et al [132]. Briefly, microbubbles were washed by flotation by placing the microbubble solution in a 3 mL syringe with one-way tap and leaving to stand. After 45 min, the subnatant was drained, and the microbubbles were suspended in 1 mL of PBS saturated with $C_4F_{10}$ and drained. Then, 110 μL of streptavidin (1 mg/mL) was

quickly spinned using a Microspin FV-2400 (Biosan Ltd), and 90 µL of the streptavidin solution was added to $7\times10^8$ microbubbles. This was incubated on ice for 30 minutes. Excess streptavidin was washed by flotation as above.

*Ligand distribution visualization*

The streptavidin-conjugated microbubbles were mounted in 87% glycerol (v/v in PBS) and were visualized three dimensionally with super resolution on a Leica TCS 4Pi confocal laser-scanning microscope [303, 304] using a matched pair of aligned opposing 100× glycerol HCX PL APO objective lenses (Numerical aperture 1.35). The lenses were aligned using 100 nm fluorescent beads [305]. Image stacks were recorded as y-stacked xz-scans in a green (500-550 nm) spectral channel. Each xz-slice consisted of 512×512 pixels with a pixel size of 30×30 nm and was averaged twofold. The y-distance between neighboring xz-slices was 90 nm. An Argon laser (488 nm) was used for excitation. Volume rendering of the image stacks was performed using the "voltex" function of the program AMIRA (Version 5.2.2, FEI, Mérignac Cedex, France).

*Semi-automatic analysis of ligand distribution heterogeneity*

The heterogeneity of the ligand distribution was analyzed with custom software written in MATLAB (Mathworks, Natick, MA, USA) using the 3D-stacks described before. For both microbubble types, 30 randomly chosen microbubbles were analyzed. In a first step, the center point of the microbubble was manually annotated in one of the xz-slices. Next, the program computed the radial intensity profiles for 100 angles (i.e. at multiples of 2 π/100 radians), using the manually selected center as starting point. After this, a circle was fitted through the intensity maxima using a MATLAB routine based on the method as described by Taubin [306], from which the radius ($R_{fit}$) and origin ($O_{fit}$) of the fluorescent contour within the xz-slice were obtained. All the pixels located within 90 nm from $R_{fit}$, defined as the region of interest (ROI), were included in the heterogeneity analysis. The ROI was subdivided in 32 angular parts (i.e. each π/16 radians); for each angular part the mean fluorescence pixel intensity ($I_{part}$) was calculated. This procedure was repeated for a range of xz-slices spatially distributed around the equatorial plane of the bubble, whereby the origin of the best circle fit ($O_{fit}$) within a slice was used as starting center point for the radial intensity profiles in the adjacent xz-slice. Only xz-slices with a value for $R_{fit}$ which was larger than 75% of the value of $R_{fit}$ in the equatorial plane of that particular bubble were included in the analysis. This was because towards the caps of the microbubbles, the xz-slices had a fluorescence pattern of filled circles, instead of a fluorescent rim surrounding a dark core, which could not be processed with the same contour tracking algorithm. On average, 35 xz-slices were included per bubble, resulting in on average 35 × 32 = 1120 angular parts per bubble, from which the median part intensity per bubble ($\hat{I}_{median}$) was calculated. An individual angular part was classified as an inhomogeneity when the absolute difference

between the mean fluorescence intensity of this part ($I_{part}$) and the median part intensity of the bubble ($\hat{I}_{median}$) was more than two-third of the value of $\hat{I}_{median}$ (i.e. $|I_{part} - \hat{I}_{median}| > 2/3 \times \hat{I}_{median}$). From this, the percentage of parts classified as an inhomogeneity per microbubble, being a measure for inhomogeneous ligand distribution, was calculated for both microbubble types.

*Statistics*

Statistical analysis was performed using IBM SPSS Statistics 20. First, Shapiro-Wilk normality tests were performed to determine if the standard deviation and mean were significantly different from a normal distribution. Both distributions were not normally distributed (DSPC: $p = 0.001$, DPPC: $p < 0.001$) and hence we used non-parametric testing. The Mann-Whitney U test was used to identify whether the percentages of parts classified as an inhomogeneity were significantly different between both microbubble types. A p-value < 0.05 was regarded as significant.

**Binding area of targeted microbubbles**

*Targeted microbubbles and surface coating*

The binding area of biotinylated microbubbles and a streptavidin surface was studied by adding the lipid dye DiD to the microbubbles before sonication and covalently linking fluorescent streptavidin Oregon Green 514 to the hydrogel-coated quartz glass. For the covalent linkage, streptavidin was first dissolved in acetate buffer (2 mM, pH 5.4) (1 mg/mL), and desalted using a PD-10 desalting column according to the manufacturer's instructions. After desalting, the concentration of streptavidin was determined spectrophotometrically using a calibration curve on a Varioskan™ Flash (Thermo Scientific). The desalted streptavidin was covalently linked to the hydrogel-coated quartz glasses according to the instructions of the manufacturer. Briefly, the quartz glass was placed in a 6-well plate (BD) and incubated with 2.5 mL of borate elution buffer (1 M sodium chloride, 0.1 M sodium carbonate buffer, pH 10) for 10 min on a rotating shaker (model KM-2, Edmund Bűhler GmbH, 125 Mot 1/min). After three washes with 3 mL MilliQ, the glasses were rinsed with 2 mL of 1.0% (w/v) EDC·HCl in activation buffer, and then incubated for 15 minutes in the dark in 3 mL of 1.0% (w/v) EDC·HCl in activation buffer. After three washes with MilliQ, the glasses were incubated for two hours with 1.6 mL of desalted streptavidin Oregon Green 514 (40 µg/mL) on the rotating shaker. This was followed by 30 minutes incubation with 2.5 mL quenching buffer. Then, the glasses were washed three times with PBS. Just before adding the microbubbles, the glass was washed once with PBS containing calcium and magnesium (PBS +/+) and the microbubbles were allowed to adhere to the streptavidin-coated surface by flotation. For this, the glasses were placed in a custom-made holder with a 10 mL volume filled with PBS +/+. The microbubbles were injected under the glass using a bended blunt 19 G-needle. After 5 minutes, the glass was gently washed three times with PBS +/+ using a

3 mL plastic Pasteur pipet, and mounted in 87% (v/v) glycerol such that the bound targeted microbubbles were on top of the coated surface.

*Targeted microbubble and surface visualization*

The microbubbles and streptavidin coating were visualized three dimensionally with the 4Pi setup as described before. Image stacks were recorded as y-stacked xz-scans in a green (500-550 nm) and far red (647-703 nm) spectral channel. An Argon laser (488 nm) and HeNe laser (633 nm) were used for excitation. Volume rendering of the image stacks was performed using the "voltex" function (for microbubbles) and "isosurface" function (for streptavidin) of the program AMIRA.

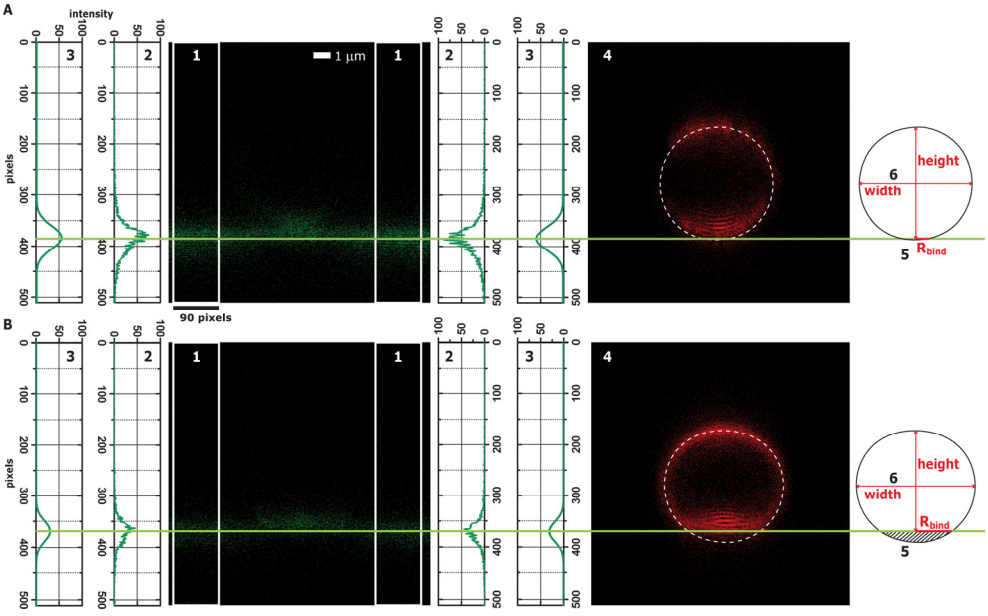


**Fig. 4.1.** Method of calculation of binding area and microbubble shape for targeted microbubbles. Example of a **(A)** DSPC microbubble and **(B)** a DPPC microbubble.

*Analysis of binding area and bound microbubble shape*

The microbubble binding area was calculated from the cross-section of the streptavidin plane with the bubble surface using Fiji (http://fiji.sc/wiki/index.php/Fiji; [307]) as illustrated in Fig. 4.1A for a DSPC microbubble, and in Fig. 4.1B for a DPPC microbubble. First, the streptavidin plane was determined by the z-position in the xz-plane where the green fluorescence intensity was maximal. This was done at the left and right of the plane (90 pixels wide) as illustrated by the white boxes labeled 1 in Fig. 4.1. The edges of the recording

were chosen to avoid possible interference with the microbubble signal. The fluorescence intensity derived at the two fixed z-positions is given in 2 in Fig. 4.1, and the Gaussian fit through the data in 3 in Fig. 4.1. The maximum was derived from the Gaussian fit and averaged between the two z-positions. The difference between the left and right maxima was 0.2 ± 2.2 pixels (i.e. 6 ± 66 nm; n = 47), which was within the z-resolution of the microscope (~130 nm [303, 304]), indicating the streptavidin plane was level within 0.3 degrees. The microbubble contour was determined in both the xz and yz-plane of the far red channel by manually drawing an ellipsoid through the top half of the microbubble as illustrated by 4 in Fig. 4.1 for the xz-plane. Then, the cross section between the streptavidin plane and the microbubble contour was determined in both planes (5 in Fig. 4.1), from which the radius of the binding area ($R_{bind}$) was derived. The microbubble radius before binding to the streptavidin surface ($R_0$) was calculated by $R_0 = \sqrt[3]{\frac{3V_0}{4\pi}}$, where $V_0$ is the volume of the total ellipsoid minus the part of the ellipsoid below the streptavidin plane (hatched in schematic of microbubble in Fig. 4.1). A linear trend line was fitted through the origin and the data points using GraphPad InStat verion 5.04 (GraphPad Software). To characterize the shape of the bound microbubbles, we derived the width and height of the bound microbubble, as illustrated in 6 in Fig. 4.1. The Mann-Whitney U test (IBM SPSS Statistics 20) was used to identify whether the shape of the bound microbubbles was significantly different between both microbubble types. A p-value < 0.05 was regarded as significant.

## 4.4. RESULTS

### Size distribution

The size distribution of the streptavidin-conjugated DSPC and DPPC microbubbles is shown in Fig. 4.2. The number weighted mean diameter was 4.2 μm for the DSPC and 3.9 μm for the DPPC microbubbles. The volume weighted mean diameter of 8.0 μm for the DSPC microbubbles was also higher than the diameter of 7.7 μm for the DPPC microbubbles. These small differences were also reflected in the SPAN, which was 1.4 for DSPC and 1.3 for DPPC microbubbles.

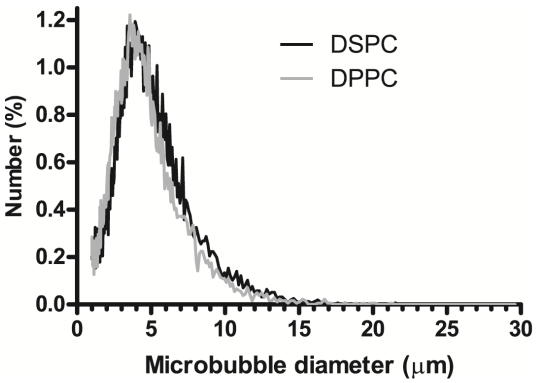


**Fig. 4.2.** Size distribution of microbubbles.

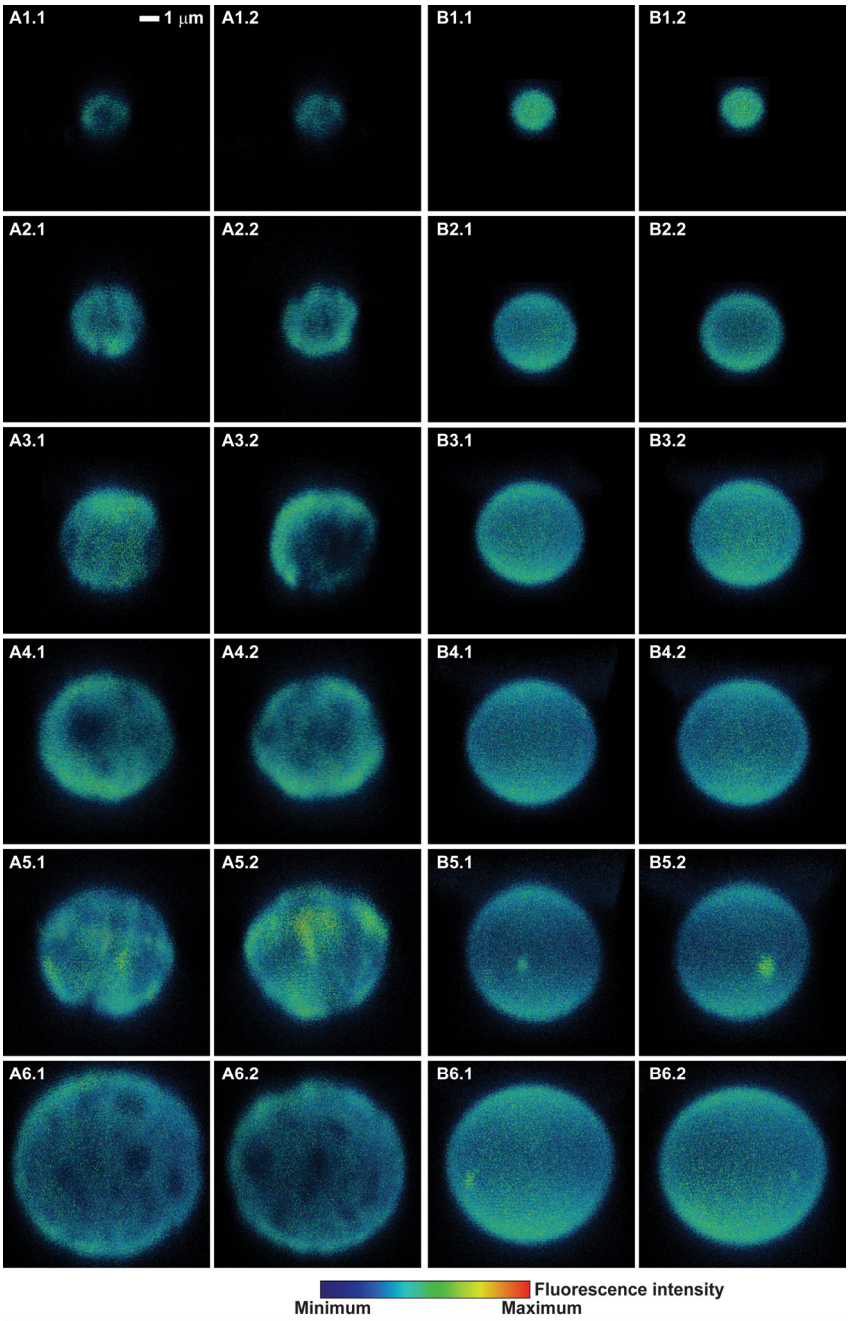


**Fig. 4.3.** Ligand distribution on **(A1-6)** DSPC microbubbles and **(B1-6)** DPPC microbubbles. Two views (**.1** and **.2**) out of the 3D reconstructions are shown for each microbubble. Smallest shown microbubble is 1.7 µm in diameter, largest is 7.5 µm.

**Ligand distribution within the coating**

The distribution of the ligand streptavidin was studied in 66 DSPC and 55 DPPC microbubbles. As shown in Fig. 4.3A, we observed heterogeneous ligand distributions for the DSPC microbubbles. Since streptavidin only conjugates to DSPE-PEG(2000)-biotin, a high fluorescence intensity area indicates a higher concentration of this lipid in that part of the coating. Also, areas with hardly any fluorescence were detected, indicating an exclusion of the DSPE-PEG(2000) lipid and hence a little higher concentration of one or both of the other coating components, namely DSPC and PEG-40 stearate. Interestingly, different patterns were found for microbubbles of the same size, for example Fig. 4.3A4 and A5. Whereas the microbubble in Fig. 4.3A4 had larger areas of hardly any fluorescence and no areas of higher fluorescence intensity, the microbubble in Fig. 4.3A5 had small areas of hardly any fluorescence and small areas of higher fluorescence intensity. Although we observed patchy heterogeneous fluorescence distributions in all DSPC microbubbles, some microbubbles showed more heterogeneity than others. Two of the most heterogeneous DSPC microbubbles are shown in Fig. 4.3A3 and 3A5. The microbubble in Fig. 4.3A3 has a large area that contains hardly any fluorescence, whilst the microbubble in Fig. 4.3A5 has a more patchy character with areas that differ in fluorescence intensity, as areas with minimum and maximum intensity were observed.In contrast to the DSPC microbubbles, the DPPC microbubbles showed a more uniform ligand distribution, indicated by the more homogeneous fluorescence, as shown in Fig. 4.3B. Dark domains with hardly any fluorescence were not observed. Occasionally a higher fluorescence intensity spot was observed (see Fig. 4.3B5 and B6), indicating a higher concentration of the DSPE-PEG(2000) lipid in that area. The observation of a more uniform lipid coating in case of DPPC microbubbles was confirmed by the semi-automatic image analysis counting the percentage of parts being classified as an inhomogeneity (see Fig. 4.4). A significant higher percentage of parts classified as an inhomogeneous

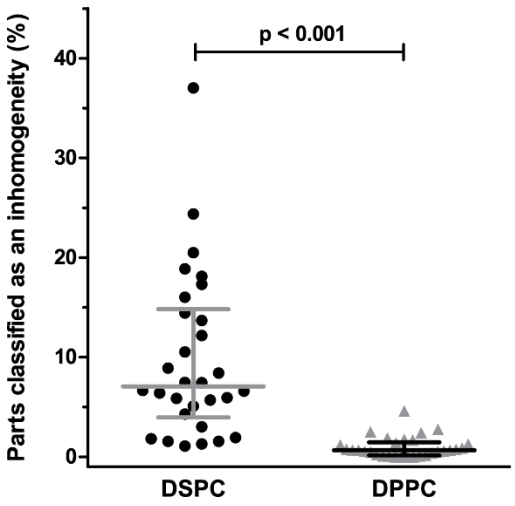


**Fig. 4.4.** Homogeneity of ligand distribution for DSPC (n = 30) and DPPC microbubbles (n = 30). Shown are the medians with the interquartile range.

were found for DSPC microbubbles than for DPPC microbubbles. No relation was found between the inhomogeneity and the microbubble diameters.

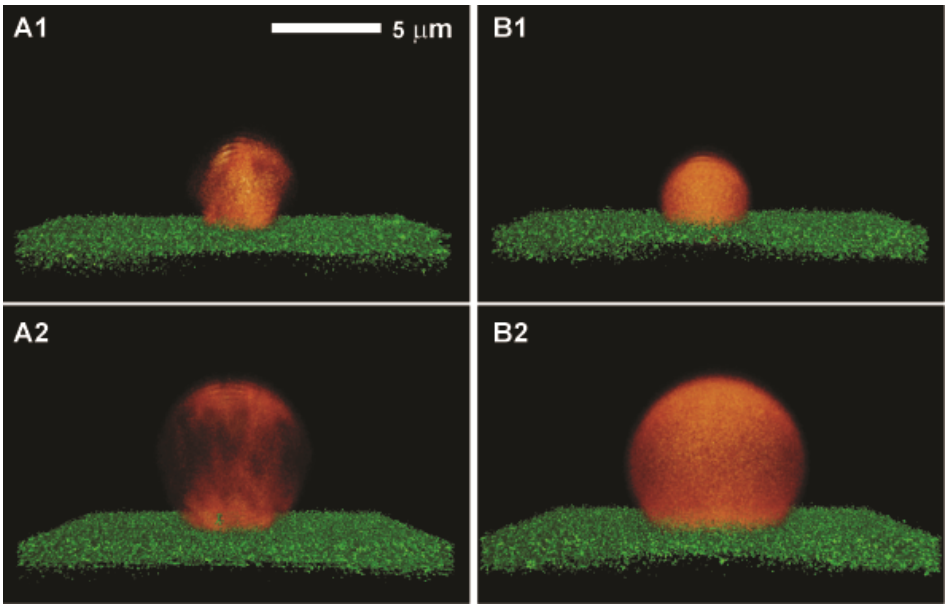


**Fig. 4.5. (A)** Targeted DSPC and **(B)** DPPC microbubbles (red fluorescent) bound to streptavidin-coated surface (green fluorescent; covalently linked).

**Binding area of targeted microbubbles**

Fig. 4.5A shows examples of targeted DSPC microbubbles (in red) bound to the streptavidin-coated surface (in green) and Fig. 4.5B shows examples of targeted DPPC microbubbles. In these cases, the streptavidin was covalently linked to the hydrogel-coated quartz glass, and we observed no streptavidin fluorescence on the microbubble surface. This in contrast to when we coated an Opticell membrane with streptavidin by physisorption (as previously described [123]), when we also observed streptavidin on both the DSPC and DPPC microbubbles, most likely due to rolling of the microbubbles before binding.

When the binding area of the targeted microbubbles to the covalently linked streptavidin was calculated, we found a factor of ~2.3 smaller binding radii for DSPC microbubbles (factor ~5.3 for binding area) than for DPPC microbubbles, based on the slope of the fit as shown in Fig. 4.6. For both microbubble types, the binding radii increased with the microbubble size, albeit that the increase was larger for the DPPC than for the DSPC microbubbles. To characterize the shape of the bound microbubbles, we derived the

width to height ratio of the microbubbles, as illustrated in Fig. 4.7. The width to height ratio was significantly smaller for the DSPC microbubbles than for the DPPC microbubbles, indicating the DSPC microbubbles were more spherical than the DPPC microbubbles, which resembled a dome-shape.

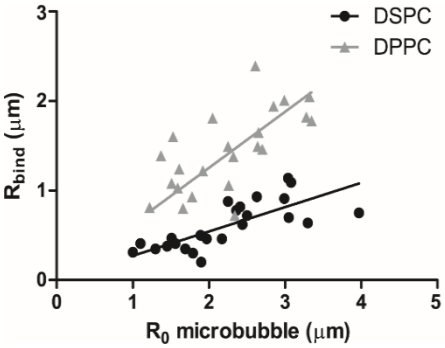


**Fig. 4.6.** Binding area radius, $R_{bind}$, as function of radius for targeted microbubbles, $R_o$. Trend line through DSPC data has slope of 0.3; slope is 0.6 for DPPC.

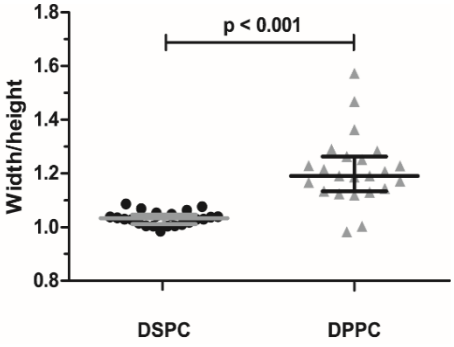


**Fig. 4.7.** Width to height ratio for targeted microbubbles. Shown are the medians with the interquartile range.

## 4.5. DISCUSSION

To the best of our knowledge, this is the first study that determined the binding area of targeted microbubbles and the dependence of that binding area on the lipid coating composition. The binding area was largest for the DPPC microbubbles which also had a significantly more homogeneous ligand distribution than the DSPC microbubbles. Whereas the bound targeted DSPC microbubbles remained spherical, the DPPC microbubbles were dome-shaped.

We used fluorescence to study the ligand distribution and the binding area of the lipid-coated targeted microbubbles. Using streptavidin Oregon Green 488, we observed differences in ligand distribution between the two microbubble types. The patches with hardly any fluorescence observed on the DSPC microbubbles are likely due to the absence of the DSPE-PEG(2000)-biotin and unlikely due to quenching of the Oregon Green 488 dye as a result of a very high concentration of streptavidin in that area. In fact, for fluorescent avidins to which no biotin is bound, it is known that fluorophore quenching occurs because the dye interacts with amino acid residues in the biotin-binding pocket. Upon biotin binding, this interaction is blocked, resulting in enhanced fluorescence [308, 309]. According to the manufacturer, the streptavidin molecule used in our study was labelled with 2-5 Oregon Green molecules, which is a fluorinated analogue of fluorescein. As streptavidin has four

biotin binding pockets, multiple biotins could have bound per streptavidin if the biotinylated lipid concentration was high enough, resulting in an even higher, not a lower, fluorescence intensity in areas with a high concentration of the DSPE-PEG(2000)-biotin lipid. This may have caused the higher intensity patches observed in the shell of the DSPC microbubbles.

Surface microstructures are common for lipid-coated microbubbles, and have also been reported for a mixture of two out of the three components of our DSPC microbubbles, namely a mixture of DSPC and DSPE-PEG(2000) [46, 47], and a mixture of DSPC and PEG-40 stearate [48, 49]. As lipid coatings on microbubbles are monolayers, the results of microbubble studies can be compared to monolayer films formed at an air/water interface. The observed heterogeneous lipid distributions in the coating of our and previously reported microbubbles is in agreement with studies of lipid monolayer films as immiscibility has been reported for all different mixtures of DSPC and DSPE-PEG(2000). PEG-40-stearate is reported to be in the expanded phase only and mixes with other expanded phase lipids, but is immiscible with lipids in the condensed phase [48]. Since DSPC is in the condensed phase only [280], PEG-40 stearate is immiscible with this lipid. DSPE-PEG(2000) can be in the expanded or condensed phase [280]. When it is in the expanded phase it will be miscible with PEG-40 stearate, but when it is in the condensed phase it will be immiscible with PEG-40 stearate. Lozano and Longo [280] showed miscibility of DPPC and DSPE-PEG(2000) in both the expanded and condensed phase, suggesting this mixture would result in a homogeneous lipid coating for microbubbles. When we replaced DSPC by DPPC, we indeed observed a homogeneous distribution of DSPE-PEG(2000) within the coating of the microbubbles. This supports our assumption that in our experiments the lipids are immiscible (DSPC microbubbles) or miscible (DPPC microbubbles) which is the explanation for respectively the presence and absence of surface microstructures. The occasionally observed small higher intensity fluorescence spots on the DPPC microbubbles could be explained by folds or buckles that form locally on the microbubble coating due to excess lipids [310].

In our study we observed different patterns for DSPC microbubbles of the same size, which is in contrast to what has previously been reported for microbubble coating mixtures of DSPC and PEG-40 stearate [49]. A different coating composition for our microbubbles could be the reason, as could be the variation in lipid concentrations per microbubble. Both could also be the explanation why we did not observe the DSPE-PEG(2000) in fine lines between domains, as previously reported by others [47].

Surface microstructures resulting in inhomogeneous lipid distributions could be disadvantageous for microbubbles used as drug carrier system when drugs are conjugated to the lipids. One such drug carrier system is drug-filled liposomes conjugated to the coating via DSPE-PEG(2000) [311]. A homogeneous DSPE-PEG(2000) distribution would be optimal to avoid competition during the conjugation of the liposomes. A maximum amount of drug

can therefore be loaded onto the microbubbles, which based on our current study favors DPPC over DSPC as main lipid for the coating.

Several strategies have been reported to improve binding of targeted microbubbles [95, 108-110, 300] , but these have not included varying the lipid coating composition. In addition to differences in ligand distribution, we also found differences in binding area between both microbubble types. DSPE-PEG(2000) is often used to conjugate ligands to the microbubble coating, either by coupling via streptavidin or by covalent coupling [138]. For the binding area experiment, we used the lipid dye DiD to fluorescently label the microbubbles. As this type of lipid dye co-localizes with the DSPE-PEG(2000)-biotin lipid [47], it is a good indicator for the binding area. We indeed observed a similar dye pattern as when streptavidin Oregon Green 488 was conjugated to the microbubbles, namely a heterogeneous distribution for the DSPC microbubbles and a homogeneous distribution for the DPPC microbubbles. It needs to be further investigated whether a heterogeneous or homogeneous ligand distribution or a smaller or larger binding area is best for binding probability, and binding strength of targeted microbubbles. Differences between small microvessels, where microbubbles will be in close proximity to the vessel wall on all sides, and larger vessels, where the blood flow is also significantly higher [301], will have to be taken into account when investigating the binding probability. Although the binding area for the DSPC microbubbles was smaller, this does not imply that the binding force is weaker. As the ligand distribution is heterogeneous throughout the coating of DSPC microbubbles, we also frequently observed areas with high concentrations of the ligand. More ligand molecules within a small area could therefore have a binding force equal to a lower amount of ligand molecules distributed over a larger area. The shape of the bound microbubble could also be very important as the effect of blood shear forces is expected to be stronger on spherical than on domed-shape microbubbles. This again favors DPPC over DSPC for targeting microbubbles. The domed shape of the DPPC microbubbles suggests a more elastic coating, which is in line with DPPC having a lower elastic compressibility modulus than DSPC [278, 279].

A limitation of our study is that microbubbles bound under static conditions using biotin-streptavidin as artificial ligand-biomarker pair. Our future research will focus on binding targeted microbubbles to disease related biomarker under flow conditions. However, our findings can be used to improve the binding of targeted microbubbles and aid in the ongoing research to distinguish bound from unbound targeted microbubbles using ultrasound. Overvelde showed that the binding itself results in a resonance frequency shift and a 30% difference in vibration amplitude [20]. It is therefore expected that a difference in binding area will also change the acoustic behavior. Acoustic stability of the bound targeted microbubbles is also important, and will have to be further investigated for both microbubble types. The relation between the acoustic behavior of microbubbles and surface microstructures is unknown [310] and will be subject for our future studies.

Nonetheless, heterogeneous lipid distributions could be contributing to differences in acoustical responses of similar sized bubbles [312]. In addition, our findings may be used for modeling, as modeling has greatly aided the understanding and prediction of non-targeted microbubble behavior in an acoustic field [5], but is still in its infancy for targeted microbubbles.

## 4.6. CONCLUSIONS

This study reveals that lipid-coated microbubbles differ in DSPE-PEG(2000) lipid and ligand distribution, binding area, and bound microbubble shape solely on the basis of their main lipid component. A homogeneous ligand distribution, larger binding area and dome-shape upon binding could be advantageous for binding of targeted microbubbles, thereby favoring DPPC over DSPC as main lipid for UCA for ultrasound molecular imaging.

**Acknowledgement**

The authors are grateful to Prof. dr. A.L. Klibanov from the University of Virginia, Cardiovascular Division, Charlottesville, Virginia, USA for discussions about the microbubble preparation. The authors thank the Erasmus Optical Imaging Centre of Erasmus MC for use of their facilities, and Michiel Manten from the Dept. of Biomedical Engineering, Erasmus MC for technical assistance. We also thank Prof. dr. A. Blume, Dept. Biophysical Chemistry, Martin Luther University Halle-Wittenberg, Germany, for discussions about the results, and Paul van den Berg from the Dept. of Clinical Genetics, Erasmus MC, for the spectrophotometer measurements, and Dr. E. Gedig from XanTec bioanalytics GmbH, Germany, for discussions about the covalent coating of streptavidin to the quartz glasses. This research is supported by the Center for Translational Molecular Medicine and the Dutch Heart Foundation (PARISk), the Dutch Technology Foundation STW, and NanoNextNL, a micro and nanotechnology consortium of the Government of the Netherlands and 130 partners.

Chapter 5

# Non-linear response and viscoelastic properties of lipid-coated microbubbles: DSPC versus DPPC

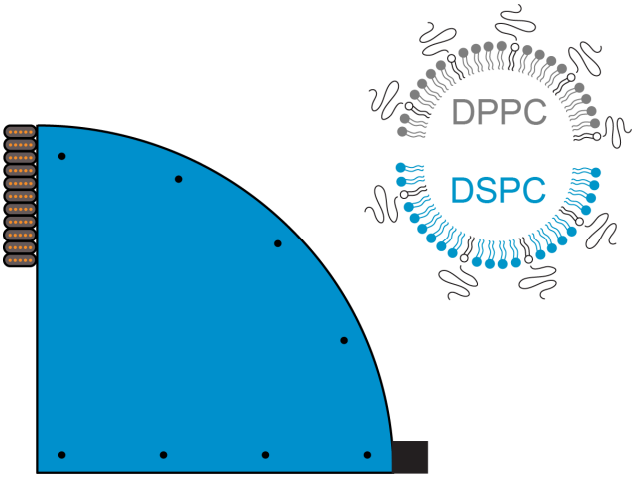


Tom van Rooij, Ying Luan, Guillaume Renaud, Antonius F.W. van der Steen, Michel Versluis, Nico de Jong, Klazina Kooiman

*Ultrasound in Medicine & Biology*, 41:5, 1432–1445 (2015)

## 5.1. ABSTRACT

For successful *in vivo* contrast-enhanced ultrasound imaging (CEUS) and ultrasound molecular imaging, detailed knowledge of stability and acoustical properties of the microbubbles is essential. Here, we compare these aspects of lipid-coated microbubbles that have either DSPC or DPPC as their main lipid; the other components were identical. The microbubbles were investigated *in vitro* over a frequency range of 1-4 MHz and at pressures between 10-100 kPa and their response to the applied ultrasound was recorded using ultra-high-speed imaging (15 Mfps). Relative to DPPC-coated microbubbles, DSPC-coated microbubbles had *1)* higher acoustical stability; *2)* higher shell elasticity as derived using the Marmottant model (DSPC: 0.26 ± 0.13 N/m, DPPC: 0.06 ± 0.06 N/m); *3)* pressure amplitudes twice as high at the second harmonic frequency; and *4)* a smaller amount of microbubbles that responded at the subharmonic frequency. Due to their higher acoustical stability and higher nonlinear response, DSPC-coated microbubbles may be more suitable for CEUS.

## 5.2. INTRODUCTION

Ultrasound contrast agents (UCAs) consist of gas-filled coated microbubbles with diameters between 1 and 10 μm. Clinically, they have been used for several decades for contrast-enhanced ultrasound imaging (CEUS) [32, 62, 313]. More recent studies have shown their potential for local drug delivery and ultrasound molecular imaging [36, 209, 297].

To increase their lifetime after injection into the bloodstream, the microbubbles are stabilized with a coating. Three lipid-coated UCAs are approved for diagnostic CEUS: Definity (Lantheus Medical Imaging, North Billerica, MA, USA), Sonazoid (Daiichi Sankyo Co. Ltd., GE Healthcare, Tokyo, Japan), and SonoVue (Bracco Imaging S.p.A., Milan, Italy). A complete and updated list of approving agencies can be found elsewhere [314]. The responses to ultrasound of Definity and SonoVue have been thoroughly characterized [125-128], as well as the responses of several lipid-coated microbubbles for research purposes [20, 135, 148, 285]. Although all of these microbubble types are coated with a combination of lipids, it is unclear how the different lipids affect their stability, and the microbubbles' response to ultrasound. The hydrophobic chain length of the phospholipids incorporated in the microbubble shell was found to influence the dissolution of the microbubbles; passive dissolution rates decreased for chains of 16 C-atoms (DPPC, 1,2-dipalmitoyl-*sn*-glycero-3-phosphocholine) up to 22 C-atoms (DBPC, 1,2-dibehenoyl-*sn*-glycero-3-phosphocholine), but increased again for chains of 24 C-atoms [50, 285]. The influence of chain length on ultrasound-driven dissolution (i.e. acoustical stability) was different from that of passive dissolution. When exposed to ultrasound, microbubbles that had lipids with 16 C-atoms incorporated in their shell were still least stable, whereas those with lipids having 18 C-atoms (DSPC, 1,2-distearoyl-*sn*-glycero-3-phosphocholine) were equally stable as the microbubbles having lipids with chain lengths of 22 C-atoms. For even longer chains (24 C-atoms) the acoustical stability decreased

again [50]. Next to dissolution or stability, other properties of microbubbles with different lipid-coatings have been studied. Helfield et al. [259] varied the shell microstructure using different cooling rates and found a change in subharmonic response, but without a clear relation to the shell microstructure. Shell viscosity was found to depend on the coating composition and manufacturing method, and the viscosity was lower when higher concentrations of emulsifier were used [315]. Wang and Yeh [316] explained this by the increased movements of lipids due to the emulsifier. The bulk linear properties of monodisperse bubbles produced using flow-focusing microfluidic devices were reported to depend on both the radius and the acoustic pressure [286, 317]. However, none of these studies investigated the properties of one specific lipid on the acoustic response of the microbubbles. Understanding the influence of this replacement on microbubbles' acoustical stability and their response to ultrasound may aid the design of circulating microbubbles for CEUS and of targeted microbubbles for local drug delivery and ultrasound molecular imaging applications.

Super-resolution microscopy was used before to study the distribution of lipids in the coating of two types of microbubbles, after changing only the main shell component [70]. In that particular study was chosen to use DPPC (1,2-dipalmitoyl-*sn*-glycero-3-phosphocholine, C16:0), which is the main coating component for Definity [9], or DSPC (1,2-distearoyl-*sn*-glycero-3-phosphocholine, C18:0), which is the main constituent of the coating of SonoVue [7] and the experimental agent BR14 [318, 319]. The microbubbles with DSPC as the main lipid had a heterogeneous lipid distribution throughout the shell, whereas the DPPC microbubbles had a more homogeneous lipid distribution. Similar results were also reported for mixtures of two out of three of the components [46, 47, 49, 280] that were used for the microbubble coating in the study by Kooiman et al. [70].

In the present study we used the Brandaris 128 ultra-high-speed camera [52] to compare the responses to ultrasound of microbubbles with either DSPC or DPPC as the main coating lipid. More specifically, we focused on their acoustical stability, their nonlinear responses at the subharmonic and second harmonic frequencies, and their shell elasticity and viscosity.

## 5.3. MATERIALS AND METHODS

### Microbubble preparation

Biotinylated lipid-coated microbubbles with a $C_4F_{10}$ gas core (F2 Chemicals Ltd, Preston, UK) were made by sonication for 10 seconds as described previously [70, 129]. The lipid-coating was composed of 59.4 mol% 1,2-distearoyl-*sn*-glycero-3-phosphocholine (DSPC) (P6517; Sigma-Aldrich, Zwijndrecht, the Netherlands) or 1,2-dipalmitoyl-*sn*-glycero-3-phosphocholine (DPPC) (850355; Avanti Polar Lipids, Alabaster, AL, USA); 35.7 mol% polyoxyethylene-40-stearate (PEG-40 stearate) (P3440; Sigma-Aldrich); 4.1 mol% 1,2-distearoyl-*sn*-glycero-3-phosphoethanolamine-N-[carboxy(polyethylene glycol)-2000 (DSPE-PEG(2000)) (880125;

Avanti Polar Lipids); and 0.8 mol% 1,2-distearoyl-*sn*-glycero-3-phosphoethanolamine-N-[biotinyl(polyethylene glycol)-2000] (DSPE-PEG(2000)-biotin) (880129; Avanti Polar Lipids). The coating components were dissolved in phosphate buffered saline (PBS) and the final concentrations were 2.5 mg/mL DSPC or DPPC, 0.625 mg/mL PEG-40 stearate, 0.625 mg/mL DSPE-PEG(2000), and 0.125 mg/m: DSPE-PEG(2000)-biotin.

**Microbubble spectroscopy**

The acoustical behavior of the microbubbles was studied using the Brandaris 128 ultra-high-speed camera [52] operated in ROI mode [320] at a frame rate of ~15 million frames per second. The camera was connected to a microscope (BX-FM, Olympus, Tokyo, Japan) with a 40× water-immersion objective (Olympus) and a 2× magnifier (U-CA, Olympus). We used the microbubble spectroscopy technique to characterize single microbubbles as described previously [18, 20]. An OptiCell™ was incubated for 1 hour with 10 mL 1 vol% bovine serum albumin in PBS to prevent unspecific binding. After washing with PBS (3×), we added 10 mL of PBS and 3 µL of microbubble suspension to the OptiCell, so the concentration was ~$1\times10^5$ microbubbles/mL as measured using a Multisizer 3 Coulter Counter (n = 3, Beckman Coulter Inc, Mijdrecht, the Netherlands).

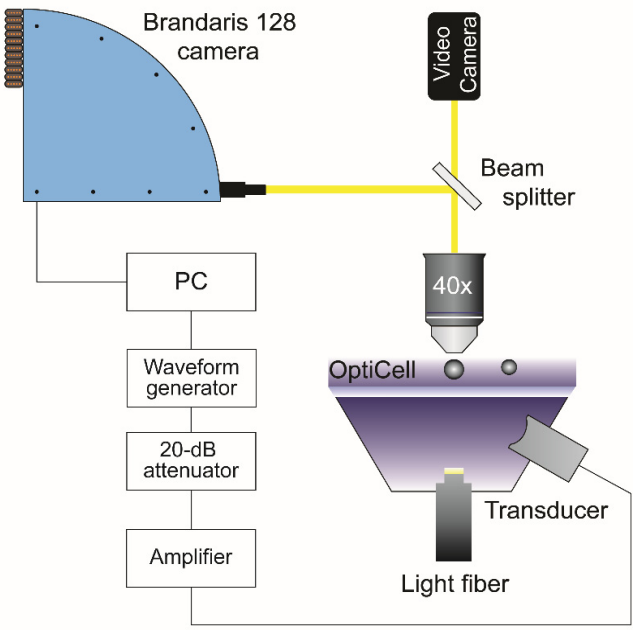


**Fig. 5.1.** Set-up for single microbubble spectroscopy: the Brandaris 128 ultra-high-speed camera coupled to the microscope to image the oscillating microbubbles.

The ultrasound signal was a 10-cycle Gaussian tapered sine wave burst generated by a Tabor 8026 arbitrary waveform generator (AWG, Tabor Electronics Ltd, Tel Hanan, Israel). This signal was then attenuated by a 20-dB attenuator (Mini-Circuits, Brooklyn, NY, USA), amplified by a broadband amplifier (ENI A-500, Electronics & Innovation Ltd., Rochester, NY, USA), and coupled to a broadband single element transducer (25 mm focal distance, center frequency 5 MHz, bandwidth 1-9 MHz, PA275, Precision Acoustics Ltd, Dorchester, UK) for the transmission of ultrasound (Fig. 5.1). Transmit frequencies were swept from 1 to 4 MHz (in steps of 200 kHz) at a peak-negative ($P_A$) driving pressure of 10, 20, 50, or 100 kPa. The pressures were calibrated with two calibrated PVDF needle hydrophones in a separate measurement beforehand (0.2 mm diameter PA2030 and 1 mm diameter PA1875, Precision Acoustics).

First, 16 movies of 128 frames were recorded at $P_A$ = 20 kPa followed by 16 recordings at $P_A$ = 10 kPa of the same microbubble to determine its shell properties. Another series of 16 recordings at $P_A$ = 50 kPa with 16 subsequent recordings at $P_A$ = 100 kPa of the same microbubble was used to study its nonlinear behavior. The ultrasound was triggered on the second recording of each microbubble to obtain the initial resting diameter and the noise level due to the uncertainty of the contour tracking algorithm in the first recording. All measurements were performed at room temperature.

**Data analysis**

Diameter-time (*D-t*) curves from all recordings were obtained using custom-designed image analysis software [20]. The D-t curves of a single experiment were used to determine the acoustical stability of the microbubble, measured by its shrinkage due to the ultrasound exposure: the difference between the mean diameter of the first and last recording divided by the mean diameter of the first recording.

The D-t curves were transformed to the frequency domain using a Fast Fourier Transformation (FFT), as analysis in this domain provides specific information on the frequency content of the recorded signal. The maximum oscillation amplitude in a frequency band of 300 kHz centered around the transmit frequency ($f_T$) was determined and fitted to the linear resonance curve by a least-mean-square method [20]:

$$Re(f) = \frac{Re_o}{\left(1 - f^2 / f_o^2\right)^2 + \left(\delta_{tot} f / f_o\right)^2} \tag{5.1}$$

with *Re* the integral of the power spectrum in the specified frequency band and $Re_o$ a scaling factor. Following Eq. (2) in van der Meer et al. [20] yields $Re_o = (F_o/2\pi\omega_o)^2$, with $F_o = |P_A|/\rho R_o^2$ [45]. The total damping coefficient $\delta_{tot}$, the eigenfrequency $f_o$, and the resonance frequency

$f_{res} = f_0\sqrt{1 - \delta_{tot}^2/2}$, were obtained from Eq. (5.1). The amplitude at the resonance frequency was divided by the diameter to obtain the maximum relative radial excursion.

The asymmetric and nonlinear behavior can be derived from the relative radial excursion of the microbubble following de Jong et al. [321]. The relative expansion *E* and the relative compression *C* of the microbubble were measured from the *D*-*t* curves and the ratio *E*/*C* was used to classify asymmetric behavior: compression-only behavior (*E*/*C* < 0.5); normal excursion (0.5 ≤ *E*/*C* ≤ 2); or expansion-only behavior (*E*/*C* > 2). Transforming the *D*-*t* curves to the frequency domain enables detailed analyses of subharmonic and second harmonic frequency responses. Similar to the analysis of the fundamental response, FFTs were calculated and the maximum amplitudes were determined in a 300 kHz frequency band centered around $½f_T$ for the subharmonic frequency or $2f_T$ for the second harmonic frequency. If at least two consecutive *D*-*t* curves of a microbubble showed a response at the subharmonic or second harmonic frequency (at a level at least 6 dB above the maximum noise level), these microbubbles were classified as responsive at the subharmonic or second harmonic frequency, respectively. The amplitudes at these frequencies were then fitted to the resonance curve, Eq. (5.1), to obtain the subharmonic resonance frequency ($f_{sub}$) and the second harmonic resonance frequency ($f_{sec}$), respectively. The frequency spectrum of the first recording without ultrasound exposure was taken as the noise level.

The theoretical acoustic pressures scattered by the nonlinear microbubble oscillations were calculated using [312]:

$$P_S = -\frac{\rho\omega_0^2 R^2 \varepsilon}{d} \tag{5.2}$$

where $P_S$ is the scattered pressure at a distance *d* from the microbubble, $\rho = 1{\cdot}10^3$ kg/m$^3$ is the density of the surrounding fluid (water), $\omega_0 = 2\pi f_0$ the angular resonance frequency as determined from the linearized harmonic resonance curve, *R* the corresponding radius, and $\varepsilon$ is the radial excursion amplitude at the resonance frequency.

The shell elasticity parameter $\chi$ was estimated by fitting the experimentally determined eigenfrequency and the corresponding microbubble diameter to the shell-buckling model introduced by Marmottant et al. [19], as demonstrated in van der Meer et al. [20]:

$$f_0 = \frac{1}{2\pi}\sqrt{\frac{1}{\rho R^2}\left(3\gamma P_0 + \frac{2(3\gamma - 1)\sigma_w}{R} + \frac{4\chi}{R}\right)} \tag{5.3}$$

The values used were the polytropic gas exponent $\gamma = 1.07$ for $C_4F_{10}$ defined as the ratio of specific heats [6], the ambient pressure $P_0 = 1{\cdot}10^5$ Pa, the surface tension $\sigma_w = 0.072$ N/m, and the elasticity parameter $\chi$ [20, 180], while the other parameters were defined as above.

Microbubbles oscillating in an ultrasound field experience different forms of damping which can be described as:

$$\delta_{tot} = \delta_{rad} + \delta_{vis} + \delta_{shell} + \delta_{th} \tag{5.4}$$

The total damping $\delta_{tot}$ contains a contribution of the sound re-radiated by the microbubble $\delta_{rad}$, a viscous contribution $\delta_{vis}$, a shell viscosity contribution $\delta_{shell}$, and a thermal contribution $\delta_{th}$. According to Leighton [44] and Medwin [322] $\delta_{th} \approx \delta_{vis}$ for microbubbles in the size range for medical use. This assumption was incorporated in Eq. (5.4) by multiplying $\delta_{vis}$ by two, resulting in Eq. (5.5):

$$\delta_{tot} = \frac{\omega_o R}{c} + 2 \cdot \frac{4\mu}{R^2 \rho \omega_o} + \frac{4\kappa_s}{R^3 \rho \omega_o} \tag{5.5}$$

The parameters used in Eq. (5.5) are $\delta_{tot}$ obtained from Eq. (5.1), the angular eigenfrequency $\omega_o = 2\pi f_o$, the radius $R$, the speed of sound in water $c = 1.5 \cdot 10^3$ m/s, the viscosity of water $\mu = 1 \cdot 10^{-3}$ Pa·s, the density of water $\rho = 1 \cdot 10^3$ kg/m$^3$, and the shell viscosity $\kappa_s$. The re-radiation damping and viscous damping are microbubble properties—not of the lipids—and therefore do not contribute to the properties of the shell. From the shell damping term the shell viscosity $\kappa_s$ was calculated similarly to the calculation in van der Meer et al. [20].

The validity of the shell properties was verified using the parameters we derived from the experiments at a 20 kPa driving pressure to simulate the D-t curves at a 50 kPa driving pressure using the Marmottant model [19]. The parameters obtained experimentally can then be used in the full nonlinear equations, incorporating different regimes of the surface tension.

All calculations were performed in MATLAB (The MathWorks Inc., Natick, MA, USA).

**Statistical analyses**

The acquired data were not normally distributed as derived from Shapiro-Wilk tests, so we used nonparametric tests. The acoustical stability of each single microbubble expressed as the difference between the initial diameter and the final diameter was compared using Wilcoxon signed-rank tests. For comparing acoustical stability, resonance frequencies, shell elasticity, and shell viscosity between the two microbubble types we used Mann-Whitney U tests. We report the median and interquartile range (IQR) instead of the mean and standard deviation; the median takes the skewness of the distribution into account and is less influenced by extreme values or outliers. Medians and IQR were calculated using Tukey´s Hinges method. All statistical analyses were performed using SPSS (Statistics 20, IBM Corp., Armonk, NY, USA) and a p-value < 0.05 was regarded as significant, unless stated otherwise.

## 5.4. RESULTS

In total, 54 DSPC and 61 DPPC microbubbles with diameters between 2 and 10 µm were analyzed: split into 39 DSPC and 47 DPPC microbubbles at pressures of 10 kPa and 20 kPa, and 15 DSPC and 14 DPPC microbubbles at pressures of 50 and 100 kPa.

### Acoustical stability

The acoustical stability of the microbubbles at all pressures is summarized in Table 5.1. At $P_A$ of 10 and 20 kPa neither type of microbubble was seen to shrink significantly. However, at higher pressures both types shrunk significantly ($p < 0.001$), with a larger median diameter decrease for DPPC-based microbubbles at both pressures ($P_A = 50$ kPa: $p = 0.04$, $P_A = 100$ kPa: $p = 0.009$). Thus, at $P_A \geq 50$ kPa, DPPC microbubbles were acoustically less stable than DSPC-based microbubbles.

**Table 5.1.** Shrinkage of DSPC and DPPC microbubbles at different driving pressures.

| $P_A$ (kPa) | Median relative shrinkage % (IQR) | | Number of microbubbles | |
|---|---|---|---|---|
| | DSPC | DPPC | DSPC | DPPC |
| 10 | 0.10 (0.85) | 0.01 (0.70) | 39 | 47 |
| 20 | 0.15 (1.10) | +0.02 (0.76) | 39 | 47 |
| 50 | 4.1 (3.6)* | 9.7 (8.2)* | 15 | 14 |
| 100 | 11.7 (6.2)* | 23.1 (22.9)* | 15 | 14 |

* statistically significant shrinkage

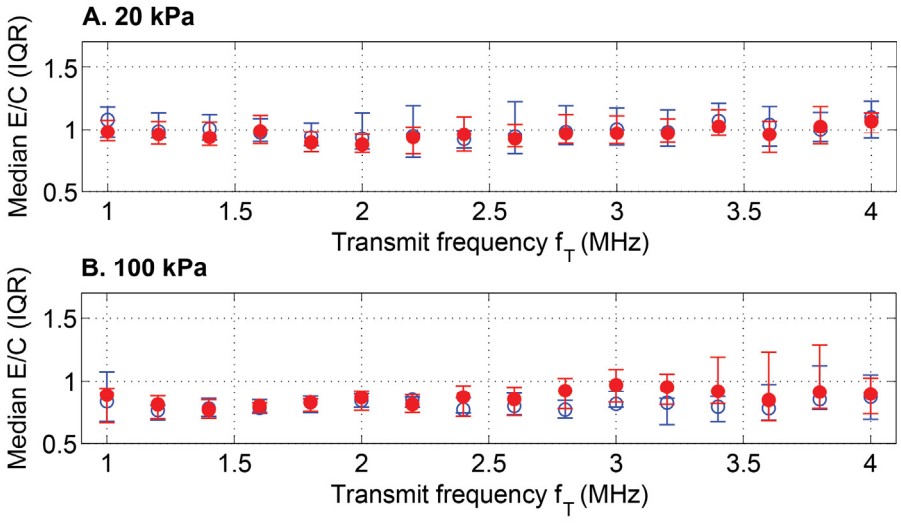


**Fig. 5.2.** Median (IQR) ratio between the relative expansion E and the relative compression C plotted versus the transmit frequency at a pressure of **(A)** 20 kPa of DSPC (n = 39, open blue circles) and DPPC (n = 47, filled red circles) and a pressure of **(B)** 100 kPa of DSPC (n = 15) and DPPC (n = 14).

**Oscillation behavior**

The asymmetry of radial excursion of the microbubbles was evaluated by means of the ratio between the relative expansion *E* and relative compression *C* (*E*/*C*). As shown in Fig. 5.2, at pressures of 10 and 20 kPa *E*/*C* ratios of both microbubble types were near 1: oscillations at these pressures were considered to be symmetric and linear. At driving pressures of 50 and 100 kPa, oscillations of both types showed more compression than expansion, particularly at a frequency $f_T$ < 2.5 MHz, see Fig. 5.2. Based on the definition of de Jong et al. [321] this behavior is not classified as compression-only behavior. We therefore termed the excursion behavior observed at 50 and 100 kPa 'compression-dominated', which was regarded as asymmetric and nonlinear.

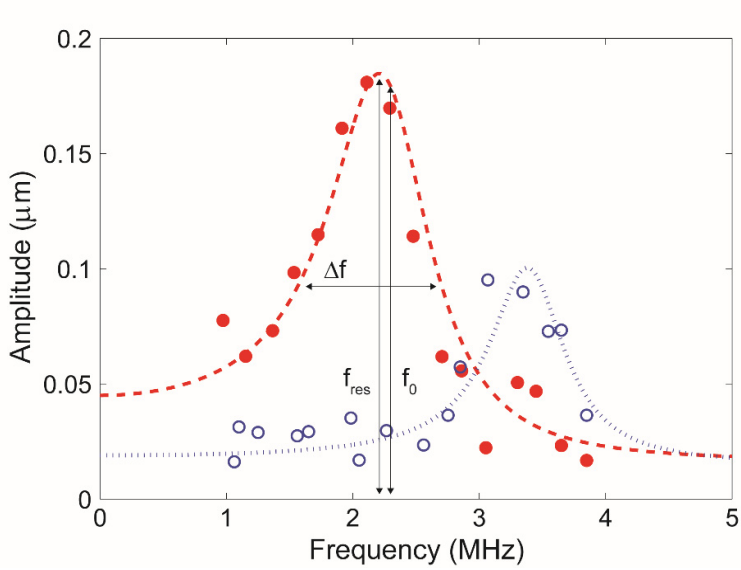


**Fig. 5.3.** The resonance curves of similar sized DSPC (open blue circles) and DPPC microbubbles (filled red circles) at a pressure of 20 kPa. The DSPC-based microbubble had a diameter of 3.4 µm and a resonance frequency of 3.4 MHz, the DPPC-based microbubble had a diameter of 3.3 µm and a resonance frequency of 2.2 MHz. Δf is the full width at half the maximum amplitude, $f_{res}$ the resonance frequency and $f_0$ the eigenfrequency.

The resonance curve was fitted to the measured amplitudes at $f_T$ from 1 to 4 MHz, as shown in Fig. 5.3 for a DSPC and DPPC microbubble of similar size. From the resonance curves the resonance frequency ($f_{res}$) and eigenfrequency ($f_0$) were determined. Microbubbles with their resonance peak below the measurement range ($f_T \leq 1$ MHz, i.e. $D_0 > \sim 6.5$ µm) were excluded from this analysis: their resonance frequency could not be determined and these microbubbles were therefore also not taken into account for the calculation of the shell properties. The resonance frequencies appeared to be slightly lower for

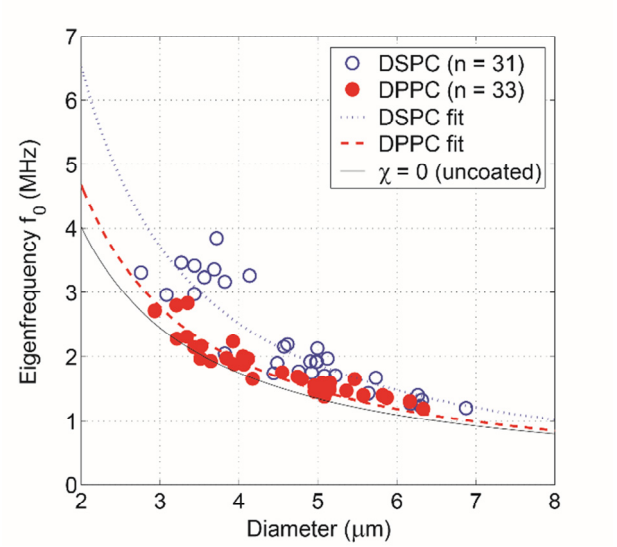


**Fig. 5.4.** Eigenfrequencies at a pressure of 20 kPa plotted versus the diameter of DSPC and DPPC microbubbles. The experimental data was fitted to Eq. (5.3) to obtain the shell elasticity parameter $\chi$.

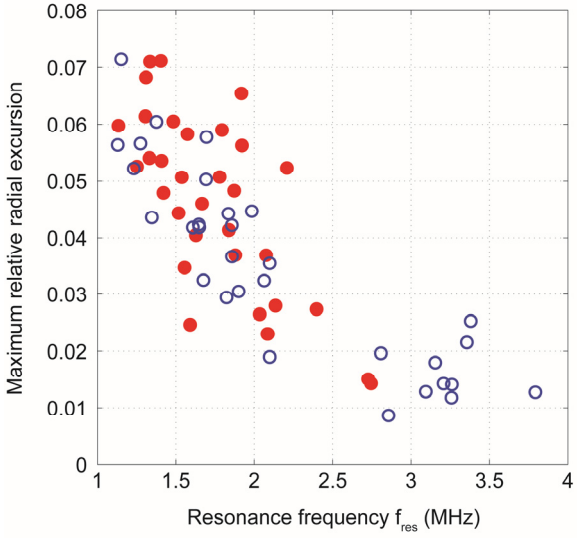


**Fig. 5.5.** Relative radial excursion at the resonance frequency of DSPC (n = 31, open blue circles) and DPPC microbubbles (n = 33, filled red circles) at 20 kPa driving pressure.

DPPC microbubbles than for similarly sized DSPC microbubbles at all applied pressures. The difference between the resonance frequencies of the two microbubble types was most significant at 10 kPa ($p = 0.007$), but at this pressure the signal-to-noise ratio was comparatively low and the oscillations of a few microbubbles were only slightly above the noise level. At a pressure of 20 kPa all bubble oscillations were well above the noise level and the responses did not show nonlinear behavior: this is required for Eq. (5.3) to be valid [19]. The difference between the resonance frequencies of both types of bubbles was only significant at the level of $p < 0.1$ ($p = 0.065$), see Fig. 5.4. The radial excursion at the resonance frequency was determined, resulting in the maximum relative radial excursion. These excursions were similar for DSPC and DPPC-based microbubbles and the maximum relative radial excursion was lower at higher resonance frequencies (i.e. for smaller bubbles), see Fig. 5.5.

Nonlinear oscillations were studied in more detail by the responses at the subharmonic and second harmonic frequency, at pressures of 50 and 100 kPa. At a pressure of 50 kPa 4 out of 15 (27%) DSPC-based and 10 out of 14 (71%) DPPC-based microbubbles responded at the subharmonic frequency. At a higher pressure of 100 kPa these numbers increased to 12 out of 15 (80%) for DSPC and 13 out of 14 (93%) for DPPC microbubbles (Fig. 5.6A). When the microbubbles were insonified at a pressure of 50 kPa both types essentially had subharmonic responses when $f_{sub} = f_0$ (T2R, transmit at twice the resonance frequency [148, 323]) On the other hand, the subharmonic responses at a pressure of 100 kPa were a mix between T2R and TR ($f_{sub} = ½f_0$, transmit at the resonance frequency [148, 180]). This suggests that the threshold for generating TR subharmonic responses is higher than that for T2R subharmonic responses, as expected.

**Table 5.2**. Responses of DSPC and DPPC microbubbles at the subharmonic and second harmonic frequency.

| Type | $P_A$ (kPa) | Subharmonic response | | | Second harmonic response | | |
|---|---|---|---|---|---|---|---|
| | | # MBs | Median diameter (IQR) (μm) | Median pressure (IQR) (Pa) | # MBs | Median diameter (IQR) (μm) | Median pressure (IQR) (Pa) |
| DSPC | 50 | 3 | 5.3 (4.7-5.4) | 0.36 (0.23-0.43) | 6 | 5.4 (4.9-5.6) | 2.86 (2.24-0.35) |
| | 100 | 7 | 4.5 (4.4-5.3) | 0.44 (0.38-0.88) | 15 | 4.7 (3.8-5.3) | 12.54 (3.03-13.51) |
| DPPC | 50 | 8 | 6.1 (4.9-7.6) | 0.61 (0.56-0.87) | 7 | 4.5 (4.3-5.0) | 3.26 (1.82-4.12) |
| | 100 | 9 | 4.4 (3.6-7.1) | 0.75 (0.28-1.30) | 10 | 4.0 (3.4-4.5) | 6.00 (2.73-7.31) |

The acoustic pressures of the nonlinear oscillations were calculated using Eq. (5.2). To translate these pressures to relevant parameters for *in vivo* imaging a distance of $d = 2$ cm was chosen as a representative depth for carotid imaging and tissue attenuation of 0.5 dB/cm/MHz [324] was accounted for. We assumed a detection limit (i.e. noise level) of 1 Pa for diagnostic US scanners, achievable with a typical high-quality transducer for harmo-

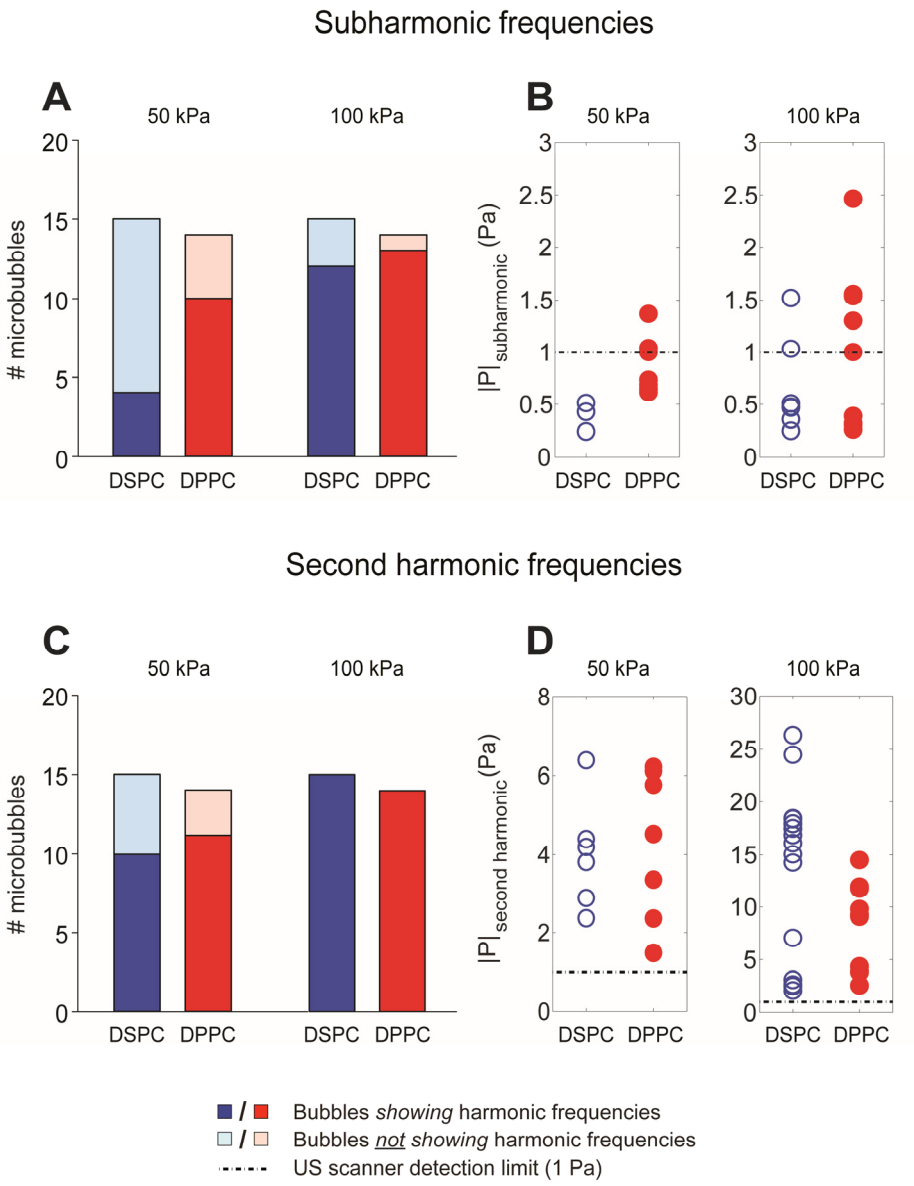


**Fig. 5.6.** Responses at the subharmonic and second harmonic frequency. **(A)** Number of microbubbles responding at the subharmonic frequency at 50 kPa (DSPC 27%; DPPC 71%) and 100 kPa (DSPC 80%; DPPC 93%). At 50 kPa both microbubble types had T2R subharmonic responses and at 100 kPa this was both TR and T2R. **(B)** Theoretical pressures scattered by the oscillations at the subharmonic frequency at 50 kPa and 100 kPa. **(C)** Number of microbubbles responding at the second harmonic frequency at 50 kPa (DSPC 67%; DPPC 79%) and 100 kPa (both 100%). **(D)** Scattered pressures at the second harmonic frequency at 50 kPa and 100 kPa. The calculated pressures take the attenuation of 2 cm of soft tissue into account.

nic imaging [325]. For the subharmonic responses this resulted in pressures below or very close to this detection limit, with lower values for DSPC-based microbubbles at both driving pressures (Table 5.2, Fig. 5.6B). Note that some microbubbles from Table 5.2 are not displayed in Fig. 5.6; these microbubbles had a response at the subharmonic frequency, but their resonance curves could not be derived due to low signal-to-noise ratios and thus their scattered pressure could not be calculated.

The number of microbubbles responding at the second harmonic frequency was similar for both types: at a pressure of 50 kPa 10 out of 15 (67%) DSPC-based and 11 out of 14 (79%) DPPC-based microbubbles showed second harmonic responses and at a pressure of 100 kPa all 29 microbubbles of both types did show harmonic response (Fig. 5.6C). Scattered pressures at the second harmonic frequency were well above the detection limit (Table 5.2, Fig. 5.6D): at $P_A$ = 50 kPa the median scattered pressures were similar for both groups, and at a pressure of 100 kPa they were two times higher for DSPC-based microbubbles than for DPPC-based microbubbles.

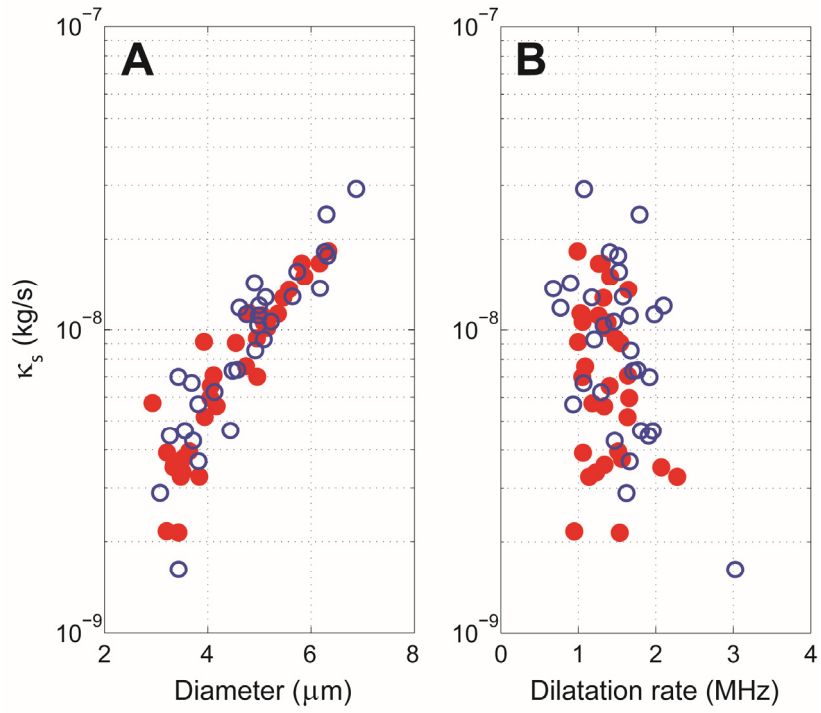


**Fig. 5.7**. Shell viscosities of DSPC (n = 30, open blue circles) and DPPC (n = 33, filled red circles) microbubbles at a pressure of 20 kPa plotted versus **(A)** diameter and **(B)** dilatation rate.

The theoretical scattered subharmonic and second harmonic pressures depend on the microbubble sizes: the scattered pressure scales quadratically with its diameter. Although the differences between the subharmonic pressure responses at a pressure of 50 kPa were small, the larger median diameter of the DPPC microbubbles may have resulted in an overestimation of the pressures. However, not enough DSPC microbubbles responded at this pressure to test whether the diameters of both microbubble types were significantly different. The number of DSPC microbubbles responding at the second harmonic frequency at a pressure of 50 kPa was also too low to test whether the diameters of both microbubble types were significantly different. At a pressure of 100 kPa the diameters of the microbubbles responding at the second harmonic frequency were not significantly different ($p = 0.346$).

**Shell properties**

To determine the shell properties using Eq. (5.3), nonlinear behavior must be kept to a minimum. Therefore the measurements performed at a pressure of 20 kPa (Fig. 5.4) were fitted to Eq. (5.3). This resulted in shell elasticity parameters of $\chi_{DSPC}$ = 0.26 ± 0.13 N/m and $\chi_{DPPC}$ = 0.06 ± 0.06 N/m. The elasticity parameter estimated for DPPC was an order of magnitude lower than that for DSPC ($p < 0.001$), and approaches that of an uncoated bubble ($\chi = 0$); the consequence of the higher elasticity for DSPC is a stiffer lipid shell.

The shell damping term was calculated using Eq. (5.5), with the total damping $\delta_{tot} = \Delta f / f_o$ [20] from the experimental resonance curves (Fig. 5.3) at a driving pressure of 20 kPa. Median (IQR) shell damping coefficients of both microbubble types were similar; 0.22 (0.10) for DSPC and 0.25 (0.07) for DPPC. From the individual shell damping coefficients we derived the shell dilatational viscosities using Eq. (5.5). The median (IQR) shell viscosities were similar for both types: $\kappa_{DSPC}$ = 1.0 (0.7) × $10^{-8}$ kg/s and $\kappa_{DPPC}$ = 0.7 (0.7) × $10^{-8}$ kg/s ($p = 0.148$). The shell viscosity increased with increasing diameter for both microbubble types (Fig. 5.7), but no significant relation was found between shell viscosity and dilatation rate, as estimated from Eq. (5.6), given the very small variation of the dilatation rate in our experiments.

$$\dot{D} / D \approx \omega_o \Delta D / D_o = 2\pi f_o (D_{max} - D_{min}) / D_o \tag{5.6}$$

The shell properties derived from the measurements at a pressure of 20 kPa were used to simulate the response of the microbubble at a pressure of 50 kPa that responded at both the subharmonic frequency and the second harmonic frequency. We assumed an initial surface tension ($\sigma(R_o)$) of $0.5\sigma_w$, which is exactly in the middle of the elastic regime. Fig. 5.8a shows good agreement between the experimentally obtained bubble oscillations (dots) of a 5.5 μm DSPC microbubble close to resonance, and the simulated response using $f_T$ = 1.35 MHz, $\chi$ = 0.26 N/m, and $\kappa_s$ = 1.88 × $10^{-8}$ kg/s (dashed line). In the compression phase, however, the simulated response is slightly underestimated. Fig. 5.8b shows a similar level

of agreement of a 5.1 μm DPPC microbubble at resonance and the corresponding simulation using $f_T$ = 1.53 MHz, $\chi$ = 0.06 N/m, and $\kappa_s$ = 1.32 × $10^{-8}$ kg/s.

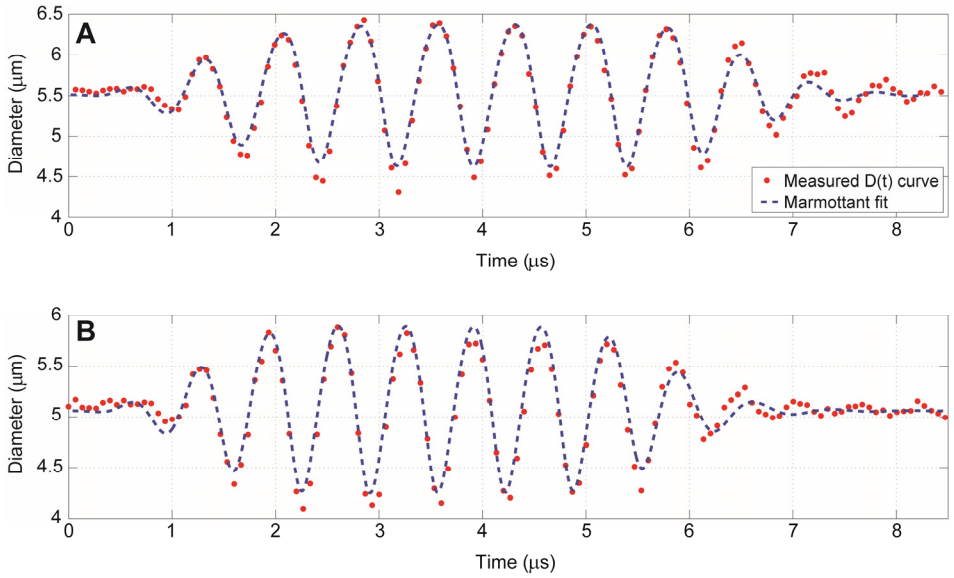


**Fig. 5.8.** Agreement between experimental results (dots) and simulated responses (dashed line) at 50 kPa driving pressure of **(A)** a DSPC microbubble (diameter = 5.5 μm, $f_T$ = 1.35 MHz, $\chi$ = 0.26 N/m and $\kappa_s$ = 1.88 · $10^{-8}$ kg/s) **(B)** and a DPPC microbubble (diameter = 5.1 μm, $f_T$ = 1.53 MHz, $\chi$ = 0.06 N/m and $\kappa_s$ = 1.32 · $10^{-8}$ kg/s).

## 5.5. Discussion

We compared the responses to ultrasound of two types of microbubbles with either DSPC or DPPC lipid as the main coating component. We found higher stability, higher responses at the second harmonic frequency, and a higher shell elasticity for DSPC than for DPPC-based microbubbles. On the other hand, less DSPC microbubbles responded at the subharmonic frequency and the magnitude of their response was slightly lower than those of the DPPC-based microbubbles. The shell viscosities were similar for both types of bubbles.

### Stability

The lower acoustical stability of DPPC-based microbubbles can be explained by the shorter acyl chain length of DPPC, which lowers the attractive intermolecular van der Waals forces between the lipids in the shell, and thus decreases the overall cohesiveness of the monolayer [49].

The miscibility of lipids in the coating is influenced by the phase-behavior of the lipids in the coating and might therefore also play a role in the acoustical stability differences we measured. At room temperature DSPC lipid is in the condensed phase [280], PEG-40 stearate is in the expanded phase [48], and DSPE-PEG(2000) can be in either of these phases [280]. As also discussed by Kooiman et al. [70] DSPC is immiscible with the components in the expanded phase; ordered and condensed DSPC domains are formed [281]. These domains are more tightly packed and may prevent gas escape and thus increase the acoustical stability. DPPC lipid on the other hand (at room temperature), may be in the phase transition area between the condensed phase [280], and the less ordered and less densely packed expanded phase [281]. This can decrease the acoustical stability of DPPC microbubbles.

Small changes in the size (< 10%) before and after insonification at $P_A$ of 10 and 20 kPa were measured for both microbubble types. Based on the estimates by van der Meer et al. [20] that suggest that the contour tracking algorithm has an error of 10%, we can conclude that both microbubble types are stable at these low pressures. When the microbubbles were insonified at higher pressures of 50 and 100 kPa the size-changes were larger than 10% and microbubbles of both types were acoustically unstable.

As pointed out in the Introduction, lipids with chains up to 24 C-atoms have also been used to produce microbubbles [50]. In the absence of ultrasound the formulation of microbubbles containing DBPC (C22-lipid) was found to have lower dissolution rates than those based on DSPC and DPPC. However, in the presence of ultrasound the *in vitro* acoustical stability of DSPC and DBPC-based microbubbles was similar, and both were more stable than DPPC. The *in vivo* contrast persistence of DBPC-based microbubbles was found to be ~20× higher than that of DPPC-based microbubbles and ~5× higher than that of DSPC-based microbubbles. Based on these results future studies should focus on investigating lipids with longer carbon chains such as DBPC and focus on nonlinear behavior rather than acoustical stability or *in vivo* half-life.

**Oscillation behavior**

The resonance frequencies of the DSPC microbubbles were higher than those of the DPPC microbubbles. This may be due to the lower compressibility modulus of DPPC lipid than that of DSPC lipid [278, 279], which results in a higher deformability of the DPPC-based bubbles as shown by [70]. The compressibility modulus ($C_s^{-1}$) that is used in surface rheology is identical to the elastic compressibility modulus ($\chi$) that is used in the Marmottant model [19]. Since a lower elasticity is related to lower resonance frequencies (Fig. 5.4), the lower compressibility modulus of DPPC lipid is thus the likely cause for the measured down-shift in resonance frequency.

For the sake of comparison with other DSPC-based microbubbles we consider a typical 4 μm SonoVue ($f_{res}$ = 2.9 MHz) [127] and a 4 μm BR14 ($f_{res}$ = 3.2 MHz) [20] microbubble: their

resonance frequencies were slightly higher than those of our DSPC microbubbles ($f_{res}$ = 2.7 MHz). Our single DPPC microbubbles, on the other hand, had much lower resonance frequencies than Definity: the resonance frequencies of bulk measurements were in the range of 10 to 18 MHz [126, 276, 326]. Since Definity microbubbles are smaller than our DPPC microbubbles (Definity: 1.1 – 3.3 μm [9], DPPC: 3.9 μm), their resonance frequency is higher. Extrapolating the fit through the eigenfrequencies in Fig. 5.4 predicted a frequency of 12 MHz for DPPC microbubbles of 1 μm, which indeed is of the same order of magnitude as found for Definity. The single microbubble measurements of the DPPC-based microbubbles by Luan et al. [18] are easier to compare with our microbubbles: the higher frequencies they found ($f_{res}$ = 2.7 MHz versus $f_{res}$ = 2.0 MHz) are likely due to the difference in coating composition (65 mol% DPPC, 35 mol% DSPE-PEG(2000)) and the preparation method (dissolved in chloroform and high-speed shaking using the Vialmix).

The maximum relative radial excursion at the resonance frequency decreased with increasing frequency and thus with decreasing size. At resonance, Eq. (5.1) reduces to $Re = Re_o / \delta_{tot}{}^2$, and as described in the Materials and Methods section $Re_o = (P_A / 2\pi\omega_o\rho R_o^2)^2$ and $Re = |x|^2$, hence, the amplitude $x$ scales with $1/\delta_{tot}$. Since $\delta_{tot}$ decreases with increasing microbubble diameter [44, 146] and thus with decreasing resonance frequency, the lower amplitude at higher resonance frequencies, as shown in Fig. 5.5, is explained by the higher damping coefficient. Indeed, van der Meer et al. [20] reported resonance curves of bubbles with lower amplitudes ($Re/Re_o$) for increasing resonance frequencies, which is in line with our observations and the increased damping.

For successful *in vivo* CEUS and molecular imaging, discriminating the microbubble signal from tissue signal is a key factor [158]. This discrimination can be accomplished by nonlinear contrast imaging, for example by detecting the responses of the microbubbles at the subharmonic or second harmonic frequencies. The second harmonic response is higher in frequency than the subharmonic response and the second harmonic response is therefore attenuated to a higher degree [324]. In addition, tissue signals can also contain second harmonic frequencies due to nonlinear propagation [327, 328], which makes discrimination based on second harmonics less specific. Thus the subharmonic response is of great interest for microbubble imaging [181]. For the generation of oscillations at the subharmonic frequency a rapid change in elasticity is required, which is highest near its buckled state [180, 323]. From theory, similar correspondence was found between the occurrence of compression-only behavior and [329, 330]. Faez et al. [180] confirmed that compression-only behavior generates responses at the subharmonic frequency. But although compression-only behavior, buckling, and a response at the subharmonic frequency are related, we did not observe a direct correspondence between the compression-dominated behavior (E/C ratio) and the response at the subharmonic frequency. In addition, microbubbles with an initial surface tension close to that of the buckled regime have a higher subharmonic response than those with a surface tension in the elastic regime [323]. Since the DPPC-based mi-

crobubbles shrank more due to gas diffusion, this might yield a higher local concentration of lipids in the shell. This over-concentration of lipids can induce buckling, which may have generated the response at the subharmonic frequency we observed in this study.

Helfield et al. [259] previously investigated the subharmonic response of individual DSPC-based microbubbles (DSPC:PEG-40 stearate (9:1)) with different microstructures due to variable cooling rates during the preparation process. They reported a variability in the subharmonic response based on the number and size of lipid islands, but no clear dependence between the shell microstructure and subharmonic response could be deduced ($P_A$ = 0.02-1.2 MPa at 25 MHz). Their most homogeneous composition resulted in the highest rate of subharmonic responses. This may suggest that the few DSPC-based bubbles in our investigated population that were responsive at the subharmonic frequency at a driving pressure of 50 kPa (Fig. 5.6A) were actually the most homogeneous DSPC-based bubbles. The heterogeneity of individual DSPC-based microbubbles indeed varies, as shown previously by Kooiman et al. [70]. Whereas Helfield et al. [259] found only a minor effect of the subharmonic threshold based on heterogeneity within their DSPC microbubbles, we saw a clear difference at 50 kPa between DPPC and DSPC microbubbles, but a similar level of response at 100 kPa. This suggests that the threshold for the generation of subharmonics is lower in our DPPC-based microbubbles than in our DSPC-based microbubbles.

While differences in the radial excursion between DSPC and DPPC microbubbles could introduce a bias in the scattered pressures we calculated, the higher subharmonic pressures of the DPPC microbubbles and the higher second harmonic pressures of the DSPC microbubbles were not caused by a difference in maximum relative radial excursions, as shown in Fig. 5.5. Since neither the diameter distributions, nor the relative radial excursions were different, the calculated pressures were assumed to be valid.

**Shell properties**

The elasticity of our DPPC microbubbles was lower than that of our DSPC microbubbles, and close to that of a free bubble: the influence of the shell on the elasticity is thus minimal for the DPPC microbubbles. One explanation for the lower shell elasticity of the DPPC bubbles is the shorter DPPC acyl chain: this results in a thinner shell, lower van der Waals forces [135], and thus a less stiff shell. In addition to this, fluorescence microscopy [70] revealed a larger binding area and domed shape of bound targeted DPPC microbubbles: this is consistent with a less stiff coating and in line with a lower elastic compressibility modulus of DPPC lipid [278, 279]. One of the underlying reasons can be phase-behavior of the different components that influences their miscibility within the coating. As discussed before DPPC may be in the phase transition area between the condensed phase and the less ordered and less densely packed expanded phase. Therefore DPPC lipid may change from the condensed phase to the expanded phase especially upon expansion of the microbubble, decreasing the stiffness of the shell and lowering the elasticity. DSPC on the other hand is immiscible with

PEG-40 stearate and DSPE-PEG(2000) in the expanded phase, therefore ordered and less compressible condensed DSPC domains are formed [281]. These domains increase locally the stiffness and thus the elasticity of the lipid shell and may explain why we found a higher elasticity for our DSPC microbubbles.

The elasticity parameters we found for both our DPPC (0.06 ± 0.06 N/m at $P_A$ = 20 kPa) and DSPC-based (0.26 ± 0.13 N/m at $P_A$ = 20 kPa) microbubbles appeared to be lower than those reported in many other studies. However, the elasticity highly depends on the used driving pressure and decreases with increasing pressure [317, 330]. When comparing the elasticities of DPPC-based microbubbles such as Definity (0.7-0.9 N/m, $P_A$ between 6 and 31 kPa) [128, 326] and those used in the study by Luan et al. [18] (0.19 ± 0.07 N/m, $P_A$ = 50 kPa), the latter is already ~4× lower. Next to the dependence on the pressure, the elasticity is likely influenced by the differences in microbubble composition. Where we used a three-component composition, Luan et al. [18] used a two-component composition, whereas Definity consists of only lipids (DPPA and DPPC) and a lipopolymer (DPPE-MPEG(5000)) [9]. As shown in multiple studies, differences in composition alter the microbubble properties [50, 70, 259, 285, 286, 315, 317]. The elasticity of DSPC-based bubbles is generally higher than that reported for DPPC-based microbubbles. Values determined for SonoVue (0.55 N/m at $P_A$ < 10 kPa; 0.22 N/m at $P_A$ = 150 kPa) [127, 331], BR14 (0.54 ± 0.10 N/m at $P_A$ < 40 kPa ) [20], and DSPC:DSPE-PEG(2000) microbubbles (0.50 N/m at $P_A$ = 25 kPa) [317] were similar and ~2× higher than we determined in our study for DSPC-based microbubbles. The contrast agents SonoVue and BR14 are both produced by Bracco and consist of lipids (DSPC, DPPG) and an emulsifier (PEG(4000)) [7, 318, 319], whereas our bubbles also have a lipopolymer incorporated in their shell (DSPE-PEG(2000)). Since we already see a large difference in elasticity when only the main lipid is replaced, the influence of two other components can thus have an even larger effect. The microbubbles used by Gong et al. [317] consist of two of the components that are incorporated in the coating of our DSPC-based microbubbles, but in different ratios (9:1) and without the presence of PEG-40 stearate. As discussed before, DSPC is immiscible with PEG-40 stearate and the microstructure will be different from that of our bubbles, thus influencing the acoustical response.

The estimated shell viscosities of the DSPC-based microbubbles (1.0 (0.7) × $10^{-8}$ kg/s) were similar to those of SonoVue (0.5 × $10^{-8}$ kg/s; 2.5 × $10^{-9}$ kg/s) [127, 331] and BR14 microbubbles ($10^{-8}$ kg/s) [20]. The viscosities of the DPPC-based microbubbles were also similar ($10^{-8}$ – $10^{-9}$ kg/s) to those of Definity [128, 326] and the DPPC microbubbles of Luan et al. [18]. Shear-thinning—a decrease in shell viscosity with increasing dilatation rate—could not be observed in our DSPC microbubbles, or in our DPPC microbubbles, due to the limited range of dilatation rates applied.

The simulations using the Marmottant model [19] as shown in Fig. 5.8 have been performed assuming an initial surface tension half of that of the gas/liquid interface ($\sigma(R_0) = 0.5\sigma_w$); this is in the middle of the elastic regime. Several other values for the initial surface

tension have also been used to simulate the experimental response ($0.01\sigma_w < \sigma(R_0) < \sigma_w$), which influenced the relative compression and expansion. Using values for the surface tension higher than $0.5\sigma_w$ resulted in a better fit in the expansion phase, but a less good fit in the compression phase. As expected, for a surface tension lower than $0.5\sigma_w$ this was exactly the other way around. However, none of the values for the surface tension were able to capture the bubble oscillations properly in both the expansion and compression phase; the peak-to-peak value did not significantly change. Next to varying the initial surface tension, the shell elasticity was also varied. Although the elasticity we estimated from our experiments was lower than that reported in literature, modeling the response using higher values for the elasticity, such as those reported for SonoVue and BR14 (0.5 N/m), did not result in a better fit to the experimentally measured results.

**Limitations of this study**

For valid use of the Marmottant model we assumed that the microbubble remained spherical when it oscillated [19]. However, Vos et al. [332] showed that microbubbles near a wall can oscillate nonspherically, through jetting and the presence of surface modes [333]; a few microbubbles indeed had surface modes at one or two transmit frequencies. Although some surface modes were present, as shown in Fig. 5.8 the agreement between the model and the experimental data is quite good.

The proximity of a wall also influences the acoustical responses of the microbubbles [124, 136, 334]. The consensus of these papers is a decrease in radial excursions when the microbubbles are brought closer to a wall. The main focus in our present paper is the comparison of DPPC-based microbubbles with DSPC-based microbubbles and the boundary proximity was similar for both types of bubbles, but should be kept in mind when comparing our results to those of others.

**DPPC vs DSPC: implications for CEUS and molecular imaging**

Next to the characterization of the microbubbles, we aimed at identifying whether DSPC or DPPC-based microbubbles would be more suitable for CEUS and ultrasound molecular imaging. For both applications the microbubbles need to circulate in the bloodstream long enough for imaging [335, 336]. This was quantified in our study as the acoustical stability, which was found to be equal for DSPC and DPPC-based microbubbles at low pressures (< 20 kPa). With increasing pressures (50 - 100 kPa), the higher acoustical stability of DSPC favored the DSPC-based microbubbles, as confirmed by others [50, 285]. Another requirement is that the microbubbles need to be distinguishable from tissue on the basis of their nonlinear oscillations [29, 209]. More specifically, the amplitudes of these oscillations must be high enough for detection by the ultrasound scanners used in clinical practice. Although more DPPC microbubbles were responsive at the subharmonic frequency at a driving pressure of 50 kPa, this advantage of DPPC microbubbles disappeared at a driving pressure of

100 kPa. In addition, the scattered pressures at the second harmonic frequency were much higher than those as the subharmonic frequency: up to ~30× higher for DSPC and ~8× for DPPC-based microbubbles at a driving pressure of 100 kPa. Since the scattered pressure at the second harmonic pressure for DSPC-based microbubbles is almost four times higher than that of DPPC-based microbubbles, this clearly favors DSPC to be used as coating material.

The requirements listed above make DSPC-based microbubbles the better choice for CEUS, even though subharmonic imaging might be preferred above second harmonic imaging due to its higher specificity for contrast [181]. Since the scattered pressures at the second harmonic frequency, measured at 2 cm away from the microbubbles, were above the detection limit (Fig. 5.6), e.g. *in vivo* carotid imaging could be performed successfully.

For ultrasound molecular imaging on the other hand, care should be taken of properties related to targeting of the microbubbles, such as ligand distribution, binding area, and binding force. Kooiman et al. [70] determined the ligand distribution and binding area by using super-resolution fluorescence microscopy, and they favored DPPC over DSPC as the main lipid for ultrasound molecular imaging, on the basis of its more homogeneous ligand distribution, larger binding area, and dome-shape upon binding. A more homogeneous distribution of the ligands may result in a higher possibility of contact between a ligand attached to the shell and its molecular target. The larger binding area also resulted in a different shape of the bound microbubbles, which may be advantageous in terms of sustaining a higher blood shear stress.

## 5.6. CONCLUSION

This study showed that the acoustical stability, the responses at the second harmonic frequency, and the shell elasticity are higher for DSPC than for DPPC-based microbubbles. The higher acoustical stability and the higher responses at the second harmonic frequency suggest that microbubble formulations based on DSPC are more suitable for clinical CEUS imaging than those based on DPPC.

**Acknowledgements**

The authors thank Robert Beurskens, Frits Mastik, Michiel Manten, and Geert Springeling for technical assistance, and Tom Kokhuis and Rik Vos for fruitful discussions (all from the Department of Biomedical Engineering, Erasmus MC). Special thanks to prof. Alfred Blume (Department of Biophysical Chemistry, Martin Luther University Halle-Wittenberg, Germany) for fruitful discussions on lipid behavior. This work is supported by NanoNextNL, a micro and nanotechnology consortium of the Government of the Netherlands and 130 partners and by the Center for Translational Molecular Medicine (CTMM) and the Netherlands Heart Foundation (PARISk).

Chapter 6

# Impulse response method for characterization of echogenic liposomes

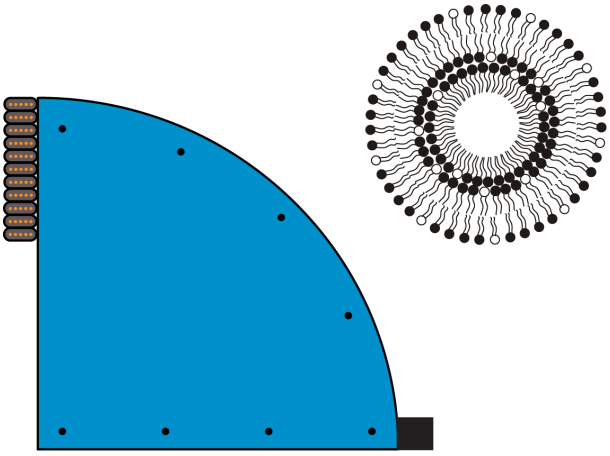

Jason L. Raymond, Ying Luan, Tom van Rooij, Klazina Kooiman, Shao-Ling Huang, David D. McPherson, Michel Versluis, Nico de Jong, Christy K. Holland

*Journal of the Acoustical Society of America*, 137:4, 1693–1703 (2015)

## 6.1. ABSTRACT

An optical characterization method is presented based on the use of the impulse response to characterize the damping imparted by the shell of an air-filled ultrasound contrast agent (UCA). The interfacial shell viscosity was estimated based on the unforced decaying response of individual echogenic liposomes (ELIP) exposed to a broadband acoustic impulse excitation. Radius versus time response was measured optically based on recordings acquired using an ultra-high-speed camera. The method provided an efficient approach that enabled statistical measurements on 106 individual ELIP. A decrease in shell viscosity, from $2.1\times10^{-8}$ kg/s to $2.5\times10^{-9}$ kg/s, was observed with increasing dilatation rate, from $0.5\times10^{6}$ $s^{-1}$ to $1\times10^{7}$ $s^{-1}$. This nonlinear behavior has been reported in other studies of lipid-shelled UCAs and is consistent with rheological shear-thinning. The measured shell viscosity for the ELIP formulation used in this study, $\kappa_s = (2.1 \pm 1.0)\times10^{-8}$ kg/s, was in quantitative agreement with previously reported values on a population of ELIP and is consistent with other lipid-shelled UCAs. The acoustic response of ELIP therefore is similar to other lipid-shelled UCAs, despite loading with air instead of perfluorocarbon gas. The methods described here can provide an accurate estimate of the shell viscosity and damping for individual UCA microbubbles.

## 6.2. INTRODUCTION

Physical models for encapsulated ultrasound contrast agent (UCA) microbubbles have been developed and improved over the past two decades. The models give accurate predictions of the nonlinear radial dynamics of individual UCA microbubbles, particularly under forced, or acoustically driven, conditions [5]. Such models are largely based on Rayleigh-Plesset-type equations, which describe the dynamics of a gas bubble in response to pressure variations. The effects of the shell encapsulation on the microbubble motion are incorporated by adding additional terms that describe the viscoelastic behavior of the shell [337]. The presence of the shell increases the resonance frequency from that of a free bubble and damps the oscillations in response to the acoustic forcing [146]. The shell also affects the nonlinear response of microbubbles, a key property of UCAs which is often exploited in diagnostic imaging modes for enhanced discrimination between the contrast agent and surrounding tissue [338].

In addition to traditional diagnostic ultrasound imaging, there has been recent interest in advancing the applications of microbubbles for molecular imaging and therapeutic applications. These applications exploit the nonlinear response for selective detection of microbubbles in a given volume for diagnosis and specific targeting of disease. Molecular imaging techniques with targeted UCAs are being used increasingly for noninvasive diagnosis of inflammation, thrombus, and neovascularization [94]. Targeted microbubble agents are also being developed for controlled drug-delivery applications [339]. Clinical application of these UCAs necessitates accurate prediction of the frequency-dependent response of

single isolated microbubbles. A better understanding of the shell properties that can be expected for individual UCA microbubbles within a population is also critical. The acoustic response of microbubbles can depend on the morphology and viscoelastic properties of the encapsulating shell [315], particularly if lipids are not homogeneously distributed throughout the shell [340]. Therefore, single microbubble characterization techniques and physical models that accurately describe the dynamics of an encapsulated microbubble are increasingly important.

The introduction of optical methods to resolve microbubble oscillations has provided new insights into the dynamic response of single microbubbles. Optical methods based on direct measurement of the bubble radius versus time can be used due to availability of ultra-high-speed imaging systems [56, 125] such as the Brandaris 128 fast-framing (0.5–25 Mfps) camera [52]. This system enables optical characterization studies by imaging single microbubble dynamical phenomena occurring at multiple time-scales [320]. Acoustic measurements of the scattered echo from an isolated microbubble have been simultaneously recorded and compared to the optically measured radial dynamics to verify the effectiveness of this approach [341].

Optical studies of the radial dynamics of UCAs typically rely on measuring the steady-state forced response of a microbubble to a narrow-band burst excitation. For example, the amplitude response of a microbubble exposed to multiple-cycle, low amplitude ultrasound bursts at various frequencies can be analyzed to build up a resonance curve and fit to a linearized model to derive the viscoelastic shell parameters [20]. This microbubble spectroscopy technique [18, 20, 330, 342] requires multiple recordings to characterize the frequency-dependent response of an individual microbubble. In addition, the shell morphology can be altered or destroyed due to multiple burst excitations [343]. A method using a single excitation would improve the efficiency of UCA characterization techniques and would minimize the effect of alterations to the microbubble shell under successive excitations.

In this study, we investigated the use of the impulse response to characterize the damping imparted by the encapsulation of microbubbles stabilized by a lipid shell, echogenic liposomes (ELIP) [344]. The shell viscosity is the dominant mechanism affecting the damping of microbubble response to acoustic excitation and most directly influences the onset of nonlinear oscillations. An understanding of this physical property of the shell encapsulation can be exploited for optimization of contrast-enhanced imaging and therapeutic applications. Through this technique, we aim to acquire a better understanding of the transient dynamics of ELIP in response to short-pulse excitations for both diagnostic and therapeutic applications. This method is also of particular interest to improve the efficiency of UCA characterization techniques in general as it requires only a single acoustic excitation when the impulse response is recorded using an ultra-high-speed camera.

ELIP are under development as theranostic ultrasound contrast agents and differ from other commercially available ultrasound contrast agents primarily in shell material and gas

content [338]. ELIP formulations include a small amount of cholesterol to increase membrane rigidity, and are echogenic due to the presence of air, which is entrapped and stabilized by the lipid during the rehydration process [344]. The exact location of the entrapped air pockets, morphology of the encapsulation, and amount of air in each carrier has not been fully ascertained [326, 344, 345]. The objective of the present study was to measure the damping due to the encapsulation and to estimate the shell viscosity based on the unforced response of individual ELIP exposed to a broadband acoustic impulse excitation.

An ultra-high-speed camera was used to capture the radius versus time response. During each recording, an isolated ELIP was excited using two ultrasound pulses with a phase difference of 180°. Following each pulse, the bubble oscillated at its natural frequency with diminishing amplitude determined by the damping, and eventually returned to its resting radius. A generic model was developed to estimate the shell viscosity based on the amplitude decay time constant, which was determined from the experimentally measured radius versus time curve for an individual ELIP. Gas diffusion was neglected in our model, and this approach was verified experimentally by comparing the resting radius before and after the impulse excitation. The shell viscosity of individual ELIP obtained using the optical method presented here is compared to our previously reported value obtained for a population of ELIP using a broadband acoustic attenuation spectroscopy technique [326].

## 6.3. MATERIALS AND METHODS

### Experimental setup

Freeze-dried ELIP dispersions consisting of EggPC/DPPC/DPPE/DPPG/Cholesterol (27:42:8:8:15, mol%) were prepared as previously described [346]. ELIP suspensions were prepared by reconstituting 10 mg/mL lyophilized lipid powder using air-saturated, filtered (Type I) water at room temperature as described by Huang [344]. The suspension was diluted (~100×) into air-saturated phosphate-buffered saline (PBS) mixed with 0.5% (wt./vol.) bovine serum albumin (BSA) solution (Sigma Chemical Co., St. Louis, USA), loaded into an OptiCell® (Nunc/Thermo Scientific, Wiesbaden, Germany), and placed on an optical stage in a 37 °C water bath. A microscope with a 60× water-immersion objective and 2× magnifier was used to image the bubble dynamics at approximately 17 Mfps using the Brandaris 128 fast-framing camera [52, 320]. A diagram of the ultra-high-speed optical imaging setup is presented in Fig. 6.1.

Fig. 6.2A shows an optical image of a dilute suspension of ELIP suspended in an Opti-Cell® using a 40× objective to obtain a larger field of view. A single frame from a Brandaris 128 recording using the 60× objective and 2× magnifier is shown in Fig. 6.2B. Fig. 6.2C and 6.2D show super-resolution fluorescence microscope images of fluorescently-labeled ELIP obtained using the methods outlined by Kooiman et al [70]. Briefly, a 4Pi confocal laser-scanning microscope (Leica TCS 4Pi) with two opposing objective lenses (100×, HCX PL APO, 1.35 NA) was used to generate super-resolution 3-D image stacks. For this supporting study, 2 mol% fluorescently-labeled rhodamine-DPPE was substituted into the ELIP formulation and the reconstituted liposomes were suspended in 87% (vol./vol.) glycerol between quartz cover slips at room temperature. The images show the distribution of the lipid molecules in the shell encapsulation of the ELIP. The size distribution of the microbubbles deduced from optical images presented in Figs. 6.2A and 6.2C is consistent with Coulter Counter measurements of the particle size distribution for this ELIP formulation, which indicated a volume-weighted mean diameter of 2 μm [326]. Previously published transmission electron

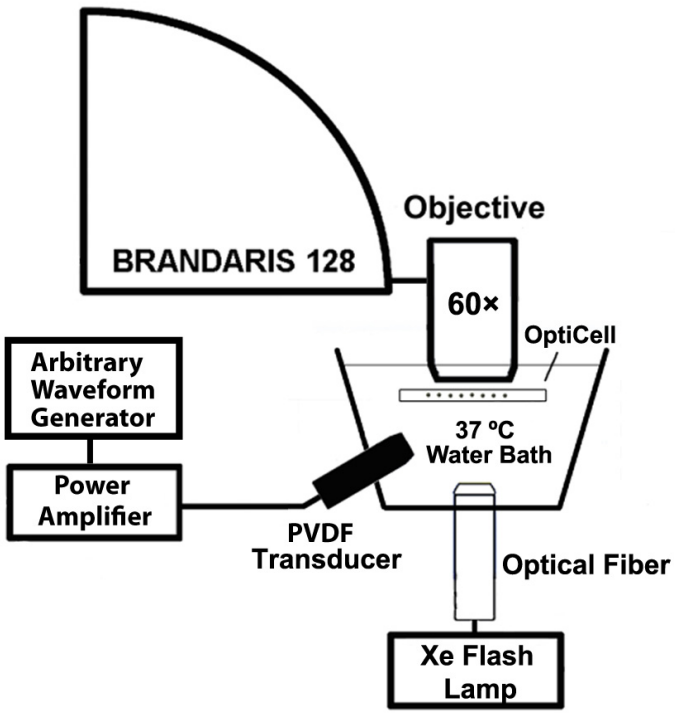


**Fig. 6.1.** Schematic of the setup used to optically record the microbubble oscillation.

microscopy images have shown liposomes on the order of 2 μm diameter [347] as well as vesicles in the nanometer size range that could not be resolved using the optical methods described here [348, 349]. Atomic force microscopy [345] and fluorescence microscopy studies [349] also indicate a broad size distribution, with particle sizes ranging over three orders of magnitude from tens of nanometers to microns.

**Acoustic excitation pulse**

A focused, broadband PVDF transducer (23 mm diameter, 25 mm focal distance, PA275; Precision Acoustics, Dorchester, United Kingdom) was positioned in the water bath at a 45° angle below the sample and the acoustic focus (0.5 mm full-width at half-maximum pressure) aligned with the optical field of view. In order to detect potential nonlinear bubble dynamics, a pulse inversion pair was utilized to excite individual ELIP. For each optical recording, a sequence of two phase-inverted acoustic pulses, temporally separated by 3 μs, was used to excite each ELIP impulsively. The pulses had a phase difference of 180° but were

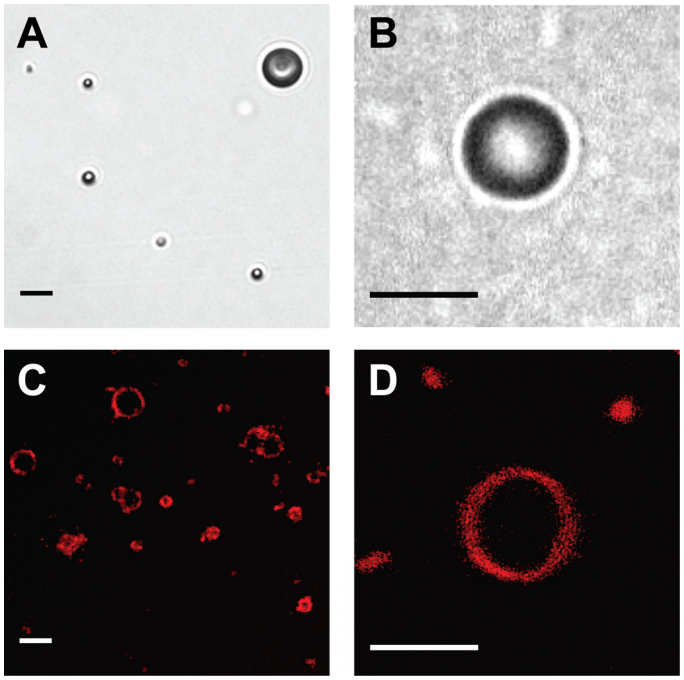


**Fig. 6.2. (A)** Optical image of a dilute suspension of ELIP suspended in an OptiCell (40× magnification) **(B)** Single frame of a Brandaris 128 recording (120× magnification) **(C)** and **(D)** Super-resolution confocal microscope images of fluorescently-labeled (2 mol% rhodamine-DPPE) ELIP in glycerol (Leica TCS 4Pi, 100× magnification). Scale bars represent 5 μm in all images.

otherwise identical with center frequency of 4 MHz and pulse duration of ~0.33 µs (1.5 cycles). Pulse excitations with peak pressure amplitude of 125, 250, or 500 kPa (210, 420, or 840 kPa peak-to-peak acoustic pressure, respectively) were generated by a programmable arbitrary waveform generator (8026, Tabor Electronics Ltd., Tel Hanan, Israel) and amplified using a wideband RF amplifier (0.3–35 MHz, A-500; Electronic Navigation Industries, Rochester, NY, USA). During calibration, a 0.2-µm needle-type hydrophone (Precision Acoustics) was positioned approximately 2 mm from the sample holder membrane (a modified OptiCell with one membrane removed), such that the hydrophone location corresponded to the location of the ELIP during the optical measurement. The transmitted acoustic pressure amplitude *in situ* was attenuated by a factor of 3 dB relative to the free-field pressure due to the presence of the membrane and the 45° angle of incidence of the acoustic wave. The *in situ* pressure waveform and power spectrum for a 250 kPa peak pressure amplitude excitation pulse are shown in Fig. 6.3.

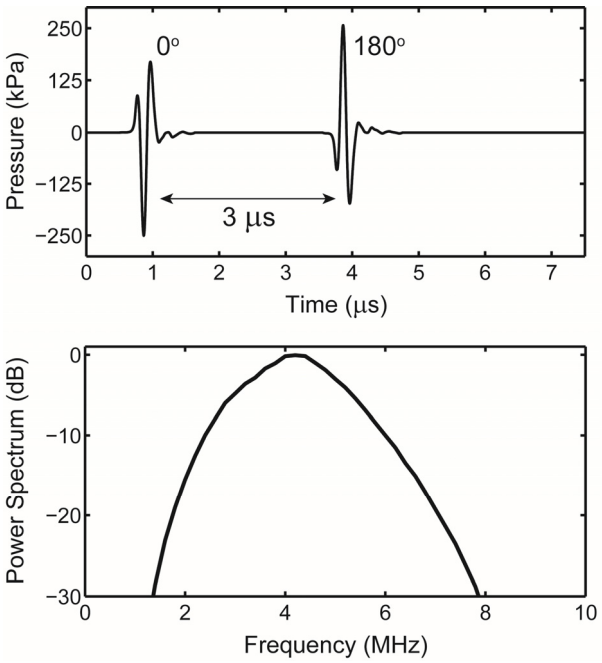


**Fig. 6.3.** Measured pressure waveform (top) and corresponding spectrum (bottom) of the acoustic excitation pulses.

**Estimation of the shell viscosity**

Linearization of a Rayleigh-Plesset-type bubble dynamics equation yields the equation of motion for a damped harmonic oscillator. In the absence of forcing this equation can be written as Eq. (6.1).

$$\ddot{x} + \omega_0 \delta \dot{x} + \omega_0^2 x = 0 \tag{6.1}$$

The eigenfrequency, $\omega_o$, is given by the Minnaert relation for a free gas bubble [330], and for an encapsulated bubble this expression can be modified to include an additional term which depends on the elasticity of the shell [258]. The damped natural frequency for unforced oscillations, $\omega_d$, is related to the eigenfrequency of the system by the damping coefficient as shown in Eq. (6.2),

$$\omega_d = \omega_0 \sqrt{(1 - \delta^2 / 4)} \tag{6.2}$$

where $\delta$ represents the total damping of the system [350, 351]. If the system is modeled as a linearized, single degree-of-freedom system which is underdamped ($\delta < 2$), the solution can be written in terms of an oscillatory signal with a decaying exponential envelope characterized by the time constant, $\tau = 2/(\delta\omega_0)$.

Analysis of the experimental data consists of calculating the envelope signal, *A(t)*, from the measured radius versus time curves for each individual pulse excitation using the Hilbert transform. The time constant can be readily determined by fitting a line to the natural logarithm of the envelope signal [352], with a slope given by Eq. (6.3).

$$\frac{d\left(\ln\left|A(t)\right|\right)}{dt} = \frac{\delta\omega_0}{2} = \frac{1}{\tau} \tag{6.3}$$

In general, the total damping consists of contributions from all of the dissipative loss mechanisms, including: acoustic radiation ($\delta_{rad}$), thermal diffusion and conduction ($\delta_{th}$), viscosity of the surrounding liquid ($\delta_{vis}$), and viscosity of the shell ($\delta_{sh}$), such that $\delta = \delta_{rad} + \delta_{th} + \delta_{vis} + \delta_{sh}$ [350]. For an encapsulated bubble the last term represents the damping imparted by the shell [146], and for an unencapsulated bubble $\delta_{sh} = 0$. Assuming a Newtonian rheology, the expression for $\delta_{sh}$ in terms of the total non-dimensional damping coefficient can be written [353] as Eq. (6.4).

$$\delta_{sh} = \delta - \delta_0 = \frac{4\kappa_s}{\rho\omega_0 R_0^3} \tag{6.4}$$

where $\delta_o = \delta_{rad} + \delta_{th} + \delta_{vis}$ represents the total damping coefficient evaluated at resonance for an unencapsulated gas bubble with the same radius and eigenfrequency as the encapsulated bubble. The shell viscosity in dimensional units, $\kappa_s$, can be estimated as a function of the time constants, $\tau$ and $\tau_o$ as described in Eq. (6.5).

$$\kappa_s = \frac{\rho R_0^3}{2}\left(\frac{1}{\tau} - \frac{1}{\tau_0}\right) \tag{6.5}$$

where $\tau$ and $\tau_o$ are the time constants for an encapsulated bubble (measured) and unencapsulated bubble with the same initial radius (calculated), respectively.

The expression given in Eq. (6.3) for the interfacial shell viscosity is consistent with the Rayleigh-Plesset-type model for phospholipid-encapsulated bubbles developed by Marmottant et al. [19]. In this model, the effective surface tension is described by three regimes of shell behavior: buckled, elastic, or ruptured. In the elastic regime, the shell contributes an additional restoring force, characterized by the elasticity $\chi$, which shifts the resonance for small amplitude oscillations of an encapsulated bubble to higher frequencies. Oscillations in the purely elastic regime occur only at exceedingly low vibrational amplitudes (e.g. $R/R_0 < 1.01$ for $\chi = 2.5$ N/m [330]). Above a threshold radius, the shell is in the ruptured regime and the interfacial dynamics are also controlled by the free air-water surface tension. We estimate the rupture radius for ELIP to be $R/R_o = 1.02$ based on the elasticity determined previously ($\chi = 1.55$ N/m [326]). Overvelde et al. [330] demonstrated that for oscillations exceeding this amplitude, the bubble is no longer oscillating in the purely elastic regime and the natural frequency for a encapsulated bubble approaches a value that is only slightly greater (~10%) than would be predicted for an unencapsulated bubble. For simplicity, we consider $\omega_o$ to be the same for both encapsulated and unencapsulated bubbles and use the eigenfrequency of an unencapsulated bubble (e.g. Eq. 5 in [349]) to calculate $\tau_o$ in Eq. (6.5).

Each ELIP was excited by both peak-negative and peak-positive pulses, which were analyzed separately. A subset of ELIP were excited several times using 125, 250, or 500 kPa peak pressure amplitude pulses. An example of the damping analysis for an individual 0° pulse excitation is shown in Fig. 6.4A and 6.4B. The natural frequency of unforced oscillation was estimated from the Fourier spectrum of the radius versus time response, shown in Fig. 6.4C.

**Simulations**

In order to evaluate the validity of the shell viscosity estimates obtained for individual ELIP, radius versus time curves were simulated using the dynamical model for lipid-encapsulated microbubbles developed by Marmottant et al. [19]. The measured acoustic pressure waveforms (see Fig. 6.3) were used as the forcing function for the bubble dynamics simulations which were compared with the experimental data. The values of the physical parameters

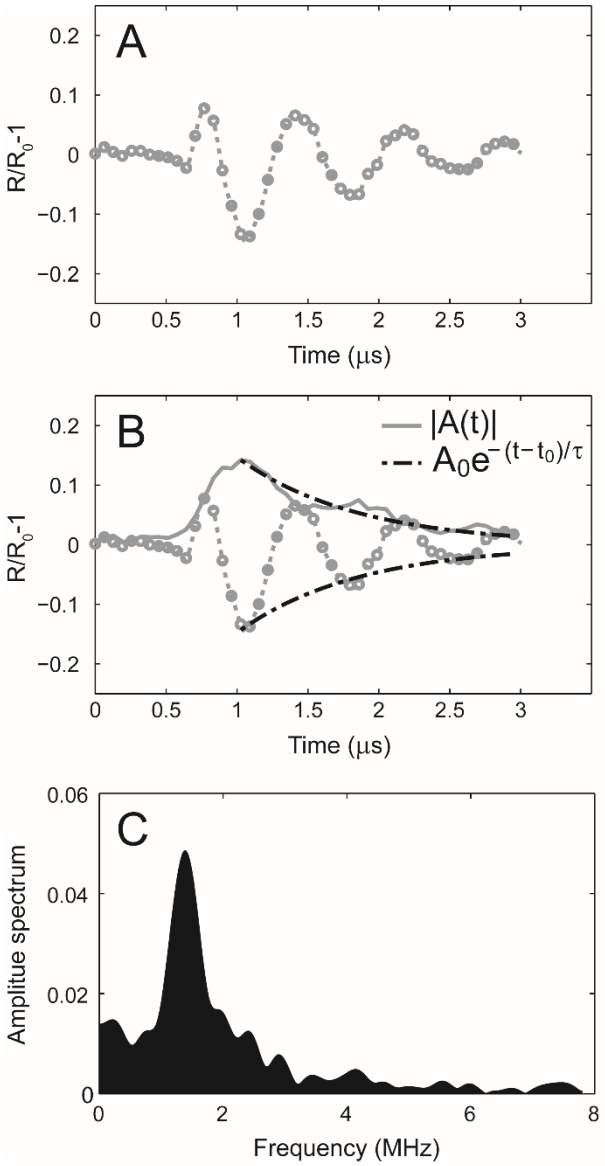


**Fig. 6.4.** Schematic of the damping analysis. **(A)** Radius versus time curve measured in response to 0° impulse excitation (the response due to 180° excitation is truncated for clarity). **(B)** The amplitude decay envelope (*solid line*) is calculated using the discrete Hilbert transform. The time constant is obtained by fitting an exponential decay (*dash-dot line*) to the envelope using Eq. (6.1). For this example, $R_0$ = 2.5 μm, τ = 0.85 μs, $\varkappa_s = 5.6\times10^{-9}$ kg/s. **(C)** Amplitude spectrum of the radius versus time curve.

used for the simulations were: ambient pressure $P_o$ = 100 kPa, density of the liquid, $\rho$ = 1007 kg/m$^3$, viscosity of the liquid (at 37 °C), $\mu = 0.76\times10^{-3}$ kg/(m·s), surface tension of the free air-water interface, $\sigma_{water}$ = 0.072 N/m, and speed of sound, $c$ = 1536 m/s. These parameters correspond to air-filled microbubbles suspended in PBS with 0.5% BSA solution at 37 °C [326]. The effective polytropic exponent was calculated from the ratio of specific heats using the expression given by Hoff et al. [354] following other researchers who have used similar expressions [355]. The parameters used in the Marmottant model for describing the interfacial rheological properties of the shell are the elasticity, $\chi$ = 0.1–1.55 N/m, and the shell surface viscosity, $\kappa_s$, which was estimated based on experimental measurements as described in the previous section. Marmottant [19] and others [330] have demonstrated that a phospholipid shell stabilizes a quiescent gas bubble by counteracting the Laplace pressure, therefore most microbubbles have an initial surface tension much lower than the surface tension of the free air-water interface, $\sigma_{water}$ [310]. In this study, we assume the shell encapsulation is initially in the pre-buckled state (i.e. the transition between the elastic and buckled regions) and consequently the initial surface tension was taken as $\sigma_0$ = 0 for all numerical simulations.

**Excitation of ELIP with a tone burst**

A subset of ELIP was also excited using a 3 MHz tone burst to record the radius versus time response to acoustic forcing. Burst excitations were generated using the same arbitrary waveform generator and transducer, but consisted of a 10-cycle, 3-MHz sinusoidal wave with a 2-cycle Gaussian ramp and taper. The *in situ* acoustic pressure amplitude for the tone burst excitation was 180 kPa, calibrated using the same methods as described above. An impulse response excitation was recorded prior to the tone burst excitation in order to obtain an estimate of the shell viscosity using the methods described above. This data acquisition scheme enabled a post hoc comparison of the measured forced response to simulations using the estimated value of shell viscosity for a particular liposome.

## 6.4. RESULTS

A total of 476 radius versus time curves for 106 individual ELIP were analyzed. The equilibrium radii of the individual ELIP ranged between 0.9–3.4 μm. Only trials for which the microbubble did not show any dissolution were analyzed in this study ($|\Delta r| < 0.1$ μm, where $\Delta r$ is the difference between the bubble resting radius before and after the acoustic excitation). A small number of recordings (12 in total, <3%) with $|\Delta r| > 0.1$ were therefore not included in the analysis.

Fig. 6.5 shows the estimated natural frequency obtained from the Fourier spectrum of the individual radius versus time responses. The median value of the measured resonance frequency was 16% higher than the eigenfrequency of an unencapsulated bubble, given by $2\pi\omega_o$.

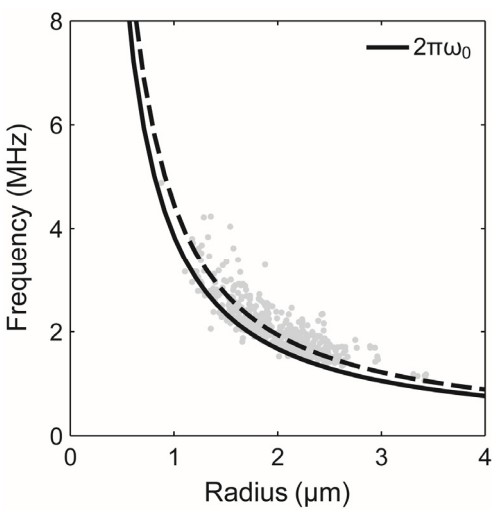


**Fig. 6.5.** Estimates of the natural frequency obtained using the Fourier transform of the radius versus time curves. The eigenfrequency for an unencapsulated bubble, $2\pi\omega_o$, which was used in the calculation of $\tau_o$ is shown for reference (*solid line*). A fit using the median of the measured values is also shown (*dashed line*).

Results of the measured shell viscosity as function of size are shown in Fig. 6.6A. Due to the large number of individual data points, the mean value and standard deviation of the points within radius bins spaced by 0.2 μm are also shown for clarity. There is a considerable spread of the shell viscosity estimates among microbubbles of the same size range (indicated by vertical error bars). However, the estimated shell viscosity increases with increasing bubble size, as has been shown in other investigations of lipid-shelled agents [20, 356, 357]. The shell viscosity estimates range from $2.1\times10^{-9}$ kg/s for microbubbles of 0.9–1.4 μm radius to $2.3\times10^{-8}$ kg/s for microbubbles of 2.5–3.4 μm radius. These values are the same order of magnitude as values obtained in other studies based on population estimates of commercially available lipid-shelled microbubbles such as SonoVue ($\kappa_s = 5.4\times10^{-9}$ kg/s [127]), Sonazoid ($\kappa_s = 1.2\times10^{-8}$ kg/s [358]), and Definity ($\kappa_s = 3\times10^{-9}$ kg/s [180]).

The dependence of the shell viscosity on the maximum dilatation rate is shown in Fig. 6.6B. The maximum dilatation rate $(\dot{R}/R)_{max}$ was determined directly from the experimentally measured radius-time curves by calculating the derivative with respect to time. Despite the dispersion in the individual shell viscosity estimates, this plot demonstrates a decrease of the shell viscosity with increasing dilatation rate. By fitting the data to a power law relation [359] of the form in Eq. (6.6), the 95% confidence interval for the power-law index *n* is between 0.1 and 0.25.

$$\kappa_s = k\left(\dot{R}/R\right)^{n-1} \tag{6.6}$$

A power-law index less than one is consistent with rheological shear-thinning behavior and has been reported earlier for lipid-shelled bubbles [20]. For dilatation rates < $0.50\times10^{6}$ $s^{-1}$, the

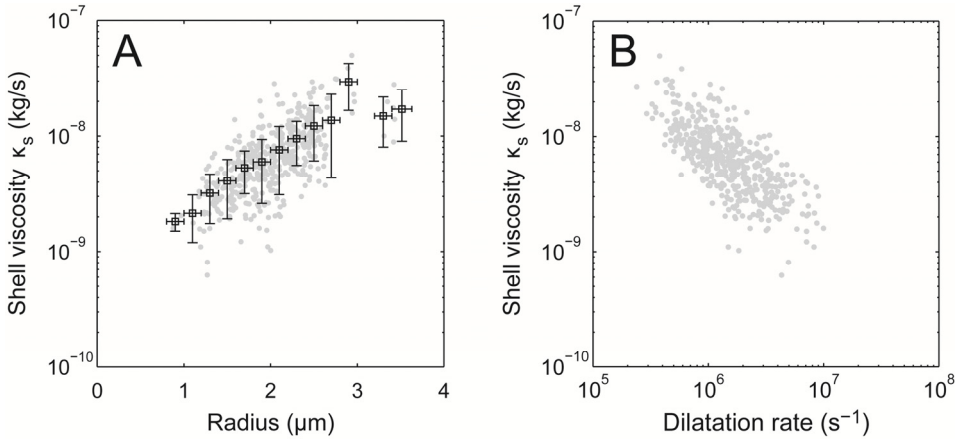


**Fig. 6.6.** Shell viscosity versus **(A)** radius and **(B)** dilatation rate. Horizontal bars represent the bin width and vertical error bars represent one standard deviation of the points within each radius bin.

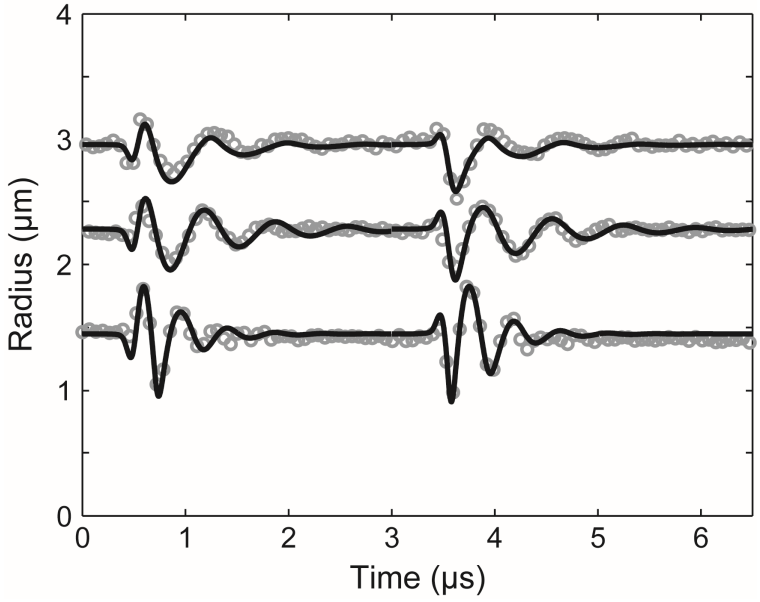


**Fig. 6.7.** Example of simulated and experimentally measured radius versus time curves for ELIP with equilibrium radii of 1.5, 2.3, and 3.0 μm. The excitation peak pressure amplitude for all cases was 250 kPa. Estimates of the shell viscosity were derived from the experimental measurements for each case and used as inputs for the numerical simulation, yielding $\kappa_s$ = 3.3 ± 0.4×10$^{-9}$, 6.0 ± 0.3×10$^{-9}$ and 2.15 ± 0.2×10$^{-8}$ kg/s, respectively. Other simulation parameters were $R_o$ = 1.5, 2.3 and 3.0 μm and $\chi$ = 0.1, 0.2 and 1.55 N/m, respectively.

mean value and standard deviation of the shell viscosity estimates in this study was $\kappa_s = (2.1 \pm 1.0)\times10^{-8}$ kg/s (n = 23).

Fig. 6.7 shows three examples of numerically simulated and experimentally measured radius versus time curves for individual ELIP with equilibrium radii of 1.5, 2.3, and 3.0 μm. The excitation peak pressure amplitude for all cases was 250 kPa. Simulations were carried out using the experimentally derived shell viscosity ($\kappa_s$) for each individual ELIP (i.e. the average of the estimates derived from both 0° and 180° impulses). The shell elasticity ($\chi$) was varied over one order of magnitude, with the upper limit corresponding to the value previously determined for ELIP in the linear regime, $\chi$ = 0.1–1.55 N/m [326] The numerical simulations show good agreement with the experimentally measured transient impulse response dynamics for each case.

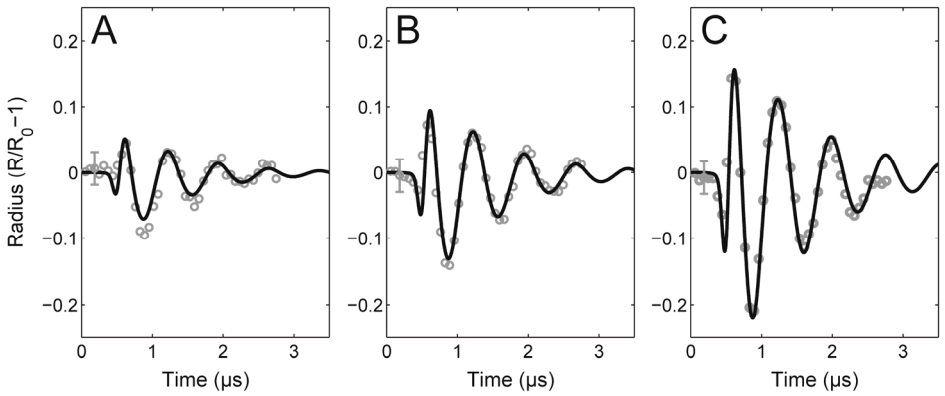


**Fig. 6.8.** Example of experimental and simulated radius-time curves for a single ELIP ($R_0$ = 2.5 μm, $\chi$ = 0.25 N/m) excited by **(A)** 125 kPa, **(B)** 250 kPa and **(C)** 500 kPa peak pressure amplitude pulses (0° pulse). Vertical bars represent the relative error of the radius tracking algorithm, which was determined by the difference between the maximum and minimum radius measured from a recording of the same ELIP without ultrasound exposure.

Fig. 6.8 shows an example of simulated and experimentally measured radius versus time curves for a single ELIP exposed to three different peak pressure amplitude pulses: 125, 250 and 500 kPa. As expected, the shell viscosity values obtained from each independent excitation are similar. The estimates of $\kappa_s$ for each pressure are 5.7, 5.6, and $5.6\times10^{-9}$ kg/s, respectively.

## 6.5. DISCUSSION

The goal of this study was to improve the understanding of the transient oscillation dynamics and shell properties of ELIP. We estimated the damping and shell viscosity from the

unforced response of individual ELIP excited by a broadband acoustic impulse excitation measured using ultra-high-speed imaging. This technique can achieve the measurement of individual ELIP in a single run using the Brandaris 128 ultra-high-speed framing camera, and provides an efficient alternative approach to the microbubble spectroscopy technique as reported previously [18, 20, 342]. The results derived from estimates for individual ELIP were in good agreement with our previously obtained values based on bulk acoustic attenuation measurements. Overall, the shell viscosity estimates for ELIP in this study are consistent with values reported for commercially available lipid-shelled UCAs. Furthermore, we found that the Marmottant model accurately describes the transient dynamics of an individual ELIP when compared with radius versus time measurements obtained from ultra-high-speed recordings. Thus, despite the encapsulation of air instead of perfluorocarbon gas, the visco-elastic shell properties of ELIP are similar to other lipid-shelled agents such as SonoVue and Definity.

**Natural frequency of unforced oscillations**

The eigenfrequency of an unencapsulated bubble is used to calculate the time constant, $\tau_o$, in Eq. (6.5). To evaluate the validity of the assumption that the surface tension dominates the bubble dynamics, we obtained estimates of the natural frequency from the Fourier transform of the radius versus time curves (Fig. 6.5). The median natural frequency measured was 16% higher than the eigenfrequency for an unencapsulated bubble, given by $2\pi\omega_o$. A 16% error in the natural frequency translates to a ~4% change in $\tau_o$ (and therefore in our estimates of $\kappa_s$) for the size range of bubbles studied.

**Contributions to damping effects**

The total damping coefficient is the summation of the shell damping ($\delta_{sh}$) and three other damping terms: the radiation damping ($\delta_{rad}$), the thermal damping ($\delta_{th}$), and the viscous damping due to the surrounding liquid ($\delta_{vis}$). Theoretical expressions for predicting the damping factors of a spherically oscillating gas bubble are well-established [350], and the latter three terms can be readily calculated based on the known equilibrium size and eigenfrequency of the microbubble. Fig. 6.9 shows the resonance damping coefficients versus radius for an air bubble under the experimental conditions used in this study. Viscous damping ($\delta_{vis}$ or $\delta_{sh}$) dominates and the radiation damping is approximately an order of magnitude smaller for bubbles in the size range considered in this study. However, thermal damping can be appreciable and is included in our model for air-filled microbubbles at resonance.

Thermal damping is not accounted for explicitly in the Rayleigh-Plesset formulation and is often neglected in linearized models of UCAs as well [5]. However, thermal damping can be significant for resonant bubbles larger than about 1 μm and is dominant for resonant bubbles larger than ~10 μm [146]. Fig. 6.9 shows that for a 1.3 μm radius bubble, $\delta_{th}$ is approximately equal to $\delta_{rad}$ and only amounts to 15% of the viscous term $\delta_{vis}$. For a bubble of

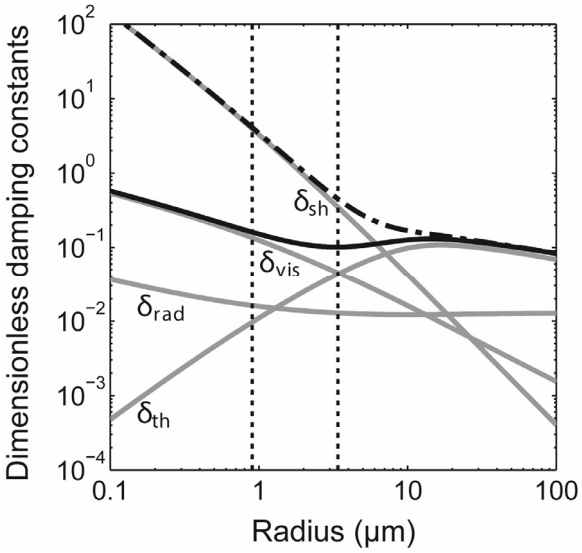


**Fig. 6.9.** The variation of dimensionless damping coefficients ($\delta_{rad}$, $\delta_{vis}$, $\delta_{th}$, $\delta_{sh}$) versus microbubble size at resonance. The total damping coefficients for a free bubble (solid line) and an encapsulated bubble with a shell viscosity of $\kappa_s = 2\times10^{-8}$ kg/s (dash-dot line) are also shown. The vertical dotted lines represent the size range of ELIP considered in this study.

about 3.5 μm radius, $\delta_{th}$ is approximately equal to the viscous damping coefficient. In this study, we estimated the thermal damping and polytropic exponent based on the resting radius of the microbubble using the expressions given by Hoff et al. [354]. It should be noted that the values of $\delta_{th}$ shown in Fig. 6.9 were calculated for an unencapsulated air bubble at resonance and include the effects of surface tension on the equilibrium gas pressure. However, $\delta_{th}$ may be less significant for an encapsulated bubble due to a lower equilibrium gas pressure resulting from the reduced initial surface tension for a bubble with a stabilizing shell (for example, $\sigma_0 = 0$ for a pre-buckled bubble as was assumed in this study) [360]. Therefore we may have a slight underestimation of the shell damping effect.

**Shell viscosity**

Overall, our estimates of the shell viscosity of individual ELIP based on the optical method developed in this study are consistent with our previous measurements obtained using a broadband attenuation spectroscopy technique [326, 348]. For low dilatation rates ($< 0.5\times10^{-6}$ s$^{-1}$), the average value of the shell viscosity in this study ($\kappa_s = (2.1 \pm 1.0)\times10^{-8}$ kg/s, n = 23) is in agreement with our previously reported bulk acoustic measurements in the linear regime ($\kappa_s = (2.0 \pm 0.14)\times10^{-8}$ kg/s [326]). Moreover, the shell viscosity estimates de-

rived from damping measurements on 106 individual ELIP in this study indicate an apparent increase of the shell viscosity with increasing radius, and a decrease with increasing dilatation rate, indicative of shear-thinning behavior. This observation is consistent with previous measurements on commercially available lipid-shelled microbubbles such as SonoVue [20] and Definity [357], but is not explained by existing shell models where the viscosity is assumed to be constant over all radii. However, there have recently been attempts to account for this behavior using ad-hoc rheological models [361, 362].

The shell viscosity estimates based on the optical approach also showed considerable variations among ELIP of the same size range (see Fig. 6.6). Variations in shell properties and acoustic response have also been reported in previous studies on lipid-shelled microbubbles. Kwan and Borden [310] and Kooiman et al. [70] present convincing microscopic images of heterogeneous lipid domains and ascribe this phenomenon to phase separation of the different lipid species on the bubble surface. Similar variations in the local lipid concentration on the shell have been found to affect the nonlinear behavior of DSPC microbubbles at high frequencies [259], although no clear relation between the nonlinear response and shell microstructure was evident. Hosny et al. [315] quantified the spatial distribution of viscosity in the microbubble shell using a fluorescence lifetime imaging technique and also found a large variation in viscosity that was correlated to differences in the ultrasound response of microbubbles of similar size. Based on the chemical composition and preparation method of ELIP, we expect similar inhomogeneities in local lipid concentration, as well as variation between individual ELIP particles within a population. Moreover, lipid diffusion and the phase transition influenced by the surrounding temperature can be other key factors affecting the heterogeneity of the ELIP shell [340, 346].

Nanostructural surface morphology which could not be resolved using the optical techniques in this study (e.g. Fig. 6.2) may nevertheless play a large role in the dynamic behavior of ELIP. For lipid-encapsulated bubbles the shell is usually assumed to be a monolayer due to thermodynamic considerations [310]. However, the shell thickness has not been directly measured for microscopic encapsulated gas bubbles and estimates based on the dynamic response of the microbubble only give information about the interfacial rheological properties of the microbubble (i.e. zero-thickness interface model) [345]. Therefore, the large variation in viscosity estimates could be due to the number of lipid layers surrounding the encapsulated microbubbles [315]. The resolution of the fluorescence images presented in Fig. 6.2 is limited by the focal spot size, which is about 220 nm in the lateral dimension. Thus, we are unable to conclude whether the shell is a lipid monolayer or if it is multilamellar. Multilamellar vesicles, in which the lipid monolayer immediately adjacent to the gas bubble is surrounded by one or more bilayers, have been observed in transmission electron microscopy images of ELIP [348]. The spread of the shell viscosity estimates for ELIP of similar size may indicate the presence of multilamellar vesicles, where the apparent viscosity depends on the number of lamallae.

Another factor affecting the interpretation of the variation in the shell viscosity estimates is the uncertainty, which can be approximated as the random error associated with separate measurements on the same ELIP. We calculated the random error by considering the relative difference between the values obtained from separate analysis of the two phase-inverted excitation pulses (0° and 180°), i.e. the absolute difference between the two shell viscosity estimates normalized by the average of the two estimates. The median random error was 40% which is approximately the same as the standard deviation shown in Figure 6.6A and 6.6B.

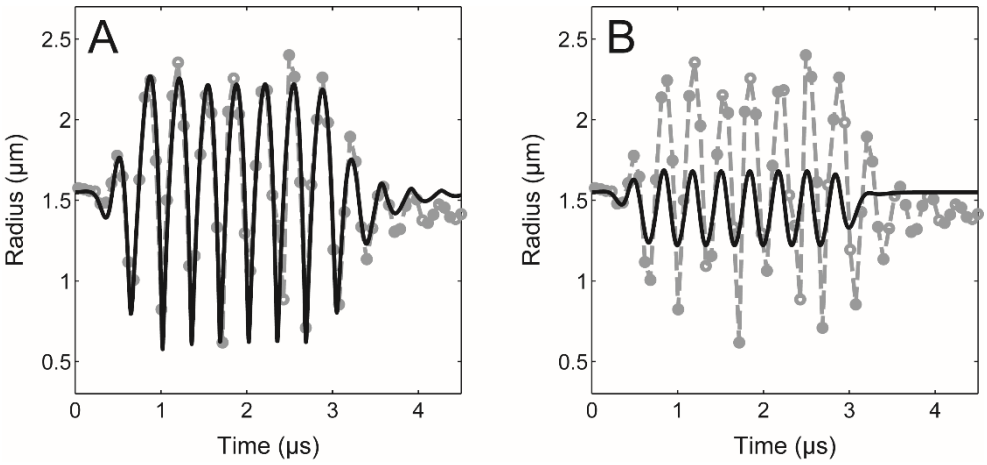


**Fig. 6.10.** Experimentally measured radius-time curve for a bubble in response to narrow-band forcing ($f$ = 3 MHz, dashed lines). Theoretical radius versus time curves for two different values of the damping coefficient are shown. The solid line represents the simulated damping using **(A)** the method described in this paper ($\kappa_s = 3.0 \times 10^{-9}$ kg/s) and **(B)** the shell damping estimated from bulk acoustic measurements ($\kappa_s = 2 \times 10^{-8}$ kg/s). The shell elasticity parameter was taken to be $\chi$ = 1.55 N/m as reported in [345].

**Impulse response measurements and analysis**

Evaluation of the damping coefficient based on the impulse response is a new and efficient approach applied to characterization of lipid-shelled ELIP in this study. A broadband pulse was applied to acquire the radius versus time impulse response of an individual ELIP, requiring only a single exposure of a few microseconds using an ultra-high-speed camera. Using the Brandaris 128, we were able to record the unforced, exponentially decaying amplitude response from two acoustic impulse excitations, a pulse inversion pair, during each high speed recording (128 frames). This method provides an efficient approach which enabled statistical measurements on a large number of individual ELIP. Additionally, data analysis was straightforward and the simulated transient response of the lipid-encapsulated microbubble accurately tracked the measured radius versus time curves (Figs. 6.7 and 6.8).

We also assessed the validity of this technique by comparing the forced response measured using an 10-cycle narrow-band burst excitation with numerical simulations. An example is shown in Fig. 6.10 in which simulations using two different shell viscosity values (derived from the optical method described here or the bulk acoustic method reported in Raymond et al. [326], respectively) are compared with experimental measurements. Excellent agreement was found between the simulated and measured radius versus time curves when the effect of the shell was taken into account using the viscosity estimate obtained in this study. For the example shown in Fig. 6.10A, the shell viscosity estimate ($\kappa_s = 3.0\times10^{-9}$ kg/s) was obtained during a previous impulse response exposure of the same particular liposome. Alternatively, using the population-averaged shell viscosity obtained in Raymond et al. [326] ($\kappa_s = 2.0\times10^{-8}$ kg/s) results in an under-prediction of the amplitude of the response to narrow-band forcing (Fig. 6.10B). Use of the estimated value obtained for a specific ELIP in this study allows one to obtain much more precise agreement between the experimental theoretical data using the Marmottant model.

**Implications for contrast-enhanced ultrasound imaging**

The size range of ELIP is known to be polydisperse, with particle sizes ranging from tens of nanometers to several microns [326, 347, 348]. Differences in the characteristics of nanoscale versus microscale ELIP vesicles may play a role in the scattering properties of individual ELIP. This study found that smaller ELIP are characterized by a substantially lower shell viscosity, which may contribute to increase nonlinear scattering, especially at higher frequencies. Such nonlinear behavior of the smaller populations of ELIP could be exploited for diagnostic ultrasound applications which utilize higher frequencies, such as intravascular ultrasound. For example, the nonlinear acoustic signatures of ELIP could be utilized for improved imaging of pathology in the *vasa vasorum*, the proliferative small vessels that play a role in atheroma progression in the cardiovascular system.

Goertz et al. [276] demonstrated that sub-populations of the lipid-shelled clinical UCA Definity® exhibited different frequency-dependent scattering properties as a function of size. These authors hypothesized that differences in the encapsulation microstructure for small and large bubbles may be a key factor influencing the nonlinear scattering at high frequencies. A subsequent study by Helfield et al. [275] demonstrated that smaller subpopulations of lipid-shelled microbubbles were not only resonant at higher frequencies, but were also characterized by a substantially lower shell viscosity, suggesting a possible frequency dependence of the lipid shell properties. It is still not clear whether this effect is due solely to the size or if frequency-dependent considerations need to be taken into account in the dynamical models. Doinikov et al. [362] point out that existing shell models may not capture the observed radius- or frequency-dependence of the shell material properties, and that full description of the rheological properties of the shell may require the use of more

complex models in order to describe the shear-thinning behavior. A more detailed exploration of alternative rheological models could be explored in future studies.

**Limitations**

Inherent limitations of the optical system resolution result in a bias of the size range of ELIP selected for analysis in this study. The optical resolution of the ultra-high-speed imaging system was 0.4 μm [52] and the smallest individual ELIP that was measured in this study was several times larger than the optical resolution limit. The size range of ELIP considered here focused on measurable particles larger than 0.9 μm in radius only and smaller ELIP were not considered for investigation.

The proximity of the microbubble to the OptiCell membrane may affect the measured response of ELIP to acoustic excitation. Previous studies have found that the presence of a membrane near an oscillating microbubble can affect the resonance frequency and oscillation amplitude in response to acoustic forcing [124, 334]. Functionalized UCAs such as ELIP are being developed for targeted imaging and drug-delivery applications, and therefore similar effects are expected to play a role *in vivo*. The acoustic response of adherent targeted bubbles may be influenced by the ligand distribution and bubble-wall interaction [70]. Therefore, future work to investigate the damping for adherent targeted agents using this approach is recommended.

The simulations presented in Figs. 6.7, 6.8 and 6.10 are not unique solutions because there is more than one free parameter in the Marmottant model, namely the shell elasticity, $\chi$, and initial surface tension, $\sigma_0$. We have chosen to assume the phospholipid shell stabilizes a gas bubble by counteracting the Laplace pressure, so that $\sigma_0 = 0$, throughout this paper. Using empirical fits, the values for the data presented in Fig. 6.7 are: $\chi$ = 0.1, 0.2 and 1.55 N/m for $R_0$ = 1.5, 2.3 and 3.0 μm, respectively. A radius-dependent shell elasticity parameter has also been observed and modeled by Chetty et al. [125] and Doinikov et al. [362]. The measured oscillation amplitudes were not always in the 'elastic' regime range of the Marmottant model ($R/R_0 < 1.02$). However, the 3.0 μm bubble did behave near this regime ($R/R_0 \sim 1.07$) and the shell elasticity determined from the optical measurements agreed with previous measurements [326].

## 6.6. CONCLUSIONS

In this study a model based on time domain analysis was developed to estimate the shell viscosity for individual ELIP using optically measured radius versus time curves. The decay time constant was measured from the unforced response of the ELIP following excitation by a short acoustic pulse. At low dilatation rates, the shell viscosity is in quantitative agreement with our previously determined values for ELIP. The viscoelastic shell of ELIP was found to behave similarly to other lipid-shelled agents. We demonstrated that qualitative

agreement between the measured and simulated radius versus time curves under transient and steady-state acoustic forcing is highly dependent on the shell viscosity. The methods described here can provide accurate estimates of the shell viscosity and damping for individual UCA microbubbles. In contrast to acoustic measurements of a microbubble population with a relatively wide size distribution, this method provides some insight on the variation of properties among single particles within a population. This method also enables efficient measurements on a large number or individual UCA microbubbles because it is based on the response to a single acoustic impulse excitation.

**Acknowledgements**

The authors would like to thank Robert Beurskens and Frits Mastik from the Dept. of Biomedical Engineering, Erasmus MC for technical assistance with Brandaris experiments. The authors would also like to thank the Erasmus Optical Imaging Centre of Erasmus MC for use of their facilities, and Wiggert A. van Cappellen and Alex Nigg from the Erasmus Optical Imaging Centre, Department of Pathology, Erasmus MC for technical assistance. JLR was supported by a fellowship from the Whitaker International Program administered by the Institute of International Education (IIE). This work was supported in part by the U.S. Department of Health and Human Services, National Institutes of Health (NIH R01HL74002, NIH R01HL059586) and NanoNextNL, a micro and nanotechnology consortium of the Government of the Netherlands and 130 partners.

Chapter 7

# Focal areas of increased lipid concentration on the coating of microbubbles during short tone-burst ultrasound insonification

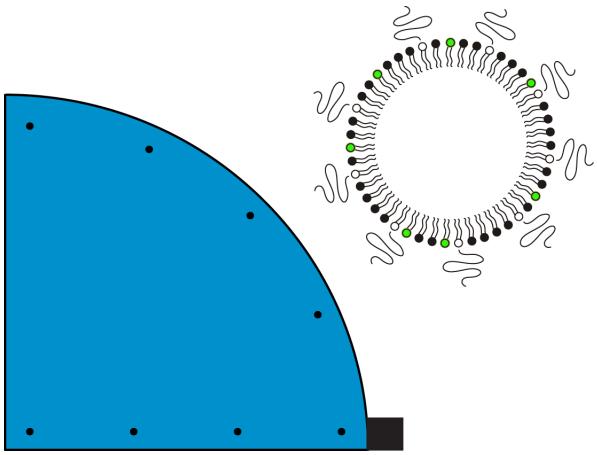

Klazina Kooiman, Tom van Rooij, Bin Qin, Frits Mastik, Hendrik J. Vos, Michel Versluis, Alexander L. Klibanov, Nico de Jong, Flordeliza S. Villanueva, Xucai Chen

*In preparation for submission*

Chapter 8

# Vibrational responses of bound and non-bound targeted lipid-coated single microbubbles

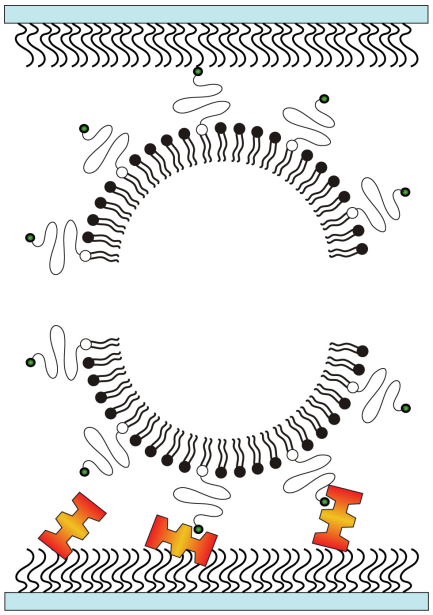

Tom van Rooij, Inés Beekers, Kirby R. Lattwein, Antonius F.W. van der Steen, Nico de Jong, Klazina Kooiman

*IEEE Transactions on Ultrasound, Ferroelectrics and Frequency Control* (2016) – *Submitted*

## 8.1. ABSTRACT

One of the main challenges for ultrasound molecular imaging is acoustically distinguishing non-bound microbubbles from those bound to their molecular target. In this *in vitro* study, we compared two types of in-house produced targeted lipid-coated microbubbles, either consisting of DPPC or DSPC lipid as the main lipid, using the Brandaris 128 ultra-high-speed camera to determine vibrational response differences between bound and non-bound biotinylated microbubbles. In contrast to previous studies that studied vibrational differences upon binding, we used a covalently bound model biomarker (i.e., streptavidin) rather than physisorption, to ensure binding of the biomarker to the membrane. The microbubbles were insonified at frequencies between 1 and 4 MHz at pressures of 50 and 150 kPa. This study shows lower acoustic stability of bound microbubbles, of which DPPC-based microbubbles deflated most. For DPPC microbubbles with diameters between 2 and 4 μm driven at 50 kPa, resonance frequencies of bound microbubbles were all higher than 1.8 MHz, whereas those of non-bound microbubbles were significantly lower. In addition, the relative radial excursions at resonance were also higher for bound DPPC microbubbles. These differences did not persist when the pressure was increased to 150 kPa, except for the acoustic stability which further decreased. No differences in resonance frequencies were observed between bound and non-bound DSPC microbubbles. Nonlinear responses in terms of emissions at the subharmonic and second harmonic frequencies were similar for bound and non-bound microbubbles at both pressures. In conclusion, we identified differences in vibrational responses of bound DPPC microbubbles with diameters between 2 and 4 μm that distinguish them from non-bound ones.

## 8.2. INTRODUCTION

Ultrasound contrast agents that consist of targeted microbubbles are emerging in their applications for ultrasound molecular imaging [31, 68, 390]. These microbubbles have a ligand attached to their shell by which they can be targeted to a specific biomarker, for example $\alpha_v\beta_3$ that is expressed on the cellular membrane of endothelial cells in neovasculature [17, 76]. For successful translation of ultrasound molecular imaging to the clinic, two major problems still need to be tackled: *1)* producing microbubbles of the same size that also behave identical in an ultrasound field, and *2)* distinguishing the response of a single targeted microbubble bound to a specific biomarker from a non-bound targeted microbubble. Since microbubbles of the same size can still have different acoustic properties [18, 20, 180, 260, 312], producing monodisperse microbubbles may not necessarily result in microbubbles that have, for example, the same resonance frequency. But if it is possible to determine the acoustic parameters that are specific for bound targeted microbubbles, they may be distinguished from non-bound targeted microbubbles based on their acoustic signal.

Several studies investigated the difference in acoustic properties of bound and non-bound microbubbles, but these studies reported conflicting results. In the low frequency range (2 - 4 MHz) a shift in resonance frequency was found for microbubbles after binding [136, 140], whereas at 11 MHz and 25 MHz no shift was observed [142]. For the responses at the subharmonic frequency either a change in frequency [142] or no change in amplitude and frequency [139] was reported upon binding. In contrast, for the response at the second harmonic frequency the results reported by Zhao et al. [139] and Casey et al. [141] were in agreement with each other: the amplitude increased for bound microbubbles. Finally, both Zhao et al. and Overvelde et al. found a decrease in the vibrational response at the fundamental frequency for bound microbubbles [136, 139].

All acoustic studies on bound versus non-bound targeted microbubbles used either physisorption as a method to attach a model biomarker to an artificial surface (membrane or capillary) [136, 139-141] or had the model biomarker embedded in agarose [142]. Physisorption of a model biomarker can result in detachment of the biomarker from the membrane or capillary which then can cover the whole targeted microbubble, including the area that is not directly in contact with the membrane. This was reported by Kooiman et al. for the model biomarker streptavidin that was physisorbed to an Opticell membrane [391]. Functionalization of lipid-coated microbubbles with streptavidin changes the properties, such as elasticity [130, 131, 262] and acoustic stability [262]. Consequently, the comparisons made in previous studies between bound microbubbles and non-bound microbubbles are in fact a comparison between bound lipid-coated microbubbles covered by streptavidin and non-bound lipid-coated microbubbles, which did not have streptavidin on their shell. In addition, both physisorption and embedding a model biomarker in agarose are far from the *in vivo* situation, where biomarkers are incorporated into the cellular membrane.

We covalently linked a model biomarker to an artificial surface to study the vibrational responses of single bound targeted microbubbles and non-bound targeted microbubbles aiming to find parameters to discriminate them acoustically. Super-resolution confocal laser scanning fluorescence microscopy showed that covalent coupling of the model biomarker streptavidin to a hydrogel prevented the streptavidin to bind to the biotinylated lipid-shell of the microbubble outside the binding area [70]. That study compared the lipid distribution and binding area of two types of targeted lipid-coated microbubbles that were either coated with mainly DPPC (1,2-dipalmitoyl-*sn*-glycero-3-phosphocholine, C16:0) which is the main shell component of Definity (Lantheus Medical Imaging, North Billerica, MA, USA) or mainly DSPC (1,2-distearoyl-*sn*-glycero-3-phosphocholine, C18:0) which is the main lipid component of SonoVue, Lumason, and BR14 (Bracco Imaging S.p.A., Milan, Italy) [7-9, 70, 260, 318]. It was shown that the lipid distribution was more homogeneous for DPPC-based microbubbles than for DSPC-based microbubbles and that the binding area for DPPC-based microbubbles was significantly larger than for DSPC-based microbubbles [70]. We previously determined the acoustic properties of these DPPC and DSPC-based microbubbles in a set-up

where the microbubbles were floating against an OptiCell wall (non-bound) [260] and hypothesized that the difference in ligand-distribution and binding area could alter the acoustic response after adherence of the microbubble to its molecular target. In the present study we investigated the vibrational response of in-house produced targeted DPPC-based and DSPC-based microbubbles using the Brandaris 128 ultra-high-speed optical camera [52] when they had bound to a streptavidin-coated hydrogel and compared their responses to those of non-bound microbubbles floating against the hydrogel. We aimed to identify differences in vibrational responses that may be used to discriminate bound from non-bound microbubbles.

## 8.3. MATERIALS AND METHODS

### Microbubble preparation

Biotinylated lipid-coated microbubbles with a $C_4F_{10}$ gas core (F2 Chemicals Ltd, Preston, UK) were made as previously described [70, 129] by sonication for 1 min. The coating was composed of 59.4 mol% DSPC (P6517, Sigma-Aldrich, Zwijndrecht, the Netherlands) or DPPC (850355, Avanti Polar Lipids, Alabaster, AL, USA), 35.7 mol% polyoxyethylene-40-stearate (PEG-40 stearate, P3440, Sigma-Aldrich), 4.1 mol% 1,2-distearoyl-*sn*-glycero-3-phosphoethanolamine-N-[carboxy(polyethylene glycol)-2000] (DSPE-PEG(2000), 880125, Avanti Polar Lipids); and 0.8 mol% 1,2-distearoyl-*sn*-glycero-3-phosphoethanolamine-N-[biotinyl(polyethylene glycol)-2000] (DSPE-PEG(2000)-biotin, 880129, Avanti Polar Lipids).
A 25 µm thick polyester membrane was mounted on a custom-made rectangular polyvinylchloride holder (same size as a microscope objective glass) and was custom coated with a 1-2 µm thick polycarboxylate hydrogel (XanTec bioanalytics GmbH, Düsseldorf, Germany). For the bound targeted microbubbles, the hydrogel was activated and streptavidin (S4762, Sigma-Aldrich) was subsequently covalently attached to the hydrogel using the amine coupling kit (K AN-50, XanTec bioanalytics GmbH) according to the instructions of the manufacturer as previously described [70]. Briefly, streptavidin was dissolved in acetate buffer (2 mM, pH 5.4) (1 mg/mL). After desalting the streptavidin by use of a PD-10 desalting column (GE Healthcare Bio-Sciences), the concentration was determined spectrophotometrically at 570 nm using a PierceTM BCA Protein Assay kit (Thermo Scientific) and Thermo Multiskan EX. Three polyester membranes were placed in a 5-Slidemailer (Heathrow Scientific, Northgate, UK) with 18 mL of 1 M NaCl + 0.1 M NaB (pH 10) elution buffer (K AN-50, XanTec bioanalytics GmbH), followed by an incubation with 18 mL of 1.6 % (w/v) EDC·HCL (K AN-50, XanTec bioanalytics GmbH) in activation NHS/MES buffer (K AN-50, XanTec bioanalytics GmbH), and 18 mL of 33 µg/mL desalted streptavidin in 2 mM acetate buffer at pH 5.2-5.4. Finally, 18 mL of 1 M ethanolamine hydrochloride (pH 8.5) quenching buffer (K AN-50, XanTec bioanalytics GmbH) was used to terminate the reaction. The targeted microbubbles were allowed to adhere to the streptavidin-coated membrane in air-

equilibrated phosphate buffered saline (PBS) containing calcium and magnesium (DPBS, 14080, Invitrogen, Thermo Fischer Scientific, Landsmeer, the Netherlands) by flotation for 5 min. Then, the membrane was gently washed with air-equilibrated PBS containing calcium and magnesium three times using a 3 mL plastic Pasteur pipet. For the non-bound targeted microbubbles the hydrogel was treated in the same way, except for the addition of streptavidin. The targeted microbubbles were added below the hydrogel-coated polyester membrane of the custom-made holder and floated up due to buoyancy. The hydrogels with the non-bound targeted microbubbles and bound targeted microbubbles were orientated in the set-up as shown in Fig. 8.1.

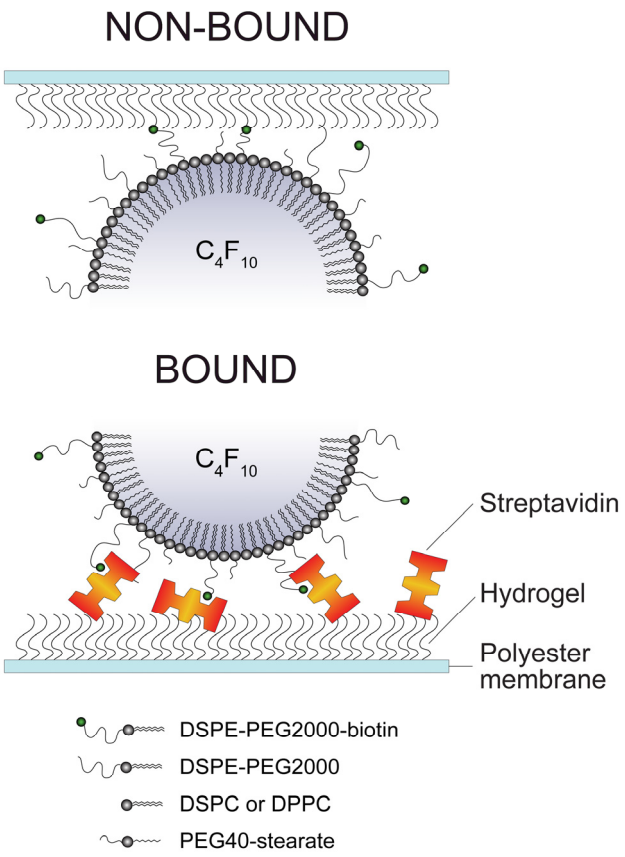


**Fig. 8.1.** Configuration and composition of non-bound targeted microbubbles (top) floating against a hydrogel and targeted microbubbles bound to this hydrogel via streptavidin in the experimental set up (not to scale).

**Microbubble spectroscopy**

The vibrational responses of the bound and non-bound targeted microbubbles were captured using the Brandaris 128 ultra-high-speed camera operated at ~15 million frames per second [52]. Single microbubbles were investigated in ROI mode [320] using the microbubble spectroscopy technique [20] in combination with the exact same set-up as in our previous study [260], except for a higher magnification microscope objective (60×, NA = 0.9, Olympus, Tokyo, Japan). Briefly, a broadband single element polyvinyl difluoride (PVDF) transducer (25 mm focal distance, f-number 1.1, center frequency 5 MHz, PA275, Precision Acoustics Ltd, Dorchester, UK) transmitted a Gaussian tapered 8-cycle sine wave burst at transmit frequencies swept from 1 to 4 MHz (increment steps of 200 kHz) at a peak-negative pressure ($P_A$) of 50 or 150 kPa at the focus. The pressures were calibrated with two calibrated PVDF needle hydrophones in a separate measurement beforehand (0.2-mm diameter PA2030 and 1-mm-diameter PA1875, Precision Acoustics). The optic focus was aligned with the acoustic focus, to ensure that the microbubble received the intended pressure. The ultrasound was triggered on the second recording of each microbubble to obtain the initial resting diameter and the noise level with our contour tracking algorithm in the first recording. The experiments were conducted at room temperature and the sample was submersed in air-equilibrated PBS containing calcium and magnesium. All microbubbles were exposed to ultrasound within 2 h after addition to the custom-made holder.

**Data analysis**

Diameter-time (*D*-*t*) curves were obtained using custom-designed image analysis software [20] that determines the vibrational responses as described elsewhere [260]. Briefly, the acoustic stability of the microbubbles was quantified as the difference between the mean diameter of the microbubble in the initial *D*-*t* curve ($D_o$) and the final *D*-*t* curve ($D_{end}$). Next, the asymmetry of the *D*-*t* curves was measured as the ratio *E*/*C* between the relative expansion *E*, defined as $(D_{max} - D_o) / D_o$, and the relative compression *C*, defined as $(D_o - D_{min}) / D_o$, of the microbubble. Where $D_{max}$ is the maximum diameter, $D_{min}$ the minimum diameter in the *D*-*t* curve, and $D_o$ the resting diameter before vibration. The *E*/*C* ratios were used to classify the asymmetry as: compression-only behavior ($E/C < 0.5$); normal excursion ($0.5 \leq E/C \leq 2$); or expansion-only behavior ($E/C > 2$) [321].

Using the fast Fourier transformation (FFT) the frequency content of the *D*-*t* curves was analyzed in terms of the amplitude at the transmit frequency ($f_T$). These amplitudes were fitted to a resonance curve of a linear oscillator by a least-mean-squares method [20, 260] to determine the resonance frequency ($f_{res}$) of the microbubble. At $f_{res}$, the diameter of the microbubble is referred to as $D_{res}$. The maximum relative radial excursions (i.e. at $f_{res}$) were defined as the maximum amplitude of the FFT divided by the corresponding resting diameter of the microbubble [260]. The same approach was used to determine the subharmonic resonance frequencies ($f_{sub}$) and the second harmonic resonance frequencies and the corre-

sponding maximum relative radial excursions. Next, the maximum relative radial excursions were transformed into pressures as described by Emmer et al. [260, 312]. All calculations were performed in MATLAB (The MathWorks Inc., Natick, MA, USA).

### Statistics

Shapiro-Wilk tests for normality showed that the data was not normally distributed, so we used nonparametric testing. For comparing the acoustic stability of the microbubbles we used Wilcoxon signed-rank tests. When comparing groups, e.g. bound DSPC and non-bound DSPC, we used Mann-Whitney U tests. Medians and interquartile ranges (IQR) are reported and were calculated using Tukey's Hinges method. Statistical analyses were performed using SPSS (Statistics 21, IBM Corp., Armonk, NY, USA) and a p-value < 0.05 was regarded as significant.

## 8.4. RESULTS

In total, 143 single microbubbles having a $D_0$ between 1.5 and 10 μm were analyzed. At 50 kPa, 46 bound DPPC microbubbles were insonified; 18 of which were also insonified at 150 kPa. For bound DSPC microbubbles, 43 were insonified at 50 kPa; 15 of which were also insonified at 150 kPa. None of the bound microbubbles detached during the experiments since every microbubble remained within the optic focus. For the non-bound microbubbles we included 26 DPPC and 28 DSPC microbubbles, which were all insonified at both 50 and 150 kPa.

### Acoustic stability

At $P_A$ = 50 kPa, both bound DPPC and DSPC-based microbubbles deflated significantly more than when they were non-bound (p = 0.0001), as shown in Fig. 8.2. The median size for the bound DPPC microbubbles after insonification was 83% of $D_0$, while this was 98% for the non-bound DPPC microbubbles. The median size of bound DSPC microbubbles was 93% of $D_0$ after insonification, whereas non-bound DSPC microbubbles maintained their original size (100% of $D_0$). At a pressure of 150 kPa, the size difference between bound DPPC and non-bound DPPC microbubbles was not significant. The median diameter after insonification decreased to 53% of $D_0$ for bound DPPC microbubbles and to 56% for non-bound DPPC microbubbles. In case of DSPC microbubbles those that had bound deflated more than those that had not (p = 0.004). For the DSPC microbubbles this was 76% for the bound ones and hardly any shrinkage (98% of their initial size) for the non-bound ones. In addition, for both bound and non-bound microbubbles, those based on DPPC deflated more than those based on DSPC at 50 kPa (bound: p = 0.001, non-bound: p = 0.031) and also at 150 kPa (both p = 0.0001).

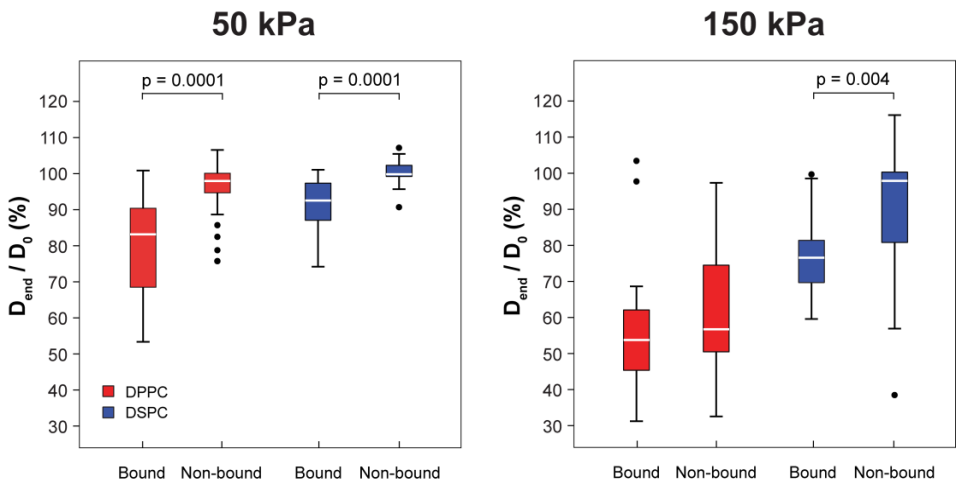


**Fig. 8.2.** Diameter change during ultrasound exposure expressed as $D_0/D_{end}$ for bound DPPC (50 kPa: n = 46, 150 kPa: n = 18), non-bound DPPC (50 kPa: n = 28, 150 kPa: n = 28), bound DSPC (50 kPa: n = 43, 150 kPa: n = 15) and non-bound DSPC microbubbles (50 kPa: n = 26, 150 kPa: n = 26). The filled black circles are outliers.

### Linear oscillation behavior

The resonance frequencies in relation to $D_{res}$ are shown in Fig. 8.3. First of all, at a pressure of 50 kPa the resonance frequencies of bound DSPC microbubbles were similar to those of non-bound DSPC microbubbles. For DPPC-based microbubbles, the resonance frequencies of bound microbubbles were significantly higher than for non-bound DPPC microbubbles ($p = 0.045$). To further highlight the differences in resonance frequencies between bound and non-bound DPPC microbubbles, we compared the resonance frequencies of those having $D_{res} < 4$ µm. For larger microbubbles all resonance frequencies were similar, but for microbubbles having a $D_{res} < 4$ µm, the resonance frequencies of bound DPPC microbubbles were significantly higher than for non-bound DPPC microbubbles ($p = 0.002$). In addition, no overlap was found between the median (IQR) resonance frequencies of bound DPPC microbubbles and non-bound DPPC microbubbles: 1.94 (1.83 – 2.25) versus 1.59 (1.40 – 1.77). In contrast, the resonance frequencies of bound and non-bound DSPC microbubbles were similar for all studied sizes ($p = 0.494$). Median (IQR) resonance frequencies were 2.39 (1.98 – 2.78) for bound DSPC and 2.63 (2.25 – 3.11) for non-bound DSPC microbubbles. The resonance frequencies of bound DSPC microbubbles were significantly higher than those of bound DPPC-based microbubbles at $P_A = 50$ kPa ($p = 0.001$), for the non-bound DSPC and DPPC microbubbles no difference was found. The resonance frequencies at a pressure of 150 kPa were all similar. The number of microbubbles included in these graphs is lower than the total number of studied microbubbles, since some resonance peaks were below or

above the measuring range (< 1 MHz or > 4 MHz); the resonance frequency could therefore not be determined.

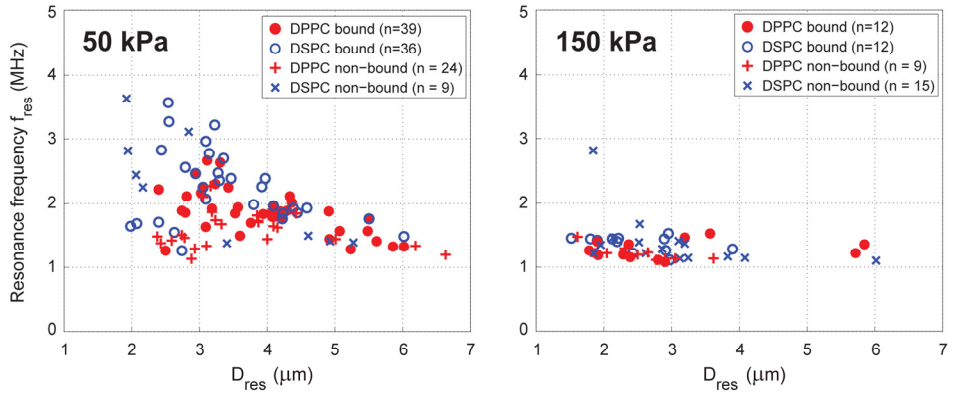


**Fig. 8.3**. Resonance frequencies ($f_{res}$) of bound DPPC (filled red circles), non-bound DPPC (red crosses), bound DSPC (blue open circles), and non-bound DSPC (blue crosses) microbubbles plotted versus the diameter at resonance ($D_{res}$) at $P_A$ = 50 kPa (top panel) and $P_A$ = 150 kPa (bottom panel).

For bound DPPC microbubbles, the median maximum relative radial excursions (median (IQR) of 0.14 (0.11 – 0.18)) at the resonance frequency at a pressure of 50 kPa was significantly higher than for the non-bound DPPC microbubbles (0.09 (0.06 – 0.13), p = 0.002, Fig. 8.4,). Although the median maximum relative radial excursions of bound DSPC microbubbles 0.11 (0.08 – 0.12) were not significantly different from non-bound DSPC microbubbles 0.05 (0.03 – 0.13, p = 0.157) over the whole resonance frequency range, the maximum relative radial excursions for bound DSPC microbubbles were significantly higher for resonance frequencies > 2 MHz (bound: 0.11 (0.08 – 0.12), non-bound: 0.03 (0.02 – 0.04), p = 0.001). In addition, the maximum relative radial excursions of bound DSPC microbubbles were significantly lower than of bound DPPC microbubbles (p = 0.0001), but similar for the non-bound DSPC and DPPC microbubbles. At a driving pressure of 150 kPa the median maximum relative radial excursions of bound and non-bound DPPC microbubbles at $f_{res}$ were similar, but significantly higher for bound DSPC than non-bound DSPC microbubbles (p = 0.001). The median (IQR) of the maximum relative radial excursions was similar for the bound microbubbles: 0.28 (0.22 – 0.33) for DPPC and 0.28 (0.23 – 0.35) for DSPC-based microbubbles (Fig. 8.4). For non-bound microbubbles the maximum relative radial excursions were significantly higher (p = 0.03) for DPPC microbubbles than for DSPC microbubbles: 0.25 (0.18 – 0.28) versus 0.11 (0.09 – 0.23).

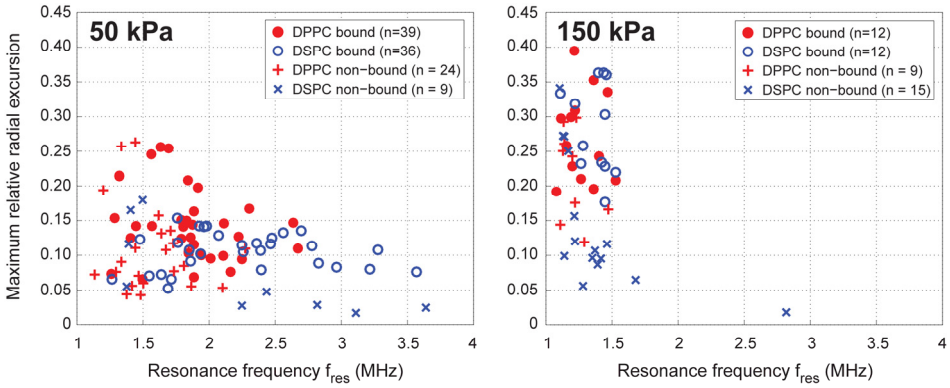


**Fig. 8.4.** Maximum relative radial excursions at the resonance frequency of bound DPPC (filled red circles) non-bound DPPC (red crosses), bound DSPC (blue open circles), and non-bound DSPC (blue crosses) microbubbles plotted versus the resonance frequency ($f_{res}$) at $P_A$ = 50 kPa (top panel) and $P_A$ = 150 kPa (bottom panel).

### Nonlinear oscillation behavior

The asymmetry of the radial excursions at each transmit frequency was expressed as the ratio between the relative expansion *E* and relative compression C. At 50 kPa the median of the radial excursions was compression-dominated with $0.5 < E/C < 1$ for bound targeted microbubbles of both types (Fig. 8.5) at all frequencies. For the non-bound microbubbles the oscillations were mostly symmetric, except for the frequencies between 1 and 1.6 MHz for which the radial excursions of DPPC microbubbles were compression-dominated. At $P_A$ = 150 kPa the excursion behavior of bound microbubbles at frequencies between 1 and 1.8 MHz ranged from symmetric to expansion-dominated, whereas at higher frequencies the behavior of both microbubble types was compression-dominated. The non-bound microbubbles showed mostly symmetric oscillations.

Responses at the subharmonic frequency at a driving pressure of 50 kPa were present in 22 out of 46 (48%) bound DPPC microbubbles and in 7 out of 43 (16%) bound DSPC microbubbles. For both non-bound DPPC and DSPC microbubbles only one (4%) responded at the subharmonic frequency. At the higher pressure of 150 kPa, the number of bound DPPC microbubbles responsive at the subharmonic frequency was similar to that at 50 kPa: 8 out of 18 (44%), but increased to 9 out of 15 (60%) for DSPC-based microbubbles. The number of non-bound microbubbles that responded at the subharmonic frequency increased to 12 out of 28 (43%) for DPPC and 6 out of 26 (23%) for DSPC microbubbles.

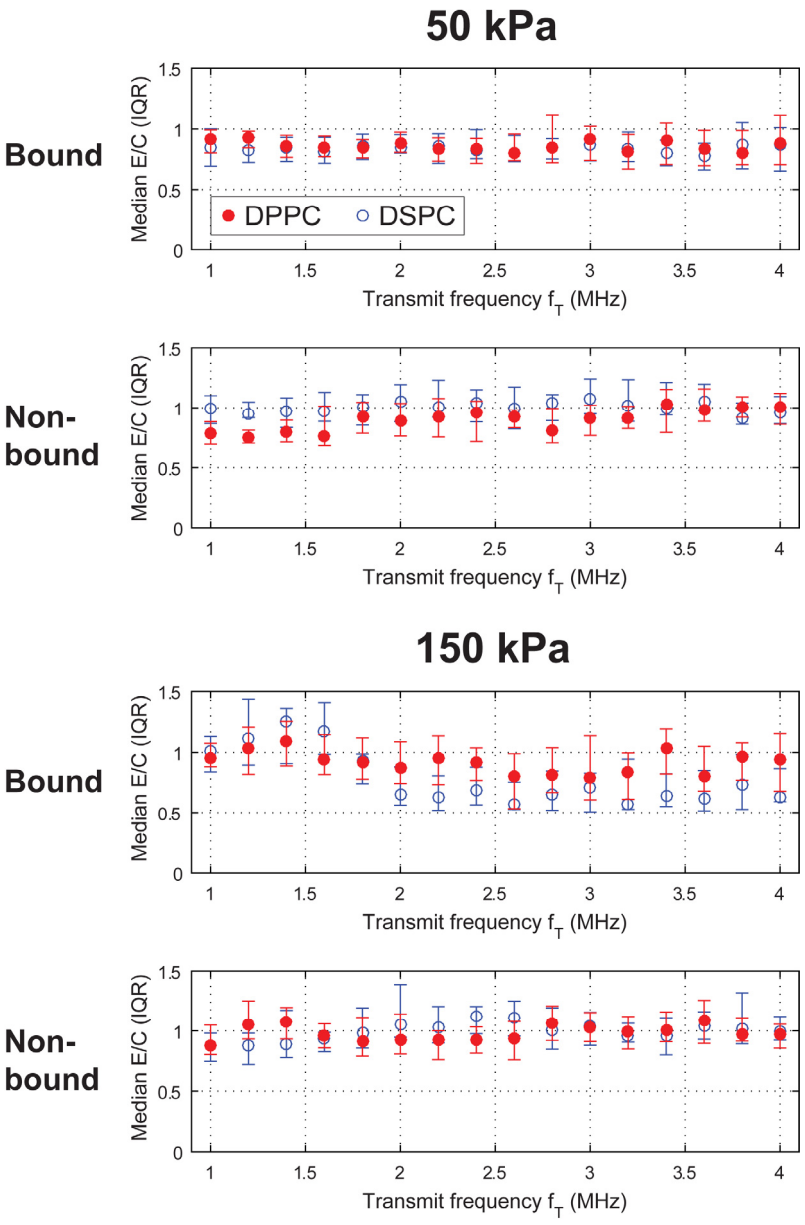


**Fig. 8.5.** Median (IQR) ratio between the relative expansion *E* and the relative compression *C* of bound DPPC (50 kPa: n = 37, 150 kPa: n = 18) and bound DSPC (50 kPa: n = 43, 150 kPa: n = 15) microbubbles, and non-bound DPPC (50 kPa: n = 28, 150 kPa: n = 28) and non-bound DSPC (50 kPa: n = 26, 150 kPa: n = 26) microbubbles plotted versus the transmit frequency at $P_A$ = 50 kPa (top panels) and $P_A$ = 150 kPa (bottom panels).

Although quite some microbubbles had a response at the subharmonic frequency, only for the ones shown in Fig. 8.6 a subharmonic resonance curve could be determined. Reasons for not being able to determine the subharmonic resonance curve were not enough points for a fit or the peak was below or above the measuring range. Emitted subharmonic pressures were similar irrespective of binding and the type of lipid coating at each acoustic pressure (Fig. 8.6). At 50 kPa, of the 17 bound DPPC microbubbles shown in Fig. 8.6, nine had a response at T2R (transmit at twice the resonance frequency with $f_{sub} = f_{res}$ [148, 323]) and four at TR (transmit at the resonance frequency, $f_{sub} = \frac{1}{2}f_{res}$ [148, 180]). Of the seven bound DSPC microbubbles, three had a clear response at T2R and none had a response at TR. At 150 kPa, of the eight bound DPPC microbubbles seven had a response at T2R and one at TR. Of the seven bound DSPC microbubbles four had a response at T2R and none at TR. In the case of non-bound microbubbles at 50 kPa the only microbubble responsive at $f_{sub}$ was a DSPC microbubble with a response at T2R. At 150 kPa, one out of the ten DPPC microbubbles had a response at T2R and two out of ten at TR. For the four non-bound DSPC microbubbles two had a response at T2R and none at TR. For the other microbubbles responding at $f_{sub}$, the relation between TR or T2R could not be determined; either because no clear relation was found between the subharmonic and fundamental frequency, or because the fundamental frequency had not been determined since the peak was located outside the measuring range. We assumed a detection limit of 1 Pa (black dashed line in Fig. 8.6) for diagnostic ultrasound scanners, achievable with a typical high-quality transducer for har-

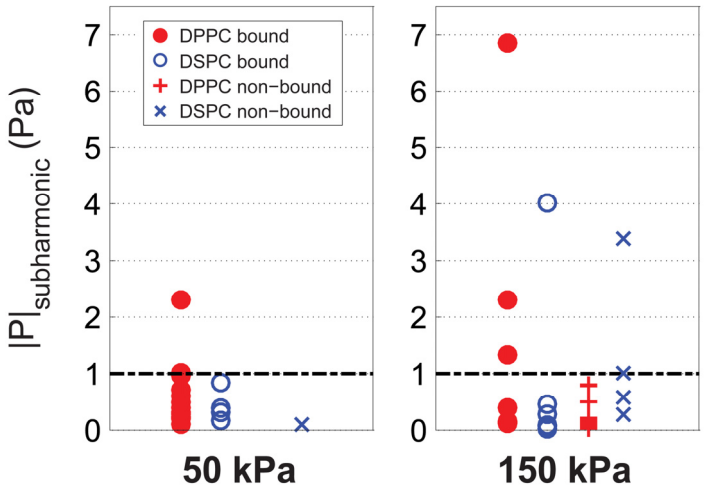


**Fig. 8.6.** Absolute pressures emitted at the subharmonic frequency of bound DPPC (50 kPa: n = 17, 150 kPa: n = 8), bound DSPC microbubbles (50 kPa: n = 7, 150 kPa: n = 7), non-bound DPPC (50 kPa: n = 0, 150 kPa: n = 10), and non-bound DSPC microbubbles (50 kPa: n = 1, 150 kPa: n = 4).

monic imaging [325]. The emitted pressures of the subharmonic responses will therefore be difficult to detect.

At $P_A$ = 50 kPa, about half of both bound DPPC (53%) and bound DSPC (57%) microbubbles responded at the second harmonic frequency. The number of responding non-bound microbubbles based on DPPC was similar (50%), but for non-bound DSPC microbubbles only 1 out of 26 (4%) was responsive at the second harmonic frequency. The number of responsive microbubbles at a driving pressure of 150 kPa increased in all cases: to 14 out of 15 (93%) for bound DPPC microbubbles, 13 out of 18 (72%) for bound DSPC microbubbles, 17 out of 28 (61%) for non-bound DPPC microbubbles, and 8 out of 26 (31%) for non-bound DSPC microbubbles. The median (IQR) pressures emitted at the second harmonic frequency when insonified at 50 kPa were 2.0 (1.0 – 2.6) Pa for bound DSPC microbubbles, hence in the same order as the only non-bound DSPC microbubble (3.1 Pa, Fig. 8.7). For bound DPPC microbubbles, the emitted pressures were 4.1 (2.1 – 12.9) Pa and 2.4 (2.0 – 2.8) Pa for non-bound DPPC microbubbles, which was not significantly different (p = 0.351). In addition, the emitted pressures at the second harmonic frequency of bound DPPC microbubbles were higher than those of bound DSPC microbubbles (p = 0.004). At the higher driving pressure of 150 kPa, the emitted pressures were significantly higher (p = 0.017) for non-bound than bound DSPC microbubbles, with median pressures of 28.5 (14.0 – 38.1) Pa for non-bound and 3.2 (2.4 – 8.4) Pa for bound DSPC microbubbles. The median pressures of the other groups were all similar.

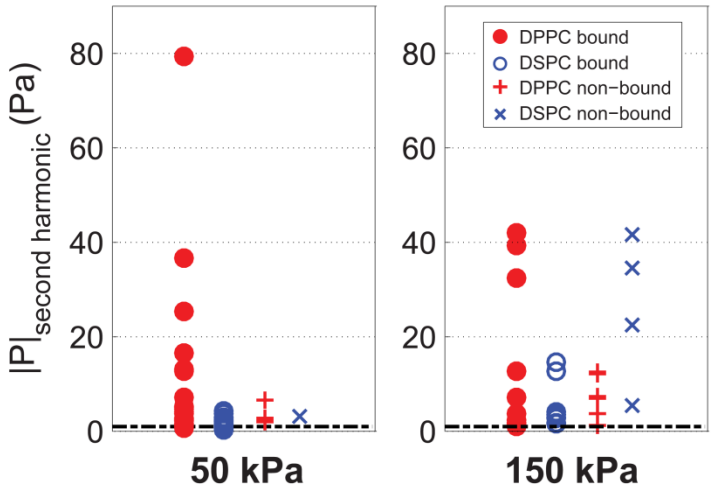


**Fig. 8.7.** Absolute pressures emitted at the second harmonic frequency of bound DPPC (50 kPa: n = 21, 150 kPa: n = 10), bound DSPC microbubbles (50 kPa: n = 19, 150 kPa: n = 8), non-bound DPPC (50 kPa: n = 6, 150 kPa: n = 6), and non-bound DSPC microbubbles (50 kPa: n = 1, 150 kPa: n = 4).

## 8.5. DISCUSSION

This study investigated vibrational responses of bound and non-bound microbubbles to identify differences to acoustically discriminate them. For DPPC-based microbubbles with diameters between 2 and 4 μm the resonance frequencies and relative radial excursions were higher than for non-bound DPPC-based microbubbles (PA = 50 kPa). In contrast, at an insonifying pressure of 150 kPa the relative radial excursions for bound and non-bound DPPC-based microbubbles were similar. Interestingly, at this higher pressure the radial excursions for bound DSPC-based microbubbles were higher than for non-bound DSPC microbubbles, whereas these were similar at 50 kPa. We also found compression-dominated behavior and a higher number of responsive microbubbles at the second harmonic frequency for bound microbubbles, irrespective of the main coating lipid.

### Acoustic stability

Bound microbubbles were acoustically less stable than non-bound microbubbles, irrespective of their main coating component. Further we found that the acoustic stability for DPPC-based microbubbles was lower than that for DSPC-based microbubbles. This was previously attributed to the shorter acyl chain length of the DPPC lipid than that of the DSPC lipid [260]. This shorter chain results in lower intermolecular van der Waals forces between the different lipids and results in less attraction and cohesion of the microbubble shell [49, 260]. The maximum relative radial excursions of bound microbubbles were higher at the resonance frequency than those of non-bound microbubbles (for DPPC at 50 kPa and DSPC at 150 kPa). This means that the radial excursions after binding were more prominent, which resulted in more shrinkage and therefore a lower acoustic stability. Others have reported lower radial excursions after binding for DSPC-based microbubbles [136, 139], but those studies had not covalently linked their model biomarker to their membrane. As a result, the biomarker that attached to the microbubble shell increased the stiffness [262] and therefore limits the radial oscillations.

Some non-bound DSPC microbubbles appeared to increase in diameter after insonification at 150 kPa. The microbubbles in which this was observed were all relatively small (< 2.5 μm). This apparent increase may be due to small changes in optical focus due to radiation forces, in combination with the error in the tracking algorithm which was previously estimated to be approximately 10% [20].

### Linear oscillation behavior

The resonance frequencies for bound DPPC microbubbles were higher than for non-bound DPPC microbubbles at a pressure of 50 kPa for microbubbles with diameters between 2 and 4 μm at resonance. Based on the IQRs, the resonance frequencies of most bound DPPC microbubbles of this size were higher than 1.8 MHz, whereas those of non-bound DPPC

microbubbles were lower than 1.8 MHz. In terms of shell properties, a higher resonance frequency is related to an increase in elasticity (i.e., a stiffer shell) by the Marmottant model [19]. It is not likely that the elasticity changes upon binding, but the apparent stiffness may increase due to binding of the microbubble to the biomarker. We may not have found a change in apparent stiffness for DSPC-based microbubbles, because their surface binding area is smaller than for DPPC-based microbubbles as previously determined by our group for the same type of microbubbles and same streptavidin biomarker [70]. Next, the initial elasticity of DSPC microbubbles is already higher than for DPPC microbubbles [260], and it has been shown that the resonance frequencies for DSPC microbubbles did not change after conjugating the relatively heavy molecule streptavidin to the lipid shell, whereas for DPPC microbubbles the resonance frequencies increased [262]. In addition, the resonance frequency exponentially decreases for increasing microbubble size [274]. As a consequence, the difference in resonance frequencies for microbubbles with diameters between 2 and 4 μm is larger than for microbubbles with diameters between 5 and 7 μm [260]. An increase in resonance frequency for bound microbubbles will therefore be more pronounced for smaller than for larger microbubbles. This may explain why the apparent increase in stiffness was only present for bound DPPC microbubbles having diameters between 2 and 4, and not for DSPC microbubbles or larger DPPC microbubbles. At 150 kPa, however, all resonance frequencies appeared the same. The microbubble oscillations at this pressure start of very violently in the first insonifications between 1 and 1.5 MHz, thereby largely decreasing the microbubble size and shifting its original resonance frequency towards higher frequencies. Since the mechanical index (MI) was ~2× lower for the insonifications at the end of the frequency sweep, the resulting relative radial excursions were lower at the new resonant microbubble size. Therefore, the oscillations of the first insonifcations dominated the resonance behavior, leading to an apparent resonance frequency between 1 and 1.5 MHz before shrinkage.

Others have also reported differences in resonance frequencies between bound and non-bound microbubbles. Casey et al. [141] reported an increase in resonance frequency for their bound in-house produced biotinylated microbubbles, but for DSPC microbubbles ($C_3F_8$ gas core and same components as our DSPC-based microbubbles, but unknown ratios) instead of for DPPC-based microbubbles as we report here. Overvelde et al. [136] found 30% lower frequencies of maximum response for targeted BG-6438 microbubbles bound to an OptiCell wall than for non-targeted BG-6437 microbubbles floating against the wall at pressures < 40 kPa (both bubble types are from Bracco Research S.A., Geneva, Switzerland). The BG-6438 microbubbles were targeted to FITC-BSA using an anti-FITC antibody attached to the microbubble shell using streptavidin-biotin bridging. The main limitation of both studies is the method of attaching the model biomarker streptavidin to the cellulose tube [141] or FITC-BSA to the OptiCell wall [136], namely by physisorption. As mentioned before, this physisorbed biomarker is likely to bind to the microbubble shell creating a lipid-coated mi-

crobubble covered with the model biomarker. These very large and heavy complexes are expected to behave completely different in an ultrasound field than a bare lipid-coated targeted microbubble, as has been shown for microbubbles that were functionalized with streptavidin depending on the initial stiffness of the microbubble coating [262]. In addition to this, Overvelde et al. [136] did not block the OptiCells to prevent unspecific binding in their experiments that compared free BG-6437 microbubbles and BG-6437 microbubbles close to the wall: the latter may have actually bound to the wall. Next to that, the BG-6437 microbubbles did not have anti-FITC antibody attached to their shell, which is not a fair comparison between microbubbles that have bound to the wall and that are floating against the wall. In our present study the covalent coupling of streptavidin to the hydrogel, and thus the membrane, was established and it was confirmed that no streptavidin was present on the microbubble shell [70].

**Nonlinear oscillation behavior**

For nonlinear contrast-enhanced ultrasound imaging the responses at the subharmonic and second harmonic frequencies are usually exploited [161]. At 50 kPa more bound than non-bound microbubbles responded at the subharmonic frequency, for both the DPPC and DSPC-based coatings. At 150 kPa more microbubbles—both bound and non-bound—were responsive at the subharmonic frequency, but the emitted pressures were close to or below the assumed detection limit for clinical use of 1 Pa [325]. The subharmonic emissions seem therefore of limited use for nonlinear contrast-enhanced imaging and discrimination of bound from non-bound microbubble based on our experimental conditions.

We found similar amplitudes at the subharmonic frequency for bound and non-bound microbubbles, in line with findings of Zhao et al. [139] for microbubbles with a coating of 82 mol% DSPC, 9 mol% DSPEPEG(2000), and 9 mol% DSPE-PEG(2000)-biotin [392]. Helfield et al. [142] reported similar amounts of bound and non-bound Target-Ready MicroMarker microbubbles that were responsive at the subharmonic frequency, whereas we found more bound microbubbles that responded. The different composition and gas core of Target-Ready MicroMarker likely contributed to these differences. As suggested by Helfield et al. [142], the membrane material could have frequency-dependent effects and their results might be biased due to aggregation of microbubbles that may have changed the echogenicity [393]. We previously performed the exact same experiments as described here for non-bound microbubbles in an OptiCell [394]. Indeed, a membrane dependent effect was observed, but was not found to be frequency related. The maximum relative radial excursions of non-bound microbubbles in an OptiCell (both DPPC and DSPC) were 2-2.5 times higher than for non-bound microbubbles floating against the hydrogel. Because the microbubbles may be partly embedded in the polymer-based hydrogel, this can damp the microbubble oscillations and therefore result in lower maximum relative radial excursions.

Another difference between our study and that of Helfield et al. [142], is that they coated their cellulose tube with streptavidin using physisorption, with the disadvantage of streptavidin covering the microbubble shell, which may have influenced the amplitude of the subharmonic signal. Indeed, their acoustic measurements showed a 20% higher subharmonic signal of Target-Ready MicroMarker, a streptavidin-functionalized lipid-coated microbubble, when bound to a biotinylated agarose phantom. The difference between the results of Helfield et al. and our results presented in this study might also be due to the used techniques: ultra-high-speed optical imaging versus acoustic measurements. In our set-up we were only able to image the top-view of the microbubble oscillations, whereas acoustic measurements can detect out-of-plane signals as well. If a larger portion of the subharmonic excursions were generated in the perpendicular plane, we might have missed those vibrations with our set-up.

Numerical simulations have shown that the subharmonic signal is optimal when the microbubble is insonified at T2R [395]. Experimental validation showed that the threshold for generating TR subharmonic responses is higher than that for T2R subharmonic responses in lipid-coated microbubbles [148, 181]. The absence of DSPC responders at TR may suggest that the threshold for generating TR subharmonic responses is lower for DPPC microbubbles than for DSPC microbubbles, irrespective of them being bound or not. On the other hand, due to the applied frequency range and studied microbubble sizes the majority of the resonance frequencies were between 1.5 and 3.5 MHz, which limits the possibility to insonify microbubbles at T2R within the frequency range we applied.

The higher second harmonic amplitudes we measured for non-bound DSPC-based microbubbles at 150 kPa are in contrast with results reported by others [140, 141]. The study by Casey et al. [141] used microbubbles similar to our DSPC microbubbles, but with a $C_3F_8$ core and attachment to a capillary wall using the physisorbed streptavidin as biomarker ($f_T$ = 2 MHz, $P_A$ = 90 kPa). The study by Zhao et al. [140] also used DSPC-based microbubbles, with a set-up and parameters comparable to those of Casey et al. [141]. Both studies used somewhat lower pressures, but may also have effectively studied bound targeted DSPC-based microbubbles coated with a streptavidin layer, which may explain the different findings. In our study, the emitted pressure amplitudes of bound microbubbles were similar or lower than for non-bound microbubbles and acoustic discrimination based on the second harmonic pressures does therefore not seem feasible.

**DSPC vs DPPC for ultrasound molecular imaging applications**

The differences between bound targeted DPPC and DSPC-based microbubbles were not as pronounced as we expected from the differences in shape change upon adherence and their surface binding areas, as previously determined by our group for the same type of microbubbles and same streptavidin biomarker [70]. The most prominent differences we did find were higher acoustic stability for non-bound microbubbles, higher resonance fre-

quencies (for DPPC microbubbles with diameters between 2 and 4 μm) and radial excursions for bound DPPC microbubbles at 50 kPa, and higher amplitudes at the second harmonic frequency for non-bound DSPC microbubbles than for bound DSPC microbubbles at 150 kPa. The lower resonance frequencies for DPPC microbubbles than for DSPC microbubbles were already observed for non-bound DPPC microbubbles [260], and were thus maintained upon binding.

For *in vivo* ultrasound molecular imaging the ideal targeted microbubble: *1)* can effectively bind to the biomarker of interest; *2)* persists binding to the biomarker after initial binding, i.e. the binding strength is larger than the shear stress induced by the flowing blood; *3)* is stable during the course of the ultrasound examination; *4)* nonlinearly scatters ultrasound that is microbubble specific; *5)* can be discriminated acoustically from non-bound microbubbles; *6)* has the same resonance frequency as the other microbubbles that are injected, i.e., all microbubbles in the population respond in the same way to ultrasound. Concerning the first two points, Kooiman et al [70] favored targeted DPPC microbubbles over DSPC microbubbles because of their larger surface binding area to a streptavidin-coated membrane, their dome shape after binding, and a more homogeneous distribution of fluorescently labeled ligands attached to DSPE-PEG(2000). The more homogeneous lipid distribution might aid the initial attachment, whereas the larger binding area and difference in shape might be able to better sustain blood shear forces. However, binding of the microbubbles was performed under static conditions and experiments in the presence of flow are needed to verify which of the two microbubble types binds best under flow. Based on the acoustic stability (*point 3*), DSPC-based microbubbles are favored over DPPC-based microbubbles. This also means that the size is better maintained during insonification and the resonance frequency will therefore be more consistent throughout the investigation. In terms of nonlinear scattering of ultrasound (*point 4*), the maximum relative radial excursions at the subharmonic frequency for both our DPPC and DSPC microbubbles resulted in ~20 dB lower scattered pressures than the second harmonic responses. The subharmonic responses were too low and unpredictable to discriminate bound from non-bound microbubbles. In contrast, the responses at the second harmonic frequency were sufficiently high to be detected, but amplitudes were similar for bound and non-bound microbubbles, or higher for the non-bound ones in terms of DSPC-based microbubbles (*point 5*). At 50 kPa, bound and non-bound DPPC microbubbles with diameters between 2 and 4 μm at resonance could be separated based on their resonance frequencies: bound DPPC microbubbles had resonance frequencies above 1.8 MHz, whereas those were significantly lower for non-bound DPPC microbubbles. Lastly (*point 6*), as mentioned in the introduction one of the main challenges for successful translation of ultrasound molecular imaging to the clinic is the production of microbubble populations that have the same acoustic signature. Both the DPPC and DSPC-based microbubbles can have different resonance frequencies and radial excursions although their sizes are similar. Several studies showed that monodisperse lipid-

coated microbubble distributions can be produced using flow-focusing devices [385, 396-398]. Talu et al. [398] and Kaya et al. [397] studied the difference between echo amplitudes of these monodisperse single microbubbles when insonified at a frequency close to resonance, and found a lower standard deviation than for polydisperse microbubbles. Segers and Versluis [399] developed an acoustic sorting chip that separated monodisperse microbubbles based on the radiation force they experienced, which resulted in an overall contrast enrichment of more than 10 dB. This is an important step towards improving the quality of *in vivo* ultrasound molecular imaging, especially if microbubbles with low shell elasticity and a diameter between 2 and 4 μm can be produced to distinguish bound from non-bound microbubbles, as shown in our study. However, this approach is still limited to specific microbubble compositions that can be produced monodispersely by means of flow-focusing devices.

Summing up all the aforementioned similarities, differences, advantages, and disadvantages of DPPC and DSPC-based microbubbles, this results in a favor for DSPC-based microbubbles for ultrasound molecular imaging solely based on a higher acoustic stability. Studying the adherence of the microbubbles under flow should reveal whether the heterogeneous lipid distribution in the DSPC shell hinders binding. On the other hand, bound DPPC microbubbles (diameters between 2 and 4 μm) at 50 kPa had resonance frequencies higher than 1.8 MHz, whereas those of non-bound DPPC microbubbles were lower than 1.8 MHz. In addition, the relative radial excursions of bound DPPC microbubbles were also higher. When monodisperse DPPC microbubbles with a diameter between 2 and 4 μm are produced, these could acoustically be discriminated based on their resonance frequency.

**Limitations and outlook**

Although we aimed to create a more *in vivo*-like set-up using covalent biomarker binding versus physisorption, the membrane we used in our experiments was still artificial. The 1-2 μm thick hydrogel created a softer layer between the microbubble and the polyester membrane, but to have a real *in vivo*-like membrane one would need to develop a material with exactly the same stiffness, viscosity, etc. to an actual cell layer or perform *in vivo* experiments. In addition, *in vivo* one can also study microbubble vibration when microbubbles are in contact with cells and under flow, for which the chorioallantoic membrane model could be used. This model has proven to be useful to study non-targeted microbubble vibration using ultra-high-speed imaging and targeted-microbubble mediated drug delivery [233, 342].

For *in vivo* ultrasound molecular imaging multiple microbubbles may bind in closer range with each other than investigated in the present study. However, the binding range actually depends on the availability of the biomarker on the cell surface, which depends both on the cell type and the biomarker of interest. When the interbubble distance is ≤ 10 μm, this will cause interaction of the bubbles in terms of secondary Bjerknes forces, and due to the secondary Bjerknes forces a bubble will deform in the direction of their neighboring bubble

[123]. Next to that, two similar sized bubbles that are close to each other result in a shift in resonance frequency and therefore a decrease in maximum relative radial excursions [124]. As a consequence, for abundant biomarkers on the cell membrane these observations may counteract the increase in resonance frequency and maximum relative radial excursions we observed for DPPC microbubbles between 2 and 4 μm at 50 kPa. This, however, should first be experimentally verified using a setup comprising of a biomarker distribution that is comparable to the *in vivo* situation. The chorioallantoic model would be a good approach to study this.

## 8.6. CONCLUSION

This study shows that binding of in-house produced DPPC-based microbubbles to a streptavidin-coated surface increased the resonance frequencies (for microbubbles with diameters between 2 and 4 μm) and the corresponding relative radial excursions at relatively low pressure (50 kPa). At this pressure, the bound 2 to 4 μm microbubbles resonated above 1.8 MHz, whereas the non-bound 2 to 4 μm DPPC microbubbles were resonant below this frequency. At higher pressure (150 kPa) this difference did not persist. No differences in resonance frequency were observed between bound and non-bound DSPC microbubbles. In terms of non-linear responses, only the responses at the second harmonic frequency of bound DSPC microbubbles at 150 kPa were lower than of non-bound DSPC microbubbles. Our in-house produced DPPC-based microbubbles were acoustically less stable than our DSPC-based microbubbles, which is the major advantage of this type of microbubble for ultrasound molecular imaging applications.

**Acknowledgements**

The authors thank Robert Beurskens, Frits Mastik, Michiel Manten, and Geert Springeling for technical assistance, Dr. Tom Kokhuis for valuable discussions (all from the Dept. of Biomedical Engineering, Thorax Center, Erasmus MC), and Dr. Jason L. Raymond for experimental assistance (visiting fellow Whitaker program). We also thank Ihsan Chrifi from the Dept. of Experimental Cardiology, Thorax Center, Erasmus MC, for the spectrophotometer measurements, and Dr. E. Gedig from XanTec bioanalytics GmbH, Germany, for discussions about the covalent coating of streptavidin to the polyester membranes. The authors are grateful to Prof. Dr. A.L. Klibanov from the University of Virginia, Cardiovascular Division, Charlottesville, Virginia, USA for discussions about the microbubble preparation.

Chapter 9

# Viability of endothelial cells after ultrasound-mediated sonoporation: Influence of targeting, oscillation, and displacement of microbubbles

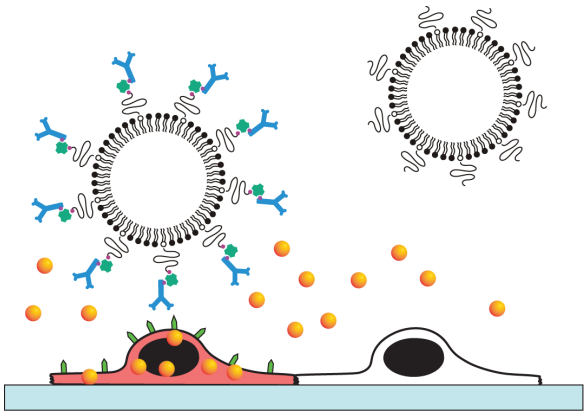

Tom van Rooij, Ilya Skachkov, Inés Beekers, Kirby R. Lattwein, Jason D. Voorneveld, Tom J.A. Kokhuis, Deep Bera, Ying Luan, Antonius F.W. van der Steen, Nico de Jong, Klazina Kooiman

*Journal of Controlled Release*, 238, 197–211 (2016)

## 9.1. ABSTRACT

Microbubbles (MBs) have been shown to create transient or lethal pores in cell membranes under the influence of ultrasound, known as ultrasound-mediated sonoporation. Several studies have reported enhanced drug delivery or local cell death induced by MBs that are either targeted to a specific biomarker (targeted microbubbles, tMBs) or that are not targeted (non-targeted microbubbles, ntMBs). However, both the exact mechanism and the optimal acoustic settings for sonoporation are still unknown. In this study we used real-time uptake patterns of propidium iodide, a fluorescent cell impermeable model drug, as a measure for sonoporation. Combined with high-speed optical recordings of MB displacement and ultra-high-speed recordings of MB oscillation, we aimed to identify differences in MB behavior responsible for either viable sonoporation or cell death. We compared ntMBs and tMBs with identical shell compositions exposed to long acoustic pulses (500-50,000 cycles) at various pressures (150-500 kPa).

Propidium iodide uptake highly correlated with cell viability; when the fluorescence intensity still increased 120 s after opening of the pore, this resulted in cell death. Higher acoustic pressures and longer cycles resulted in more displacing MBs and enhanced sonoporation. Non-displacing MBs were found to be the main contributor to cell death, while displacement of tMBs enhanced reversible sonoporation and preserved cell viability. Consequently, each therapeutic application requires different settings: non-displacing ntMBs or tMBs are advantageous for therapies requiring cell death, especially at 500 kPa and 50,000 cycles, whereas short acoustic pulses causing limited displacement should be used for drug delivery.

## 9.2. INTRODUCTION

Microbubbles (MBs) are ultrasound (US) contrast agents that consist of gas bubbles with diameters between 1 and 10 μm, which are encapsulated by a stabilizing coating. Non-targeted microbubbles (ntMBs) are clinically used as blood pool agents for contrast-enhanced US imaging in cardiology and radiology [32, 313] and also have therapeutic potential [45, 296]. Targeted microbubbles (tMBs) are promising agents for US molecular imaging and therapy; in particular for diseases that can alter the endothelium, such as cancer and inflammation. The tMBs can adhere to specific disease-associated intravascular biomarkers by the addition of targeting ligands to the MB coating [31, 262].

When MBs are insonified by US, they oscillate due to the acoustic pressure wave [45]. Oscillating MBs can increase cell membrane permeability to facilitate intracellular drug uptake (sonoporation), stimulate endocytosis, and open cell-cell junctions [36, 45]. Although the exact mechanisms of MB-mediated drug uptake still remain unknown, many studies have attempted to pinpoint the US settings that best stimulate intracellular drug uptake [45, 400]. So far the key findings are: *1)* cell membrane pores induced by oscillating

MBs can be reversible or irreversible [38]; *2)* a MB has to oscillate with sufficient amplitude to induce sonoporation [35]; *3)* tMBs stimulate drug uptake better than ntMBs both *in vitro* [232, 234, 235, 238, 239] and *in vivo* [236, 237, 240, 241]. Recently, it has also been shown that the cell membrane pore size and pore resealing coefficient can be mathematically obtained from real-time observed MB-mediated intracellular drug uptake [34].

While reversible sonoporation likely facilitates cellular drug uptake without causing lethal damage to the cell, irreversible sonoporation is thought to lead to significant cell damage and eventually cell death. Different therapeutic approaches may require reversible or irreversible sonoporation, and a balance is expected between therapeutic effectiveness and cell damage. Hu et al. [38] revealed the size of the created cell membrane pore to be a predictor for reversible or irreversible sonoporation: pores < 30 $\mu m^2$ successfully resealed within 1 min after insonification, while pores > 100 $\mu m^2$ had not resealed within 30 min. An established method to study drug uptake by sonoporation relies on the intracellular uptake of the model drug propidium iodide (PI) [34, 35, 37, 233, 401], because this molecule can only pass the cell membrane of a live cell when it has been disrupted. After entering the cell it binds to DNA and RNA and becomes fluorescent [402]. Fan et al. [34] showed that intracellular PI fluorescence intensity directly relates to the amount of PI-DNA and PI-RNA complexes that have formed in the cell. They proposed a model to relate intracellular fluorescence intensity to the size of the created pore and its resealing time, which corresponded well with their experimental *in vitro* results on kidney [34] and endothelial cells [403].

For MB-mediated drug uptake, MB dynamics also have to be considered. The frequency generally used for MB-mediated drug delivery is 1 MHz [45], which means that the MBs oscillate one million times per second. These MB oscillations can only be resolved using an ultra-high-speed camera, capable of recording at least two million frames per second (Mfps) to satisfy the Nyquist sampling criterion [404]. While our group used ultra-high-speed recordings to determine that the relative oscillation amplitude of tMBs had to be above 50% to successfully sonoporate a cell [35] (6× 10 cycles at 1 MHz and 80-200 kPa peak negative acoustic pressure), others used high-speed cameras (in the order of a few thousand fps) to reveal that MB displacement is an important contributor to sonoporation-mediated cell death (1.25 MHz, 60-600 kPa, pulse repetition frequency (PRF) 10-1000 kHz, duty cycles 0.016-20%) [405]. MBs displace due to acoustic radiation forces, especially when longer acoustic pulses are used [81, 406]. Long acoustic pulses have sparsely been used in MB-mediated drug delivery studies [40, 407-409], even though one of these studies reported that 7,000 cycles resulted in significantly more luciferase activity than 1,000 and 5,000 cycles in endothelial cells *in vitro* (2.25 MHz, 330 kPa, PRF 20 Hz, 120 s treatment) [40]. On the other hand, no significant differences between 1,000, 5,000, and 10,000 cycles were observed; different US pulse lengths thus affected luciferase activity. So far, in depth sonoporation studies on the effect of longer acoustic pulses at different acoustic pressures

are lacking, as is the relation between MB oscillation and sonoporation efficiency. In addition, the effect of the same type of ntMBs and tMBs on endothelial cells has never been directly compared *in vitro*. All prior studies comparing ntMBs and tMBs were performed on cancer [232, 235, 238, 239] and smooth muscle cells [234], despite that MBs are primarily in contact with endothelial cells when injected intravenously [31, 45].

In this study we used long US pulses (500-50,000 cycles) at various pressures (150-500 kPa) to investigate how these settings affect US-mediated endothelial cell membrane permeability and cell death. In order to properly compare ntMBs and tMBs, we used home-made MBs with identical shell compositions to investigate their effect. The real-time observed PI uptake patterns were fit to the previously proposed diffusion model of Fan et al. [34] and additional Principal Component Analysis was used to determine whether cells were reversibly or irreversibly damaged. In combination with high-speed optical recordings of MB displacement and ultra-high-speed recordings of MB oscillation, we aimed to identify MB behavior responsible for viable sonoporation or cell death.

## 9.3. MATERIALS AND METHODS

### Microbubble preparation

Lipid-coated MBs with a $C_4F_{10}$ gas core (F2 Chemicals, Preston, UK) were made by sonication as described previously [129, 233]. The coating of the non-targeted MBs (ntMBs) consisted of 1,2-distearoyl-*sn*-glycero-3-phosphocholine (DSPC; 59.4 mol%; P6517; Sigma-Aldrich, Zwijndrecht, the Netherlands), polyoxyethylene-(40)-stearate (PEG-40 stearate; 35.7 mol%; P3440; Sigma-Aldrich), and 1,2-distearoyl-*sn*-glycero-3-phosphoethanolamine-N-carboxy(polyethylene glycol) (DSPE-PEG(2000); MW 2000; 4.9 mol%; 880125P; Avanti Polar Lipids, Alabaster, AL, USA). Before the experiment, the ntMBs were washed three times using centrifugation for 1 min at 400 *g*. After washing the ntMBs, the size distribution and concentration were measured using a Coulter Counter (n = 3; Multisizer 3; Beckman Coulter, Mijdrecht, the Netherlands). The mean (± standard deviation, SD) diameter of the ntMB was 2.54 (± 0.02) µm.

The same components were used for the targeted MBs (tMBs), except 0.8% of DSPE-PEG(2000) was replaced with DSPE-PEG(2000)-biotin (MW2000; 880129C; Avanti Polar Lipids). This allows for adding targeting moieties to the MBs via biotin-streptavidin bridging as previously described [132, 233]. Briefly, after three washing steps by centrifugation at 400 *g* for 1 min, the concentration of the MBs was measured using a Coulter Counter (n = 3) and 1 x $10^9$ biotinylated MBs were incubated with 20 µg of streptavidin (S4762; Sigma-Aldrich) on ice for 30 min. Following incubation, the streptavidin-conjugated MBs were washed once to remove non-bound streptavidin. Next, 5 µg of biotinylated anti-human CD31-antibody (BAM3567; R&D Systems, Abingdon, United Kingdom) were conjugated to the MB shell, during incubation for 30 min on ice. Following this, tMBs were washed once to

remove non-bound antibodies. Directly afterwards the size distribution and concentrations were measured using a Coulter Counter (n = 3) and mean (± SD) diameter for the tMBs was 2.82 (± 0.09) µm.

**Endothelial cell culture**

Human umbilical vein endothelial cells (HUVECs; C2519A; Lonza, Verviers, Belgium) were cultured in EGM-2 medium (CC-3162; Lonza) in T-75 flasks (353136; BD Falcon Fisher Scientific, Breda, the Netherlands), and maintained in a humidified incubator under standard conditions (37 °C, 5% $CO_2$). Thereafter the cells were trypsinized using trypsin in EDTA (CC-5012; Lonza) and replated on one side of an OptiCell™ (Thermo Scientific, NUNC GmbH & Co, Wiesbaden, Germany). Experiments were performed two days later with 100% confluence of HUVECs in the OptiCell.

**Experimental set-up**

For visualization of the MBs and HUVECs, the microscopic set-up consisted of a fluorescence microscope (Olympus, Zoeterwoude, the Netherlands) equipped with a 5× objective (LMPlanFl 5X, NA 0.13, Olympus) for the sonoporation and cell viability assays or a 40× objective (LUMPlanFl 40XW, NA 0.80, water immersion, Olympus) to capture MB behavior. For bright field imaging the sample was illuminated from below via a light fiber using a continuous light source and for fluorescence imaging a mercury lamp and a suitable set of fluorescent filters were used for the detection of propidium iodide (U-MWG2 filter, Olympus), Hoechst 33342 (U-MWU2 filter, Olympus), and calcein (U-MWIB2, Olympus). On top of the microscope three different cameras were mounted: *1)* a high sensitivity CCD camera (AxioCam MRc, Carl Zeiss, Germany) for fluorescence imaging, *2)* a high-speed Redlake Motion Pro Camera (10K, San Diego, CA, USA), and *3)* the ultra-high-speed Brandaris 128 camera [52]. The experimental set-up is illustrated in Fig. 9.1.

For the acoustical set-up, a 1 MHz single-element, focused transducer (focal distance 75 mm; V303; Panametrics-NDTTM, Olympus NDT, Waltham, MA, USA) was mounted in the water bath at a 45° angle below the sample (Fig. 9.1). Each OptiCell was divided into eight equally sized, acoustically non-overlapping sections (19 × 33 mm each; for schematic see Fig. 9.1), which covered the beam area (-6 dB beam width of 6.5 mm) at the focus of the transducer, as verified in advance with a calibrated 0.2 mm PVDF needle hydrophone (Precision Acoustics Ltd, Dorchester, UK). The acoustic focus was aligned with the optic focus.

During the experiment, the position of the OptiCell was adjusted to place the center of each subsection in the focal zone. The sample was insonified by a single Gaussian tapered sine wave burst generated by an arbitrary waveform generator (33220A, Agilent, Palo Alto, CA, USA) and amplified using a broadband amplifier (ENI A-500, Electronics & Innovation, Rochester, NY, USA). The peak negative acoustic pressure of the US burst (150, 300, or

500 kPa) was kept constant for the entire OptiCell, whereas the number of cycles in the single US burst (500; 1,000; 2,000; 5,000; 10,000; 20,000; and 50,000) varied per OptiCell subsection (Fig. 9.1). For each Opticell one of the subsections was used as a control where no US was applied.

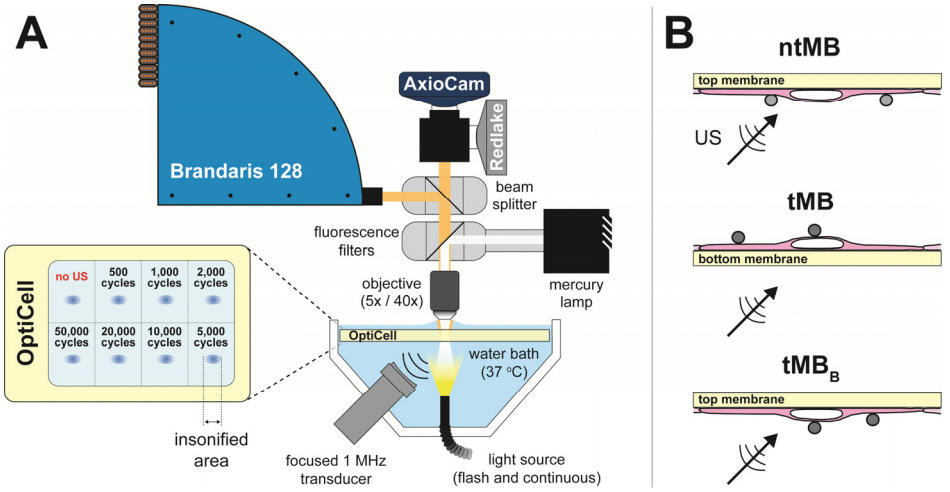


**Fig. 9.1.** Experimental set-up. **(A)** Illustration of the optical imaging systems combined with the acoustical set-up. Brandaris 128 is the ultra-high-speed camera, Redlake the high-speed camera, and AxioCam the fluorescence and bright field CCD camera. The enlarged OptiCell shows the insonification scheme. **(B)** Orientation of the microbubbles (MBs) with respect to the cells and the direction of ultrasound (US) insonification. Non-targeted MBs (ntMBs) were floating against the cells, targeted MBs (tMBs) were adhered on top of the cells, or tMBs adhered below the cells ($tMB_B$), similar to the ntMB orientation.

### Time-lapse sonoporation assay

The time-lapse sonoporation assay was used to monitor sonoporation over time for the different US pressures and number of cycles and is illustrated in Fig. 9.2. First, calcein-AM (C3100MP; Invitrogen; prepared in DMSO (Sigma-Aldrich)) was added to the HUVECs in the OptiCell in a final concentration of 0.25 µg/mL. We used calcein-AM as a live-cell stain as it passively crosses into cellular membranes, has high cell retention, and is only converted to fluorescent calcein in living cells [410]. After 30 min of incubation (37 °C, 5% $CO_2$) of the HUVECs with calcein-AM, we added propidium iodide (PI; final concentration 25 µg/mL; P-4864; Sigma-Aldrich) and Hoechst 33342 (final concentration 5 µg/mL; H3570; Invitrogen, Breda, the Netherlands) to the OptiCell. PI, which is live cell-impermeable, was used to determine the presence and intensity of sonoporation, or disruption of cell membranes, since it only becomes fluorescent when bound to DNA and RNA inside cells [402]. The Hoechst 33342 fluorescent dye was used to stain the nuclei of living and dead HUVECs, as it

rapidly diffuses into all cells, binds specifically and quantitatively to DNA, and has low toxicity to viable cells [411]. Since Hoechst is a nonintercalating dye which binds to the minor groove of DNA [412] and PI binds to DNA and RNA by intercalating between the bases [413], no competition between both dyes is expected.

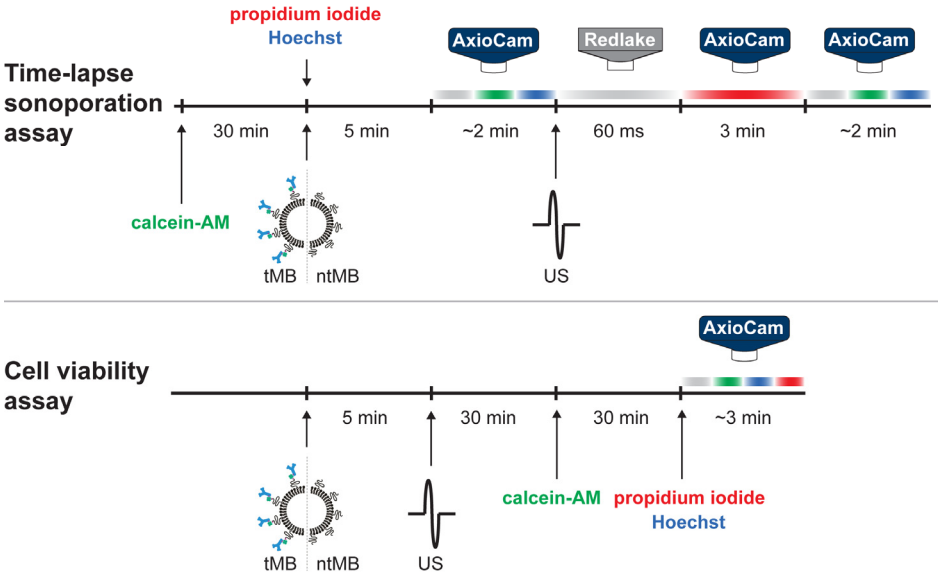


**Fig. 9.2.** Procedural time line (not to scale) for the time-lapse sonoporation and cell viability assays. Arrows indicate when fluorescence dyes or MBs were added, or when US was applied. The cameras show which imaging system was used and the colored bars indicate the type of imaging: bright field (grey), calcein (green), Hoechst (blue), or propidium iodide (red).

At the same time as PI and Hoechst, ~$10^7$ MBs were added to the OptiCell to obtain a ratio of 1-2 MBs per cell. After mixing, we incubated the OptiCell for 5 min at 37 °C, with the cells on the top membrane. This allowed for the MBs to float up and the tMBs to adhere to the cells. The OptiCell was then placed in a 37 °C water bath (Fig. 9.1). For the experiments using tMBs, the OptiCell was placed with the cells on the bottom membrane, so any non-adhered MBs would float away from the cell surface, whereas the OptiCell for the ntMB experiments was placed with the cells on the top membrane to ensure that the ntMBs were floating against the cell membranes. To investigate whether the difference in orientation of tMBs influenced sonoporation outcome, we also performed experiments on tMBs located below the cells ($tMB_B$). The AxioCam was used to take snapshots in bright field (indicated by the gray bar in Fig. 9.2), and of the fluorescent signals of calcein (green) and Hoechst (blue). Just before US exposure, the Redlake camera was started and ran for 60 ms to completely cover the full US exposure. Consequently, this camera recorded more frames after

insonification for the shorter pulses than for the longest pulse. The Redlake camera recorded the MB displacement and clustering at 2,000 frames per second (fps). After these 60 ms, the AxioCam recorded the fluorescence intensity change over time for 3 min (1.5 s exposure and 5 s time intervals) caused by cellular PI uptake after US application. At the end of the protocol, snapshots in bright field and of calcein and Hoechst signal were taken for comparison with the initial situation. This procedure was repeated for each subsection and the experiment was performed in triplicate.

**Cell viability assay**

For each US setting, cell viability was determined as shown in Fig. 9.2. The same amount of MBs as described in the previous section (~$10^7$) were added to the OptiCell and left in the incubator (37 °C) for 5 min. Within 3 to 4 min after the US treatment of all eight subsections of the OptiCell, HUVECs were incubated at 37 °C, 5% $CO_2$. Thirty minutes after the US treatment, calcein-AM was added to the OptiCell and incubated for another 30 min under the same conditions. After the final incubation, PI and Hoechst were added to the Opticell. This procedure was followed directly with bright field and fluorescent (calcein, Hoechst, and PI) microscopic examination using the AxioCam (Fig. 9.2). For each condition, five different fields of view were acquired within a 6 mm circle around the center of the insonified area. All experiments were done in triplicate.

**Oscillatory behavior of microbubbles**

To relate MB behavior to sonoporation, high imaging speeds in the range of a few million frames per second (Mfps) are required. Since these high speeds cannot be achieved using the Redlake camera, we used the Brandaris 128 ultra-high-speed camera [52] in segmented mode [320]. The protocol was similar to the time-lapse sonoporation assay, but the Redlake camera was replaced by the Brandaris 128 camera. The segmented mode of the Brandaris 128 allows for optical recording of long US pulses by dividing the CCD sensor arc into four segments. During each exposure all four segments were illuminated, however only one segment was triggered to transfer the data to the buffer channel. These triggered transfers from the consecutive segments were equally spaced over the time span of the applied US pulse. The start of the acquisition was triggered at a frame rate of 3.85 Mfps, resulting in a corresponding intersegment time of ~328 µs. During one US pulse a full recording then captured four equally spaced movies of ~8 µs in bright field using a Xenon flash source (MVS-7010, Perkin-Elmer Optoelectronics, Wiesbaden, Germany). These settings resulted in a total acquisition time of 1017 µs. The recording time of the ultra-high-speed movies was a few µs longer than the US pulse to ensure that the start and end of the MB oscillations were fully captured. MB behavior was recorded for both tMBs and ntMBs, at 1,000 cycles for pressures of 150 and 300 kPa. The number of cycles was limited to 1,000 cycles (i.e. 1 ms duration), because the Xenon flash duration could not be extended.

**Analysis of fluorescence images**

All images acquired with the Axiocam (bright field and fluorescence) were analyzed using a custom-built plugin for ImageJ [414]. To segment the nuclei, first a composite image of the Hoechst image after insonification and the final PI image was produced, to ensure clear visibility of all nuclei. We chose to use the Hoechst image after insonification, since less cell displacement was expected between this image and the first PI image. The composite image was thresholded using the method of Otsu [415], resulting in a binary image with white nuclei on a black background. A mask of this image was created and watershedding was applied to separate overlapping nuclei. The watershedding algorithm calculates the centers of the nuclei and dilates them until touching another dilated boundary or a white pixel. At the meeting point, a watershed line is drawn. Using the Analyze Particles function, the nuclei and the area of the nuclei were located and stored in the ROI manager. The center of the nuclei was found using the Find Maxima function, added to the ROI manager, and copied to a blank image. Next, the cell borders were automatically segmented using Voronoi tessellation [416] which is a built-in option in the Find Maxima function. Voronoi tessellation is based on the theory that every point $p$ has a distance to another point $q$ that is less than or equal to its distance to any other point $r$. The lines in a Voronoi diagram are thus equidistant to two points in space (i.e., the cell nuclei) and correspond to the most likely position of the cell boundaries. The resulting Voronoi segmentation was transformed into a mask and stored in the ROI manager. The ROI manager now contained the center of each nucleus, the area of each nucleus, and the cell borders.

For assessing cell death using the cell viability assay, the number of cells that showed PI uptake on the images without the application of US was analyzed as described above. Next, the number of cells that had taken up PI after receiving US was normalized to the number of cells that had taken up PI in the control sections, to correct for cells that were already dead when the experiment started.

For assessing the dynamic uptake of PI after sonoporation the segmented nuclei and cell borders were overlaid on every frame of the PI fluorescence time-lapse recording after the application of US. The mean signal intensity of PI for each nucleus and each cell was obtained frame by frame. The nuclear PI uptake was used for further analysis because the segmentation of the nuclei was based on intensity thresholding of Hoechst stained nuclei, which is more accurate than the segmentation of cell borders that is based on the highest probability of a cell border being present.

**PI model fit and data classification**

The temporal PI intensity values in the nuclei were loaded into RStudio (RStudio, Inc., Boston, MA, USA) for further quantification of sonoporation. Fan et al. [34] derived Eq. (9.1)

to model sonoporation dynamics of a single cell, based on the resealing of the created pore and the diffusion rate of PI into the cell.

$$F(t) = \alpha \cdot \pi D C_o \cdot r_o \cdot \frac{1}{\beta}\left(1 - e^{-\beta t}\right) \tag{9.1}$$

In Eq. (9.1), $F(t)$ is the fluorescence intensity as a function of time, $\alpha$ is a coefficient that relates the amount of PI molecules to the fluorescence intensity of PI-DNA and PI-RNA. This coefficient is determined by the sensitivity of the fluorescence imaging system. The other parameters are the diffusion coefficient of PI, $D$, the extracellular PI concentration, $C_o$, the initial radius of the pore, $r_o$, the pore resealing coefficient, $\beta$, and time, $t$. The pore size coefficient, $\alpha \cdot \pi \cdot D \cdot C_o \cdot r_o$, determines the initial slope of the PI uptake pattern and is the scaling factor for the exponential increase. Therefore, a steep initial slope corresponds to a larger pore size. The overall slope follows $F(t) = (\alpha \cdot \pi D C_0 \cdot r_o) \cdot e^{-\beta t}$, in which the pore resealing coefficient $\beta$ is the time constant that determines the time to reach the asymptotic value of the maximum PI intensity. This asymptotic maximal PI intensity value is given by the inverse relationship between the pore size and pore resealing coefficients (Eq. (9.2)). Therefore a cell with a high pore resealing coefficient quickly reaches the asymptotic value, resulting from quick resealing of the pore.

$$F(\infty) = \frac{\alpha \cdot \pi D C_o \cdot r_o}{\beta} \tag{9.2}$$

To obtain the pore size coefficient, $\alpha \cdot \pi \cdot D \cdot C_o \cdot r_o$, and the pore resealing coefficient, $\beta$, the PI intensities recorded in the time-lapse sonoporation assay were fit to Eq. (9.1) using a nonlinear least-squares approach. Classification, based on the distributions of both coefficients, was performed using Principal Component Analysis (PCA) [417, 418] on the complete data set (all settings, both ntMB and tMB). We chose PCA because this method captures as much of the variation in the data as possible by computing eigenvectors (for determining the direction in which the data has largest variance) and corresponding eigenvalues (to determine how much variance there is in the data in that direction). The principal components (PCs) are uncorrelated with each other since the eigenvectors are perpendicular to each other. In this data set we chose two PCs because we only used the pore size coefficients and pore resealing coefficients to fit the data to Eq. (9.1). Classification thresholding was applied on the PC with the largest variance, separating the complete data set in two groups. Using these PCs, the cell populations at each different setting were classified. Based on Eq. (9.1), two additional thresholds were chosen to classify the cells that were most likely irreversibly damaged based on very low pore resealing coefficients. In these cells, PI intensities still increased at the end of the time-lapse

sonoporation assay (i.e. at 180 s), or > 120 s. Because pores remaining open for more than 1 min would not close [38], we assumed these pores to most likely result in cell death.

**Displacement of microbubbles**

Tracking of displacing MBs was implemented in Python™ (v2.7, Python Software Foundation). The recordings on which the tracking was performed were obtained with the Redlake camera and had an isotropic spatial resolution of 0.63 µm/pixel. Gaussian Mixture-based background subtraction [419] was applied to remove all but the displacing MBs from each frame. This was required to correct for illumination fluctuations among the frames and in different regions of the image, which hindered accurate MB tracking. The remaining MBs were tracked using Trackpy [420], an open source blob tracking algorithm, to obtain the trajectory of each displacing MB.

To differentiate between sonoporation due to displacing or non-displacing MBs, the latter were segmented from the AxioCam bright field images before US application. Since the FOV of the Redlake camera was smaller than that of the AxioCam, only the part of the FOV that overlapped was analyzed. We used the Laplacian of Gaussian (LoG) blob detection algorithm (scikit-image [421]); this algorithm convolves Gaussian kernels of a range of standard deviations with an image. In this way it determines the centroid and diameter of non-displacing MBs, approximated by the standard deviation of the corresponding Gaussian kernel. In order to detect most MBs, their diameters were limited to a range between 1.7 and 5.0 µm, and a 20% overlap was allowed to properly deal with clusters and focal differences.

After locating the displacing and non-displacing MBs, their effect on cellular PI uptake was assessed. For segmentation of the nuclei from the Hoechst images, we also used the LoG blob detection algorithm, which performed best when the range to detect nuclei was limited between 5.0 and 6.7 µm in diameter, and overlapping at most 20%, to separate nuclei with seemingly overlapping borders. Centroids of the segmented cell nuclei were used as seeding points for cell border segmentation using Voronoi tessellation. For segmenting regions with PI uptake in the initial and final frame of the PI stained image sequences, the LoG blob detection algorithm was limited to diameters between 5.0 and 8.3 µm, and allowed 25% overlap. More overlap and larger regions were allowed than for nuclei segmentation since PI can also stain the cytoplasm by binding to RNA. Regions in which PI uptake was detected in both the first and last frame were neglected, because these cells had already taken up PI before US application. Cells were defined as sonoporated when 70% of their equivalent circular diameter overlapped with a region showing PI uptake. This percentage was used to compensate for the overestimation of cellular diameters due to odd shaped cells, e.g. rectangular shaped cells. If a cell's equivalent diameter intersected with 1.25 times a MB diameter (to account for MB expansion) it was considered to be in contact with a non-displacing MB. Similarly, contact with displacing MBs occurred when the

cell's full equivalent diameter intersected with a MB's trajectory (the lines connecting a MB between frames, as determined by Trackpy).

The relations between MB displacement and sonoporation outcome at all acoustic settings were visualized using scatter plots and linear fits through these data using a least-squares approach in MATLAB (The MathWorks, Natick, MA, USA).

### Statistics

To compare the various acoustical settings, we performed statistical testing using Student's *t*-tests to identify significantly different outcomes. All statistics were performed using Student's *t*-tests for independent samples, where a p-value of 0.05 was regarded as significant.

For both sonoporation and cell death, different insonifying pressures were compared at the same number of cycles for both ntMBs and tMBs. One-sided *t*-tests were used to reveal whether higher pressures at the same number of cycles resulted in more sonoporation and cell death. The same *t*-tests were performed to verify whether the experimental acoustic settings resulted in more sonoporation than in the control experiments. For comparing sonoporation with cell death, we used 2-sided *t*-tests to verify whether the percentage of sonoporated cells was different from the percentage of cell death. The effect of ntMBs, tMBs, and $tMB_B$ on the amount of sonoporated cells and on cell death were tested using 2-sided *t*-tests.

The cells that were classified as non-resealing within 120 s were compared to the cells that were determined as dead by the cell viability assay. We used 2-sided *t*-tests to verify whether the assumption that both populations were equal was true.

## 9.4. RESULTS

### Sonoporation and cell death

The influence of various acoustic settings on cellular responses, for both ntMBs and tMBs, was evaluated by the amount of sonoporated cells and cell death, as illustrated in Fig. 9.3. The sonoporation and cell death data are presented as the mean of three experiments at the same settings, with a mean (± SD) of 1,727 (± 338) cells in the FOV for ntMBs and 3,104 (± 130) cells for tMBs. The amount of injected microbubbles was adjusted accordingly, resulting in 1.9 (± 0.8) ntMBs per cell and 1.6 (± 0.3) tMBs per cell. No controls are shown for the cell death data, since these were already subtracted at all settings to correct for natural, non-US related, cell death (6.7 ± 1.1%).

The data show that applying higher acoustic pressures and more cycles increased both the number of sonoporated cells (Fig. 9.3A, C) and the number of dead cells (Fig. 9.3B, D). This trend was seen for both ntMBs (Fig. 9.3A, B) and tMBs (Fig. 9.3C, D). However, when statistically comparing the same number of cycles at increasing pressures, the increase in

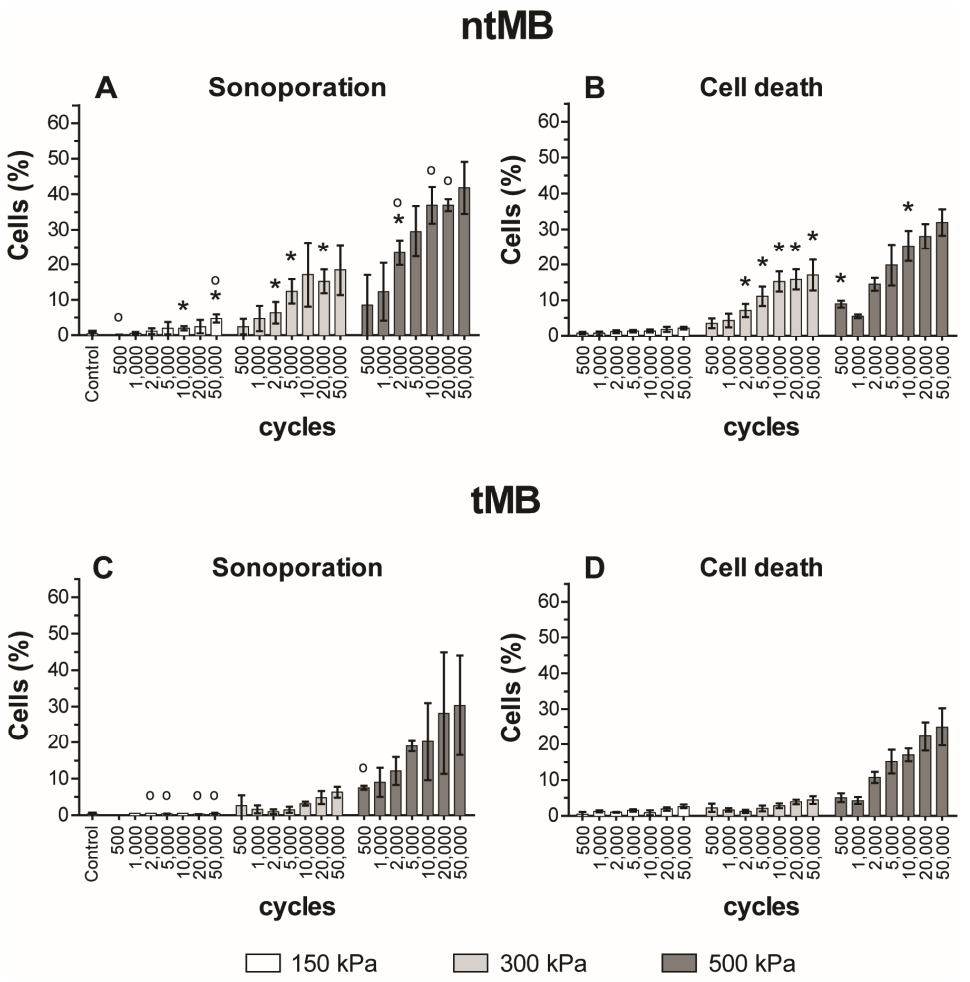


**Fig. 9.3**. Targeted and non-targeted microbubble-mediated sonoporation and cell death after ultrasound exposure at different acoustic pressures (150, 300, and 500 kPa) and number of cycles (500 – 50,000). **(A)** Mean (± SD) percentage of sonoporated cells and **(B)** cell death after insonification of ntMBs. **(C)** Mean (± SD) percentage of sonoporated cells and **(D)** cell death after insonification of tMBs. Results were based on n = 3 repetitions of each experiment. Significant differences ($p < 0.05$) between sonoporation and cell death after US insonification in the presence of ntMB or tMB are indicated by (*). Significantly more sonoporation than cell death is indicated by (o).

sonoporation at higher acoustic pressure was only significant ($p < 0.05$) for ntMBs with at least 2,000 cycles. For tMBs sonoporation at 500 kPa was always higher than at 300 kPa, whereas at 300 kPa at least 10,000 cycles had to be applied to sonoporate more cells than at 150 kPa. Cell death for the same number of cycles at increasing pressures was

significantly higher when using ntMBs, in all cases. For tMBs, cell death at 500 kPa was always significantly higher than at 300 kPa. Conversely, when comparing 300 kPa and 150 kPa, cell death was not significantly different between 1,000 and 5,000 cycles.

The amount of sonoporated cells, in the presence of ntMBs at 150 kPa, only resulted in significantly more sonoporation than in control experiments (0.4% sonoporation) when applying 10,000 or 50,000 cycles (2.0% or 4.7%, respectively). At 300 kPa at least 2,000 cycles were required to significantly yield more PI uptake than in the control experiments, whereas at 500 kPa pressure, 1,000 cycles were already sufficient. For tMBs, 150 kPa did not result in significantly more sonoporation than in the experiments without US. However, application of 300 or 500 kPa sonoporated significantly more cells than in the control experiments for all cycles considered.

The amount of sonoporated cells was expected to be higher than the amount of dead cells, because cells that are sonoporated can also remain viable. However, for most of the settings we applied, cell death was similar to the amount of sonoporated cells. The settings for which the difference between cell death and sonoporation was significant are indicated by (o) in Fig. 9.3A and C. Since cell death was assessed from the viability assays—which were performed separately from the sonoporation assays—cell death could even be higher than the amount of sonoporated cells. This was the case for the 150 kPa experiments in the presence of tMBs.

To validate whether ntMBs or tMBs were more efficient in inducing sonoporation and cell death, we statistically compared them for significance. The asterisks (*) in Fig. 9.3 indicate significant differences between ntMB and tMB for sonoporation (A) and cell death (B). Although Fig. 9.3A and C may suggest that ntMB more efficiently sonoporated cells than tMB at 500 kPa using long US pulses, this difference was not significant, probably due to the high standard deviations in the tMB sonoporation experiments. Cell death due to ntMBs was significantly higher for almost all number of cycles at a pressure of 300 kPa, and comparable for all settings at 150 kPa and for most settings at 500 kPa.

**Sonoporation-induced PI uptake over time**

Before US exposure, bright field imaging was used to discern MB locations (Fig. 9.4A); the black dots in this figure are the MBs, examples indicated by white arrows. The grey background of the image shows spherical structures; these are the nuclei of the endothelial cells in the monolayer. Fluorescence microscopy established individual cell nuclei locations by Hoechst staining (Fig. 9.4B), cell membrane integrity by the absence of PI fluorescence (Fig. 9.4C), and live cells by the presence of calcein (Fig. 9.4D). After US insonification, less MBs were present because they had dissolved, coalesced, or displaced (Fig. 9.4E). Intracellular PI uptake was observed by increase of fluorescence signal, thus indicating sonoporation (Fig. 9.4G).

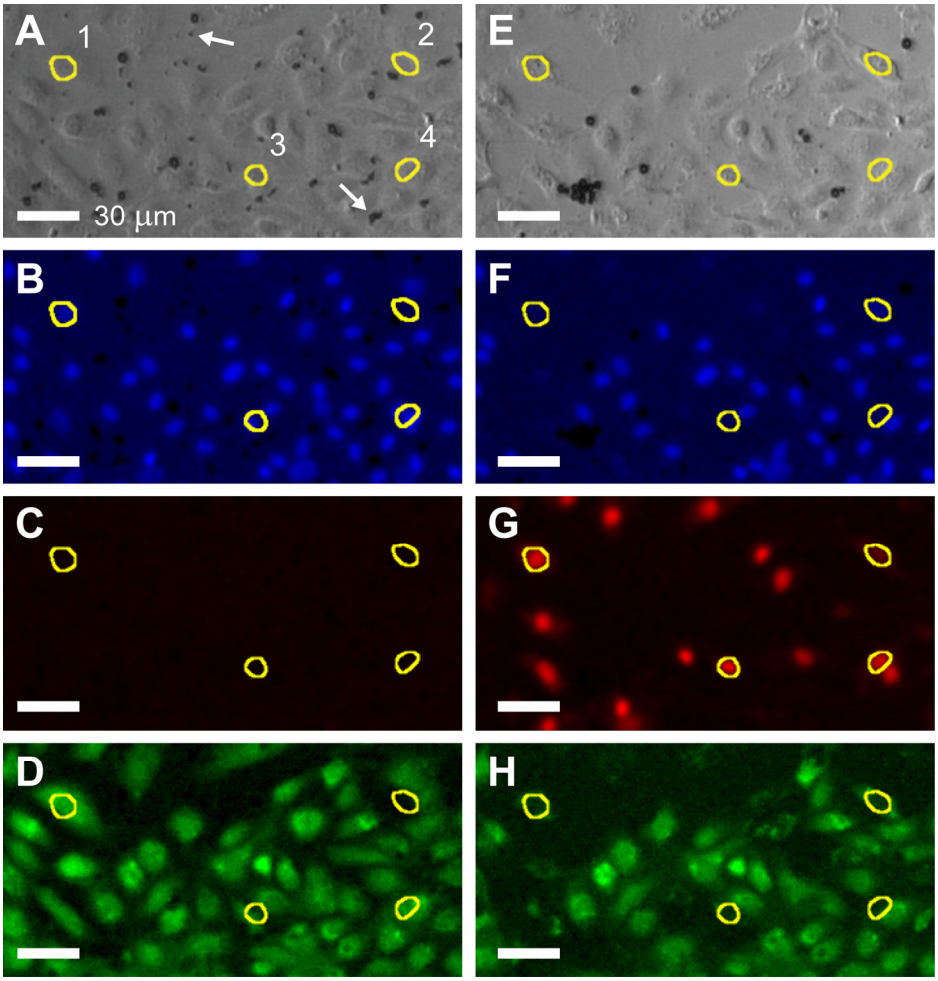


**Fig. 9.4.** Optical recordings of microbubbles and the HUVEC monolayer. **(A)** Bright field image of ntMB locations (black dots) before US exposure; an example of a single ntMB and a ntMB cluster are indicated by a white arrow. Yellow circles indicate highlighted sonoporated cells. **(B)** Hoechst fluorescence imaging of HUVEC nuclei before US application. **(C)** Fluorescence image of PI uptake before insonification; no uptake was present in the field of view. **(D)** Calcein stained image of live cells before US application. **(E)** Bright field image after US treatment; ntMBs dissolved, displaced, and clustered. **(F)** Hoechst stained image of nuclei after US application; signal in sonoporated cells was lower than before US application. **(G)** Fluorescence image of PI signal after US application; red stained nuclei indicate sonoporated cells. **(H)** Calcein stained image after US application; calcein leaked out of some sonoporated cells. (**I**) PI fluorescence intensity as a function of time up to 180 s after US treatment (colored circles) and fit to the Fan model (Eq. 1, solid lines); black circles indicate 90% of theoretical maximum PI intensity that could be reached with the fit parameters. Cells 1 to 4 are marked with yellow circles in panels **A-H**, and the numbers correspond to those in panel **A**. US settings: 500 kPa acoustic pressure, 10,000 cycles. Scale bar 30 µm.

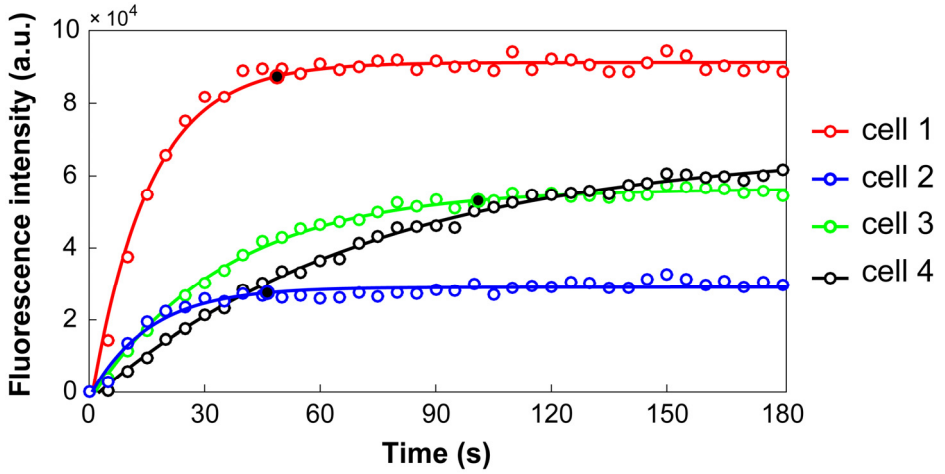


**Fig. 9.5.** PI fluorescence intensity as a function of time up to 180 s after US treatment (colored circles) and fit to the Fan model (Eq. 1, solid lines); black circles indicate 90% of theoretical maximum PI intensity that could be reached with the fit parameters. Cells 1 to 4 are marked with yellow circles in Fig. 9.4A-H, and the numbers correspond to those in Fig. 9.4A. US settings: 500 kPa acoustic pressure, 10,000 cycles. Scale bar 30 µm.

Interestingly, when increasing PI signal was observed, Hoechst signal decreased (Fig. 9.4F). Because the segmentation was done on the image after US application, the segmented cell nuclei did not always exactly match the nuclei in the Hoechst image before US (compare panel B and F). In between the recording of these images, there can be small displacements of cells due to the radiation force of the applied US, movement of the MBs, or retraction of cells because of cell-cell contact opening. In cells that had taken up PI, calcein signal was found to decrease (Fig. 9.4H), which has previously been described as an additional measure for sonoporation [34].

The PI time-lapse images (example shown in Fig. 9.4G) were analyzed for all acoustic settings, resulting in time-intensity curves showing the dynamic PI uptake from just after US application, up to 180 s later. The time-intensity curves were fit to the Fan model (Eq. (9.1)) and revealed a variety of uptake dynamics. Because PI signal intensity could fluctuate between frames, we chose a robust method that only considered cells as actually sonoporated when the time-intensity curve could be fit to the model with an $R^2 > 0.8$. For $R^2 < 0.8$ the fit was regarded as less reliable, because already dead cells at the start of the experiment without clear increase in PI uptake would also be marked as sonoporated. In Fig. 9.5, four different types of uptake curves are shown corresponding to the numbered cells in Fig. 9.4A. The curves obtained for ntMB insonified at 500 kPa for 10,000 cycles illustrate the general differences in PI uptake rates found at all other acoustic settings. The red and blue curve reach 90% of the maximum intensity value predicted by the model within

50 s, whereas the green curve reached this 90% value after more than 90 s, and the black one did not reach this 90% value within 180 s.

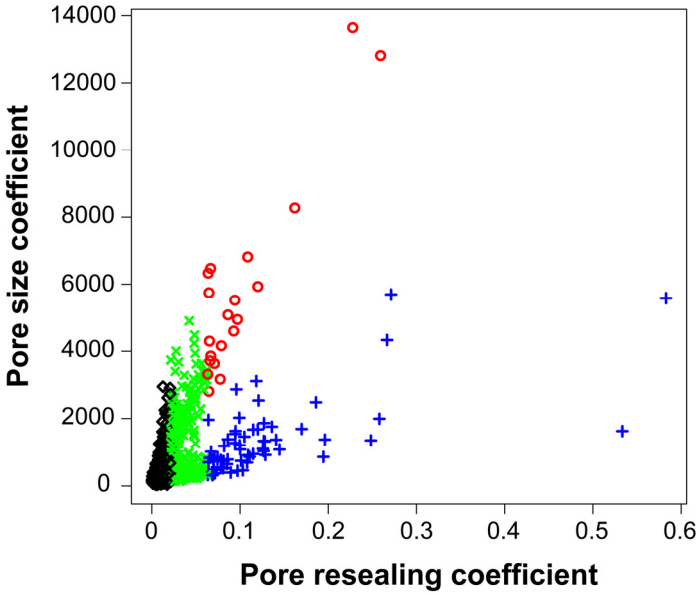


**Fig. 9.6.** Classification of cell populations based on pore size and pore resealing coefficients. This graph originates from the same data set as Figs. 9.4 and 9.5 and shows cells with high PI uptake (red), low PI uptake (blue), cells with pores that resealed within 120 – 180 s (green), and cells with pores that did not reseal within 180 s (black). US settings: 500 kPa acoustic pressure, 10,000 cycles.

**PI uptake as a function of pore size and pore resealing coefficients**

The pore size and pore resealing coefficients of the cells that resulted in a reliable fit to Eq. (9.1) ($R^2$ > 0.8) were used to classify those cells into groups using PCA. This approach divided the total population of cells into two groups: one with relatively high pore resealing coefficients and relatively low pore size coefficients (Fig. 9.6, blue), and one with relatively low pore resealing coefficient and relatively large pore size coefficients (Fig. 9.6, red). The cells in the blue population had low PI uptake suggesting small pores that sealed quickly, whereas the cells classified as red had high PI uptake suggestive of large pores that sealed slower, but within 120 s. By applying the additional thresholds (based on Eq. (9.1), as described in the Materials and Methods section), the cells that were likely to be irreversibly damaged were identified and classified into two separate populations: cells with pores that did reseal, but only after 120 s (Fig. 9.6, green), and cell with pores that did not reseal within 180 s (Fig. 9.6, black).

**Influence of acoustic settings on sonoporation-induced uptake and cell death**

The impact of the acoustic pressure and the number of cycles in a single burst sine wave on sonoporation-induced PI uptake is illustrated in Fig. 9.7. These graphs show the populations of the time-lapse sonoporation assays classified as high PI uptake cells (red), low PI uptake cells (blue), cells with pores that had not resealed within 120 s (grey, this is the sum of the

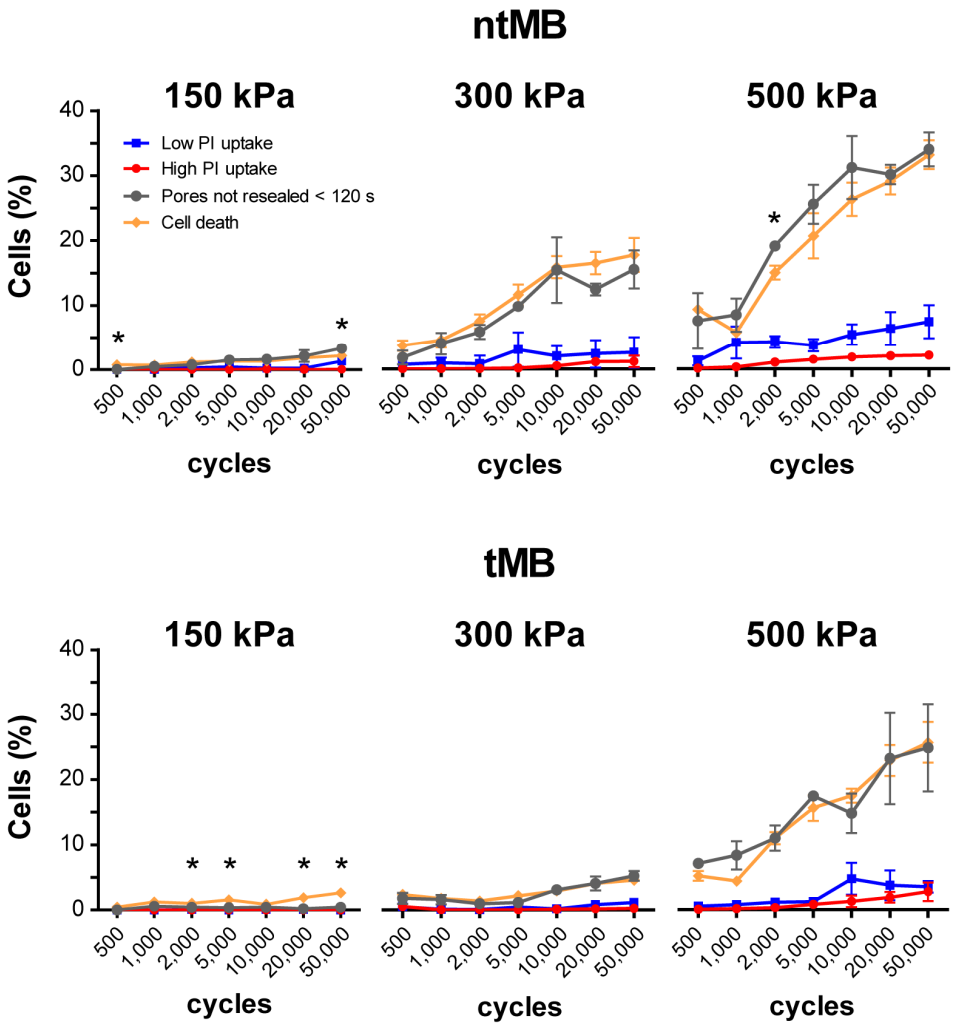


**Fig. 9.7.** Percentage of cell death and cells classified per category by PCA and additional thresholding under various experimental acoustic pressures and cycles. The amount of cells with pores that did not reseal within 120 s (grey line) correlated well with cell death (yellow line) and was only significantly different ($p < 0.05$) at the acoustic settings marked by (*).

cells previously classified as green or black), and cell death (yellow) determined from the cell viability assays for each corresponding treatment. The cells with pores that did not reseal within 120 s were expected to be dead, and statistical comparison with cell death indeed confirmed that these two populations were not significantly different except for a few settings, mainly those with very low amounts of sonoporated cells (indicated by (*) in Fig. 9.7). The proportion of cells with low and high PI uptake (blue and red, respectively) significantly increased with increasing pressure, but did not significantly increase when only more cycles were applied. These cells were determined to be reversibly sonoporated and viable. On the other hand, the amount of cells with slow resealing pores (> 120 s, grey) and cell death (yellow), continued to increase with increasing pressure and cycles. Only increasing the number of cycles resulted in more cell death, but not necessarily in more cells that were viably sonoporated.

**Oscillatory behavior of microbubbles**

The ultra-high-speed movies recorded by the Brandaris 128 camera were qualitatively analyzed per segment. For each segment the number of single MBs and the number of MB clusters were counted and classified into four categories: *1)* non-oscillating (white), *2)* oscillating (dark grey), *3)* oscillating with coalescence of MBs (black), and *4)* oscillating with separation of MBs (light grey), as illustrated in Fig. 9.8. The time line shows the US signal (for visualization purposes, only 20 cycles are shown in the schematic instead of the 1,000 cycles that were actually applied) and the segments of the US pulse at which the ultra-high-speed movies were recorded. The FOV of Brandaris is smaller than that of the AxioCam or Redlake camera, therefore we could only study oscillatory behavior of a subset of MBs.

When ntMBs were insonified at 150 kPa and 1,000 cycles, more single MBs were counted than MB clusters. In the first segment about 60% of single MBs oscillated, whereas > 90% of MB clusters were oscillating. Towards the end of the US burst, only 25% of single MBs and 60% of MB clusters were still oscillating. From segment a to segment b most coalescence occurred (black). At a pressure of 300 kPa, more ntMBs oscillated: 75% of single MBs and all MB clusters. The higher pressure ensured that MBs below resonance, i.e. smaller MBs, also started oscillating. In segment a and b, most clusters coalesced into larger clusters that kept oscillating until the end of the US pulse. This higher degree of clustering was probably caused by more displacement of MBs, due to higher acoustic radiation forces. At the end of the pulse, in segment 4, the large clusters split into smaller clusters or single MBs.

At 150 kPa less tMBs coalesced than ntMBs. This was hypothesized to be due to less displacement of tMBs, as tMBs were attached and higher forces are needed to dislocate them [123]. Fewer clusters were present for tMBs, but more of them were oscillating (~75% in all segments). At a higher pressure of 300 kPa, the overall trend of oscillating single tMBs and clusters was not very different than that at 150 kPa. This has already been shown in Figs. 9.3 and 9.7 in terms of sonoporation efficiency. However, at 300 kPa more clusters were present and more coalescence occurred.

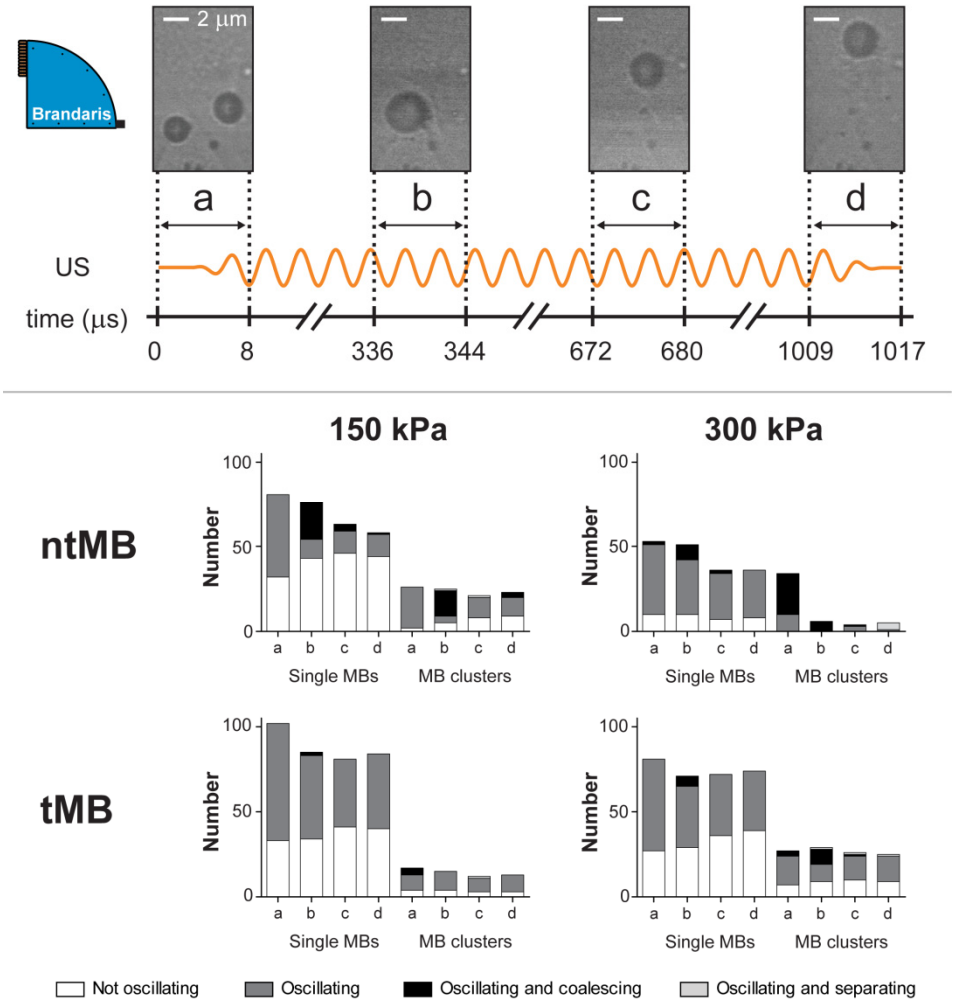


**Fig. 9.8.** Ultra-high-speed imaging of microbubble oscillation behavior. Top: illustration of the segments at which microbubble oscillation was captured and still frames of a recording of tMBs insonified at 300 kPa and 1,000 cycles. Bottom: ntMBs and tMBs oscillation behavior categorized into single MBs and clusters at 150 and 300 kPa insonifying pressure.

**Displacement of microbubbles**

As described in the previous section, more coalescence and clustering were observed for ntMBs, which was hypothesized to be caused by more displacing ntMBs. For each sonoporated cell, in a subset of the original image (ntMB: ~1100 cells, tMB: ~ 1700 cells), we determined it to be either in contact with: *1)* both non-displacing and displacing MBs (dark grey), *2)* a MB that displaced (black), *3)* a MB that had not displaced (light grey), or *4)* when no MB could be detected nearby the cell (white), as shown by the stacked bars in Fig. 9.9 as percentages of the total amount of sonoporated cells. The red solid line illustrates the amount of sonoporated cells as a percentage of the total amount of cells in the FOV. This amount was, on average, 2.7% higher than the amount of sonoporated cells shown in Figs. 9.3 and 9.7. This was expected, since the data for those figures only accounted for the cells that fitted properly to the model. Both methods showed the same trends, thus the determination of PI uptake was performed on a representative subset of the full-size AxioCam images.

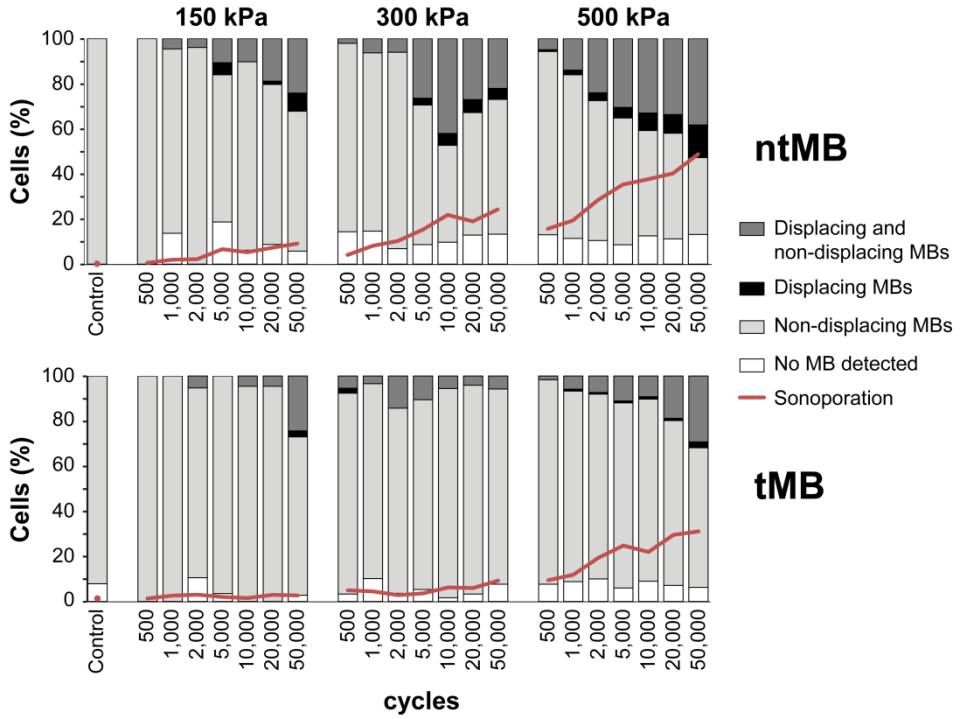


**Fig. 9.9.** Displacement of ntMBs and tMBs under varying experimental acoustic pressures and cycles. For each acoustic setting, the stacked bar graph indicates the percentage of sonoporation caused by displacing MBs, non-displacing MBs, both, or when no MB could be detected. The red line shows the percentage of cells that were sonoporated.

Overall, most sonoporation was induced by non-displacing MBs (light grey, Fig. 9.9), whereas for ntMBs at 500 kPa and 50,000 cycles both displacing and non-displacing MBs accounted for similar amounts of sonoporation. The use of ntMBs resulted in the highest amount of displacing MBs, which supports the previously stated hypothesis that the higher degree of clustering was due to more displacing MBs. Overall, when comparing the contribution of displacing MBs (dark grey and black in Fig. 9.9) to the amount of sonoporated cells (red line in Fig. 9.9), they followed the same trend.

To relate MB displacement to sonoporation outcome, we compared the two cell classifications: *1)* reversibly sonoporated cells that had resealing pores < 120 s (Fig. 9.7, blue and red lines) and *2)* irreversibly sonoporated cells (Fig. 9.7, grey line) with *A)* cells that were sonoporated by displacing MBs (Fig. 9.9, dark grey and black) and *B)* those that were sonoporated by non-displacing MBs (Fig. 9.9, dark grey and light grey as shown in Fig. 9.10). The slope of the linear fit shows the ratio of increase between two groups; a ratio of 1 implies that the values are identical and increase proportionally (data follows the line $y = x$).

A proportional increase was found for the amount of irreversibly sonoporated cells and the amount of cells that were sonoporated by non-displacing MBs (slope 1.0 for ntMB in Fig. 9.10A; slope 1.1 for tMB in Fig. 9.10B, both $R^2 = 0.99$). In addition, the amount of sonoporated cells that was in contact with non-displacing MBs (Fig. 9.10C and D) increased four times faster than the amount of reversibly sonoporated cells (slope of 3.7 and 4.1, respectively). This strongly suggest that cells in contact with non-displacing MBs were irreversibly damaged.

On the other hand, the amount of sonoporation for cells in contact with displacing ntMBs increased twice as fast as the amount of reversibly sonoporated cells (Fig. 9.10G, slope of 2.1), while still contributing to irreversible sonoporation (Fig. 9.10E, slope of 0.57). This suggest that displacing ntMBs can both induce reversible and irreversible sonoporation. For cells in contact with displacing tMBs the amount of reversibly sonoporated cells increased proportionally (Fig. 9.10H, slope of 1.0). Further, displacing tMBs minimally contributed to irreversible sonoporation (Fig. 9.10F, slope of 0.27). This suggests that displacing tMBs mainly resulted in reversible sonoporation.

The relation between the presence of displacing and non-displacing MBs and the classification of cells was confirmed on a single cell basis, as shown in Fig. 9.11 and Fig. 9.5. Cells 1 and 2 were both reversibly sonoporated due to MBs displacing over their cell membranes, of which cell 1 had high PI uptake and cell 2 low uptake. Cell 1 also had non-displacing MBs in its vicinity, which might be the reason for the higher uptake of PI. Cells 3 and 4 had slow resealing pores (> 120 s) and only non-displacing MBs nearby their cell membranes.

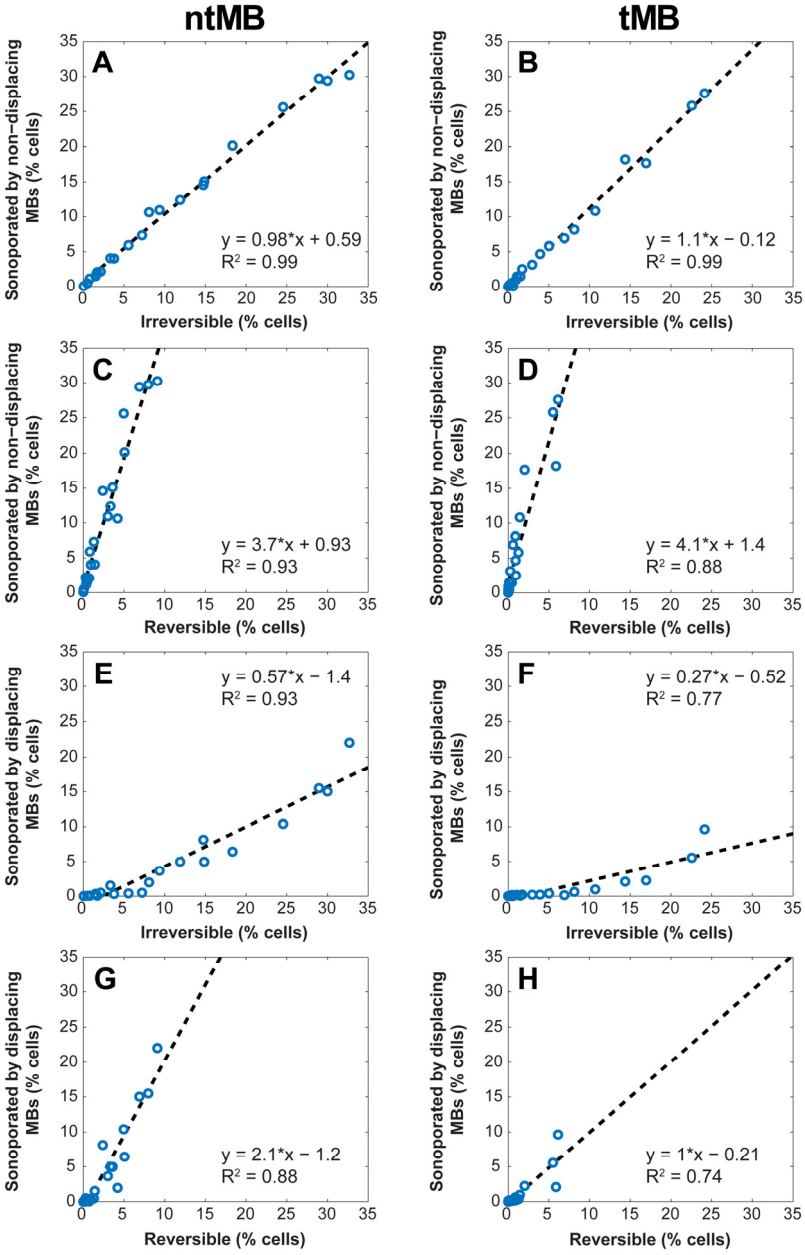


**Fig. 9.10.** Scatter plots visualizing the relation between MB displacement and sonoporation outcome. The slope of the linear fit shows the ratio of increase between each two groups. Blue circles are the experimental data points at all 21 acoustic settings, the black dashed line the linear fit. Irreversible sonoporation is the grey data set from Fig. 9.7; reversible sonoporation is the sum of the red and blue data sets from Fig. 9.7.

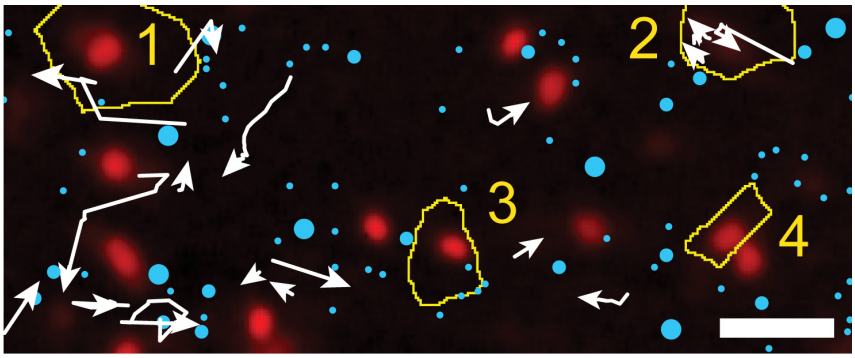


**Fig. 9.11.** Microbubble displacement. White arrows indicate displacing ntMBs and blue filled circles indicate non-displacing ntMBs, overlaid on the same PI stained image as shown in Fig. 9.4G. Cells 1-4 (yellow lines) are the same ones as shown in Figs. 9.4 and 9.5. MB displacement was not correlated to the direction of US application. US settings: 500 kPa acoustic pressure, 10,000 cycles. Scale bar indicates 30 μm.

**Orientation of tMBs**

For all experiments concerning ntMBs, the cells were on the upper membrane of the OptiCell with the MBs floating against the cells. For the tMB experiments described so far, the cells were on the bottom membrane with the tMBs adhered on top of the cells. In addition to the comparison between ntMBs and tMBs, we also investigated the effect of the orientation of tMBs with respect to the cells and US application. We therefore placed the OptiCell containing tMBs in the same orientation as the experiments on ntMBs, so the cells were on the upper membrane with the tMBs below the cells ($tMB_B$). These experiments were repeated two times at 500 kPa for all investigated number of cycles with on average 3,106 (± 139) cells in the FOV.

The amount of US-induced sonoporated cells with $tMB_B$ was higher than for the control experiments for the four settings with the smallest error bars: 1,000; 2,000; 10,000; and 50,000 cycles. Although, especially for the longer pulses, $tMB_B$ seemed to more efficiently sonoporate cells than both tMBs and ntMBs, this was not statistically significant for most cycles. Only with 10,000 cycles were $tMB_B$ more efficient than ntMBs (*); and only with 500 cycles were $tMB_B$ more efficient than tMB (o) (Fig. 9.12A, $p < 0.05$). Cell death for $tMB_B$ was significantly higher than for the $tMB_B$ controls after applying 2,000; 5,000; 20,000; and 50,000 cycles. In addition, cell death and the total amount of sonoporated cells were significantly different for all experimental settings. For most settings cell death of $tMB_B$ was similar to ntMBs or tMBs, except for 1,000 cycles with ntMBs (*) and 1,000 and 2,000 cycles with tMBs (o) as shown in Fig. 9.12B. Cell death controls are not shown, since these were subtracted from cell death at the other settings to correct for natural cell death.

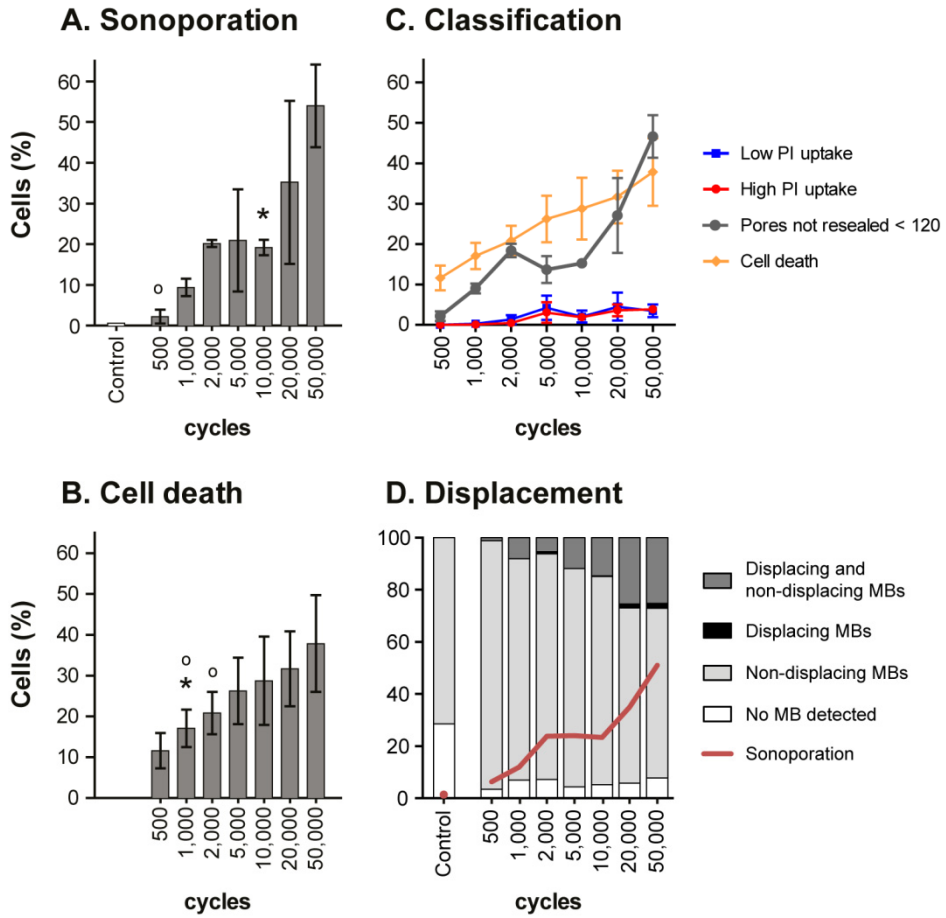


**Fig. 9.12.** tMBs adhered below the cells ($tMB_B$) insonified at 500 kPa. **(A)** Mean (± SD) percentage of sonoporated cells and **(B)** cell death after insonification of $tMB_B$. Asterisks (*) indicate significant differences between $tMB_B$ and ntMBs, and (o) between $tMB_B$ and tMBs. **(C)** Classification of cells based on their pore size and pore resealing coefficient. The amount of cells with non-resealing pores within 120 s (grey) was significantly different from the amount of dead cells (yellow) for all settings. **(D)** Displacement of $tMB_B$. For each acoustic setting, the bar graph indicates the percentage of cells that were sonoporated by displacing MBs, non-displacing MBs, both, or when no MB could be detected. The red line shows the percentage of cells that were sonoporated.

Cell classification based on PI uptake patterns showed similar trends for $tMB_B$ as for ntMBs and tMBs, in terms of the amount of cells in each group. However, the cells with non-resealing pores within 120 s (Fig. 9.12C, grey) did not correlate with the amount of cell death (Fig. 9.12C, yellow), since they were significantly different for all applied settings, possibly of lower statistical power (only n = 2).

As expected, displacement of $tMB_B$ was very similar to the displacement of tMBs (Fig. 9.12D and Fig. 9.9), since the binding strength that has to be overcome to displace them is identical.

## 9.5. DISCUSSION

This is the first study that directly compares ntMB and tMB-mediated sonoporation in primary endothelial cells *in vitro* using long acoustic pulses (500 – 50,000 cycles). At 1 MHz and three different acoustic pressures (150 - 500 kPa), we aimed to identify differences in MB behavior responsible for either viable sonoporation or cell death. The real-time observed uptake of PI upon sonoporation was fit using a previously reported diffusion model [34] and subsequently classified using PCA. Cell viability highly correlated with the four different PI uptake patterns derived from this classification. Further, displacing tMBs resulted in viably sonoporated cells, whereas non-displacing tMBs and ntMBs accounted for more cell death.

### Cellular response dynamics

Four cell populations with different PI uptake profiles were found for ntMB and tMB-mediated sonoporation at each US setting. The cells that had non-resealing pores within 120 s after US application were irreversibly damaged (Fig. 9.7, grey) as this correlated well with cell death (Fig. 9.7, yellow). Further, cells having low PI uptake (Fig. 9.7, blue) and high PI uptake (Fig. 9.7, red) had pores that resealed within 120 s. Other researchers have shown that cells remained viable when pores resealed within a few seconds up to 60 s [37, 38, 422]. However, these studies were not performed on human endothelial cells, but on human fibroblasts [38], bovine endothelial cells [37], and Xenopus oocytes [422]. Enhanced drug uptake up to several hours has also been reported [423, 424], but cells having non-resealed pores for such long periods are not expected to be viable. We therefore believe that the route of model drug uptake in their experiments was most likely not due to pore formation, but possibly stimulated endocytosis. Our results suggest that human endothelial cells showing increasing nuclear PI signal up to 120 s were also viably sonoporated. This may imply that pores open for longer than 60 s can still result in viably sonoporated cells.

Cells that had taken up PI also showed an efflux of calcein, which is another indicator of sonoporation [34]. Next to calcein efflux, those cells also revealed lower Hoechst signals in the fluorescence images taken after US treatment than in those taken before (Fig. 9.4). Since the literature agrees upon non-competitive binding of PI and Hoechst [412, 413], we believe this decrease in signal was caused by Förster resonance energy transfer (also known as FRET) [425]. The emission spectrum of Hoechst (maximum intensity at 461 nm) overlaps with the excitation spectrum of PI (491 - 495 nm); the presence of PI can therefore result in considerable quenching of the Hoechst signal [426]. Hoechst signal intensity was therefore

lower in cells that had taken up PI. In addition, the amount of PI uptake was found to be related to the level of quenching; cells 1, 3, and 4 had high PI uptake (Fig. 9.4G) and Hoechst signal was almost completely quenched (Fig. 9.4F), whereas cell 2 had low PI uptake and less quenching of Hoechst signal.

**Influence of oscillation and displacement of microbubbles**

Quantitative assessment of the displacement of MBs revealed more PI uptake when more tMBs or ntMBs displaced (Fig. 9.9). We studied the relation between MB displacement and reversibility of sonoporation and found a clear relation between non-displacing MBs and irreversible sonoporation (Fig. 9.10A and 9.10B); an increase in sonoporation by non-displacing MBs coincides with a similar increase in irreversible sonoporation. We therefore concluded that irreversible sonoporation was mainly caused by non-displacing MBs, explained by prolonged MB oscillation at the same location on the cell membrane. The relation between displacing MBs and sonoporation is less straightforward. For ntMBs (Fig. 9.10G) the amount of cells sonoporated by displacing ntMBs increased twice as fast as those that were reversibly sonoporated (slope of 2.1), which implies that displacing ntMBs did not only induce reversible sonoporation, but also irreversible sonoporation (Fig. 9.10E). Because longer pulses at higher acoustic pressure cause more displacement, the ntMBs can affect multiple cells or multiple displacing ntMBs can affect a single cell.

For tMBs we found an increase in reversible sonoporation that coincides with a similar increase in sonoporation caused by displacing tMBs (Fig. 9.10H). We therefore conclude that displacing tMBs mainly resulted in reversible sonoporation. The amount of irreversibly sonoporated cells by displacing tMBs is much smaller than for ntMBs (compare Fig. 9.10E and 9.10F). When tMBs detach and displace, they float away from the cells and will not contribute to more sonoporation.

Displacing tMBs resulted mainly in reversible sonoporation, whereas the much larger amount of displacing ntMBs also induced irreversible sonoporation. This may imply that reversibility is only achieved with limited displacement of MBs. Fan et al. [403, 405] concluded that displacement of both ntMBs and tMBs correlated with irreversible sonoporation, while we related displacement to reversibility. This difference may be explained by larger MB displacements in their study because they used pulsed US (1.25 MHz, 60-600 kPa, PRF 10-1,000 Hz, duty cycles 0.016-20%), whereas the single US burst we used resulted in less and slower displacement for the second half of the pulse (Fig. 9.8).

In the high-speed and ultra-high-speed recordings we observed clustering of MBs. Higher pressures enhanced cluster formation, and ntMBs formed more clusters because they displaced more than tMBs. Since the amount of sonoporated cells was similar for ntMBs and tMBs (Fig. 9.3), clustering did thus not result in more sonoporation.

Mannaris and Averkiou [427] were the first to show acoustically that MBs remained oscillating during 1,000 acoustic cycles at 100 kPa. Our ultra-high-speed recordings revealed

the presence and oscillation of both single MBs and MB clusters at the end of the 1,000-cycle US burst at 150 and 300 kPa, albeit that we observed more oscillating MB clusters at the end of the US pulse than single MBs. Chen, et al. [370] reported contrasting observations. After 1,000 cycles their ultra-high-speed recordings only showed oscillating clusters; no single MBs were present anymore. The most likely cause for these different findings is the high pressure (up to 1.5 MPa) they applied, which resulted in more displacement due to acoustic radiation force [81, 392] and more clustering.

**Sonoporation efficiency: ntMB versus tMB**

The sonoporation efficiency of ntMB and tMB showed the same trend: higher pressures and more cycles resulted in more sonoporation (Fig. 9.3), as also shown by others [40, 41]. However, for tMBs the amounts of sonoporated and dead cells at 300 kPa were lower than for ntMBs, which is most likely caused by MB displacement or oscillation behavior. Increasing the pressure from 150 to 300 kPa resulted in more displacing ntMBs, but the number of displacing tMBs did not increase (Fig. 9.9). In addition, the ultra-high-speed recordings showed more oscillating ntMBs for increasing pressure, while no change was observed for tMBs (Fig. 9.8). This is caused by functionalization of our tMBs with CD31 antibodies via streptavidin-biotin binding, but we did not add streptavidin nor control-antibodies to our ntMBs, as clinical ntMBs would not have this either. Functionalization of MBs alters shell properties [262] and therefore oscillation behavior [260]. Since our tMBs and ntMBs had identical lipid shells with DSPC as the main lipid, the targeting moieties would result in a higher elasticity and thus a stiffer shell of our tMBs [262]. As a consequence, higher pressures are required for tMBs to obtain the same oscillation amplitude as for ntMBs [45], which likely influences sonoporation efficiency.

The sonoporation experiments with tMBs at 500 kPa and 10,000 to 50,000 cycles showed very large error bars (Fig. 9.3C). Two of the OptiCells in which the experiments were done showed similar uptake percentages, but the amount of sonoporated cells in the third OptiCell was almost twice as high. The underlying cause for this observation is unclear; all cell layers were confluent, the total amount of cells and MB concentration was similar, as well as the average number of MBs per cell. Hence, we can only conclude that sonoporation caused by tMBs is less predictable than by ntMBs.

Our findings, that in general tMBs did not induce higher PI uptake than ntMBs, contradict other *in vitro* studies that report tMBs to be more efficient for drug delivery than ntMBs in a direct comparison. The five reported *in vitro* studies [232, 234, 235, 238, 239] all show that the lipid-shell tMBs are 1.1 [238] to 7.7 [239] fold more efficient for drug delivery than ntMBs. Four out of these five studies describe drug-loaded MBs (with paclitaxel or plasmid DNA), the other one describes co-administration of PI [232]. A direct comparison between our study and the five reported studies is difficult, due to the differences in experimental conditions. None of these studies assessed MB-mediated drug delivery in

endothelial cells. Instead, smooth muscle [234] or cancer cells were used. The study that reported the largest difference between ntMBs and tMBs, rinsed the cells to remove free MBs that had not adhered [239]. As a result, the ntMBs would almost all have been washed away, which could explain the large difference. Another study treated cancer cells in suspension [235], whereas we treated a fully confluent monolayer of endothelial cells. Two studies [235, 238] used ntMBs with a different shell composition and smaller mean diameter than their tMBs, which without doubt results in differences in MB behavior [45, 259, 260]. In addition, one study reported that the 5.5 fold higher uptake could only be achieved with 70% confluent cells [234]. Consequently, our results are not supported by other studies, since none directly compared ntMB and tMB-mediated drug delivery in endothelial cells *in vitro*. Several studies reported more efficient drug delivery or transfection *in vivo* for tMBs than for ntMBs [236, 237, 240, 241]. Due to blood flow, ntMBs flow by and thus have shorter contact with tissue, thereby making ntMBs less efficient. Inclusion of flow in the *in vitro* experiments is thought to result in more efficient sonoporation for tMB than for ntMB and will be subject for future studies.

**Microbubble orientation**

We used a different orientation of MBs relative to the cells and US direction for tMBs and ntMBs (Fig. 9.1B and Fig. 9.12). Therefore, the ntMBs could have been pushed towards the cells by the US, while the tMBs could have been pushed away from the cells. To study whether this influenced sonoporation efficiency, we performed experiments with tMBs in the same orientation as the ntMBs, which we referred to as $tMB_B$ (tMB below cells). Because $tMB_B$ adhered below the cells, non-adhered $tMB_B$ would also be in contact with the cells and could have contributed to sonoporation as well. Higher amounts of non-adhered $tMB_B$ would results in more displacing $tMB_B$ and thus enhance sonoporation. However, since the amounts of $tMB_B$ and tMBs in the FOV were the same (~3,100 cells), we can assume that all $tMB_B$ had adhered and that non-adhered $tMB_B$ did not account for the variation in PI uptake.

Sonoporation efficiency for $tMB_B$ seemed higher than for tMBs (compare Fig. 9.3C and Fig. 9.12A), possibly caused by MBs that detached during insonification and remained in contact with the cells. In contrast, the configuration for tMBs allowed them to float away after detachment. The sonoporation efficiency, however, was not significantly different to conclude that $tMB_B$ were more efficient than tMBs. To the best of our knowledge, no previously published studies investigated the orientation of MBs relative to the cells and US direction. Others that directly compared the effect of ntMBs and tMBs either did not mention the orientation [235, 238], had the MBs on top of the cells with US applied from the MB-side [239], or had the MBs below the cells and applied US from below [232, 234].

**Experimental considerations**

To obtain the amount of sonoporation from the nuclear PI uptake and the associated model fit, we used algorithms implemented in ImageJ and RStudio, whereas a different algorithm in Python was used to obtain sonoporation from PI uptake in the entire cell and its relation to displacing and non-displacing MBs. Although this is not ideal, we chose this approach to optimally utilize the strengths of each method: segmentation (ImageJ) and tracking of moving particles (Python). Since both methods relied heavily on correct detection of cell nuclei, we manually counted the nuclei on the Hoechst images and compared this to the outcomes of the ImageJ and Python algorithms: both detected, on average, only 6% of the nuclei incorrectly (n = 6 images). Since the errors were small, the additional analyses were expected to be comparable as well. Indeed, the segmented cell borders by Voronoi tessellation closely overlapped between the two methods. As already mentioned, sonoporation was slightly higher (2.7% on average) for the tracking method in Python, than for the more robust fitting method using RStudio. This was caused by additional detection of cytoplasmic PI uptake and by cells of which the model could not be fit ($R^2 < 0.8$) to the nuclear uptake profile.

In contrast to the paper by Fan et al. [34], we did not calculate the size of the pores, since not all parameters of our system were known. However, if we would have done this, possible multiple pores in a single cell could still have been detected as one larger pore. In addition, we only included PI uptake in the nucleus because determination of the cell borders was based on probability, whereas the nucleus could be more precisely segmented from the Hoechst images.

On average, 7.4% of sonoporated cells that were found using the tracking algorithm were classified as being sonoporated without the presence of a MB nearby (Fig. 9.9, white). Since control experiments with only MBs showed sonoporation of < 0.9% of all cells, this was not caused by spontaneous uptake of PI, but most likely due to the size of the MBs—only a few pixels in diameter—and the quality of the images. Accurately detecting ntMBs was more difficult due to the optical focus in the corresponding bright field images; the cells were better in focus, resulting in lower discriminative power between cell structures and MBs. The error for ntMB detection was therefore higher. Manual counting of the number of MBs that was not counted by the algorithm resulted in an average of 9% more MBs per image (n = 9). This is slightly higher than the average amount of sonoporated cells without MBs nearby, because MBs that were in contact with non-sonoporated cells could have also been missed.

**Limitations of this study**

A limitation to our study is the use of CD31 as the ligand on our tMBs, because this is a constitutively expressed adhesion molecule on endothelial cells [428]. It can therefore not be used *in vivo*, since CD31-tMBs would adhere to the entire vasculature. Also, the MBs

circulate within the vasculature *in vivo*, while we performed our studies under static conditions. Flow is expected to have an influence on the sonoporation efficiency, as ntMBs will be taken away by the flow, while tMBs will still adhere to the cells under flow [301]. A higher sonoporation efficiency for tMBs is therefore expected and shown [236, 237, 241] under flow and *in vivo* conditions.

**Therapeutic applications**

Based on our results, ntMBs exposed to an acoustic pressure of 500 kPa and a pulse length of 1,000 cycles would be most beneficial for drug delivery. These settings resulted in relatively high amounts of viably sonoporated cells (Fig. 9.7, blue) and minimal cell death (Fig. 9.7, grey/yellow). For drug delivery, high drug uptake would be most beneficial since higher doses of therapeutics can be delivered (Fig. 9.7, red). Nevertheless, we always observed equal or lower red uptake patterns in comparison to the blue uptake patterns of lower PI uptake, implying there is not one US setting that favors one over the other. On the other hand, for therapeutic applications where high cell death is desired, e.g. cancer therapies, high pressures and long pulses should be applied (e.g., 500 kPa and 50,000 cycles). Both tMBs and ntMBs were shown to effectively kill cells, but ntMBs were more efficient. For therapies requiring sonoporation of specific cells under flow, ntMBs would need to be replaced with tMBs. ntMBs could sonoporate cells as they move along the cells, or when pressed against a thrombus occluding a blood vessel, as in the case of sonothrombolysis [296, 429]. On the other hand, for locally enhanced drug delivery in tumors tMBs are required, since the MBs need to be close to the cell membrane [37, 242]. Hence, the choice of using either ntMBs or tMBs highly depends on the desired therapeutic application.

## 9.6. CONCLUSION

In depth sonoporation studies on the effect of longer acoustic pulses at 1 MHz at different acoustic pressures revealed a clear relation between sonoporation efficiency and MB behavior. Different patterns of PI uptake derived from the diffusion model and subsequent classification using PCA highly correlated with cell viability. Limited displacement of the MBs enhanced drug delivery and preserved cell viability, while non-displacing MBs were the main contributor to cell death. Longer pulses resulted in more dead cells, but did not result in significant increase in viably sonoporated cells. In addition, the effect of the same type of ntMBs and tMBs to sonoporate endothelial cells was similar *in vitro* under static conditions.

**Acknowledgements**

The authors thank Robert Beurskens, Frits Mastik, Michiel Manten, and Geert Springeling from the department of Biomedical Engineering, Thoraxcenter, Erasmus MC, the

Netherlands for technical assistance. This work is financially supported by NanoNextNL, a micro- and nanotechnology consortium of the Government of the Netherlands and 130 partners and by the Dutch Technology Foundation STW (Veni-project 13669), which is part of the Netherlands Organization for Scientific Research (NWO), and which is partly funded by the Ministry of Economic Affairs.

Chapter **10**

# Laser-activated polymer microcapsules for acoustic imaging and therapy: an in vitro feasibility study

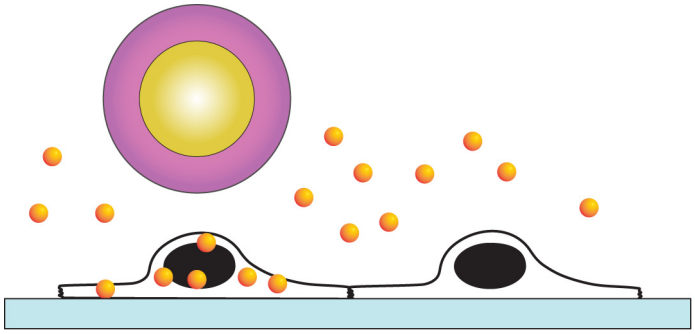

Tom van Rooij*, Guillaume Lajoinie*, Ilya Skachkov, Emilie Blazejewski, Gert Veldhuis, Nico de Jong, Klazina Kooiman, Michel Versluis (* both first authors contributed equally)

*Biophysical Journal* (2016) – *Submitted*

## 10.1. ABSTRACT

Polymeric microcapsules with a light-absorbing dye incorporated in their shell can generate vapor microbubbles that can be spatiotemporally controlled by pulsed laser irradiation. These contrast agents of 6-8 μm in diameter can circulate through the vasculature offering possibilities for ultrasound (molecular) imaging and targeted therapies. Here, we study the impact of such vapor bubbles on human endothelial cells in terms of cell poration and cell viability to establish the imaging and therapeutic windows. Two capsule formulations were used: the first one consisted of a high boiling point oil (hexadecane), whereas the second was loaded with a low boiling point oil (perfluoropentane, PFP). Poration probability was already 40% for the smallest bubbles that were formed (< 7.5 μm diameter), and reached 100% for the larger bubbles. The hexadecane-loaded capsules also produced bubbles while their shell remained intact. These encapsulated bubbles could therefore be used for non-invasive ultrasound imaging after laser-activation without inducing any cell damage. The controlled and localized cell destruction achieved by activation of both capsule formulations may provide an innovative approach for specifically inducing cell death *in vivo*, e.g for cancer therapy.

## 10.2. INTRODUCTION

Commercially available ultrasound (US) contrast agents are primarily based on the highly echogenic scattering of small stabilized gas spheres called microbubbles [314], for contrast enhancement of the blood [313]. Next to contrast enhancement, microbubbles have also been functionalized with targeting moieties that can adhere to specific clinically relevant biomarkers [69, 262], hereby extending the applicability of microbubbles to molecular imaging with US. Ultrasound contrast agents have also been developed that can be loaded with drugs [45, 430] for improved delivery of genetic material and drug molecules to cells [28, 36, 45, 431] for theranostic applications [237, 432, 433]. This improved delivery to cells is enabled by microbubble oscillations that cause increased membrane permeability, termed sonoporation [36, 45], which is considered as one of the most promising routes for US-mediated drug delivery [36].

The efficiency of ultrasound contrast agents for drug delivery has been shown *in vivo* [434-436], and extensive literature can be found that investigates the mechanisms by which drugs are delivered to cells through the use of microbubbles and US [33, 35, 38, 41, 372, 422, 437, 438]. Although the mechanisms are still not fully understood, these studies clearly showed that microbubble oscillations are key to a locally increased cell membrane permeability resulting in enhanced drug delivery. However, a delicate balance between drug delivery achieved through viable sonoporation and cell death has been shown [38, 372]. These studies reported that the therapeutic windows of irreversible sonoporation resulting in cell death and reversible sonoporation resulting in viable cells suitable for drug delivery,

are associated with oscillation and displacement of microbubbles [372], and with the size of the resulting pore [38].

Oscillation of microbubbles can either result in stable or inertial cavitation, both of which play a role in enhancing sonoporation [439]. Next to microbubbles, other types of agents such as phase-change droplets [440], polymer nanoparticles [441] and microparticles [45, 442] can also induce cavitation. In contrast to microbubbles, these agents offer longer shelf life and prolonged stability [443]. Unlike microbubbles that are confined to the blood pool, polymeric particles can be made small enough to extravasate into the interstitial tissue [444, 445]. These polymeric micro- and nanoparticles also offer an unprecedented versatility; they can, for example, carry a larger drug payload in their hydrophobic core than microbubbles [14], they can stably entrap a multitude of elements such as metallic nanoparticles [446], generate gas by hydrolysis of the shell material [447], or be shaped as a porous matrix to be stable under sustained US exposure [448]. On the other hand, polymeric microparticles have been shown to be less responsive to US than microbubbles due their stiffer shell, which makes US imaging of intact polymeric microcapsules challenging [13, 21].

To investigate the potential for laser activation of liquid particles and to improve their imaging capabilities, previous studies have incorporated light absorbers either in perfluorocarbon droplets [58] as plasmonic nanoparticles or as a dye in the shell of polymeric capsules [57]. It was shown that single polymeric capsules can be triggered by a laser, leading to vaporization and the formation of a bubble. The scattering strength of these vapor bubbles is promising for US imaging applications. Downsizing the polymeric capsules to nanometer sizes would allow them to extravasate into tumor tissue, which lies beyond the endothelial cell layer lining the blood vessels and which may open up possibilities for delivering cytostatics into the tumor [449]. Additionally, the use of an oil with a low boiling point (i.e. perfluoropentane) appears as a viable approach to reduce the vaporization threshold of these light-absorbing particles below the FDA-approved laser intensity limit [450]. Until now, little is known on the biological effects of such confined and controlled vaporization events in the vicinity of cells and the imaging and therapeutic windows have to be assessed before these agents can be further developed for clinical use.

Here, we designed an experiment to study the effects of laser-induced vaporization bubbles *in vitro*, created by two types of light-absorbing polymeric microcapsules. The first type of capsules is loaded with a high boiling point oil (hexadecane) and the second type contains a low boiling point oil (perfluoropentane). By means of ultra-high-speed bright field imaging combined with fluorescence imaging, we studied the effects of these laser-activated polymeric microcapsules on human endothelial cells, and we particularly assessed the resulting effect of the created vapor bubbles on the cells. All measured quantities were therefore considered as a function of the vapor bubble properties, e.g. size and lifetime. For example, we recorded the microsecond timescale dynamics of the vapor bubbles in order to

relate these to both cell poration and cell viability. The uptake of a model drug upon cell poration was quantified dynamically and was related to the vapor bubble size and cell death.

## 10.3. MATERIALS AND METHODS

### Capsule production

Hexadecane-loaded polymethylmethacrylate (PMMA) microcapsules were prepared by an emulsion solvent evaporation technique, using microsieve emulsification [451]. Prior to emulsification, hexadecane (H6703, Sigma-Aldrich, Zwijndrecht, the Netherlands), PMMA ($T_g$ = 103 °C, MW 120,000, Sigma-Aldrich) and Sudan red 7B (Sigma-Aldrich) dye were dissolved in dichloromethane (Sigma-Aldrich) in order to achieve a dye concentration of 4.85% w/w.

Poly(lactic-co-glycolic acid) Resomer RG502 microcapsules (hereafter called Resomer) containing perfluoropentane oil (PFP, Fluoromed, Round Rock, TX, USA) were fabricated in a similar way as the PMMA capsules. Poly(lactic-co-glycolic acid) ($T_g$ = 50 °C, Corbion Purac, Amsterdam, the Netherlands) was dissolved in dichloromethane along with PFP and Sudan red 7B dye, and only with PFP for the control capsules, and was placed in a 20 °C bath to ensure full miscibility of the oil in dichloromethane. Ultrapure water containing an emulsifier (polyvinyl alcohol 4% (w/w) or sodium cholate 1.5% (w/w)) maintained below 15 °C was used as continuous phase. The solutions were filtered through a 0.45 µm PTFE filter and emulsified through a microsieve membrane (Nanomi B.V., the Netherlands) with uniform pores. The emulsions were then spread in an aqueous solution containing the aforementioned emulsifiers. This was left to stir at room temperature for at least 3 h to evaporate the dichloromethane. The hardened microcapsules were concentrated and washed repeatedly by vacuum filtration and 0.05% w/w Tween 20 solution (VWR, Amsterdam, the Netherlands). Subsequently, the washed suspensions were stored at 4 °C. Size distributions and concentrations were determined using a Multisizer 3 Coulter Counter (average of n = 3, Beckman Coulter, Mijdrecht, the Netherlands) equipped with a 100 µm aperture. Both capsule types were monodisperse, but PMMA-hexadecane capsules were smaller (average diameter 6.4 µm) than Resomer-PFP capsules (average diameter 7.5 µm). Undiluted concentrations were $7.3\times10^7$ PMMA-hexacecane capsules/mL and $6.8\times10^6$ Resomer-PFP capsules/mL.

### Endothelial cell culture

Human umbilical vein endothelial cells (HUVEC) (C2519A, Lonza, Verviers, Belgium) were cultured in T75 flasks (353136, BD Falcon Fisher Scientific, Breda, the Netherlands) in 10 mL EGM-2 medium (CC-3162, Lonza) in a humidified incubator under standard conditions (37 °C and 5% $CO_2$). Cells were harvested (passage number 6) from the flask using trypsin in EDTA

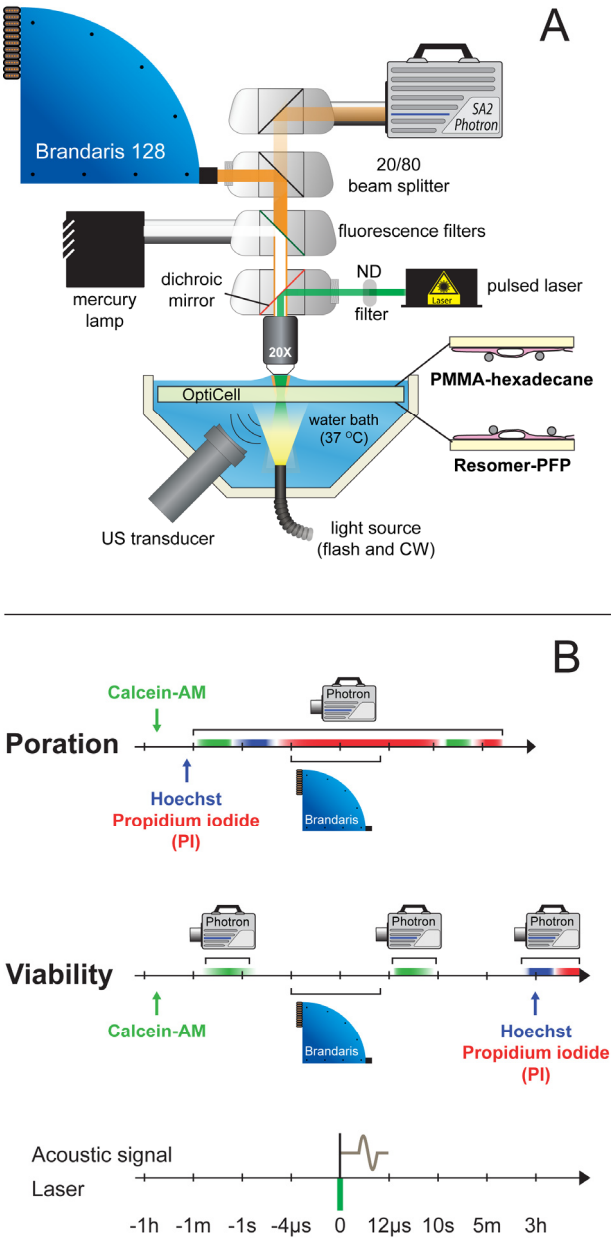


**Fig. 10.1.** Setup and timing. **(A)** Experimental setup comprising a temperature controlled bath in which the OptiCell® containing the cells and the capsules was immersed. An Olympus microscope was used for excitation by the laser, bright field recordings were made using the Brandaris 128 ultra-high-speed camera, and both bright field and fluorescent images were recorded using a Photron SA2 high-speed camera. A 1- MHz focused US transducer recorded the generated acoustic pressures. **(B)** Timing scheme for the poration and cell viability experiments.

(CC-5012, Lonza) and replated on one side of an OptiCell (Thermo Scientific, Nunc GmbH & Co, Wiesbaden, Germany) in 10 mL EGM-2 medium. Two days later the cells (passage number 6) reached 100% confluence and were ready to be used in the experimental setup.

**Experimental setup**

The experimental setup is shown in Fig. 10.1A. For visualization of the capsules and the cells, we used a fluorescence microscope (Olympus, Zoeterwoude, the Netherlands) equipped with a 20× water-immersion objective (UMPLFLN 20XW, N.A = 0.5, Olympus). For imaging in bright field, the sample was illuminated from below via a light fiber using a continuous light source (Schott, KL2500LED) and for fluorescence imaging we used a mercury lamp in an epifluorescent setup. In addition, a set of fluorescence filters was used for the detection of propidium iodide (PI, U-MWG2 filter, Olympus), Hoechst 33342 (U-MWU2 filter, Olympus), and calcein (U-MWIB2, Olympus). For excitation of the polymeric capsules a pulsed laser (8 ns, 532 nm, Quantel Evergreen 150 mJ) was directed through the microscope on the sample using a dichroic mirror. Different laser energies were used by adjusting the internal settings of the laser, the settings of a polarized attenuator, and a set of neutral density filters. The resulting energy coupled into the microscope was varied from 0.75 to 3.75 mJ for the PMMA-hexadecane capsules and from 0.23 to 2.25 mJ for the Resomer-PFP capsules.

Two cameras were used for imaging: a FASTCAM SA2 high-speed color camera (Photron Europe Ltd, Bucks, UK) for bright field and fluorescence imaging, and the Brandaris 128 ultra-high-speed camera [52, 320] for bright field recording of the laser-activated bubble dynamics. For enabling simultaneous recordings of fluorescence and ultra-high-speed bright field imaging a beamsplitter was used that directed 20% of the light to the high-speed camera and 80% of the light to the Brandaris 128 camera. The high-speed camera recorded at 50 frames per second (fps) and the Brandaris 128 ultra-high-speed camera recorded at 10 million frames per second (Mfps). Sufficient illumination was provided by a Xenon strobe light through the same optical fiber as the continuous light source.

The acoustic signal was received by a focused 1 MHz transducer (C302, Panametrics, 90% bandwidth) and was amplified 5× (SR445A, Stanford Research Systems Inc., Sunnyvale, CA, USA). The transducer was mounted in the water bath (37 $^{o}$C) at a 45$^{o}$ angle below the OptiCell. The optical and acoustical foci were aligned using a 0.2 mm metal needle. The acoustic signals were recorded using an oscilloscope (DPO4034, Tektronix, Beaverton, OR, USA) and were automatically saved to a computer using MATLAB (The MathWorks, Natick, MA, USA). The main trigger sent by the Brandaris 128 camera was received by a pulse-delay generator (BNC model 575) that in turn controlled the timing of the laser, the flash source, exposure of both cameras, and recording of the acoustic signals.

**Poration experiments**

The poration experiments were used to study permeabilization of the cell membranes by means of fluorescent stains. For visualization of live cells, we used calcein-AM (C3100MP, Molecular Probes, Life Technologies, Bleiswijk, the Netherlands), a dye that can passively cross the cellular membranes and is enzymatically converted into fluorescent calcein by live cells. We used the efflux of calcein also as a measure of poration [452], in combination with the inflow of the membrane impermeable model drug PI, that can only enter a cell when the membrane integrity is compromised [453, 454]. Before each experiment calcein-AM was added to the cells in the OptiCell (final concentration 0.4 μg/mL prepared from a 1 μg/mL stock in dimethyl sulfoxide (D5879, Sigma-Aldrich)) and was incubated for 40 min (37 °C, 5% $CO_2$). Prior to each experiment, PI (final concentration 25 μg/mL; P-4864; Sigma-Aldrich, Zwijndrecht, the Netherlands) and Hoechst 33342 (final concentration 5 μg/mL; H3570; Molecular Probes, Life Technologies) were added to the OptiCell. The Hoechst stain was used to label the nuclei of all cells, allowing for accurate cell counting. For the capsules, approximately $1\times10^7$ PMMA-hexadecane capsules or $2\times10^6$ Resomer-PFP capsules were added to an OptiCell containing a monolayer of HUVECs. The OptiCell was placed in a 37 °C water bath. The PMMA-hexadecane capsules float, so in these experiments the OptiCell was placed with the cells on the top membrane to ensure that the capsules were close to the cells. For the experiments on Resomer-PFP capsules, the OptiCell was placed with the cells on the bottom membrane, because these capsules sink (Fig. 10.1A). The timing of the poration experiments is illustrated in Fig. 10.1B. A field of view (FOV) with live cells, i.e. presence of calcein signal and absence of PI signal before laser-activation, was chosen and the high-speed camera recorded the initial Hoechst and calcein fluorescent signals. Immediately after that, a Brandaris 128 recording was initiated, the capsules were activated by the laser, and their dynamics were captured by the Brandaris 128 camera and PI uptake was simultaneously recorded using the high-speed camera. The fluorescence PI recording lasted for approximately 10 s after the Brandaris recordings had finished. 1-2 min after that, another PI fluorescence image set was recorded to assess the prolonged uptake caused by the vapor bubbles that were formed.

**Assessment of cell viability**

To assess long-term (3 h) cell viability, separate experiments were required in which PI was added 3 h after laser activation of the capsules, to visualize which cells had membranes that were still disrupted. A custom made grid was put on an OptiCell with a confluent layer of HUVECs to mark the same irradiated spot before and after incubation. Calcein-AM was used for staining live cells and was added 40 min before the experiment to a final concentration of 0.4 μg/mL in the OptiCell. Prior to starting the experiment approximately $1\times10^7$ PMMA-hexadecane capsules or $2\times10^6$ Resomer-PFP capsules were added. Directly after laser irradiation, the Brandaris 128 camera recorded the bubble dynamics in bright field and the

high-speed camera recorded the calcein signal before and after activation to assess live cells and poration. After the last recording the OptiCell was incubated for 3 h to study long-term cell viability. After this time had elapsed, PI and Hoechst were added to the OptiCell to a final concentration of 25 µg/mL and 5 µg/mL, respectively. Fluorescence was recorded again for calcein, Hoechst and PI at the same activation spot as before. The timing of the viability experiments is shown in Fig. 10.1B.

**Capsule and laser toxicity**

Next to the effect of the created vapor bubbles, the capsule toxicity and the influence of the laser intensity on the cells also had to be accounted for. Cell viability of HUVECs in the presence of PMMA-hexadecane and Resomer-PFP capsules (i.e. capsule toxicity) was assessed by means of PI staining in the viability experiments at locations without laser activation. Cell viability was defined as the ratio of live cells and the total number of cells ((number of Hoechst-stained nuclei - number of cells showing PI uptake)/number of Hoechst-stained nuclei). The total cell death count in the viability experiments was corrected for the cell death in the presence of the capsules alone, in principle to correct for cell death due to handling of the cells during the experiments. Next to toxicity of the capsules themselves, interaction with the laser could cause local heating of the cells due to absorption of the laser energy. To assess this effect we used Resomer-PFP capsules with similar composition, but in which no Sudan red 7B was incorporated in the shell, which prevented the capsules from vaporization upon laser irradiation. These experiments were performed with the highest laser intensities that were applied in our experiments.

**Image analysis and signal processing**

Data processing was performed entirely in MATLAB (The MathWorks, Natick, MA, USA). Image registration had to be performed, since the Brandaris 128 camera had a smaller FOV and was rotated with respect to the high-speed camera. A 2D cross-correlation method was used to register the fluorescence recordings with the corresponding bright field Brandaris recordings. The fluorescence images were contrast-enhanced to facilitate analysis, because the calcein images had limited signal intensity.

Automatic counting of the Hoechst stained nuclei (live and dead cells) and PI stained cells (porated or dead cells) was achieved through Gaussian convolution filtering (20 pixels, Gaussian width = 10 pixels) and thresholding (10 levels for an image depth of 8 bits) to filter the noise, and detection by counting the local image maxima (`imregionalmax` function). In order to extract the PI uptake curves, images were filtered using singular value decomposition (SVD) [455], after removal of the median pixel intensity taken from the part of the image that was not exposed to the laser. Finally, the pixel intensity was summed for each frame to produce a poration curve, which was later rescaled to the number of porated cells in the FOV. First, free fitting to an exponential curve was applied. Since the noise was

too large to allow reliable fitting of the two independent parameters, for all curves the characteristic time was fixed to be the median of the fitted characteristic times. This allowed a fit the amplitude in a second step. As an objective measure of the poration speed the initial velocity of the curve was calculated, which is represented by the prefactor (or amplitude) divided by the characteristic time. In most cases more than one bubble was formed within the FOV, we therefore report the average maximum radius of these bubbles.

The Brandaris recordings were used to extract the radius-time curves of the vapor bubbles, resulting from the laser activation. These radius-time curves were extracted using a MATLAB script developed in-house that was based on contrast compensation, image equalization, 2D convolution filtering, background subtraction and local thresholding. Pixel sizes were converted into micrometers using recordings of a test target with known resolution (USAF 1951 Resolution Test Targets, Edmund Optics, York, UK). The resulting set of images, radius-time curves, and cell counts were interpreted manually: PI uptake and calcein efflux were attributed to a bubble when this was in close proximity to the affected cell.

## 10.4. RESULTS

**Endothelial cell membrane poration by PMMA-hexadecane capsules**

Fig. 10.2 shows the result of a typical poration experiment using PMMA-hexadecane microcapsules. This figure shows the overlay of calcein and corresponding Hoechst signal of the cells (Fig. 10.2A) and the capsules and absence of PI uptake (Fig. 10.2B). The capsules just after laser-irradiation are shown in Fig. 10.2C, and an example of a radius-time curve is shown in Fig. 10.5E. The PI uptake curve of the sample, normalized to the number of bubbles in the FOV, is shown in Fig. 10.2D, where a clear increase in intracellular PI fluorescence intensity was observed after laser activation. Example frames from this fluorescence recording are shown in Fig. 10.2E and F; the time points of these frames correspond to the black dots in Fig. 10.2D. Panel E shows the same image as panel B, but now with background subtraction to remove the capsules and focus on the PI signal only. The contours of the vapor bubbles, which were tracked simultaneously, are superimposed on the PI images. The different lines indicate the contour of the bubble in separate frames of the recording. Another PI fluorescence image, taken after approx. 1 min is displayed in Fig. 10.2H. The fluorescence intensity in Fig. 10.2H clearly increased locally, and four cell nuclei became visible through increased PI fluorescence staining. The four affected cells were observed to be in direct contact with the vapor bubbles. Because the concentration of genetic material to which PI can bind is higher in the nucleus (DNA) than in the cytoplasm (RNA) [456], we only observed a clear signal increase in the nucleus. The overlay of Hoechst fluorescence recordings before and PI recordings after activation (Fig. 10.2G) clearly shows poration of three cells that were alive before laser-activation. The PI staining of the nucleus

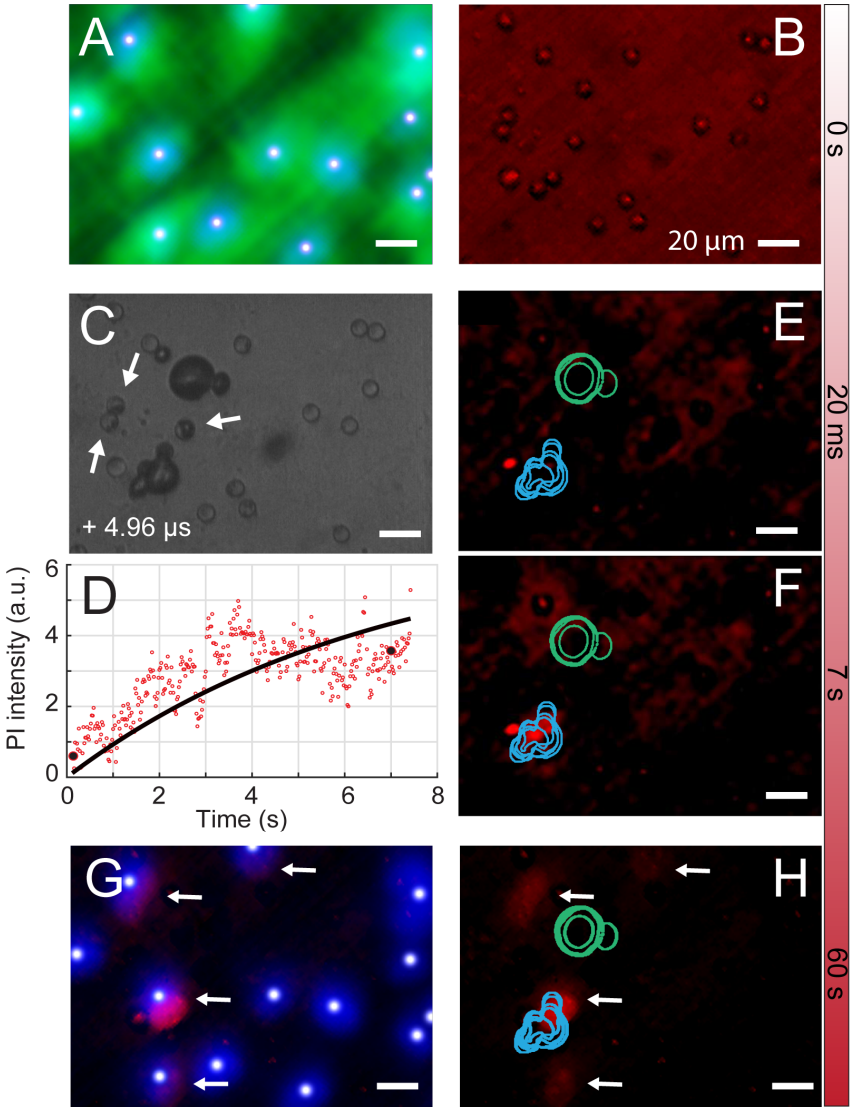


**Fig. 10.2.** Cell membrane poration PMMA-hexadecane capsules. **(A)** and **(B)** Set of images showing the situation before laser irradiation. The overlay of the calcein (green) and Hoechst (blue) images shows the presence of **(A)** live cells and the capsules and **(B)** absence of PI uptake. The white dots on the nuclei are the result of our automated counting algorithm. **(C)** Shows a frame of the ultra-high-speed recording during vaporization, in which the white arrows indicate internal bubbles that were formed. **(D)** Poration curve showing the increase in PI fluorescence intensity over time after irradiation by the pulsed laser. The black-filled red circles are the time points at which PI image E and F were recorded. The contours of the vapor bubbles are superimposed on the PI images. **(G)** and **(H)** Set of images showing the situation after activation. **(G)** The overlay of Hoechst before and PI after laser activation, shows the poration of three cells and **(H)** shows the PI fluorescence signal. The white arrows in G and H point to the porated cells.

shows slight displacement of the cells with respect to the location of the nucleus before the experiment.

It is interesting to note here that two different types of activation responses were observed for the capsules upon laser irradiation: a vapor bubble (termed "external bubble") or an "internal" bubble that can also be observed in Fig. 10.2C. In case of internal bubble formation, the PMMA coating does not break open and the gas probably forms by depolymerization [457] of the shell on the inner side, owing to the high temperatures that are reached in the polymer upon laser irradiation [57]. Fig. 10.2C shows several external bubbles, and three capsules formed internal bubbles (white arrows). We also observed that single floating capsules had a higher probability of producing internal bubbles than capsules that were close to each other.

Time-intensity curves as shown in Fig. 10.2D were obtained for a collection of 21 experiments, as displayed in Fig. 10.3A. The color of the curve relates to the size of the vapor bubble: the smallest bubbles (5 µm radius) are represented by light yellow colored curves, whereas the largest bubbles (40 µm radius) are represented by dark red colored curves. The initial poration speeds were extracted from the poration curves by means of an exponential fit and the result is displayed in Fig. 10.3A which shows a clear relationship: the larger bubbles induced faster intracellular uptake of PI. The resulting PI fluorescence rate is shown in Fig. 10.3B for each bubble radius.

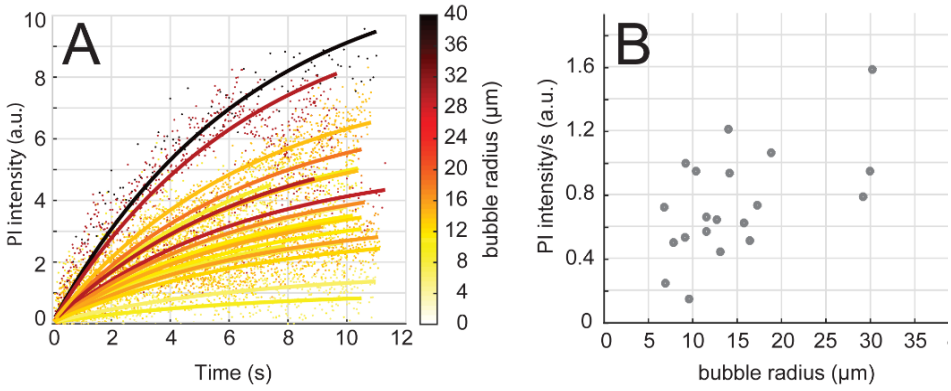


**Fig. 10.3.** Dynamic PI uptake. **(A)** Time-intensity curves of the PI signal (n = 21). The color of the curve corresponds to the size of the vapor bubble (color bar). The bubble size was measured from the Brandaris 128 recordings. **(B)** Slope extracted from the curves in A versus bubble size.

### Endothelial cell membrane poration by Resomer-PFP capsules

The same poration experiments were performed on the Resomer-PFP microcapsules and a typical example is depicted in Fig. 10.4. The overlay of calcein and Hoechst fluorescence

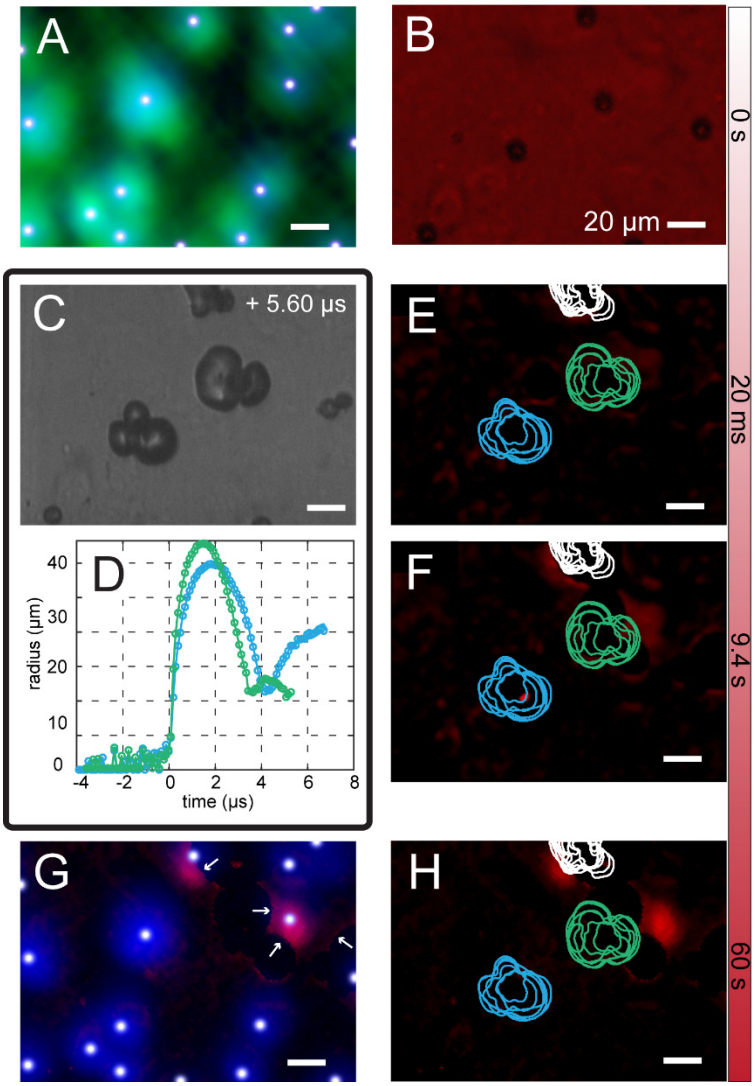


**Fig. 10.4.** Cell membrane poration Resomer-PFP capsules. **(A)** and **(B)**. Set of images showing the situation before laser irradiation. The overlay of the calcein (green) and Hoechst (blue) images shows the presence of live cells **(A)**. The white dots on the nuclei are the result of our automated counting algorithm. The PI fluorescence signal **(B)** shows that no dead cells were present in the FOV. **(C)** Corresponding frame of the ultra-high-speed recording showing the vapor bubbles created upon irradiation by the pulsed laser. **(D)** Radius-time curves of the bubbles in C. **(E)** and **(F)**. PI fluorescence pictures at two time points showing the uptake of PI by two cells, with the contours of the vapor bubbles superimposed on them. **(G)** and **(H)**. Set of images showing the situation after activation. The overlay of Hoechst before and PI after laser activation shows the poration of two cells **(G)**, with the white arrows indicating partial obstruction of PI signal. The PI fluorescence signal is shown in **(H)**.

images is shown in Fig. 10.4A and the capsules and absence of PI uptake are shown in Fig. 10.4B. The vapor bubbles generated by the capsules upon laser irradiation are shown in Fig. 10.4C, and the corresponding radius-time curves are shown in Fig. 10.4D. Fig. 10.4E and F show the evolution of the PI fluorescence intensity as a consequence of PI uptake by the cells that were porated, but now with background subtraction to remove the capsules and focus on the PI signal only. The contours during oscillation of the vapor bubbles are superimposed on Figs. 10.4E and F; the colors correspond to the colors of the curves in Fig. 10.4D. The affected cells were always in direct contact with a vapor bubble. Those bubbles created by Resomer-PFP capsules did not collapse, but remained on top of the cells. The bubbles then grew slowly over the few seconds during which the PI uptake was recorded. In Fig. 10.4G the small white arrows indicate bubble contours that partly obstructed the PI signal, and the difference between the green contour and the actual vapor bubble size in Fig. 10.4H shows the bubble growth over 1 min. This growth, leading to a false positive PI signal in the bubble core and to the partial obstruction of the PI signal from the porated cells, prevented extraction of reliable poration curves (Fig. 10.4H). As said, the bubbles did not float up which suggests that they adhered to the underlying cell layer.

**Cell viability after PMMA-hexadecane capsule activation**

Control experiments (n = 10, on average 16 cells in FOV) showed cell viability over 96% in the presence of PMMA-hexadecane capsules, but without laser irradiation. When the capsules were irradiated by the laser, both in the poration and viability experiments, some capsules did not vaporize presumably because insufficient dye was encapsulated in their shell. This offered a useful control experiment (n = 3, on average 18 cells in FOV) to assess how the combination of capsules and laser irradiation affected the cells; no PI staining was observed. As a consequence, cell death by means of PI staining in the viability experiments could be directly attributed to the vapor bubbles that were formed.

The cell viability experiments after activation of PMMA-hexadecane capsules (n = 29) were performed to assess whether the produced bubbles induced cell death. Fig. 10.5A shows a bright field image with the capsules floating below the cells before laser irradiation. Fig. 10.5B shows a calcein image before laser irradiation, while Fig. 10.5D shows the difference between the calcein image taken immediately after laser irradiation and that taken before. Comparison of the calcein signal in the white dashed circles in Figs. 10.5B and D reveal an intensity decrease after laser irradiation. This decrease is indicative of poration since calcein can only leave the cell when the membrane has lost its integrity [452]. The bubble contours extracted from the ultra-high-speed Brandaris recording are superimposed on Fig. 10.5D. The sizes of the vapor bubbles in the viability experiments ranged from 6.5 μm in radius for the smallest, up to 40 μm for the largest bubble. In the example shown in Fig. 10.5, the radii were between 7.5 and 12.5 μm, and the corresponding radius-time curves (Fig. 10.5E) show that the vapor bubble expanded, compressed, and stopped oscillating.

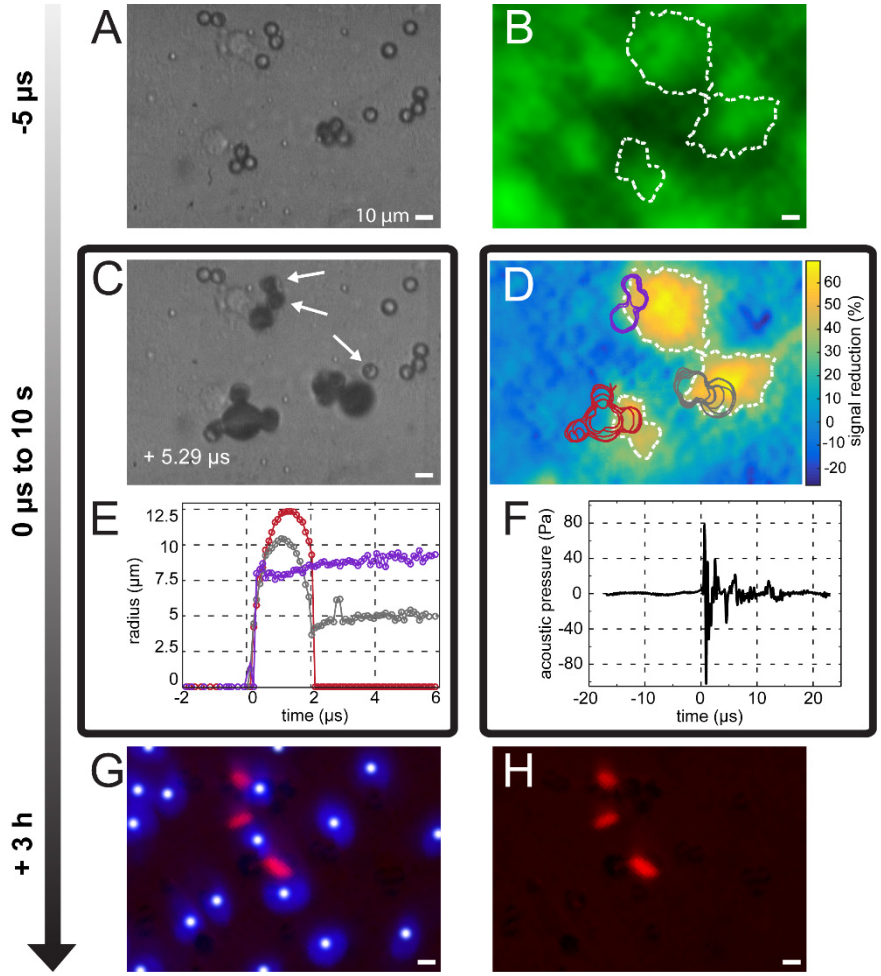


**Fig. 10.5.** Cell viability after PMMA-hexadecane capsule activation**. (A)** Bright field image of the cell monolayer with the capsules floating below them. **(B)** Fluorescence image of calcein used to stain live cells before laser irradiation. **(C)** Bright field image where the bubbles are visible, internal bubbles are indicated by the white arrows. **(D)** Image resulting from the subtraction of the fluorescence images of calcein recorded just after and the one recorded just before laser-activation. Yellow indicates the regions of calcein signal decrease. The contours of the bubbles, extracted from the Brandaris recording, are superimposed on the fluorescence image. The white dashed lines, identical to those in B, delineate the areas with more than 35% signal reduction. **(E)** Radius-times curves corresponding to the vapor bubbles in D, and **(F)** the acoustic signal of the vapor bubbles. **(G)** Fluorescence image showing nuclei locations stained by Hoechst and cells that had taken up PI. The white dots on the nuclei are the result of our automated counting algorithm. The image was recorded at the same location as A-D after re-incubation of the cells for 3 h. The re-incubation allowed live cells to move slightly on the membrane, resulting in the imperfect collocation of B and D on the one hand and G and H on the other hand. **(H)** Corresponding fluorescence image of PI uptake that shows the dead cells.

The lifetime of PMMA-hexadecane bubbles was found to be approximately 2 µs. Fig. 10.5F shows the acoustic signal emitted from the PMMA-hexadecane capsules. Fig. 10.5G shows the PI fluorescence image overlayed on the Hoechst stained cell nuclei. The cells that were stained by PI in this experiment (Fig. 10.5G and H) died within 3 h after PMMA-hexadecane capsule activation. The Hoechst and PI stained images were both recorded after a 3 h incubation period, so the cell nuclei exactly overlapped. However, the intensity of the Hoechst signal of cells that were stained by PI was considerably lower than for the other nuclei, which were therefore not detected using our tracking algorithm. This phenomenon has recently been described [372] and was attributed to Förster resonance energy transfer (also known as FRET) [425]. The PI stained nuclei in Fig. 10.5G appear smaller than the Hoechst stained nuclei; this shrinkage of cells and their nuclei after sonoporation has been described by others [458].

When comparing the cell nuclei locations in Fig. 10.5G to those depicted in Fig. 10.5D (brightest green), they do not exactly match. Our grid-approach ensured that the exact same spot within the OptiCell was located, but cells could have displaced due to cell division, cellular processes involving disruption of tight junctions, or simply by sample handling, because the OptiCell had to be moved from the setup to the incubator and back.

**Cell viability after Resomer-PFP capsule activation**

Control experiments of Resomer-PFP capsules without laser irradiation showed cell viability over 87% (n = 8, on average 20 cells in FOV). The control experiments with non-absorbing Resomer-PFP capsules (n = 10, on average 18 cells in FOV) showed only one single cell that had taken up PI. Since no bubbles were formed, this uptake of PI was not related to an activation event.

In the cell viability experiments with Resomer-PFP capsules (n = 37) similarly sized bubbles were formed as for the PMMA-hexadecane capsules (compare Figs. 10.5C, E and Figs. 10.6C, E). Before and after laser irradiation, calcein fluorescence images were recorded and the white dashed circles again indicate regions of interest where calcein signal had decreased (Fig. 10.6B, D), suggesting poration. In contrast to the PMMA-hexadecane vapor bubbles, the Resomer-PFP bubbles were capable of not only decreasing calcein signal, but completely depleting the signal (Fig. 10.6D, bottom circle). Interestingly, Fig. 10.6D shows that the PFP vapor bubble exactly co-locates with the center of the ring shape of the calcein fluorescent signal. The corresponding radius-time curve (Fig. 10.6E) and acoustic signal (Fig. 10.6F) of this PFP vapor bubble showed sustained oscillations after the laser was turned off. Fluorescence imaging after the 3 h incubation period showed Hoechst stained nuclei and PI staining of one cell. Due to the violent impact of the PFP vapor bubbles on the cells, parts of the cell monolayer were disrupted. It was therefore not always possible to correlate the cell nuclei (Hoechst) after laser activation (Fig. 10.6G), to the location of the cells before activation. This hindered a quantitative assessment of cell viability.

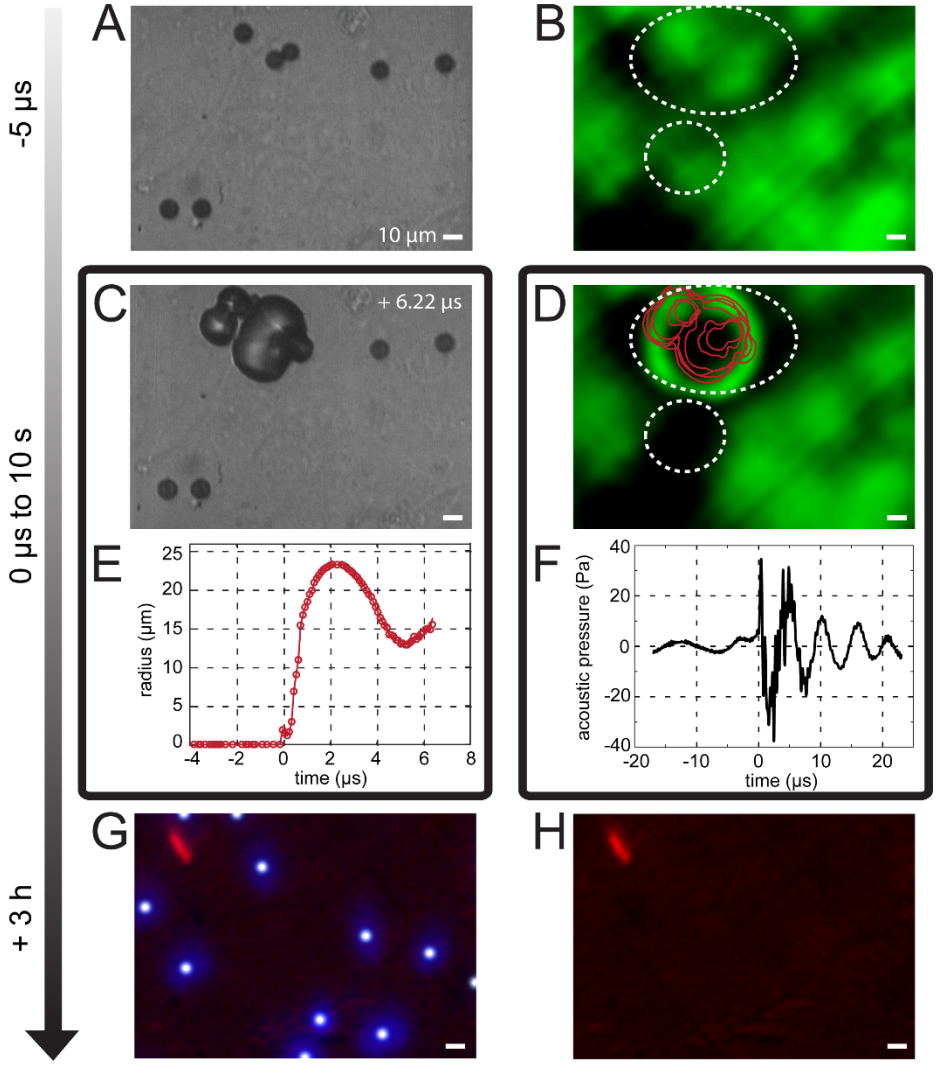


**Fig. 10.6.** Cell viability after Resomer-PFP capsule activation. **(A)** Bright field image of the cell monolayer with the capsules on top. **(B)** Fluorescence image of calcein used to stain live cells before laser irradiation. **(C)** Bright field image showing the vapor bubbles. **(D)** Fluorescence image of calcein just after laser activation. The bubble contours, extracted from the Brandaris recording, are superimposed on the fluorescence image. The white dashed circles, identical to those in B, show the locations where the calcein had depleted. **(E)** Radius-time curves corresponding to the bubble contours in B and **(F)** the acoustic signal of the vapor bubbles. **(G)** Fluorescence image showing nuclei locations stained by Hoechst and the white dots on the nuclei are the result of our automated counting algorithm. The image was recorded at the same location as A-D after re-incubation of the cells for 3 h. **(H)** Corresponding fluorescence image showing PI uptake and thus a dead cell.

The stable vapor bubbles (n = 44) that were observed in the calcein fluorescence recordings (example in Fig. 10.6D) ranged from 7.5 to 27 µm in radius, measured within 1 min after laser irradiation. The obtained size distribution of these stable bubbles is shown in Fig. 10.7.

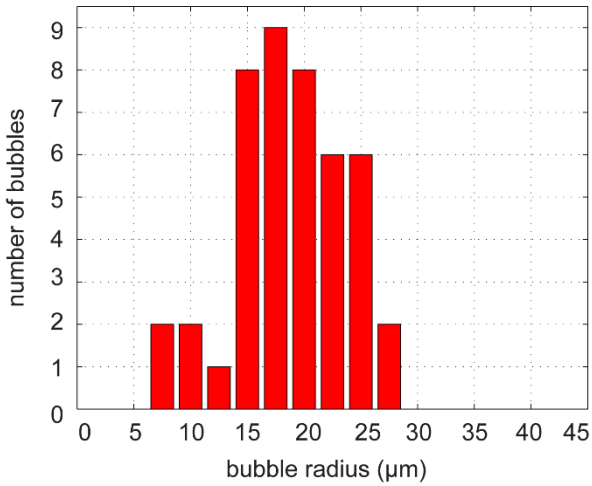


**Fig. 10.7.** Radii of remaining PFP bubbles**.** Bar diagram showing the size distribution of microbubbles that remained on top of the cells after laser-activation of the Resomer-PFP capsules.

**Comparison of formulations: PMMA-hexadecane versus Resomer-PFP**

A summary of the poration and cell death probability is shown in Fig. 10.8A and B for the PMMA-hexadecane capsules and Fig. 10.8C and D for the Resomer-PFP capsules. For the PMMA-hexadecane capsules only those that formed external bubbles were considered, since the internal bubbles never induced any cell poration and could not be sized. The bars in the figures are centered around the values on the x-axis, with a bin width of 5 µm. The bar centered at 5 µm thus includes bubbles between 2.5 and 7.5 µm. The numbers above the bars represent the amount of bubbles within each bar and the height of the bar indicates the average percentage of porated or dead cells due to a single bubble. The vapor bubbles larger than 45 µm could not be accurately sized, since they often expanded beyond the FOV of the Brandaris 128 camera (175.8 µm × 125.9 µm).

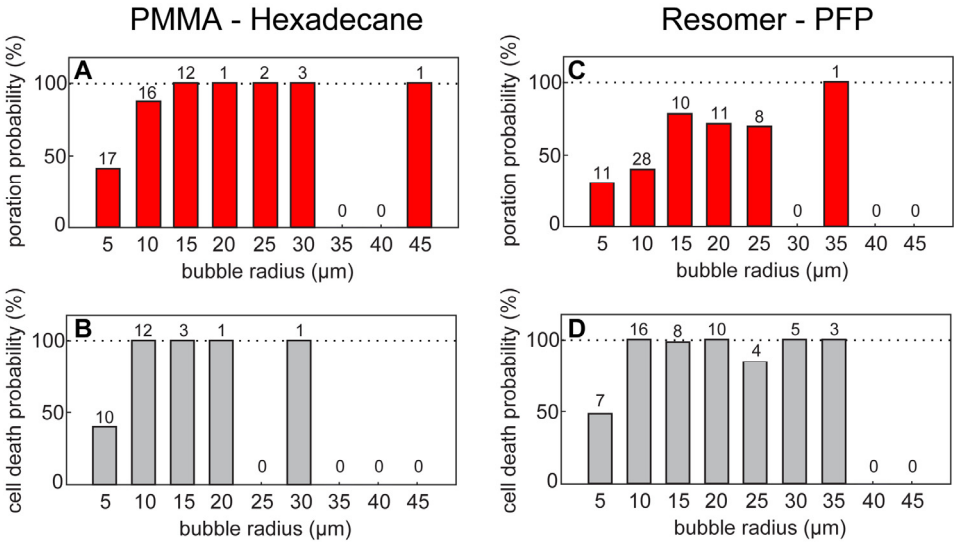


**Fig. 10.8.** Poration and cell death probability of PMMA-hexadecane and Resomer-PFP capsules. Bar diagrams showing the probability of poration (red) and cell death (grey) per bubble as a function of its maximum radius. The numbers above the bars represent the amount of bubbles within each bar, the bin width is 5 μm centered around the value on the x-axis. **(A)** Poration probability and **(B)** cell death for the PMMA-hexadecane capsules and **(C)** poration probability and **(D)** cell death for the Resomer-PFP capsules.

For both capsule types larger vapor bubbles had a higher probability of porating a cell. A PMMA-hexadecane external bubble < 7.5 μm had a ~40-45% chance of cell poration and of killing a cell in its vicinity. PMMA-hexadecane bubbles > 7.5 μm that were in contact with a cell resulted in 100% cell death (Fig. 10.8A and B). Since the poration experiments were performed separately from the cell viability experiments, the probability of killing a cell could be higher than the poration probability. This could explain the small difference (~10%) between the bar at 10 μm in the PMMA-hexadecane poration (Fig. 10.8A) and the cell viability experiments (Fig. 10.8B). At equal bubble size, Resomer-PFP bubbles had a lower probability of porating a cell than external PMMA-hexadecance bubbles. The poration probability increased for increasing bubble size, only reaching a near 100% probability for bubbles > 32.5 μm radius. Cell death, however, already reached this ~100% probability for bubbles of the same size as the PMMA external bubbles, i.e. > 7.5 μm.

### Acoustic characteristics

Fig. 10.9A and B display the recorded acoustic traces for PMMA-hexadecane capsules and Resomer-PFP capsules, respectively, for both the poration and viability experiments. The colormap encodes the size of the vapor bubbles. The transient existence of the bubbles generated by the PMMA-hexadecane capsules induced the generation of two large positive pressure peaks, corresponding to the fast bubble expansion and its violent collapse. The time delay between these peaks thus coincides with the lifetime of the vapor bubble (< 7.5 µs). The Resomer-PFP capsules on the other hand, only generated one large positive pressure peak, owing to the higher stability of the vapor PFP bubble that prevented the violent collapse. For these capsules prolonged low frequency oscillations were detected (> 25 µs), corresponding to the free oscillations of the created bubbles.

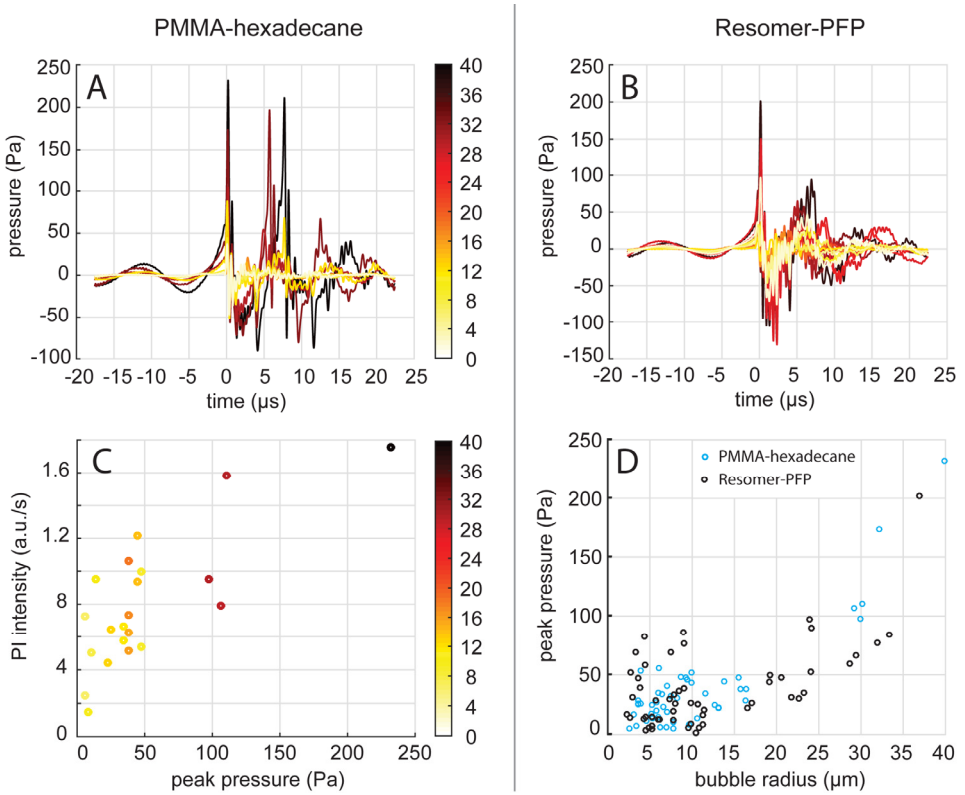


**Fig. 10.9.** Acoustic emissions from the microcapsules**.** Acoustic waveforms generated by **(A)** PMMA-hexadecane capsules and **(B)** Resomer-PFP capsules for diverse bubble sizes. **(C)** Initial rise of the PI intensity signal as a function of the generated peak acoustic pressure by vaporization of PMMA-hexadecane capsules, showing a clear relation. **(D)** Peak pressures generated by PMMA-hexadecane (blue circles) and Resomer-PFP capsules (black circles) as a function of the bubble size.

Fig. 10.9C shows the initial PI influx speed into the cell as a function of the bubble radius of PMMA-hexadecane external vapor bubbles, showing faster PI influx with increasing pressure. As a consequence, therapeutic effects may be monitored remotely by a measure of the acoustic emissions, using both the frequency content and the emitted peak pressure.

Fig. 10.9D displays the peak pressure that was generated as a function of the bubble size. It appears that vapor bubbles formed by both capsule types generated very similar pressure amplitudes (up to $P_{peak} \cdot r$ = 10 Pa·m, i.e. approximately 250 Pa for our transducer with 1.63 inch focal distance), also with a clear dependency on the bubble size: small bubbles (< 30 µm) generated up to 50-100 Pa, whereas large bubbles (> 30 µm) generated up to 250 Pa. One of our experiments resulted in only internal PMMA-hexadecane bubbles. The acoustic pressure emitted by these bubbles was ~15 Pa, which would be detectable by an US scanner [325].

## 10.5. DISCUSSION

Despite the capsules' size monodispersity, their responses were found to vary from capsule to capsule. Therefore, not all capsules could be activated upon irradiation at the same laser intensity. We therefore focused on single bubble events related to cell outcome, i.e. reporting bubble sizes rather than laser intensities. Less clustering of Resomer-PFP capsules was observerd than of PMMA-hexadecane capsules. More reactive capsule clusters creating multiple bubbles that merged were treated as a single bubble.

Since the boiling point $T_b$ of hexadecane ($T_b$ = 286,5 °C, PubChem CID 11006) is higher than that of water, the PMMA-hexadecane capsules vaporize the surrounding water [57], resulting in a water vapor bubble. In contrast, the Resomer-PFP capsules vaporize preferentially the lower boiling point PFP core ($T_b$ = 29 °C, PubChem CID 12675), which requires substantially less energy. We therefore applied higher laser intensities in our experiments on PMMA-hexadecane capsules. We verified that the highest laser intensity in the presence of non-absorbing capsules was not sufficient to directly kill cells. Nevertheless, the higher heat deposition on the cell monolayer could have influenced cell viability due to the short thermal shock wave for a duration of several microseconds. On the other hand, Fig. 10.8 showed no noticeable differences in cell death between PMMA-hexadecane and Resomer-PFP capsules, suggesting that the increased heat deposition had no significant influence on cell viability. It should be noted that because of the higher activation threshold, the laser intensities required to vaporize the PMMA-hexadecane capsules exceed the clinically allowed FDA limit [450].

Differences between poration and cell death by Resomer-PFP activated capsules were larger than expected. This apparent discrepancy can partly be attributed to the optical obstruction by the growing PFP bubbles, and partly by adsorption of the cell material onto the bubble (as further discussed later on). Such violent cell destruction may induce the

stained genetic material to flow away in the medium, which then cannot be recorded. In addition, cell death at the start of the cell viability experiments with the Resomer-PFP capsules was found to be already slightly higher than for the poration experiments, which could have resulted in overestimation of cell death for these capsules as well.

The probability that a cell in contact with a PMMA-hexadecane or Resomer-PFP bubble died, was as high as or higher than the probability that a cell was porated. This implies that either a PMMA-hexadecane or a Resomer-PFP vapor bubble in direct contact with a cell is lethal to this cell and viable poration was not achieved. In contrast, most studies on ultrasound-mediated sonoporation report that cells can be either viably porated or irreversibly damaged [34, 38, 372]. In terms of vapor bubble formation, phase-change agents that rely on acoustic vaporization are closer to the polymeric laser-activated microcapsules we used. These phase-change agents were smaller, and either showed mainly cell death and cell detachment [440] or both viable sonoporation and cell death [459]. The smaller vapor bubbles in our experiments resulted in less and slower PI uptake (see Fig. 10.5). This implies that, here as well, smaller capsules may be more suitable for inducing viable poration and may open up more possibilities for drug delivery. For the formation of bubbles having diameters of ~3 µm, the capsules should be down-sized to ~800 nm. Making them even smaller (< 200 nm) would allow for extravasation and increased penetration of the capsules into the tumor tissue of interest [449]. However, producing stable nano-sized particles is challenging and requires optimization of the manufacturing process. Consequently, here we first focused on micrometer-sized capsules. Secondly, the resolution of our ultra-high-speed imaging system is not sufficiently high for visualization of nanocapsules. Downsizing to nanocapsules and their impact on endothelial cells and extravasation capabilities should therefore be further investigated. For our PI uptake curves we used a mono-exponential fit, in line with Fan et al. [34] and van Rooij et al. [372]. In the poration curves we extracted after activation of PMMA-hexadecane some variation can be observed (Fig. 10.3B) at the same bubble size, probably owing to differences in the location of the capsules with respect to the surrounding cells. Next to that, our method of averaging the bubble size could have influenced the relation we observed. The x-axis in Fig. 10.3B represents the average bubble size in the FOV. Consequently, what appears as a 10 µm bubble could either be a single bubble of 10 µm or an average of for example a bubble of 8 µm and one of 12 µm. Since Fig. 10.8 showed that larger vapor bubbles induced more damage, the larger bubble of 12 µm would result in more damage. Nonetheless, the plot clearly shows a faster PI intensity increase for larger vapor bubbles.

After laser-activation of the Resomer-PFP capsules, the calcein fluorescence recordings showed a ring of bright fluorescence signal surrounding a non-dissolving vapor bubble (Fig. 10.6D). In previous *in vitro* experiments without cells the stability of similar bubbles was investigated [460]. Although these bubbles were generated acoustically, based on their

results the lifetime of the Resomer-PFP bubbles was expected to be less than a few milliseconds, while the size was expected to be only several micrometers. The interesting observation that Resomer-PFP bubbles were stable for several seconds and adhered to the underlying cells could possibly be exploited for additional contrast-enhanced US imaging. Further *in vitro* or *in vivo* studies should assess whether Resomer-PFP bubbles are also stabilized in the presence of flow. This observation aids further understanding of the biophysical response of the cells to these types of vapor bubbles. Since calcein-AM only becomes fluorescent when the AM part is enzymatically cleaved off by a living cell, the ring of fluorescence has to originate from the inside of a live cell of which the membrane was disrupted. Although only calcein was visible, it is likely that other cell constituents were also incorporated within the coating of these bubbles, since the cell had completely disappeared. This particular aspect would be worthwhile to investigate in future studies to aid better understand the interaction of the vapor bubble with the cellular membrane.

The activation energy could be even lower (up to 2×) by incorporating more Sudan Red 7B in the polymer shell. This, however, resulted in a morphology change from spherical capsules to acorn, or cup-shaped particles [461]. The PFP core of these particles is not completely enclosed by the Resomer, allowing easier access to the PFP core and thus a lower activation energy. Here, we also found that the poration probability of HUVECs was higher for the Resomer-PFP cups than for the Resomer-PFP capsules, consistent with the decrease in activation energy.

The work presented here aimed at studying the effect of laser-induced microbubbles on cells, in particular poration for enhanced drug delivery and cell death. In that regard, this study positions itself in the framework of photoacoustics where the penetration depth is known to be limited to a few centimeters. Consequently, only superficial tissues could be successfully treated. This represents the main limitation with respect to acoustically driven microbubbles as an alternative for enhancing drug delivery and locally controlling cell death.

## 10.6. CONCLUSIONS

We showed that laser-induced vaporization of polymeric microcapsules can porate and kill human endothelial cells. We studied PMMA-hexadecane capsules and Resomer-PFP capsules, of which the first formulation contained a high-boiling point oil and resulted in a higher degree of cell poration. Poration probability was already 40% for the smallest bubbles that were formed (< 7.5 µm diameter), and reached 100% for the larger bubbles. Cells that were in contact with a vapor bubble and that were porated, died. Because of the lower activation threshold of Resomer-PFP capsules, this type of capsules has the highest potential to be used *in vivo* to induce and monitor cell death. The internal capsules produced by laser-activation of PMMA-hexadecane microcapsules did not induce poration, while still producing a detectable acoustic signal. Finally, a clear relationship between the

acoustic emissions and the cell poration efficiency indicated a potential application for acoustic monitoring of the therapeutic action of such systems.

**Acknowledgements**

This work is supported by NanoNextNL, a micro and nanotechnology consortium of the Government of the Netherlands and 130 partners.

Chapter 11

# Feasibility of quantitative in vivo contrast-enhanced ultrasound imaging of the renal cortex in hemorrhagic shock

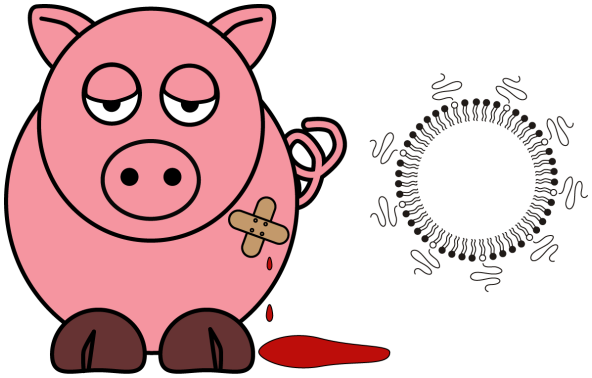

Tom van Rooij, Verya Daeichin, Alexandre Lima, Patricia A. C. Specht, Bulent Ergin, Yasin Ince, Can Ince, Nico de Jong, Klazina Kooiman

Chapter 12

# Renal contrast-enhanced ultrasound and sublingual video-microscopy identify microcirculatory dysfunction in acute kidney injury

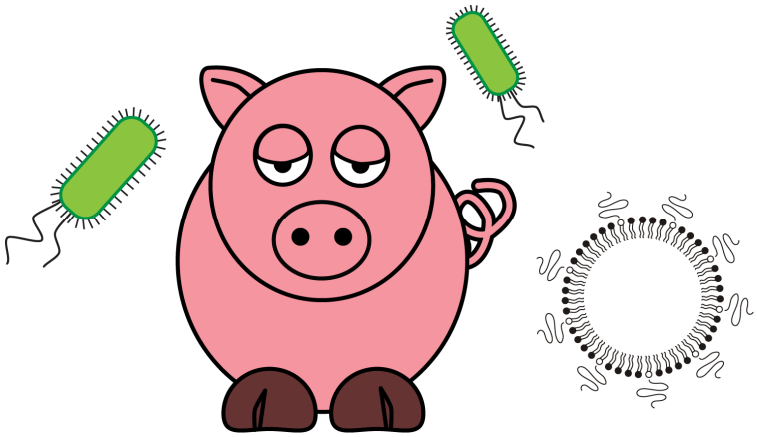

Tom van Rooij*, Alexandre Lima*, Bulent Ergin, Michele Sorelli, Yasin Ince, Patricia A. C. Specht, Egbert G. Mik, Leonardo Bocchi, Klazina Kooiman, Nico de Jong, Can Ince

(* both first authors contributed equally)

*In preparation for submission*

Chapter 13

# Cellular to systemic impact of microbubbles and ultrasound on the human body: potential risks and how to control them


Tom van Rooij, Guillaume Lajoinie, Klazina Kooiman, Nico de Jong, Michel Versluis, Ine Lentacker

## 13.1. ABSTRACT

The injection of foreign substances into the blood stream of a patient comprises several risks. Ultrasound contrast agents (UCAs), such as the microbubbles and echogenic liposomes that are described in this thesis, can induce strong mechanical and chemical effects on biological structures when combined with ultrasound. They therefore present potential risks that ought to be controlled. Here, we review these potential issues on the different length scales relevant to the problem to allow for safe use of UCAs.

## 13.2. INTRODUCTION

After decades of clinical use of UCAs [62, 68], clinicians and researchers have built-up a deeper knowledge of the behavior of microbubbles under ultrasound exposure [5, 31, 45, 68, 262, 511]. Extensive literature reporting on *in vivo* experiments [21, 120, 161, 271, 290, 335, 435, 512, 513] is available and clinical cohorts of tens of thousands of patients have been analyzed and published on the safety of microbubbles combined with ultrasound *in vivo* [22, 283, 514-516]. These datasets have been mainly used for retrospective analysis of scans performed with all generations of UCAs and a wide range of ultrasound parameters.

These studies, however, either report very specific conditions or effects on short time scales. Here, we review the information available concerning the potential risks of UCAs on the different length scales in order to gain a better overview of the impact of UCAs in combination with ultrasound on patients. We start with an overview of the impact of UCAs on a cellular level, continue to the tissue level and end with the systemic risks in clinical practice.

## 13.3. CELLULAR RISKS

### Cell poration

UCAs and ultrasound have become widely recognized as interesting drug delivery tools, due to the fact that oscillating microbubbles can increase cellular permeability and as such stimulate the uptake of cell-impermeable drugs [36]. Because microbubbles can temporarily disturb cellular membranes, the main risk factor is the impact of these cellular disruptions on cellular viability and functionality. As such, several methods have been used to study cellular viability after sonoporation. In general, the viability of sonoporated cells has been evaluated by including a small cell impermeable dye like propidium iodide during flow cytometry measurements [39, 517-522]. Because only irreversibly damaged cells will stay permeable for more than a few minutes after sonoporation, cellular uptake of these small molecular dyes allows for the determination of the percentage of dead cells. The main advantage is that both drug delivery efficiency and cell toxicity can be determined within

the same experiment. In general, cellular toxicity with these compounds has been reported between 5 and 20% depending on acoustic conditions [39, 518] and microbubble concentrations.

**Ultrasound parameters**

Since only direct microbubble-cell interactions are responsible for pore formation, acoustic conditions and microbubble concentrations [517, 522, 523] have been shown to have a major impact on the sonoporated cell area and its recovery process. Lower ultrasound pressures (50-200 kPa) mainly induce stable microbubble oscillations (stable cavitation) resulting in only small cell membrane disruptions originating from cavitation induced shear stresses that may arise. In contrast, higher ultrasound intensities (> 200 kPa) can cause violent microbubble collapse (inertial cavitation) leading to shock waves and jet formation [45]. These harsh conditions create micrometer-sized cell membrane disruptions and require complex cell membrane repair mechanisms to patch these disruptions [36, 524, 525]. The length of the ultrasound pulse is another acoustic parameter that influences microbubble behavior. Longer pulses at moderate ultrasound intensities can lead to microbubble translation due to acoustic radiation force [81, 406]. Translating microbubbles can impact cellular monolayers and may consequently cause direct cell disruption when they take part of the lipid membrane with them while translating. It has even been described that intact microbubbles can enter cells due to translational movements [41, 526]. A third ultrasound parameter which determines the level of cellular toxicity is the pulse repetition frequency of the applied ultrasonic wave. Karshafian et al. [39] showed that cell survival increases when the time between successive ultrasound pulses increases. They attributed this to two possible reasons: *1)* the fact that cells might be able to restore cellular damage within two pulses, or *2)* the fact that uncoated gas bubbles that can arise after microbubble fragmentation, already dissolve within the medium between two successive ultrasound pulses. As a result, the amount of cavitation events that can affect cellular membranes decreases.

**Microbubble-cell ratio**

Another important player is the microbubble concentration in relation to the number of cells. When higher microbubble concentrations are used, the microbubble to cell ratio increases, thereby increasing the amount of cell membrane pores per cell [522]. Related to this is the microbubble size, that can have a major influence on cell viability; larger microbubbles will lead to larger cell membrane pores and increase cellular toxicity [527]. The reason for this may be the fact that above a certain sonoporation threshold, cellular mechanisms fail to reseal the cell membrane as nicely demonstrated by Hu and colleagues [38].

### Induction of cell death

The use of small cell impermeable dyes only allows for identifying permanently permeabilized cells with flow cytometry, indicating the necrotic cell population. To gain more insight in cell death mechanisms associated with sonoporation, cells can be stained with annexin-V to determine the fraction of apoptotic cells. During apoptosis, phosphatidylserine, which is normally associated with the inner leaflet of the cell membrane, is exposed on the outer cell membrane surface and can hence be detected by annexin-V staining. Because inertial cavitation due to microbubble oscillation mainly induces cell necrosis when cell perforation becomes too violent, only a few sonoporation studies have been performed with annexin-V labeling. These studies reported the apoptotic fraction of cells to be rather small and in the order of 2-5% [528, 529].

### Chemical effects

Although the biophysical aspects of cavitation and imploding microbubbles have been the main subject of investigation when it comes to cellular toxicity, the influence of chemical components in microbubble formulations has often been neglected in literature. Honda et al. [529] used galactose-coated Levovist microbubbles to study apoptosis induction and found out that the fraction of apoptotic cells was elevated due to the hypertonicity of the medium, due to the high galactose concentration in the microbubble formulation. However, it is unlikely that clinically used doses are high enough to change blood isotonicity. It remains however poorly investigated how polymer shell fragments can be cleared from the body, while for lipid-coated microbubbles it is believed that released lipids and lipid micelles can enter normal lipid metabolism. The microbubble shell composition can also promote cellular uptake. Sonazoid microbubbles consist mainly of egg phosphatidylserine and are therefore recognized and quickly endocytosed by liver Kupffer cells and other phagocytic cells [530]. This makes these specific cells very sensitive to ultrasound as intact gas cores are remaining inside these cells [531]. On the other hand, the inclusion of PEGylated lipids within the microbubble shell can prevent opsonization and recognition of microbubbles by the immune system [262].

## 13.4. MEASURING CELL TOXICITY

### Cytometry

Although flow cytometry has been widely applied as a quick and easy method to screen the impact of acoustic variables on sonoporation-induced cytotoxicity, it also has some major disadvantages. Because only non-fragmented cells become visible within the scatter plot, cellular toxicity can be underestimated since completely lysed cells will not be detected [531, 532]. Moreover, it has been demonstrated that a part of adherent cells detaches [12, 533] during sonoporation, which means that these cells are not taken into account when

performing flow cytometry as they will be washed away during sample preparation. A good alternative can be to measure cellular toxicity with colorimetric assays like the ones based on the conversion of 3-(4,5-dimethylthiazol-2-yl)-2,5-diphenyltetrazolium bromide (MTT-assay) [534, 535]. These assays assess the metabolic activity of cells and account for the metabolic activity of all cells, even detached ones, when comparing them to untreated samples.

**Confocal microscopy**

Only recently, the impact of sonoporation on cellular morphology and functionality has been more thoroughly studied using more advanced techniques, such as confocal scanning microscopy. This enables not only registration of morphological changes like cell shrinkage [458, 529] and cell membrane blebbing [525], but even allows for studying more complex cellular mechanisms. Although a lot of debate is still ongoing on sonoporation induced toxicity, it is becoming clear that depending on microbubble-cell interactions, cellular toxicity can be divided in three main categories: *a)* complete cell lysis *b)* cell poration and *c)* more subtle effects like intracellular free radical production [536], endoplasmic reticulum stress, or cytoskeleton disassembly [33], leading to apoptosis or necrosis at a longer time scale. In this regard, Hutcheson et al. [527] have shown that cells which contained higher amounts of model drug expelled it again after several hours while the cells underwent apoptosis. These findings indicate the importance of evaluating clonogenic viability of sonoporated cells as evidenced by Karshafian et al. [523], who found that only 50 and 70% of the sonoporated cells was able to divide. In contrast, this might be less important for drug delivery studies dealing with gene delivery such as plasmid DNA (pDNA) or messenger RNA (mRNA) translation and subsequent protein expression, because these processes already indicate cell functionality.

**Acoustic monitoring**

To predict sonoporation and sonoporation-induced toxicity levels, researchers have also tried to correlate these effects with the total acoustic energy that was applied to the cells [518]. This, however, does not account for any differences in pulse length or pulse repetition frequency which also influence microbubble cavitation, as already mentioned above. An alternative and more realistic parameter is to register inertial cavitation activity by measuring broadband noise [517]. Although this is an interesting parameter during sonoporation studies, it still lacks several other variables like microbubble composition, size distribution and concentration which will in the end all influence microbubble-cell interactions and therefore drug delivery efficiency and sonoporation-induced cell damage.

## 13.5. THERAPY AND TOXICITY

It is obvious that sonoporation events are inevitably associated with a certain level of cellular toxicity. The balance between viably porated cells and irreversible damaged cells is however very delicate and it remains difficult to predict in which direction it will drift. Recently, van Rooij et al. [372] reported a relation between viably sonoporated cells and displacing microbubbles, and cell death and non-displacing microbubbles. They did, however, not relate this to the cellular behavior. Prof. Yu's group [33, 458, 525, 537] aims to gain detailed knowledge of cellular behavior in response to sonoporation, which may further clarify which microbubble-cell interactions are favorable to induce reversible cell membrane damage and maximal drug uptake. This knowledge can be used to select the most optimal ultrasound settings to stimulate identical cavitation behavior of recently developed monodisperse microbubbles and for achieving better controllable microbubble-cell interaction aiming to fully maximize sonoporation-assisted drug delivery and minimize the associated toxicity.

On the other hand, ultrasound induced membrane damage can be used as a major advantage as well [536], more specifically when sonoporation is applied as a tool to deliver chemotherapeutics to cancer cells. It has even been shown that this physical damage can be used to revert chemoresistance [538] and render cancer cells again sensitive to chemotherapeutics. This could be a very interesting strategy to treat blood cancers or lymphomas that can benefit from direct microbubble-cell interaction.

## 13.6. RISKS ON TISSUE LEVEL

### Chemical effects due to cavitation

Microbubbles can oscillate gently, and in a controlled way (stable cavitation) or violently and randomly (inertial cavitation). Inertial cavitation of a microbubble is typically achieved with high pressures at low frequency [539]. Locally, pressures can increase up to 100 MPa and temperatures can rise locally over 1000 K [539, 540]. These conditions are associated with certain chemical effects that may pose a risk to living tissue, such as the production of free radicals, sonoluminescence, and lysis of adjacent cells [539-541]. Free radicals are highly reactive molecules [539, 540] and can react with polyunsaturated fatty acids in cellular membranes, nucleotides in DNA, and sulfhydryl bonds in proteins [542]. This can result in cell damage and eventually cell death. Free radicals are produced in the final phase of bubble collapse, when the temperature and density of the gas increase rapidly. This results in the formation of ·H and ·OH free radicals, superoxide ($H_2O_2$), and nitrogen oxides [536, 540, 541] which react to stable molecules within only a few microseconds. Due to their high reactivity their radius of action is rather small, and the free radicals produced in blood can react with proteins and other molecules containing sulphhydryl groups (-SH) that act as free

radical scavengers. It has been shown *in vitro* that the aminoacids cysteine and cysteamine can protect the cell against free radical damage. When present in the blood, it has the ability to mostly cancel the effect of the free radicals produced by the cavitating bubble. Due to the free radical production, ultrasound therapies that rely on producing cavitation bubbles such as lithotripsy, could cause larger lesions when UCAs are still present in the blood.

Next to free radical production, inertial cavitation of microbubbles is also associated with lysis of erythrocytes (hemolysis) [540]. However, in animal models this effect has been shown to be lower than 4%, which means that it is almost without clinical importance. Mornstein et al. studied hemolysis in the presence of Albunex (2.17 MHz, 22.4 W/cm$^2$) and the effect was only present with hematocrit values < 10% [541], which is unrealistically low to be reached clinically. When the power was increased to 420 W/cm$^2$ lysis was achieved up to hematocrit values of 40%. Also, Hu et al. [244] reported reduced blood flow after destruction of bound targeted microbubbles due to aggregation of platelets as a response to endothelial damage (7 MHz, 2 or 4 MPa). Due to angiogenesis, this effect was expected to play a larger role in tumor vessels.

**Blood-brain barrier disruption**

In healthy individuals molecules larger than a few nm cannot cross the biological barrier between the blood and the brain [543]. This barrier is better known as the blood-brain barrier (BBB). Ultrasound-mediated blood-brain barrier disruption (BBBD) using UCAs is a promising technique for enabling drug delivery to the brain. This is generally only achievable with relatively high acoustic pressures (> 0.5 MPa) and low frequencies (< 1 MHz) [34, 544, 545], exactly the combination of parameters that are also associated with inertial cavitation and the production of free radicals, as discussed in the previous subsection. Other risks of BBBD include intracranial hemorrhage (0.98 MPa, 0.4 MHz, MI 1.6, in rats) [544], reduced cell viability *in vitro* (0.5 MPa, 10,000 cycles, on human embryonic kidney cells 293) [34], inflammatory reactions (0.9 MPa, 1 MHz, single exposure, in rats), formation of vacuoles, and degeneration (0.9 MPa, 1 MHz, two exposures, in rats) [545]. Although quite some risks might be associated with BBBD, in 2015 a team at Sunnybrook Health Sciences Centre (Toronto, Ontario, Canada) were the first to successfully open the BBB using a frequency of 220 kHz in a patient to deliver doxorubicin in a brain tumor, as part of a clinical trial (ClinicalTrials.gov Identifier NCT02343991). In addition, Carpentier et al. [546] reported monthly disruption of the BBB in 17 patients using an implantable US transducer (SonoCloud) and pressures of 1.1 MPa. Opening of the BBB was assessed by means of MRI and no detectable adverse effects were present. These studies show the feasibility and possibilities of BBBD opening using ultrasound and UCAs, but the perfect set of acoustic parameters and type of microbubbles still needs to be determined.

### Vascular damage

Cavitation caused by oscillating microbubbles has been shown to induce vascular damage. Hwang et al. showed that in an *in vivo* rabbit model endothelial damage was induced in blood vessels larger than capillaries when they contained UCAs [547]. This was attributed to inertial cavitation rather than thermal damage (threshold at 1.1 MHz and pressures between 1 and 3.35 MPa). This vascular damage has been confirmed by others in *ex vivo* rat venules (1 MHz, 1.5-5.6 MPa, 1 cycle) [548], chorioallantoic membrane tissue (1 MHz, 2.3 MPa, 10 cycles, PRF 500 Hz for 5 s) [549] and after histology on rabbit arteries (4.7 MHz, 9.5 MPa for 30 min) [550].

## 13.7. RISKS IN CLINICAL PRACTICE

Ultrasound contrast agent (UCA) injection has all kinds of possible risks associated with it when injected into the blood stream. Due to the injection, the possibility of an embolism cannot be ruled out (although unlikely as shown by animal studies) [551] and the patient could be extremely sensitive or allergic to one the components which can result in anaphylactic shock [22, 23, 552]. Next to that, a single burst of high intensity ultrasound during a cardiac contrast-enhanced ultrasound examination in diastole (T-P segment) can produce premature contraction in mammalian and amphibian hearts [553-555].

Other concerns may rise on the obstruction of vessels and the clearance of the microbubbles from the circulation; where does the gas end up, what happens to the coating components, how quickly is everything cleared, when can another dose be administered, what is the maximum dose, etc. Different UCAs that are marketed worldwide all have their own potential risks [551]. They differ in the type of gas in the core, the coating that is used for stabilization, and the solution in which the microbubbles are dispersed. Currently, five agents are approved for clinical use by regulatory agencies: Definity, Lumason, Optison, Sonazoid, and SonoVue [314]. In this section we evaluate the potential and proven risks that are associated to contrast-enhanced ultrasound (CEUS) examinations in clinical practice.

### CEUS contraindications

Nowadays, CEUS is approved for application in most organs: heart, liver, breast, vascularity, prostate, and many more [22, 23]. Especially in Europe, UCAs are used extensively off-label for other applications as long as no contraindications are present. These contraindications mainly comprise cardiac diseases, which exclude 10-35% of the world's population from undergoing CEUS examinations. Being overly careful in using UCAs for improving ultrasound imaging, medical professionals might have even increased patient risk; due to suboptimal image quality and the need for other techniques, such as CT and X-ray, patients have been subjected to ionizing radiation [551]. In addition to this, Kurt et al. [556] showed that UCAs

even had a positive impact on cardiac examinations: additional procedures were avoided or therapy changed in over 35% of patients.

Although, the risks of CEUS examinations have never been thoroughly and systematically evaluated, general consensus has been reached that UCAs are very safe and have a low incidence of side effects [23]. In contrast to contrast agents used for other modalities, such as CT, X-ray, or MRI, UCAs are not nephrotoxic, not toxic for the heart or liver, do not interact with the thyroid gland, and anaphylactic reactions have only been reported in less than 1 in 50,000 to 100,000 examinations [23, 557]. The risk for anaphylaxis is lower than for CT and X-ray, and similar to that for MRI contrast agents. However, as discussed before, the combination of ultrasound and UCAs can induce cellular effects such as sonoporation, hemolysis, and cell death. Although these effects have so far only been observed *in vitro*, or *in vivo* in small animals, it can most likely also occur in patients [23]. These risks become higher for increasing mechanical index (MI) and in hyperthermia. The MI is defined as the pressure (in MPa) divided by the square root of the frequency (in MHz) ($MI = P_A/\sqrt{f}$) and quantifies the probability to generate cavitation. According to the clinical guidelines the MI cannot exceed 1.9 and the maximum temperature rise with the use of ultrasound cannot exceed 1.5 °C [558].

**Dosing and clearance of UCAs**

The safety studies for the introduction of new agents as commissioned by the United States Food and Drug Administration (FDA) provide specific risks for different agents, but give an indication for the general safety of UCAs. First of all, the rules are much more stringent than for general clinical use, as for the clinical trials preceding the approval of, for example Definity, the maximum MI that could be used was only 0.8 [559]. In terms of dosing, it is recommended that an intravenous (IV) bolus injection does not exceed 10 µL/kg followed by a 10 mL saline flush, if necessary repeated 30 minutes later. For IV infusion the recommended rate is 1.3 mL in 50 mL saline, not to exceed 10 mL/minute [559]. Definity contains $C_3F_8$ gas which is stable and not metabolized. After injection of free $C_3F_8$ gas, i.e. not encapsulated, it was undetectable after 10 minutes in the blood and in the expired air. Blood concentrations declined monoexponentially with a mean half-life of 1.3 minutes in healthy subjects [559]. Definity is encapsulated by phospholipids [259] that are thought to be metabolized by the normal lipid metabolism to free fatty acids [559]. Although these tests have to be performed on each new agent, the results are not expected to be very different.

**Clinical experience**

After the introduction of UCAs in clinical practice, adverse effects such as anaphylactic shock and even death occurred, that could be associated to the CEUS examination. Several large cohort studies have contradicted these adverse effects and showed that the use of

UCAs is in fact very safe [283, 560, 561], even in children [562]. A retrospective study that compared the number patients that died after receiving either CEUS examinations with Definity (> 6000) or non-CEUS (> 12,000) examinations showed no significant difference between the two groups [561]. Another retrospective study at three different institutions included 42,408 patients who received UCAs and had baseline suboptimal images and/or underwent myocardial perfusion imaging and of which 18,749 underwent stress echocardiography [283]. The outcomes (death and myocardial infarction) within 30 min, 24 h, and during long-term follow-up were recorded; no difference was found when comparing this to a matched cohort of 15,989 patients who had not received contrast. Another, even larger study, of 80,000 injections of Optison and Definity attributed no deaths to the use of UCAs, and only 0.01% of the patients had probable severe reactions [516]. This study included over 10,000 injections in critically-ill patients in the ICU with acute chest pain or suspected cardiac origin. Hauben et al. performed disproportionality analyses on the adverse events that had been reported to the FDA between 1969 and 2014 on the use of Definity [563]. No relation was found between major cardiovascular events that were previously reported to be possibly associated with UCA injection, except for ventricular tachycardia and ventricular tachyarrhythmia. Even in critically-ill patients, the risks associated with CEUS are lower or equal than for other cardiac imaging methods such as transesophageal echo (TEE), and contrast-enhanced CT or MRI. Other studies even attributed a better survival rate to populations that underwent CEUS examinations versus a population that had not [515]. However, since no systematic risk analysis has been performed in different critically-ill patient groups, usage of UCAs in these patients is still not considered as completely safe. Soman et al. [564], studied the cardiopulmonary and hemodynamic effects after bolus injections of SonoVue (2 or 4 mL) in patients with severe left ventricular dysfunction, congestive heart failure, and in patients with pulmonary hypertension. Even in these patient groups, no significant effects were found following SonoVue injection. Other severe adverse events that have been reported in relation to UCAs are cardiac arrest, sustained ventricular tachycardia, and other cardiac arrhythmias [565], including premature ventricular contraction. Minor adverse events such as backache, headache, abdominal pain, chest pain, nausea, vomiting, and dyspnea have also been reported [514, 565].

## 13.8. CONCLUSIONS

Ultrasound parameters have been shown to be the main determinant for safe you use *in vitro* and consequently also in clinical practice. At pressures < 200 kPa microbubbles mainly undergo stable cavitation resulting in only minimal cell toxicity, whereas higher pressures induce inertial cavitation that can result in sonoporation and severe cell toxicity. Several research groups have aimed to pin point the acoustic parameters that results in maximum *in*

*vitro* and *in vivo* drug delivery efficiency, with minimal cell toxicity. However, so far no consensus on the optimal set of parameters for each specific application (e.g. local drug delivery or sonothrombolysis) has been reached. Although less research has been performed on tissue level than on single cells or cell populations, severe damage has only been reported when using MI > 1.9 and thus exceeding the clinically allowed limit. Blood-brain barrier disruption is a hot topic for which the settings are delicate, because it is best achieved at high acoustic pressures at low frequencies, ideal for inducing inertial cavitation. Now the BBB has been successfully opened in a patient, the way is paved for more clinical studies to establish the perfect set of acoustic parameters for this procedure and to map the associated risks. For the clinical areas that have already recognized the usefulness of UCAs, the risks associated with CEUS have been proven to be lower than for any other imaging modality that uses contrast agents, such as CT or MRI.

## 13.9. OUTLOOK

Of the most innovative applications, e.g. enhanced gene therapy, local drug delivery, and sonothrombolysis, little to no information is available on the long-term effects on the tissue or systemic level. Many biological pathways that can lead to cell survival or cell death have been observed *in vitro* on single cells or cell populations, but future research should focus on long-term systemic risk assessment in order to successfully bring those techniques to the clinic. In addition, for every new UCA formulation that will be marketed for clinical use, a thorough risk analysis should be performed to assess possible toxicity and the specific clearance pathways.

Chapter 14

# Discussion & Outlook

## 14.1. OVERVIEW

The research in this thesis describes the oscillatory behavior of single microbubbles, both targeted and non-targeted and their use for local drug delivery and locally induced cell death. A thorough evaluation of the contrast agents that have been used in our lab over the past few years was performed *in vitro* and was also tested in our *in vivo* experimental model of acute kidney injury. These *in vivo* experiments were conducted on pigs to study hypovolemic shock due to hemorrhage and sepsis-induced acute kidney injury, two major causes of hospital deaths. In addition, two other classes of ultrasound contrast agents were investigated: echogenic liposomes and laser-activated polymer microcapsules. Lastly, we focused on the risks associated with the use of microbubbles and ultrasound on the cellular level, tissue level, and on clinical patient outcome.

## 14.2. PERFORMANCE OF DIFFERENT TYPES OF ULTRASOUND CONTRAST AGENTS

Nowadays, mostly the same contrast agents (e.g., SonoVue and Definity) are used for applications in the clinic, as well as for preclinical research. Clinical investigations are generally performed at low frequencies (typically around 1 – 2 MHz) to ensure significant penetration depth. Especially for preclinical research in mice, rats, and other small animals, high-frequency ultrasound scanners such as the Vevo 2100 (FUJIFILM VisualSonics Inc, Toronto, ON, Canada) are usually used to obtain high resolution images. Ultrasound contrast agent detection with these high-frequency scanners is optimal when the agents comprise small microbubbles, because of their high resonance frequencies. Since SonoVue contains microbubbles with relatively large diameters [7], these are not suited for high-frequency contrast imaging. Definity microbubbles, on the other hand, are smaller [9], and provide good contrast *in vivo*. However, flexibility of commercially available ultrasound contrast agents is low.

In **Chapter 3** we compared different methods of ultrasound contrast agent (UCA) fabrication for high-frequency contrast-enhanced ultrasound imaging (CEUS), either based on DSPC (C:18) or DPPC (C:16). Although the most common method of UCA production is sonication [264], the vial shaking method is easier and quicker. We showed that this method is highly reproducible and resulted in small microbubbles with similar *in vitro* and *in vivo* performance as Target-Ready MicroMarker (FUJIFILM VisualSonics Inc). The first selection criterion was the scattering power *in vitro* at 15 MHz in B-mode (1% power, 1 cycle). After selection of the two best performing UCAs made by sonication and the two best performing UCAs made by vial shaking, their fundamental and subharmonic responses were compared at 30 MHz transmit frequency (pulse inversion, 10% power, 20 cycles). Two UCAs made by vial shaking were most similar to Target-Ready MicroMarker: formulation F (DSPC-based) and L (DPPC-based). The performance of those three UCAs was compared in an *in vivo* pig model on the exposed kidney. We showed that contrast enhancement of our UCA

formulation L did not provide sufficient contrast to even distinguish the larger vessels. This formulation was therefore not further studied. Contrast enhancement for formulation F was slightly lower than for Target-Ready MicroMarker, but also resulted in less signal loss with increasing depth than Target-Ready MicroMarker. The latter implies lower attenuation for our formulation F. Our in-house produced UCAs can therefore compete with the commercially available Target-Ready MicroMarker and offer additional options for other targeting moieties than biotin-streptavidin, which cannot be used clinically due to reactions of the immune system [80]. The design and fabrication of smaller agents as described in **Chapter 3** offers increased versatility for targeting and can increase the resolution of high-frequency contrast-enhanced ultrasound imaging. In addition, the possibility to produce these agents in-house could greatly reduce the costs of preclinical research. Our study also shows that the development of new contrast agents should encompass both *in vitro* and *in vivo* studies: imaging of microbubbles *in vitro* in a controlled and simplified setup is essential before translation towards complex *in vivo* applications in which e.g. blood pressure, the immune system, and clearance by the Reticulo Endothelial System (RES; i.e. the lung and liver) play a role. In addition, agents performing well *in vitro* may not do so *in vivo,* as was the case for our L formulation.

The underlying reason for the difference in contrast enhancement between the DSPC-based formulation F and the DPPC-based formulation L is the difference in properties of the microbubble shell and the subsequent acoustic behavior. In **Chapter 4** we showed by means of super-resolution microscopy that the lipid distribution in the shell of DPPC-based microbubbles is more homogeneous than that of DSPC-based microbubbles. Optical ultra-high-speed Brandaris recordings revealed higher acoustic stability and a stiffer shell of DSPC-based microbubbles (**Chapter 5**) and may explain the longer contrast persistence of UCA formulation F *in vivo* (**Chapter 3**). We attributed the lower acoustic stability to the shorter acyl chain length of DPPC and the resulting lower intermolecular van der Waals forces between the individual lipids [49]. Additional fluorescence ultra-high-speed recordings using the UPMC Cam suggested irreversible collapse of the DSPC-based microbubble shell when the microbubble acoustically deflated (**Chapter 7**). Combined with the higher compressibility rate [278, 279] and lower ability of DPPC lipids to re-adsorb on and re-spread as a monolayer [376] over the microbubble surface during expansion, this may also explain the lower acoustic stability of DPPC-based microbubbles. Next to that, Garg et al. [50] showed that without ultrasound application the *in vivo* contrast persistence in rat kidneys of DSPC-based microbubbles was ~5× higher than that of DPPC-based microbubbles. Our *in vivo* comparison in **Chapter 3** also revealed higher mean intensities in the three ROIs in the kidney; 15× higher in ROI 1, 6× higher in ROI 2, and 2.5× higher intensity in ROI 3. Next to a higher stability, DSPC-based microbubbles scattered four times higher second harmonics than DPPC-based microbubbles.

Next to the DSPC and DPPC-based microbubbles we also investigated echogenic liposomes (ELIP) in **Chapter 6**, which are another type of lipid-coated UCAs. For the first time, individual ELIP were characterized and found to have similar viscoelastic properties as other lipid-shelled agents, such as SonoVue [127, 331], Definity [128, 326], and our own lipid-coated microbubbles (**Chapter 5**). This is surprising, since the air in the core was expected to result in differences in oscillatory behavior. However, the main goal of this study was trying to also identify whether the shell is a lipid monolayer or a multilamellar shell. Multilamellar vesicles, in which the lipid monolayer immediately adjacent to the gas bubble is surrounded by one or more bilayers, have been previously observed in transmission electron microscopy images of ELIP [348]. The variation in the shell viscosity estimates for ELIP of similar size may indicate the presence of multilamellar vesicles, where the apparent viscosity depends on the number of lamallae. The new method we introduced to study the damping coefficient based on the impulse response is a more efficient approach than the spectroscopy technique used previously [18, 20, 342] and in **Chapters 5** and **8**.

## 14.3. LIPID COATING AND ACOUSTIC BEHAVIOR

The research described in this thesis has improved our understanding of the influence of lipid composition on the microbubble microstructure, lipid movement, and acoustic properties. This may aid in the quest for the perfect lipid coating that results in identical microbubble behavior in order to accelerate the translation of ultrasound molecular imaging and drug delivery towards the clinic. For these purposes the perfect lipid coating should ensure *1)* an identical shell composition for each single microbubble, *2)* stability upon ultrasound insonification, *3)* a monodisperse size distribution, *4)* effective binding to the biomarker of interest, and *5)* persistent binding under flow. These requirements have, however, not all been met. To ensure a homogeneous and uniform shell (*requirement 1*), the different components have to properly mix [70]. The components of our in-house produced DPPC microbubbles do mix as demonstrated by a homogeneous shell distribution, but lack sufficient acoustic stability (*requirement 2*). Other lipids such as DSPC or 1,2-dibehenoyl-sn-glycero-3-phosphocholine (DBPC, C:22) increase the stability as shown in this thesis and by others [50, 285], but result in heterogeneous shell distributions [47, 48, 377]. Another route would be investigating other lipids as coating that are all in the same phase. Other types than phosphocholines, the class of lipids to which DPPC and DSPC belong, for example phosphoethanolamines such as DPPE, could be worth investigating further. DPPE lipids have the same phase as DPPC, but have a smaller head group and may therefore increase lipid packing and acoustic stability. This is also likely the reason why the clinically used Definity microbubbles are stable *in vivo* because the coating formulation contains DPPE in the form of DPPE-PEG(5000) [9]. Monodisperse microbubbles can already be produced [16, 385, 397, 398] and have less variability in their response than polydisperse microbubbles

(*requirement 3*). Additional contrast-enrichment methods such as acoustic bubble sorting by means of their acoustic response [399], have further decreased the variability in their resonance frequencies. In terms of biomarker binding (*requirement 4*) the surface area of our DPPC-based microbubbles was larger than that of our DSPC-based microbubbles, but studies on binding strength and persistence under flow (*requirement 5*) should be performed in the future. Possible experimental approaches to study microbubble adherence and persistence under flow could be the OrganoPlate® cell-culture platform (MIMETAS B.V., Leiden, the Netherlands) or the *in vivo* CAM model.

## 14.4. BOUND VERSUS NON-BOUND MICROBUBBLES

For molecular imaging, the microbubbles need to be targeted to the desired point of action by means of functionalization of the microbubbles, which is likely beneficial for microbubble-mediated local drug delivery and induced cell death. An overview of the functionalization methods and techniques to enhance binding have been described in **Chapter 2** and include functionalization of the microbubble coating with antibodies, nanobodies, or peptides. To increase the imaging speed of ultrasound molecular imaging and to enhance specificity, it would be desirable to be able to discriminate microbubbles that have bound to their biomarker from those that are freely floating in the blood vessel. Previous studies described conflicting differences in the acoustic responses between bound and non-bound microbubbles [136, 139-142]. One of the reasons for these discrepancies can be found in the method of linking the biomarker to the surface, because most researchers used physisorption, which was shown by Kooiman et al. [23] to result in detachment of the biomarker from the surface and adherence to the microbubble shell. In **Chapter 8** we therefore covalently linked the biomarker to a hydrogel in order to prevent detachment. Our study thus shows for the first time a fair comparison between identical bound and non-bound microbubbles, and also compared our in-house produced DSPC-based with DPPC-based microbubbles. Binding of DPPC-based microbubbles to a streptavidin-coated surface induced acoustic deflation at both low and high pressures. In addition, the resonance frequency and the corresponding relative radial excursions increased at relatively low pressure (50 kPa). At this pressure, bound DPPC-based microbubbles with diameters at resonance between ~2 and 4 μm had resonance frequencies > 1.8 MHz, while those were < 1.8 MHz for non-bound DPPC-based microbubbles. These findings may be useful in this experimental setting, but these differences were not present at 150 kPa, a pressure closer to those applied clinically. The differences in nonlinear responses did not significantly change for bound microbubbles, which implies that the nonlinear responses cannot be exploited to discriminate bound from non-bound microbubbles. Since the differences in resonance frequencies were not present at higher pressures, we could not provide parameters to be used to discriminate bound from non-bound microbubbles acoustically at

clinically relevant pressures. Because the acoustic behavior of microbubbles in blood has been shown to be different than in an aqueous solution [342], the next step in trying to achieve this separation would be *in vivo* experiments, for example on the chorioallantoic membrane (CAM) of a chicken embryo. This can be combined with ultra-high-speed imaging [233, 342] to compare the responses of single bound and non-bound microbubbles.

## 14.5. DRUG DELIVERY AND CELL DEATH

The effects of targeted (bound) and non-targeted (non-bound) microbubbles on human endothelial cells is described in **Chapter 9** in terms of microbubble oscillation and displacement. We derived different patterns of PI uptake from the previously published diffusion model by Fan et al. [34] and correlated these patterns with cell viability using Principal Component Analysis and additional thresholding. Microbubble displacement enhanced drug delivery and preserved cell viability, while non-displacing microbubbles were the main contributor to cell death. Although long ultrasound pulses have been shown to increase sonoporation efficiency [40], these have only sparsely been used to study sonoporation [40, 407-409]. Therefore, we applied long pulses (500 – 50,000 cycles) at pressures ranging from 150 – 500 kPa at a frequency of 1 MHz. Our results show that non-targeted microbubbles exposed to an acoustic pressure of 500 kPa and a pulse length of 1000 cycles would be most beneficial for drug delivery. For therapeutic applications where high cell death is desired, such as cancer therapies, high pressures and long pulses should be applied (e.g., 500 kPa and 50,000 cycles). Both targeted and non-targeted microbubbles were shown to effectively kill cells, but the non-targeted ones were more efficient. Others that used shorter pulses found higher cell viability [34, 403] which may be the direction to improve sonoporation efficiency and thus drug delivery.

Based on all observations made in this thesis, DSPC-based microbubbles are recommended for CEUS imaging. On the other hand, the lower threshold for the generation of subharmonics, the larger binding area, and the more homogeneous shell of DPPC-based microbubbles seem more advantageous for molecular imaging and targeted drug delivery. However, the lower *in vitro* and *in vivo* stability might be the bottleneck.

As a different method for localized drug delivery and cell death, we studied polymer microcapsules that were activated upon irradiation with a pulsed laser (**Chapter 10**). The theory and experimental validation of the activation of these types of microcapsules have been described by one of my collaborators [15, 57]. To assess the imaging and therapeutic windows and the theranostic potential of these capsules, we performed the experiments in the presence of human endothelial cells. We showed that laser-induced vaporization mediated by two different types of polymeric microcapsules can porate and kill human endothelial cells. The PMMA-hexadecane capsules contained a high-boiling point oil and resulted in more poration than the low-boiling point Resomer-PFP capsules. Poration

probability was already 40% for the smallest bubbles that were formed (< 7.5 µm diameter), and reached 100% for the larger bubbles. Cells that were in contact with a vapor bubble and that had taken up PI, all died. Because of the lower activation threshold of Resomer-PFP capsules, this type of capsules has the highest potential to be used *in vivo* to induce and monitor cell death, for instance to monitor tumor treatment. The internal capsules produced by PMMA-hexadecane did not induce poration, while still producing a detectable acoustic signal and may therefore open up opportunities for ultrasound contrast imaging.

The laser-activated polymeric capsules (**Chapter 10**) more efficiently induced cell death than lipid-coated microbubbles (**Chapter 9**), but their effects were less controlled. When the size of the capsules can be decreased to nanometer scales and when the dye concentration in the coating of each microcapsule would be identical, their vaporization can be better controlled. Due to the limited penetration depth of the laser that is required for activation only superficial organs can be treated, such as superficial tumors. Because of their oil core they also have a large reservoir that can be loaded with hydrophobic cytostatic drugs to not only kill cells by the vaporization of the oil, but also aid drug delivery. In addition, the feasibility of *in vivo* laser-activation and the potential risks associated with the violent vaporization of microcapsules should be assessed. Although currently used UCAs are very safe (**Chapter 13**), for each new type of agent new risk assessments should be performed.

## 14.6. CLINICAL APPLICATION OF ULTRASOUND MOLECULAR IMAGING AND THERAPY

Although the therapeutic application of ultrasound contrast agents has already been shown *in vitro* in 1997 by Bao et al. [231], sonoporation has still not found its way to daily clinical practice. The first clinical trials for inducing sonoporation, however, have already been conducted and used the commercially available non-targeted contrast agents SonoVue [546, 566] or Definity (ClinicalTrials.gov Identifier NCT02343991). The most efficient approach towards clinical translation of drug delivery by means of sonoporation would be using those clinically approved agents. In case of targeted microbubbles for ultrasound molecular imaging and drug delivery the most logical step is using BR55 (Bracco Diagnostics, Milan, Italy). These lipid-coated microbubbles are targeted to the angiogenesis biomarker VEGFR2 [84] and have been shown to effectively bind to HUVECs *in vitro* and accumulated *in vivo* in tumors in mice. Since clinical trials with this agent have already been carried out for ultrasound molecular imaging of the prostate (ClinicalTrials.gov Identifier NCT02142608), the chances of successful translation for molecular imaging are expected to be the highest. As a next step, contrast agents targeted to other biomarkers can be developed for ultrasound molecular imaging. For drug delivery additional steps have to be taken; the risks and most efficient settings for sonoporation in different tissues need to be evaluated in preclinical studies using BR55. Based on our own work (**Chapter 9**) and that of others [34, 35, 37, 38, 234, 403], we recommend starting with the following settings: short

pulses (< 100 cycles), moderate pressures (in-situ < 200 kPa), a frequency between 1 and 2 MHz, and microbubbles with mean diameters between 4 and 5 μm .

The imaging and therapeutic windows of laser-activated polymer microcapsules have been assessed in **Chapter 10**, but several steps have to be taken before this technique can be used in patients. Advantages of the microcapsules are their monodisperse size, efficacy of inducing cell death, smaller microbubbles that resulted in slower uptake op the model drug by the cell, and the stabilized Resomer-PFP microbubbles that may be used for imaging. These advantages could be further optimized by decreasing the size of the capsules to < 200 nm to allow for extravasation into tumors by means of the enhanced permeability and retention (EPR) effect, and possibly even enabling viable poration of cells for drug delivery. What has to be further studied and understood is the mechanism responsible for the large stabilized Resomer-PFP microbubbles which may pose embolization risks, due their size. Next, the internal PMMA-hexadecane bubbles may be used for imaging, but understanding of the formation process and how to control it requires further research.

## 14.7. CEUS FOR DIAGNOSIS OF ACUTE KIDNEY INJURY

The potential of CEUS for diagnosis and monitoring of acute kidney injury in pigs was studied in two models: hypovolemic shock induced by severe hemorrhage (**Chapter 11**) and septic shock (**Chapter 12**). We were able to detect a larger difference in contrast arrival time between the small arteries and the microcirculation in the renal cortex in hemorrhagic shock, which increased again upon fluid resuscitation. This change in arrival time can be used as a measure for the intrarenal velocity in hypovolemic shock and for fluid therapy monitoring. In addition to that, the flow and peak-enhancement in the microcirculation were found to increase. This is possibly caused by a higher relative microbubble concentration and opening of more capillaries in the microcirculation to ensure enough transport of oxygen in shock and when the blood pressure drops below 50 mmHg vasoconstriction to compensate for the decrease in flow. During resuscitation, flow decreased again towards baseline values. In septic shock, flow and peak-enhancement decreased and further decreased during resuscitation. This decrease in peak-enhancement after fluid resuscitation shows that the microcirculatory alterations persisted, despite restoring systemic hemodynamics and fluid balance. In addition to that, capillary vessels get plugged in sepsis [488-490] and we derived a new parameter (final plateau intensity/peak intensity) in order to quantify this. In both studies, CEUS results were confirmed by laser-speckle imaging on the kidney and by sublingual Cytocam-IDF imaging. We found that sublingual Cytocam-IDF is a non-invasive and simple method to assess plugged capillaries and to diagnose sepsis, which may also aid in diagnosis of hemorrhagic shock. The advantage of Cytocam-IDF imaging is that is can easily be implemented in routine clinical

workflow, while for CEUS imaging some additional translational steps may be required, as discussed in the following section.

## 14.8. OUTLOOK AND FUTURE RESEARCH

**CEUS and acute kidney injury**

Future studies on acute kidney injury should focus on patient studies aiming to identify whether clinical scanners are sensitive enough to detect the changes we measured with our high-resolution scanner. In our study we were able to detect changes in very small regions in the microvasculature and in small arteries, which may not be visible when lower frequencies are used because of their lower resolution. It would therefore be very helpful to gain a full overview of parameters in the renal microcirculation, for example in terms of peak-enhancement, mean transit time, and wash-in rate. To obtain this full overview of parameters, i.e. real-time parametric imaging, for example VueBox® analysis software developed by Bracco could be used. This could aid in clinical validation and would also simplify interpretation by clinicians. Next to parametric imaging, visually assessing contrast persistence could already aid in the diagnosis of sepsis-induced alterations.

**The future of ultrasound contrast agents in the clinic**

In the recent years, contrast-enhanced ultrasound imaging has been approved for use in more organs [23, 314] and is securing its position in routine clinical workflow. With the recent approval of Lumason in the USA (branded as SonoVue in Europe), this is also the first ultrasound contrast agent approved by the FDA for liver imaging and for use in pediatric patients. Together with the re-introduction of Definity in Europe this will likely further boost the use of contrast-enhanced ultrasound imaging. The next step is the introduction of ultrasound molecular imaging in the clinic. As mentioned before, the first clinical trial has been conducted which needs to be thoroughly evaluated in order to initiate more clinical trials. The main advantage of ultrasound molecular imaging over for instance magnetic resonance molecular imaging are a higher sensitivity, lower costs, and the possibility to image in real-time. Another advantage is the theranostic application: after adherence of a targeted contrast agent to the biomarker of interest it can be imaged, and in the same examination the therapy (e.g. local drug delivery by means of sonoporation) can be applied. This can further decrease costs and is more time efficient. With the current focus on drug delivery and molecular imaging this could well be clinically accepted within the coming ten years.

# BIBLIOGRAPHY


[1] A. C. Guyton and J. E. Hall, *Textbook of Medical Physiology*, 10th ed., 2000.

[2] S. Campbell. "A short history of sonography in obstetrics and gynaecology", *Facts Views Vis Obgyn,* **5**, 213-229 (2013).

[3] R. Gramiak and P. M. Shah. "Echocardiography of the aortic root", *Invest Radiol,* **3**, 356-366 (1968).

[4] C. C. Coussios, C. K. Holland, L. Jakubowska, S. L. Huang, R. C. MacDonald, A. Nagaraj, and D. D. McPherson. "In vitro characterization of liposomes and Optison by acoustic scattering at 3.5 MHz", *Ultrasound Med Biol,* **30**, 181-190 (2004).

[5] T. Faez, M. Emmer, K. Kooiman, M. Versluis, A. van der Steen, and N. de Jong. "20 years of ultrasound contrast agent modeling", *IEEE Trans Ultrason Ferroelectr Freq Control,* **60**, 7-20 (2013).

[6] N. de Jong, L. Hoff, T. Skotland, and N. Bom. "Absorption and scatter of encapsulated gas filled microspheres: theoretical considerations and some measurements", *Ultrasonics,* **30**, 95-103 (1992).

[7] M. Schneider, M. Arditi, M. B. Barrau, J. Brochot, A. Broillet, R. Ventrone, and F. Yan. "BR1: a new ultrasonographic contrast agent based on sulfur hexafluoride-filled microbubbles", *Invest Radiol,* **30**, 451-457 (1995).

[8] B. D. Inc.. "Lumason Safety Label", FDA/Center for Drug Evaluation and Research, Silver Spring, USAMarch 2016 2016.

[9] L. M. Imaging. "Definity Safety Label", FDA/Center for Drug Evaluation and Research, Silver Spring, USAOctober 2011 2011.

[10] C. K. Holland, R. A. Roy, R. E. Apfel, and L. A. Crum. "In vitro detection of cavitation induced by a diagnostic ultrasound system", *IEEE Trans Ultrason Ferroelectr Freq Control,* **39**, 95-101 (1992).

[11] P. C. Sontum. "Physicochemical characteristics of Sonazoid, a new contrast agent for ultrasound imaging", *Ultrasound Med Biol,* **34**, 824-833 (2008).

[12] C. D. Ohl, M. Arora, R. Ikink, N. de Jong, M. Versluis, M. Delius, and D. Lohse. "Sonoporation from jetting cavitation bubbles", *Biophys J,* **91**, 4285-4295 (2006).

[13] S. V. Kothapalli, V. Daeichin, F. Mastik, L. A. Brodin, B. Janerot-Sjoberg, G. Paradossi, N. de Jong, and D. Grishenkov. "Unique pumping-out fracturing mechanism of a polymer-shelled contrast agent: an acoustic characterization and optical visualization", *IEEE Trans Ultrason Ferroelectr Freq Control,* **62**, 451-462 (2015).

[14] K. Kooiman, M. R. Bohmer, M. Emmer, H. J. Vos, C. Chlon, W. T. Shi, C. S. Hall, S. H. de Winter, K. Schroen, M. Versluis, N. de Jong, and A. van Wamel. "Oil-filled polymer microcapsules for ultrasound-mediated delivery of lipophilic drugs", *J Control Release,* **133**, 109-118 (2009).

[15] G. Lajoinie. "Ultrasound Contrast Agents - Bubbles, Drops and Particles", PhD thesis, Phyics of Fluids, University of Twente, Enschede, 2015.

[16] T. Segers, L. de Rond, N. de Jong, M. Borden, and M. Versluis. "Stability of Monodisperse Phospholipid-Coated Microbubbles Formed by Flow-Focusing at High Production Rates", *Langmuir,* **32**, 3937-3944 (2016).

[17] A. L. Klibanov. "Ultrasound Contrast Materials in Cardiovascular Medicine: from Perfusion Assessment to Molecular Imaging", *J Cardiovasc Transl Res,* (2013).

[18] Y. Luan, T. Faez, E. Gelderblom, I. Skachkov, B. Geers, I. Lentacker, T. van der Steen, M. Versluis, and N. de Jong. "Acoustical properties of individual liposome-loaded microbubbles", *Ultrasound Med Biol,* **38**, 2174-2185 (2012).

[19] P. Marmottant, S. van der Meer, M. Emmer, M. Versluis, N. de Jong, S. Hilgenfeldt, and D. Lohse. "A model for large amplitude oscillations of coated bubbles accounting for buckling and rupture", *J Acoust Soc Am,* **118**, 3499-3505 (2005).

[20] S. M. van der Meer, B. Dollet, M. M. Voormolen, C. T. Chin, A. Bouakaz, N. de Jong, M. Versluis, and D. Lohse. "Microbubble spectroscopy of ultrasound contrast agents", *J Acoust Soc Am,* **121**, 648-656 (2007).

[21] S. Fokong, B. Theek, Z. Wu, P. Koczera, L. Appold, S. Jorge, U. Resch-Genger, M. van Zandvoort, G. Storm, F. Kiessling, and T. Lammers. "Image-guided, targeted and triggered drug delivery to tumors using polymer-based microbubbles", *J Control Release,* **163**, 75-81 (2012).

[22] ICUS. "Comparison of Adverse Event Rates", International Contrast Ultrasound Society, Chicago, USA23/07/2016 2009.

[23] F. Piscaglia, C. Nolsoe, C. F. Dietrich, D. O. Cosgrove, O. H. Gilja, M. B. Nielsen, T. Albrecht, L. Barozzi, M. Bertolotto, O. Catalano, M. Claudon, D. A. Clevert, J. M. Correas, M. D'Onofrio, F. M. Drudi, J. Eyding, M. Giovannini, M. Hocke, A. Ignee, E. M. Jung, A. S. Klauser, N. Lassau, E. Leen, G. Mathis, A. Saftoiu, G. Seidel, P. S. Sidhu, G. ter Haar, D. Timmerman, and H. P. Weskott. "The EFSUMB Guidelines and Recommendations on the Clinical Practic of Contrast Enhanced Ultrasound (CEUS): Update 2011 on non-hepatic applications", *Ultraschall Med,* **33**, 33-59 (2012).

[24] H. A. Al-Mansour, S. L. Mulvagh, G. M. Pumper, K. W. Klarich, and D. A. Foley. "Usefulness of harmonic imaging for left ventricular opacification and endocardial border delineation by optison", *Am J Cardiol,* **85**, 795-799, A710 (2000).

[25] E. Leen, P. Ceccotti, C. Kalogeropoulou, W. J. Angerson, S. J. Moug, and P. G. Horgan. "Prospective multicenter trial evaluating a novel method of characterizing focal liver lesions using contrast-enhanced sonography", *AJR Am J Roentgenol,* **186**, 1551-1559 (2006).

[26] W. Lepper, T. Belcik, K. Wei, J. R. Lindner, J. Sklenar, and S. Kaul. "Myocardial contrast echocardiography", *Circulation,* **109**, 3132-3135 (2004).

[27] D. M. McDonald and P. L. Choyke. "Imaging of angiogenesis: from microscope to clinic", *Nat Med,* **9**, 713-725 (2003).

[28] S. Hernot and A. L. Klibanov. "Microbubbles in ultrasound-triggered drug and gene delivery", *Adv Drug Deliv Rev,* **60**, 1153-1166 (2008).

[29] A. L. Klibanov. "Ultrasound molecular imaging with targeted microbubble contrast agents", *J Nucl Cardiol,* **14**, 876-884 (2007).

[30] F. Tranquart, M. Arditi, T. Bettinger, P. Frinking, J. M. Hyvelin, A. Nunn, S. Pochon, and I. Tardy. "Ultrasound Contrast Agents For Ultrasound Molecular Imaging", *Z Gastroenterol,* **52**, 1268-1276 (2014).

[31] L. Abou-Elkacem, S. V. Bachawal, and J. K. Willmann. "Ultrasound molecular imaging: Moving toward clinical translation", *Eur J Radiol,* (2015).

[32] D. Cosgrove and C. Harvey. "Clinical uses of microbubbles in diagnosis and treatment", *Med Biol Eng Comput,* **47**, 813-826 (2009).

[33] X. Chen, R. S. Leow, Y. Hu, J. M. Wan, and A. C. Yu. "Single-site sonoporation disrupts actin cytoskeleton organization", *J R Soc Interface,* **11**, 20140071 (2014).

[34] Z. Fan, H. Liu, M. Mayer, and C. X. Deng. "Spatiotemporally controlled single cell sonoporation", *Proc Natl Acad Sci U S A,* **109**, 16486-16491 (2012).

[35] K. Kooiman, M. Foppen-Harteveld, A. F. van der Steen, and N. de Jong. "Sonoporation of endothelial cells by vibrating targeted microbubbles", *J Control Release,* **154**, 35-41 (2011).

[36] I. Lentacker, I. De Cock, R. Deckers, S. C. De Smedt, and C. T. Moonen. "Understanding ultrasound induced sonoporation: definitions and underlying mechanisms", *Adv Drug Deliv Rev,* **72**, 49-64 (2014).

[37] A. van Wamel, K. Kooiman, M. Harteveld, M. Emmer, F. J. ten Cate, M. Versluis, and N. de Jong. "Vibrating microbubbles poking individual cells: drug transfer into cells via sonoporation", *J Control Release,* **112**, 149-155 (2006).

[38] Y. Hu, J. M. Wan, and A. C. Yu. "Membrane perforation and recovery dynamics in microbubble-mediated sonoporation", *Ultrasound Med Biol,* **39**, 2393-2405 (2013).

[39] R. Karshafian, P. D. Bevan, R. Williams, S. Samac, and P. N. Burns. "Sonoporation by Ultrasound-Activated Microbubble Contrast Agents: Effect of Acoustic Exposure Parameters on Cell Membrane Permeability and Cell Viability", *Ultrasound Med Biol,* **35**, 847-860 (2009).

[40] B. D. M. Meijering, R. H. Henning, W. H. Van Gilst, I. Gavrilovic, A. Van Wamel, and L. E. Deelman. "Optimization of ultrasound and microbubbles targeted gene delivery to cultured primary endothelial cells", *J Drug Target,* **15**, 664-671 (2007).

[41] I. De Cock, E. Zagato, K. Braeckmans, Y. Luan, N. de Jong, S. C. De Smedt, and I. Lentacker. "Ultrasound and microbubble mediated drug delivery: acoustic pressure as determinant for uptake via membrane pores or endocytosis", *J Control Release,* **197**, 20-28 (2015).

[42] L. Rayleigh. "VIII. On the pressure developed in a liquid during the collapse of a spherical cavity", *Philosophical Magazine Series 6,* **34**, 94-98 (1917).

[43] M. S. Plesset and A. Prosperetti. "Bubble Dynamics and Cavitation", *Annual Review of Fluid Mechanics,* **9**, 145-185 (1977).

[44] T. G. Leighton, *The Acoustic Bubble.* London: Academic Press Limited, 1994.

[45] K. Kooiman, H. J. Vos, M. Versluis, and N. de Jong. "Acoustic behavior of microbubbles and implications for drug delivery", *Adv Drug Deliv Rev,* **72C**, 28-48 (2014).

[46] M. M. Lozano and M. L. Longo. "Microbubbles coated with disaturated lipids and DSPE-PEG2000: phase behavior, collapse transitions, and permeability", *Langmuir,* **25**, 3705-3712 (2009).

[47] M. A. Borden, G. V. Martinez, J. Ricker, N. Tsvetkova, M. Longo, R. J. Gillies, P. A. Dayton, and K. W. Ferrara. "Lateral phase separation in lipid-coated microbubbles", *Langmuir,* **22**, 4291-4297 (2006).

[48] M. A. Borden, G. Pu, G. J. Runner, and M. L. Longo. "Surface phase behavior and microstructure of lipid/PEG-emulsifier monolayer-coated microbubbles", *Colloids Surf B Biointerfaces,* **35**, 209-223 (2004).

[49] D. H. Kim, M. J. Costello, P. B. Duncan, and D. Needham. "Mechanical properties and microstructure of polycrystalline phospholipid monolayer shells: Novel solid microparticles", *Langmuir,* **19**, 8455-8466 (2003).

[50] S. Garg, A. A. Thomas, and M. A. Borden. "The effect of lipid monolayer in-plane rigidity on in vivo microbubble circulation persistence", *Biomaterials,* **34**, 6862-6870 (2013).

[51] A. J. Mortimer, *Physical Characteristics of Ultrasound.* Clifton, NJ, USA: The Humana Press Inc., 1928.

[52] T. C. Chin, C. T. Lancee, J. Borsboom, F. Mastik, M. E. Frijlink, and N. de Jong. "Brandaris 128: A digital 25 million frames per second camera with 128 highly sensitive frames", *Rev Sci Instrum,* **74**, 5026-5034 (2003).

[53] S. L. Huang, A. J. Hamilton, A. Nagaraj, S. D. Tiukinhoy, M. E. Klegerman, D. D. McPherson, and R. C. Macdonald. "Improving ultrasound reflectivity and stability of echogenic liposomal dispersions for use as targeted ultrasound contrast agents", *J Pharm Sci,* **90**, 1917-1926 (2001).

[54] S. L. Huang, D. D. McPherson, and R. C. Macdonald. "A method to co-encapsulate gas and drugs in liposomes for ultrasound-controlled drug delivery", *Ultrasound Med Biol,* **34**, 1272-1280 (2008).

[55] K. B. Bader, G. Bouchoux, T. Peng, M. E. Klegerman, D. D. McPherson, and C. K. Holland. "Thrombolytic efficacy and enzymatic activity of rt-PA-loaded echogenic liposomes", *J Thromb Thrombolysis,* **40**, 144-155 (2015).

[56] X. Chen, J. Wang, M. Versluis, N. de Jong, and F. S. Villanueva. "Ultra-fast bright field and fluorescence imaging of the dynamics of micrometer-sized objects", *Rev Sci Instrum,* **84**,(2013).

[57] G. Lajoinie, E. Gelderblom, C. Chlon, M. Bohmer, W. Steenbergen, N. de Jong, S. Manohar, and M. Versluis. "Ultrafast vapourization dynamics of laser-activated polymeric microcapsules", *Nat Commun,* **5**, 3671 (2014).

[58] K. Wilson, K. Homan, and S. Emelianov. "Biomedical photoacoustics beyond thermal expansion using triggered nanodroplet vaporization for contrast-enhanced imaging", *Nat Commun,* **3**,(2012).

[59] R. Bellomo, J. A. Kellum, and C. Ronco. "Acute kidney injury", *Lancet,* **380**, 756-766 (2012).

[60] E. A. Hoste, S. M. Bagshaw, R. Bellomo, C. M. Cely, R. Colman, D. N. Cruz, K. Edipidis, L. G. Forni, C. D. Gomersall, D. Govil, P. M. Honore, O. Joannes-Boyau, M. Joannidis, A. M. Korhonen, A. Lavrentieva, R. L. Mehta, P. Palevsky, E. Roessler, C. Ronco, S. Uchino, J. A. Vazquez, E. Vidal Andrade, S. Webb, and J. A. Kellum. "Epidemiology of acute kidney injury in critically ill patients: the multinational AKI-EPI study", *Intensive Care Med,* **41**, 1411-1423 (2015).

[61] S. S. Waikar, K. D. Liu, and G. M. Chertow. "Diagnosis, epidemiology and outcomes of acute kidney injury", *Clin J Am Soc Nephrol,* **3**, 844-861 (2008).

[62] S. Kaul. "Myocardial contrast echocardiography: a 25-year retrospective", *Circulation,* **118**, 291-308 (2008).

[63] A. Alzaraa, G. Gravante, W. Y. Chung, D. Al-Leswas, B. Morgan, A. Dennison, and D. Lloyd. "Contrast-enhanced ultrasound in the preoperative, intraoperative and postoperative assessment of liver lesions", *Hepatol Res,* **43**, 809-819 (2013).

[64] J. M. Correas, O. Helenon, L. Pourcelot, and J. F. Moreau. "Ultrasound contrast agents. Examples of blood pool agents", *Acta Radiol Suppl,* **412**, 101-112 (1997).

[65] C. Greis. "Ultrasound contrast agents as markers of vascularity and microcirculation", *Clin Hemorheol Microcirc,* **43**, 1-9 (2009).

[66] H. Wu, N. G. Rognin, T. M. Krupka, L. Solorio, H. Yoshiara, G. Guenette, C. Sanders, N. Kamiyama, and A. A. Exner. "Acoustic characterization and pharmacokinetic analyses of new nanobubble ultrasound contrast agents", *Ultrasound Med Biol,* **39**, 2137-2146 (2013).

[67] L. Wang, L. Li, Y. Guo, H. Tong, X. Fan, J. Ding, and H. Huang. "Construction and in vitro/in vivo targeting of PSMA-targeted nanoscale microbubbles in prostate cancer", *Prostate,* **73**, 1147-1158 (2013).

[68] A. Alzaraa, G. Gravante, W. Y. Chung, D. Al-Leswas, M. Bruno, A. R. Dennison, and D. M. Lloyd. "Targeted microbubbles in the experimental and clinical setting", *Am J Surg,* **204**, 355-366 (2012).

[69] S. Unnikrishnan and A. L. Klibanov. "Microbubbles as Ultrasound Contrast Agents for Molecular Imaging: Preparation and Application", *Am J Roentgenol,* **199**, 292-299 (2012).

[70] K. Kooiman, T. J. A. Kokhuis, T. van Rooij, I. Skachkov, A. Nigg, J. G. Bosch, A. F. W. van der Steen, W. A. van Cappellen, and N. de Jong. "DSPC or DPPC as main shell component influences ligand distribution and binding area of lipid-coated targeted microbubbles", *Eur J Lipid Sci Technol,* **116**, 1217-1227 (2014).

[71] T. van Rooij, Y. Luan, G. G. J. Renaud, A. F. W. van der Steen, N. De Jong, and K. Kooiman. "Acoustical response of DSPC versus DPPC lipid-coated microbubbles", in *IEEE Ultrasonics Symposium Proceedings*, Prague, Czech Republic (2013).

[72] A. H. Myrset, H. B. Fjerdingstad, R. Bendiksen, B. E. Arbo, R. M. Bjerke, J. H. Johansen, M. A. Kulseth, and R. Skurtveit. "Design and characterization of targeted ultrasound microbubbles for diagnostic use", *Ultrasound Med Biol,* **37**, 136-150 (2011).

[73] D. Marsh, R. Bartucci, and L. Sportelli. "Lipid membranes with grafted polymers: physicochemical aspects", *Biochim Biophys Acta,* **1615**, 33-59 (2003).

[74] S. Ottoboni, R. E. Short, M. B. Kerby, E. G. Tickner, E. Steadman, and T. B. Ottoboni. "Characterization of the in vitro adherence behavior of ultrasound responsive double-shelled microspheres targeted to cellular adhesion molecules", *Contrast Media Mol Imaging,* **1**, 279-290 (2006).

[75] C. C. Chen and M. A. Borden. "The role of poly(ethylene glycol) brush architecture in complement activation on targeted microbubble surfaces", *Biomaterials,* **32**, 6579-6587 (2011).

[76] F. Kiessling, S. Fokong, J. Bzyl, W. Lederle, M. Palmowski, and T. Lammers. "Recent advances in molecular, multimodal and theranostic ultrasound imaging", *Adv Drug Deliv Rev,* **72**, 15-27 (2014).

[77] S. Hernot, S. Unnikrishnan, Z. M. Du, T. Shevchenko, B. Cosyns, A. Broisat, J. Toczek, V. Caveliers, S. Muyldermans, T. Lahoutte, A. L. Klibanov, and N. Devoogdt. "Nanobody-coupled microbubbles as novel molecular tracer", *J Control Release,* **158**, 346-353 (2012).

[78] M. A. Nakatsuka, R. F. Mattrey, S. C. Esener, J. N. Cha, and A. P. Goodwin. "Aptamer-crosslinked microbubbles: smart contrast agents for thrombin-activated ultrasound imaging", *Adv Mater,* **24**, 6010-6016 (2012).

[79] M. A. Wheatley, J. D. Lathia, and K. L. Oum. "Polymeric ultrasound contrast agents targeted to integrins: Importance of process methods and surface density of ligands", *Biomacromolecules,* **8**, 516-522 (2007).

[80] G. Paganelli, C. Belloni, P. Magnani, F. Zito, A. Pasini, I. Sassi, M. Meroni, M. Mariani, M. Vignali, A. G. Siccardi, and F. Fazio. "Two-step tumour targetting in ovarian cancer patients using biotinylated monoclonal antibodies and radioactive streptavidin", *Eur J Nuc Med,* **19**, 322-329 (1992).

[81] T. J. Kokhuis, I. Skachkov, B. A. Naaijkens, L. J. Juffermans, O. Kamp, K. Kooiman, A. F. van der Steen, M. Versluis, and N. de Jong. "Intravital microscopy of localized stem cell delivery using microbubbles and acoustic radiation force", *Biotechnol Bioeng,* **112**, 220-227 (2015).

[82] D. H. Kim, A. L. Klibanov, and D. Needham. "The Influence of Tiered Layers of Surface-Grafted Poly(ethylene glycol) on Receptor-Ligand-Mediated Adhesion between Phospholipid Monolayer-Stabilized Microbubbles and Coated Glass Beads", *Langmuir,* **16**, 2808-2817 (2000).

[83] X. Wei, Y. Li, S. Zhang, X. Gao, Y. Luo, and M. Gao. "Ultrasound targeted apoptosis imaging in monitoring early tumor response of trastuzumab in a murine tumor xenograft model of her-2-positive breast cancer(1.)", *Transl Oncol,* **7**, 284-291 (2014).

[84] S. Pochon, I. Tardy, P. Bussat, T. Bettinger, J. Brochot, M. von Wronski, L. Passantino, and M. Schneider. "BR55: a lipopeptide-based VEGFR2-targeted ultrasound contrast agent for molecular imaging of angiogenesis", *Invest Radiol,* **45**, 89-95 (2010).

[85] S. Fokong, A. Fragoso, A. Rix, A. Curaj, Z. J. Wu, W. Lederle, O. Iranzo, J. Gatjens, F. Kiessling, and M. Palmowski. "Ultrasound Molecular Imaging of E-Selectin in Tumor Vessels Using Poly n-Butyl Cyanoacrylate Microbubbles Covalently Coupled to a Short Targeting Peptide", *Invest Radiol,* **48**, 843-850 (2013).

[86] J. K. Willmann, A. M. Lutz, R. Paulmurugan, M. R. Patel, P. Chu, J. Rosenberg, and S. S. Gambhir. "Dual-targeted contrast agent for US assessment of tumor angiogenesis in vivo", *Radiology,* **248**, 936-944 (2008).

[87] H. Y. Jun, S. H. Park, H. S. Kim, and K. H. Yoon. "Long Residence Time of Ultrasound Microbubbles Targeted to Integrin in Murine Tumor Model", *Acad Radiol,* **17**, 54-60 (2010).

[88] K. Otani and K. Yamahara. "Feasibility of Lactadherin-Bearing Clinically Available Microbubbles as Ultrasound Contrast Agent for Angiogenesis", *Molecular Imaging and Biology,* **15**, 534-541 (2013).

[89] H. Wijkstra, M. Smeenge, J. de la Rosette, S. Pochon, I. Tardy-Cantalupi, and F. Tranquart. "Targeted microbubble prostate cancer imaging with BR55", in *Abstract book of the 17th European Symposium on Ultrasound Contrast Imaging*, 2012.

[90] B. A. Kaufmann, J. M. Sanders, C. Davis, A. Xie, P. Aldred, I. J. Sarembock, and J. R. Lindner. "Molecular imaging of inflammation in atherosclerosis with targeted ultrasound detection of vascular cell adhesion molecule-1", *Circulation,* **116**, 276-284 (2007).

[91] B. A. Kaufmann, C. Lewis, A. Xie, A. Mirza-Mohd, and J. R. Lindner. "Detection of recent myocardial ischaemia by molecular imaging of P-selectin with targeted contrast echocardiography", *Eur Heart J,* **28**, 2011-2017 (2007).

[92] H. Kim, M. R. Moody, S. T. Laing, P. H. Kee, S. L. Huang, M. E. Klegerman, and D. D. McPherson. "In Vivo Volumetric Intravascular Ultrasound Visualization of Early/Inflammatory Arterial Atheroma Using Targeted Echogenic Immunoliposomes", *Invest Radiol,* **45**, 685-691 (2010).

[93] B. A. Kaufmann, C. L. Carr, J. T. Belcik, A. Xie, Q. Yue, S. Chadderdon, E. S. Caplan, J. Khangura, S. Bullens, S. Bunting, and J. R. Lindner. "Molecular Imaging of the Initial Inflammatory Response in Atherosclerosis Implications for Early Detection of Disease", *Arteriosclerosis Thrombosis and Vascular Biology,* **30**, 54-U132 (2010).

[94] Q. N. Wen, S. R. Wan, Z. L. Liu, S. Xu, H. R. Wang, and B. Yang. "Ultrasound Contrast Agents and Ultrasound Molecular Imaging", *J Nanosci Nanotechnol,* **14**, 190-209 (2014).

[95] J. J. Rychak, J. R. Lindner, K. Ley, and A. L. Klibanov. "Deformable gas-filled microbubbles targeted to P-selectin", *J Control Release,* **114**, 288-299 (2006).

[96] X. Wang, C. E. Hagemeyer, J. D. Hohmann, E. Leitner, P. C. Armstrong, F. Jia, M. Olschewski, A. Needles, K. Peter, and I. Ahrens. "Novel single-chain antibody-targeted microbubbles for molecular ultrasound imaging of thrombosis: validation of a unique noninvasive method for rapid and sensitive detection of thrombi and monitoring of success or failure of thrombolysis in mice", *Circulation,* **125**, 3117-3126 (2012).

[97] P. A. Schumann, J. P. Christiansen, R. M. Quigley, T. P. McCreery, R. H. Sweitzer, E. C. Unger, J. R. Lindner, and T. O. Matsunaga. "Targeted-microbubble binding selectively to GPIIb IIIa receptors of platelet thrombi", *Invest Radiol,* **37**, 587-593 (2002).

[98] C. Cheng, F. Helderman, D. Tempel, D. Segers, B. Hierck, R. Poelmann, A. van Tol, D. J. Duncker, D. Robbers-Visser, N. T. C. Ursem, R. van Haperen, J. J. Wentzel, F. Gijsen, A. F. W. van der Steen, R. de Crom, and R. Krams. "Large variations in absolute wall shear stress levels within one species and between species", *Atherosclerosis,* **195**, 225-235 (2007).

[99] M. A. Nakatsuka, C. V. Barback, K. R. Fitch, A. R. Farwell, S. C. Esener, R. F. Mattrey, J. N. Cha, and A. P. Goodwin. "In vivo ultrasound visualization of non-occlusive blood clots with thrombin-sensitive contrast agents", *Biomaterials,* **34**, 9559-9565 (2013).

[100] I. M. Thompson, D. K. Pauler, P. J. Goodman, C. M. Tangen, M. S. Lucia, H. L. Parnes, L. M. Minasian, L. G. Ford, S. M. Lippman, E. D. Crawford, J. J. Crowley, and C. A. Coltman. "Prevalence of prostate cancer among men with a prostate-specific antigen level <= 4.0 ng per milliliter", *N Engl J Med,* **350**, 2239-2246 (2004).

[101] S. Perner, M. D. Hofer, R. Kim, R. B. Shah, H. J. Li, P. Moller, R. E. Hautmann, J. E. Gschwend, R. Kuefer, and M. A. Rubin. "Prostate-specific membrane antigen expression as a predictor of prostate cancer progression", *Human Pathology,* **38**, 696-701 (2007).

[102] V. Sanna, G. Pintus, P. Bandiera, R. Anedda, S. Punzoni, B. Sanna, V. Migaleddu, S. Uzzau, and M. Sechi. "Development of polymeric microbubbles targeted to prostate-specific membrane antigen as prototype of novel ultrasound contrast agents", *Mol Pharm,* **8**, 748-757 (2011).

[103] J. K. Tsuruta, N. Klauber-DeMore, J. Streeter, J. Samples, C. Patterson, R. J. Mumper, D. Ketelsen, and P. Dayton. "Ultrasound Molecular Imaging of Secreted Frizzled Related Protein-2 Expression in Murine Angiosarcoma", *Plos One,* **9**,(2014).

[104] A. M. Lutz, S. V. Bachawal, C. W. Drescher, M. A. Pysz, J. K. Willmann, and S. S. Gambhir. "Ultrasound Molecular Imaging in a Human CD276 Expression-Modulated Murine Ovarian Cancer Model", *Clinical Cancer Research,* **20**, 1313-1322 (2014).

[105] K. Foygel, H. J. Wang, S. Machtaler, A. M. Lutz, R. Chen, M. Pysz, A. W. Lowe, L. Tian, T. Carrigan, T. A. Brentnall, and J. K. Willmann. "Detection of Pancreatic Ductal Adenocarcinoma in Mice by Ultrasound Imaging of Thymocyte Differentiation Antigen 1", *Gastroenterology,* **145**, 885-+ (2013).

[106] J. A. Knowles, C. H. Heath, R. Saini, H. Umphrey, J. Warram, K. Hoyt, and E. L. Rosenthal. "Molecular Targeting of Ultrasonographic Contrast Agent for Detection of Head and Neck Squamous Cell Carcinoma", *Archives of Otolaryngology-Head & Neck Surgery,* **138**, 662-668 (2012).

[107] G. Koopman, C. P. M. Reutelingsperger, G. A. M. Kuijten, R. M. J. Keehnen, S. T. Pals, and M. H. J. Vanoers. "Annexin-V for Flow Cytometric Detection of Phosphatidylserine Expression on B-Cells Undergoing Apoptosis", *Blood,* **84**, 1415-1420 (1994).

[108] E. A. Ferrante, J. E. Pickard, J. Rychak, A. Klibanov, and K. Ley. "Dual targeting improves microbubble contrast agent adhesion to VCAM-1 and P-selectin under flow", *J Control Release,* **140**, 100-107 (2009).

[109] J. M. Warram, A. G. Sorace, R. Saini, H. R. Umphrey, K. R. Zinn, and K. Hoyt. "A Triple-Targeted Ultrasound Contrast Agent Provides Improved Localization to Tumor Vasculature", *J Ultrasound Med,* **30**, 921-931 (2011).

[110] A. S. Ham, A. L. Klibanov, and M. B. Lawrence. "Action at a Distance: Lengthening Adhesion Bonds with Poly(ethylene glycol) Spacers Enhances Mechanically Stressed Affinity for Improved Vascular Targeting of Microparticles", *Langmuir,* **25**, 10038-10044 (2009).

[111] T. M. Maul, D. D. Dudgeon, M. T. Beste, D. A. Hammer, J. S. Lazo, F. S. Villanueva, and W. R. Wagner. "Optimization of Ultrasound Contrast Agents With Computational Models to Improve Selection of Ligands and Binding Strength", *Biotechnol Bioeng,* **107**, 854-864 (2010).

[112] K. Soetanto and H. Watarai. "Development of magnetic microbubbles for drug delivery system (DDS)", *Jpn J Appl Phys,* **39**, 3230-3232 (2000).

[113] E. Stride, C. Porter, A. G. Prieto, and Q. Pankhurst. "Enhancement of Microbubble Mediated Gene Delivery by Simultaneous Exposure to Ultrasonic and Magnetic Fields", *Ultrasound Med Biol,* **35**, 861-868 (2009).

[114] K. Soetanto and H. Watarai. "Ferromagnetic ultrasound microbubbles contrast agent", *Proceedings of the 25th Annual International Conference of the IEEE Engineering in Medicine and Biology Society, Vols 1-4,* **25**, 1226-1229 (2003).

[115] J. Owen, Q. Pankhurst, and E. Stride. "Magnetic targeting and ultrasound mediated drug delivery: Benefits, limitations and combination", *Int J Hyperthermia,* **28**, 362-373 (2012).

[116] G. R. Torr. "The Acoustic Radiation Force", *Am J Phys,* **52**, 402-408 (1984).

[117] M. A. Borden, M. R. Sarantos, S. M. Stieger, S. I. Simon, K. W. Ferrara, and P. A. Dayton. "Ultrasound radiation force modulates ligand availability on targeted contrast agents", *Mol Imaging,* **5**, 139-147 (2006).

[118] M. A. Borden, J. E. Streeter, S. R. Sirsi, and P. A. Dayton. "In Vivo Demonstration of Cancer Molecular Imaging with Ultrasound Radiation Force and Buried-Ligand Microbubbles", *Mol Imaging,* **12**,(2013).

[119] S. Y. Wang, J. A. Hossack, A. L. Klibanov, and F. W. Mauldin. "Binding dynamics of targeted microbubbles in response to modulated acoustic radiation force", *Phys Med Biol,* **59**, 465-484 (2014).

[120] P. J. Frinking, I. Tardy, M. Theraulaz, M. Arditi, J. Powers, S. Pochon, and F. Tranquart. "Effects of Acoustic Radiation Force on the Binding Efficiency of BR55, a VEGFR2-Specific Ultrasound Contrast Agent", *Ultrasound Med Biol,* **38**, 1460-1469 (2012).

[121] V. Sboros, E. Glynos, J. A. Ross, C. M. Moran, S. D. Pye, M. Butler, W. N. McDicken, S. B. Brown, and V. Koutsos. "Probing microbubble targeting with atomic force microscopy", *Colloids and Surfaces B-Biointerfaces,* **80**, 12-17 (2010).

[122] A. M. Takalkar, A. L. Klibanov, J. J. Rychak, J. R. Lindner, and K. Ley. "Binding and detachment dynamics of microbubbles targeted to P-selectin under controlled shear flow", *J Control Release,* **96**, 473-482 (2004).

[123] T. J. Kokhuis, V. Garbin, K. Kooiman, B. A. Naaijkens, L. J. Juffermans, O. Kamp, A. F. van der Steen, M. Versluis, and N. de Jong. "Secondary bjerknes forces deform targeted microbubbles", *Ultrasound Med Biol,* **39**, 490-506 (2013).

[124] V. Garbin, D. Cojoc, E. Ferrari, and E. Di Fabrizio. "Changes in microbubble dynamics near a boundary revealed by combined optical micromanipulation and high-speed imaging", *App Phys Lett,* (2007).

[125] K. Chetty, E. Stride, C. A. Sennoga, J. V. Hajnal, and R. J. Eckersley. "High-speed optical observations and simulation results of SonoVue microbubbles at low-pressure insonation", *IEEE Trans Ultrason Ferroelectr Freq Control,* **55**, 1333-1342 (2008).

[126] T. Faez, D. Goertz, and N. De Jong. "Characterization of Definity ultrasound contrast agent at frequency range of 5-15 MHz", *Ultrasound Med Biol,* **37**, 338-342 (2011).

[127] J. M. Gorce, M. Arditi, and M. Schneider. "Influence of bubble size distribution on the echogenicity of ultrasound contrast agents: a study of SonoVue", *Invest Radiol,* **35**, 661-671 (2000).

[128] B. L. Helfield and D. E. Goertz. "Nonlinear resonance behavior and linear shell estimates for Definity and MicroMarker assessed with acoustic microbubble spectroscopy", *J Acoust Soc Am,* **133,** 1158-1168 (2013).

[129] A. L. Klibanov, P. T. Rasche, M. S. Hughes, J. K. Wojdyla, K. P. Galen, J. H. Wible, Jr., and G. H. Brandenburger. "Detection of individual microbubbles of ultrasound contrast agents: imaging of free-floating and targeted bubbles", *Invest Radiol,* **39**, 187-195 (2004).

[130] J. E. G. McKendry, C.A. Johnson, B.R.G. Coletta, P.L. Evans, J.A. Evans, S.D.. "Force spectroscopy of streptavidin conjugated lipid coated microbubbles", *Bubble Sci Eng Technol,* **2**,(2010).

[131] R. H. Abou-Saleh, S. A. Peyman, K. Critchley, S. D. Evans, and N. H. Thomson. "Nanomechanics of lipid encapsulated microbubbles with functional coatings", *Langmuir,* **29**, 4096-4103 (2013).

[132] J. R. Lindner, J. Song, J. Christiansen, A. L. Klibanov, F. Xu, and K. Ley. "Ultrasound assessment of inflammation and renal tissue injury with microbubbles targeted to P-selectin", *Circulation,* **104**, 2107-2112 (2001).

[133] S. Dieluweit, A. Csiszar, W. Rubner, J. Fleischhauer, S. Houben, and R. Merkel. "Mechanical Properties of Bare and Protein-Coated Giant Unilamellar Phospholipid Vesicles. A Comparative Study of Micropipet Aspiration and Atomic Force Microscopy", *Langmuir,* **26**, 11041-11049 (2010).

[134] S. A. Darst, M. Ahlers, P. H. Meller, E. W. Kubalek, R. Blankenburg, H. O. Ribi, H. Ringsdorf, and R. D. Kornberg. "Two-dimensional crystals of streptavidin on biotinylated lipid layers and their interactions with biotinylated macromolecules", *Biophys J,* **59**, 387-396 (1991).

[135] M. A. Borden, D. E. Kruse, C. F. Caskey, S. Zhao, P. A. Dayton, and K. W. Ferrara. "Influence of lipid shell physicochemical properties on ultrasound-induced microbubble destruction", *IEEE Trans Ultrason Ferroelectr Freq Control,* **52**, 1992-2002 (2005).

[136] M. Overvelde, V. Garbin, B. Dollet, N. de Jong, D. Lohse, and M. Versluis. "Dynamics of coated microbubbles adherent to a wall", *Ultrasound Med Biol,* **37**, 1500-1508 (2011).

[137] Life Technologies. Proteins and Amino Acids [Online]. Available: http://www.lifetechnologies.com/nl/en/home/references/ambion-tech-support/rna-tools-and-calculators/proteins-and-amino-acids.html

[138] A. L. Klibanov. "Preparation of targeted microbubbles: ultrasound contrast agents for molecular imaging", *Med Biol Eng Comput,* **47**, 875-882 (2009).

[139] S. Zhao, K. W. Ferrara, and P. A. Dayton. "Asymmetric oscillation of adherent targeted ultrasound contrast agents", *Appl Phys Lett,* **87**, 1341031-1341033 (2005).

[140] S. Zhao, D. E. Kruse, K. W. Ferrara, and P. A. Dayton. "Acoustic response from adherent targeted contrast agents", *J Acoust Soc Am,* **120**, EL63-69 (2006).

[141] J. Casey, C. Sennoga, H. Mulvana, J. V. Hajnal, M. X. Tang, and R. J. Eckersley. "Single bubble acoustic characterization and stability measurement of adherent microbubbles", *Ultrasound Med Biol,* **39**, 903-914 (2013).

[142] B. L. Helfield, E. Cherin, F. S. Foster, and D. E. Goertz. "The effect of binding on the subharmonic emissions from individual lipid-encapsulated microbubbles at transmit frequencies of 11 and 25 MHz", *Ultrasound Med Biol,* **39**, 345-359 (2013).

[143] B. J. Schmidt, I. Sousa, A. A. van Beek, and M. R. Bohmer. "Adhesion and ultrasound-induced delivery from monodisperse microbubbles in a parallel plate flow cell", *J Control Release,* **131**, 19-26 (2008).

[144] B. Cerroni, E. Chiessi, S. Margheritelli, L. Oddo, and G. Paradossi. "Polymer Shelled Microparticles for a Targeted Doxorubicin Delivery in Cancer Therapy", *Biomacromolecules,* **12**, 593-601 (2011).

[145] D. Grishenkov, L. Kari, L. A. Brodin, T. B. Brismar, and G. Paradossi. "In vitro contrast-enhanced ultrasound measurements of capillary microcirculation: Comparison between polymer- and phospholipid-shelled microbubbles", *Ultrasonics,* **51**, 40-48 (2011).

[146] N. de Jong, A. Bouakaz, and P. Frinking. "Basic acoustic properties of microbubbles", *Echocardiography,* **19**, 229-240 (2002).

[147] A. I. Eller and H. G. Flynn. "Generation of Subharmonics of Order One-Half by Bubbles in a Sound Field", *J Acoust Soc Am,* **46**, 722-727 (1969).

[148] J. Chomas, P. Dayton, D. May, and K. Ferrara. "Nondestructive subharmonic imaging", *IEEE Trans Ultrason Ferroelectr Freq Control,* **49**, 883-892 (2002).

[149] D. E. Goertz, M. E. Frijlink, D. Tempel, V. Bhagwandas, A. Gisolf, R. Krams, N. de Jong, and A. F. W. van der Steen. "Subharmonic contrast intravascular ultrasound for vasa vasorum imaging", *Ultrasound Med Biol,* **33**, 1859-1872 (2007).

[150] A. Needles, D. E. Goertz, R. Karshafian, E. Cherin, A. S. Brown, P. N. Burns, and F. S. Foster. "High-frequency subharmonic pulsed-wave Doppler and color flow imaging of microbubble contrast agents", *Ultrasound Med Biol,* **34**, 1139-1151 (2008).

[151] C. Y. Wu, J. Tsao, and Y. H. Chou. "An ultrasonic microbubble semi-intermodulated imaging technique", *Ultrasound Med Biol,* **31**, 1199-1210 (2005).

[152] C. X. Deng, F. L. Lizzi, A. Kalisz, A. Rosado, R. H. Silverman, and D. J. Coleman. "Study of ultrasonic contrast agents using a dual-frequency band technique", *Ultrasound Med Biol,* **26**, 819-831 (2000).

[153] W. T. Shi and F. Forsberg. "Ultrasonic characterization of the nonlinear properties of contrast microbubbles", *Ultrasound Med Biol,* **26**, 93-104 (2000).

[154] S. G. Chen, R. Kinnick, J. F. Greenleaf, and M. Fatemi. "Difference frequency and its harmonic emitted by microbubbles under dual frequency excitation", *Ultrasonics,* **44**, E123-E126 (2006).

[155] P. N. Burns, J. E. Powers, D. H. Simpson, A. Brezina, A. Kolin, C. T. Chin, V. Uhlendorf, and T. Fritzsch. "Harmonic Power Mode Doppler Using Microbubble Contrast Agents - an Improved Method for Small Vessel Flow Imaging", *IEEE Ultrasonics Symposium Proceedings, Vols 1-3,* 1547-1550 (1994).

[156] C. Pi Hsien, K. K. Shun, W. Shih-Jeh, and H. B. Levene. "Second harmonic imaging and harmonic Doppler measurements with Albunex", *IEEE Trans Ultrason Ferroelectr Freq Control,* **42**, 1020-1027 (1995).

[157] D. H. Simpson and P. N. Burns. "Pulse inversion Doppler: a new method for detecting nonlinear echoes from microbubble contrast agents", *IEEE Ultrasonics Symposium Proceedings, vol 1592,* 1597-1600 (1997).

[158] N. de Jong, P. J. Frinking, A. Bouakaz, and F. J. Ten Cate. "Detection procedures of ultrasound contrast agents", *Ultrasonics,* **38**, 87-92 (2000).

[159] C. X. Deng and F. L. Lizzi. "A review of physical phenomena associated with ultrasonic contrast agents and illustrative clinical applications", *Ultrasound Med Biol,* **28**, 277-286 (2002).

[160] F. S. Foster, J. Hossack, and S. L. Adamson. "Micro-ultrasound for preclinical imaging", *Interface Focus,* **1**, 576-601 (2011).

[161] A. Needles, M. Arditi, N. G. Rognin, J. Mehi, T. Coulthard, C. Bilan-Tracey, E. Gaud, P. Frinking, D. Hirson, and F. S. Foster. "Nonlinear contrast imaging with an array-based micro-ultrasound system", *Ultrasound Med Biol,* **36**, 2097-2106 (2010).

[162] A. Lyshchik, A. C. Fleischer, J. Huamani, D. E. Hallahan, M. Brissova, and J. C. Gore. "Molecular imaging of vascular endothelial growth factor receptor 2 expression using targeted contrast-enhanced high-frequency ultrasonography", *J Ultrasound Med,* **26**, 1575-1586 (2007).

[163] J. J. Rychak, J. Graba, A. M. Cheung, B. S. Mystry, J. R. Lindner, R. S. Kerbel, and F. S. Foster. "Microultrasound molecular imaging of vascular endothelial growth factor receptor 2 in a mouse model of tumor angiogenesis", *Mol Imaging,* **6**, 289-296 (2007).

[164] J. K. Willmann, R. Paulmurugan, K. Chen, O. Gheysens, M. Rodriguez-Porcel, A. M. Lutz, I. Y. Chen, X. Chen, and S. S. Gambhir. "US imaging of tumor angiogenesis with microbubbles targeted to vascular endothelial growth factor receptor type 2 in mice", *Radiology,* **246**, 508-518 (2008).

[165] C. M. Moran, R. J. Watson, K. A. A. Fox, and W. N. McDicken. "In vitro acoustic characterisation of four intravenous ultrasonic contrast agents at 30 MHz", *Ultrasound Med Biol,* **28**, 785-791 (2002).

[166] G. L. ten Kate, G. G. Renaud, Z. Akkus, S. C. van den Oord, F. J. ten Cate, V. Shamdasani, R. R. Entrekin, E. J. Sijbrands, N. de Jong, J. G. Bosch, A. F. Schinkel, and A. F. van der Steen. "Far-wall pseudoenhancement during contrast-enhanced ultrasound of the carotid arteries: clinical description and in vitro reproduction", *Ultrasound Med Biol,* **38**, 593-600 (2012).

[167] M. X. Tang, N. Kamiyama, and R. J. Eckersley. "Effects of Nonlinear Propagation in Ultrasound Contrast Agent Imaging", *Ultrasound Med Biol,* **36**, 459-466 (2010).

[168] G. Renaud, J. G. Bosch, N. de Jong, A. F. W. van der Steen, V. Shamdasani, and R. Entrekin. "Counter-propagation interaction for contrast-enhanced ultrasound imaging", *2012 IEEE International Ultrasonics Symposium,* (2012).

[169] H. J. Yu, H. J. Jang, T. K. Kim, K. Khalili, R. Williams, G. Lueck, J. Hudson, and P. N. Burns. "Pseudoenhancement Within the Local Ablation Zone of Hepatic Tumors Due to a Nonlinear Artifact on Contrast-Enhanced Ultrasound", *Am J Roentgenol,* **194**, 653-659 (2010).

[170] A. Thapar, J. Shalhoub, M. Averkiou, C. Mannaris, A. H. Davies, and E. L. S. Leen. "Dose-Dependent Artifact in the Far Wall of the Carotid Artery at Dynamic Contrast-enhanced US", *Radiology,* **262**, 672-679 (2012).

[171] R. Hansen, B. A. J. Angelsen, P. N. Burns, A. Bouakaz, J. Borsboom, M. Versluis, and N. de Jong. "Radial modulation imaging", in *Proc. 10th European Symp. Ultrasound Contrast Imaging, Rotterdam, The Netherlands*, 2005.

[172] M. E. Frijlink, D. E. Goertz, A. Bouakaz, and A. F. W. van der Steen. "A simulation study on tissue harmonic imaging with a single-element intravascular ultrasound catheter", *J Acoust Soc Am,* **120**, 1723-1731 (2006).

[173] J. Jimenez-Fernandez. "Nonlinear response to ultrasound of encapsulated microbubbles", *Ultrasonics,* **52**, 784-793 (2012).

[174] J. Park, X. Li, Q. F. Zhou, and K. K. Shung. "Combined chirp coded tissue harmonic and fundamental ultrasound imaging for intravascular ultrasound: 20-60 MHz phantom and ex vivo results", *Ultrasonics,* **53**, 369-376 (2013).

[175] C. C. Shen and C. H. Lin. "Chirp-Encoded Excitation for Dual-Frequency Ultrasound Tissue Harmonic Imaging", *IEEE Trans Ultrason Ferroelectr Freq Control,* **59**, 2420-2430 (2012).

[176] J. Park, Y. Huang, R. M. Chen, J. Lee, T. M. Cummins, Q. F. Zhou, C. L. Lien, and K. K. Shung. "Pulse Inversion Chirp Coded Tissue Harmonic Imaging (PI-CTHI) of Zebrafish Heart Using High Frame Rate Ultrasound Biomicroscopy", *Annals of Biomedical Engineering,* **41**, 41-52 (2013).

[177] A. Novell, C. A. Sennoga, J. M. Escoffre, J. Chaline, and A. Bouakaz. "Evaluation of chirp reversal power modulation sequence for contrast agent imaging", *Phys Med Biol,* **59**, 5101-5117 (2014).

[178] M. R. Sprague, E. Cherin, D. E. Goertz, and F. S. Foster. "Nonlinear Emission from Individual Bound Microbubbles at High Frequencies", *Ultrasound Med Biol,* **36**, 313-324 (2010).

[179] J. N. Tjotta and S. Tjotta. "An Analytical Model for the Nearfield of a Baffled Piston Transducer", *J Acoust Soc Am,* **68**, 334-339 (1980).

[180] T. Faez, M. Emmer, M. Docter, J. Sijl, M. Versluis, and N. de Jong. "Characterizing the subharmonic response of phospholipid-coated microbubbles for carotid imaging", *Ultrasound Med Biol,* **37**, 958-970 (2011).

[181] P. M. Shankar, P. Dala Krishna, and V. L. Newhouse. "Advantages of subharmonic over second harmonic backscatter for contrast-to-tissue echo enhancement", *Ultrasound Med Biol,* **24**, 395-399 (1998).

[182] F. Forsberg, J. B. Liu, W. T. Shi, J. Furuse, M. Shimizu, and B. B. Goldberg. "In vivo pressure estimation using subharmonic contrast microbubble signals: Proof of concept", *IEEE Trans Ultrason Ferroelectr Freq Control,* **52**, 581-583 (2005).

[183] D. Zhang, Y. Gong, X. Gong, Z. Liu, K. Tan, and H. Zheng. "Enhancement of subharmonic emission from encapsulated microbubbles by using a chirp excitation technique", *Phys Med Biol,* **52**, 5531-5544 (2007).

[184] V. Daeichin, T. Faez, G. Renaud, J. G. Bosch, A. F. W. v. d. Steen, and N. d. Jong. "Effect of self-demodulation on the subharmonic response of contrast agent microbubbles", *Phys Med Biol,* **57**, 3675 (2012).

[185] H. R. Zheng, O. Mukdadi, H. Kim, J. R. Hertzberg, and R. Shandas. "Advantages in using multifrequency excitation of contrast microbubbles for enhancing echo particle image velocimetry techniques: Initial numerical studies using rectangular and triangular waves", *Ultrasound Med Biol,* **31**, 99-108 (2005).

[186] E. Biagi, L. Breschi, E. Varmacci, and L. Masotti. "Subharmonic emissions from microbubbles: Effect of the driving pulse shape", *IEEE Trans Ultrason Ferroelectr Freq Control,* **53**, 2174-2182 (2006).

[187] L. Masotti, E. Biagi, L. Breschi, and E. Vannacci. "Study and characterization of subharmonic emissions by using shaped ultrasonic driving pulse", *Acoustical Imaging, Vol 28,* **28**, 307-315 (2007).

[188] D. Zhang, X. Y. Xi, Z. Zhang, X. F. Gong, G. Chen, and J. R. Wu. "A dual-frequency excitation technique for enhancing the sub-harmonic emission from encapsulated microbubbles", *Phys Med Biol,* **54**, 4257-4272 (2009).

[189] J. E. Streeter, R. Gessner, I. Miles, and P. A. Dayton. "Improving Sensitivity in Ultrasound Molecular Imaging by Tailoring Contrast Agent Size Distribution: In Vivo Studies", *Mol Imaging,* **9**, 87-95 (2010).

[190] S. Zhao, D. E. Kruse, K. W. Ferrara, and P. A. Dayton. "Selective imaging of adherent targeted ultrasound contrast agents", *Phys Med Biol,* **52**, 2055-2072 (2007).

[191] X. W. Hu, H. R. Zheng, D. E. Kruse, P. Sutcliffe, D. N. Stephens, and K. W. Ferrara. "A Sensitive TLRH Targeted Imaging Technique for Ultrasonic Molecular Imaging", *IEEE Trans Ultrason Ferroelectr Freq Control,* **57**, 305-316 (2010).

[192] A. Needles, O. Couture, and F. S. Foster. "A Method for Differentiating Targeted Microbubbles in Real Time Using Subharmonic Micro-Ultrasound and Interframe Filtering", *Ultrasound Med Biol,* **35**, 1564-1573 (2009).

[193] F. W. Mauldin, A. H. Dhanaliwala, A. V. Patil, and J. A. Hossack. "Real-time targeted molecular imaging using singular value spectra properties to isolate the adherent microbubble signal", *Phys Med Biol,* **57**,(2012).

[194] M. A. Pysz, S. S. Gambhir, and J. K. Willmann. "Molecular imaging: current status and emerging strategies", *Clin Radiol,* **65**, 500-516 (2010).

[195] A. G. Sorace, R. Saini, M. Mahoney, and K. Hoyt. "Molecular Ultrasound Imaging Using a Targeted Contrast Agent for Assessing Early Tumor Response to Antiangiogenic Therapy", *J Ultrasound Med,* **31**, 1543-1550 (2012).

[196] J. E. Streeter, R. C. Gessner, J. Tsuruta, S. Feingold, and P. A. Dayton. "Assessment of Molecular Imaging of Angiogenesis with Three-Dimensional Ultrasonography", *Mol Imaging,* **10**, 460-468 (2011).

[197] S. M. Stieger, P. A. Dayton, M. A. Borden, C. F. Caskey, S. M. Griffey, E. R. Wisner, and K. W. Ferrara. "Imaging of angiogenesis using Cadence contrast pulse sequencing and targeted contrast agents", *Contrast Media Mol Imaging,* **3**, 9-18 (2008).

[198] M. Piedra, A. Allroggen, and J. R. Lindner. "Molecular imaging with targeted contrast ultrasound", *Cerebrovasc Dis,* **27 Suppl 2**, 66-74 (2009).

[199] P. A. Dayton and J. J. Rychak. "Molecular ultrasound imaging using microbubble contrast agents", *Frontiers in Bioscience,* **12**, 5124-5142 (2007).

[200] C. R. Anderson, X. W. Hu, H. Zhang, J. Tlaxca, A. E. Decleves, R. Houghtaling, K. Sharma, M. Lawrence, K. W. Ferrara, and J. J. Rychak. "Ultrasound Molecular Imaging of Tumor Angiogenesis With an Integrin Targeted Microbubble Contrast Agent", *Invest Radiol,* **46**, 215-224 (2011).

[201] M. Itani and R. F. Mattrey. "The Effect of Inhaled Gases on Ultrasound Contrast Agent Longevity In Vivo", *Molecular Imaging and Biology,* **14**, 40-46 (2012).

[202] J. H. Wible, Jr., J. K. Wojdyla, G. L. Bales, W. N. McMullen, E. A. Geiser, and D. D. Buss. "Inhaled gases affect the ultrasound contrast produced by Albunex in anesthetized dogs", *J Am Soc Echocardiogr,* **9**, 442-451 (1996).

[203] N. McDannold, Y. Z. Zhang, and N. Vykhodtseva. "Blood-Brain Barrier Disruption and Vascular Damage Induced by Ultrasound Bursts Combined with Microbubbles Can Be Influenced by Choice of Anesthesia Protocol", *Ultrasound Med Biol,* **37**, 1259-1270 (2011).

[204] L. Mullin, R. Gessner, J. Kwan, M. Kaya, M. A. Borden, and P. A. Dayton. "Effect of anesthesia carrier gas on in vivo circulation times of ultrasound microbubble contrast agents in rats", *Contrast Media Mol Imaging,* **6**, 126-131 (2011).

[205] M. A. Pysz, I. Guracar, L. Tian, and J. K. Willmann. "Fast microbubble dwell-time based ultrasonic molecular imaging approach for quantification and monitoring of angiogenesis in cancer", *Quant Imaging Med Surg,* **2**, 68-80 (2012).

[206] V. Daeichin, Z. Akkus, A. Hoogi, J. G. Bosch, A. Needles, K. Kooiman, I. Skachkov, J. Sluimer, B. Janssen, M. J. A. P. Daemen, A. F. W. van der Steen, and N. de Jong. "Quantification of targeted microbubbles in contrast enhanced ultrasound", in *IEEE Ultrasonics Symposium Proceedings*, 1825-1828 (2013).

[207] H. Liu, X. Wang, K. B. Tan, P. Liu, Z. X. Zhuo, Z. Liu, X. Hua, Q. Q. Zhuo, H. M. Xia, and Y. H. Gao. "Molecular Imaging of Vulnerable Plaques in Rabbits Using Contrast-Enhanced Ultrasound Targeting to Vascular Endothelial Growth Factor Receptor-2", *J Clin Ultrasound,* **39**, 83-90 (2011).

[208] A. Hamilton, S. L. Huang, D. Warnick, A. Stein, M. Rabbat, T. Madhav, B. Kane, A. Nagaraj, M. Klegerman, R. MacDonald, and D. McPherson. "Left ventricular thrombus enhancement after intravenous injection of echogenic immunoliposomes - Studies in a new experimental model", *Circulation,* **105**, 2772-2778 (2002).

[209] N. Deshpande, A. Needles, and J. K. Willmann. "Molecular ultrasound imaging: current status and future directions", *Clin Radiol,* **65**, 567-581 (2010).

[210] G. Korpanty, J. G. Carbon, P. A. Grayburn, J. B. Fleming, and R. A. Brekken. "Monitoring response to anticancer therapy by targeting microbubbles to tumor vasculature", *Clinical Cancer Research,* **13**, 323-330 (2007).

[211] N. Deshpande, Y. Ren, K. Foygel, J. Rosenberg, and J. K. Willmann. "Tumor Angiogenic Marker Expression Levels during Tumor Growth: Longitudinal Assessment with Molecularly Targeted Microbubbles and US Imaging", *Radiology,* **258**, 804-811 (2011).

[212] D. B. Ellegala, H. L. Poi, J. E. Carpenter, A. L. Klibanov, S. Kaul, M. E. Shaffrey, J. Sklenar, and J. R. Lindner. "Imaging tumor angiogenesis with contrast ultrasound and microbubbles targeted to alpha(v)beta(3)", *Circulation,* **108**, 336-341 (2003).

[213] A. Barua, A. Yellapa, J. M. Bahr, S. A. Machado, P. Bitterman, S. Basu, S. Sharma, and J. S. Abramowicz. "Enhancement of ovarian tumor detection with alphavbeta3 integrin-targeted ultrasound molecular imaging agent in laying hens: a preclinical model of spontaneous ovarian cancer", *Int J Gynecol Cancer,* **24**, 19-28 (2014).

[214] M. A. Kuliszewski, H. Fujii, C. Liao, A. H. Smith, A. Xie, J. R. Lindner, and H. Leong-Poi. "Molecular imaging of endothelial progenitor cell engraftment using contrast-enhanced ultrasound and targeted microbubbles", *Cardiovascular Research,* **83**, 653-662 (2009).

[215] S. V. Bachawal, K. C. Jensen, A. M. Lutz, S. S. Gambhir, F. Tranquart, L. Tian, and J. K. Willmann. "Earlier Detection of Breast Cancer with Ultrasound Molecular Imaging in a Transgenic Mouse Model", *Cancer Research,* **73**, 1689-1698 (2013).

[216] C. Grouls, M. Hatting, A. Rix, S. Pochon, W. Lederle, I. Tardy, C. K. Kuhl, C. Trautwein, F. Kiessling, and M. Palmowski. "Liver Dysplasia: US Molecular Imaging with Targeted Contrast Agent Enables Early Assessment", *Radiology,* **267**, 487-495 (2013).

[217] E. Khanicheh, M. Mitterhuber, L. F. Xu, S. P. Haeuselmann, G. M. Kuster, and B. A. Kaufmann. "Noninvasive Ultrasound Molecular Imaging of the Effect of Statins on Endothelial Inflammatory Phenotype in Early Atherosclerosis", *Plos One,* **8**,(2013).

[218] E. Khanicheh, Y. Qi, A. Xie, M. Mitterhuber, L. F. Xu, M. Mochizuki, Y. Daali, V. Jaquet, K. H. Krause, Z. M. Ruggeri, G. M. Kuster, J. R. Lindner, and B. A. Kaufmann. "Molecular Imaging Reveals Rapid Reduction of Endothelial Activation in Early Atherosclerosis With Apocynin Independent of Antioxidative Properties", *Arteriosclerosis Thrombosis and Vascular Biology,* **33**, 2187-2192 (2013).

[219] M. A. Pysz, K. Foygel, J. Rosenberg, S. S. Gambhir, M. Schneider, and J. K. Willmann. "Antiangiogenic Cancer Therapy: Monitoring with Molecular US and a Clinically Translatable Contrast Agent (BR55)", *Radiology,* **256**, 519-527 (2010).

[220] M. B. Toaldo, V. Salvatore, S. Marinelli, C. Palama, M. Milazzo, L. Croci, L. Venerandi, M. Cipone, L. Bolondi, and F. Piscaglia. "Use of VEGFR-2 Targeted Ultrasound Contrast Agent for the Early Evaluation of Response to Sorafenib in a Mouse Model of Hepatocellular Carcinoma", *Molecular Imaging and Biology,* **17**, 29-37 (2015).

[221] M. Palmowski, J. Huppert, G. Ladewig, P. Hauff, M. Reinhardt, M. M. Mueller, E. C. Woenne, J. W. Jenne, M. Maurer, G. W. Kauffmann, W. Semmier, and F. Kiesslin. "Molecular profiling of angiogenesis with targeted ultrasound imaging: early assessment of antiangiogenic therapy effects", *Molecular Cancer Therapeutics,* **7**, 101-109 (2008).

[222] S. R. Sirsi, M. L. Flexman, F. Vlachos, J. Z. Huang, S. L. Hernandez, H. K. Kim, T. B. Johung, J. W. Gander, A. R. Reichstein, B. S. Lampl, A. T. Wang, A. H. Hielscher, J. J. Kandel, D. J. Yamashiro, and M. A. Borden. "Contrast Ultrasound Imaging for Identification of Early Responder Tumor Models to Anti-Angiogenic Therapy", *Ultrasound Med Biol,* **38**, 1019-1029 (2012).

[223] J. E. Streeter, S. G. Herrera-Loeza, N. F. Neel, J. J. Yeh, and P. A. Dayton. "A Comparative Evaluation of Ultrasound Molecular Imaging, Perfusion Imaging, and Volume Measurements in Evaluating Response to Therapy in Patient-Derived Xenografts", *Technology in Cancer Research & Treatment,* **12**, 311-321 (2013).

[224] T. Flisikowska, A. Kind, and A. Schnieke. "The new pig on the block: modelling cancer in pigs", *Transgenic Research,* **22**, 673-680 (2013).

[225] H. Kim, G. L. Britton, T. Peng, C. K. Holland, D. D. McPherson, and S. L. Huang. "Nitric oxide-loaded echogenic liposomes for treatment of vasospasm following subarachnoid hemorrhage", *Int J Nanomedicine,* **9**, 155-165 (2014).

[226] S. M. Chadderdon, J. T. Belcik, L. Bader, M. A. Kirigiti, D. M. Peters, P. Kievit, K. L. Grove, and J. R. Lindner. "Proinflammatory Endothelial Activation Detected by Molecular Imaging in Obese Nonhuman Primates Coincides With Onset of Insulin Resistance and Progressively Increases With Duration of Insulin Resistance", *Circulation,* **129**, 471-478 (2014).

[227] B. P. Davidson, S. M. Chadderdon, J. T. Belcik, S. Gupta, and J. R. Lindner. "Ischemic Memory Imaging in Nonhuman Primates with Echocardiographic Molecular Imaging of Selectin Expression", *J Am Soc Echocardiogr,* **27**, 786-U151 (2014).

[228] J. E. Streeter and P. A. Dayton. "An In Vivo Evaluation of the Effect of Repeated Administration and Clearance of Targeted Contrast Agents on Molecular Imaging Signal Enhancement", *Theranostics,* **3**, 93-98 (2013).

[229] J. Bzyl, M. Palmowski, A. Rix, S. Arns, J. M. Hyvelin, S. Pochon, J. Ehling, S. Schrading, F. Kiessling, and W. Lederle. "The high angiogenic activity in very early breast cancer enables reliable imaging with VEGFR2-targeted microbubbles (BR55)", *Eur Radiol,* **23**, 468-475 (2013).

[230] X. Hu, C. F. Caskey, L. M. Mahakian, D. E. Kruse, J. R. Beegle, A. E. Decleves, J. J. Rychak, P. L. Sutcliffe, K. Sharma, and K. W. Ferrara. "In vivo validation and 3D visualization of broadband ultrasound molecular imaging", *Am J Nucl Med Mol Imaging,* **3**, 336-349 (2013).

[231] S. P. Bao, B. D. Thrall, and D. L. Miller. "Transfection of a reporter plasmid into cultured cells by sonoporation in vitro", *Ultrasound Med Biol,* **23**, 953-959 (1997).

[232] J. McLaughlan, N. Ingram, P. Smith, S. Harput, P. Coletta, S. Evans, and S. Freear. "Increasing the sonoporation efficiency of targeted polydisperse microbubble populations using chirp excitation", *IEEE Trans Ultrason Ferroelectr Freq Control,* **60**, 2511-2520 (2013).

[233] I. Skachkov, Y. Luan, A. F. van der Steen, N. de Jong, and K. Kooiman. "Targeted microbubble mediated sonoporation of endothelial cells in vivo", *IEEE Trans Ultrason Ferroelectr Freq Control,* **61**, 1661-1667 (2014).

[234] L. C. Phillips, A. L. Klibanov, B. R. Wamhoff, and J. A. Hossack. "Intravascular ultrasound detection and delivery of molecularly targeted microbubbles for gene delivery", *IEEE Trans Ultrason Ferroelectr Freq Control,* **59**, 1596-1601 (2012).

[235] S. Chang, J. Guo, J. Sun, S. Zhu, Y. Yan, Y. Zhu, M. Li, Z. Wang, and R. X. Xu. "Targeted microbubbles for ultrasound mediated gene transfection and apoptosis induction in ovarian cancer cells", *Ultrason Sonochem,* **20**, 171-179 (2013).

[236] A. Xie, T. Belcik, Y. Qi, T. K. Morgan, S. A. Champaneri, S. Taylor, B. P. Davidson, Y. Zhao, A. L. Klibanov, M. A. Kuliszewski, H. Leong-Poi, A. Ammi, and J. R. Lindner. "Ultrasound-Mediated Vascular Gene Transfection by Cavitation of Endothelial-Targeted Cationic Microbubbles", *Jacc-Cardiovasc Imag,* **5**, 1253-1262 (2012).

[237] J. L. Tlaxca, J. J. Rychak, P. B. Ernst, P. R. Konkalmatt, T. I. Shevchenko, T. T. Pizzaro, J. Rivera-Nieves, A. L. Klibanov, and M. B. Lawrence. "Ultrasound-based molecular imaging and specific gene delivery to mesenteric vasculature by endothelial adhesion molecule targeted microbubbles in a mouse model of Crohn's disease", *J Control Release,* **165**, 216-225 (2013).

[238] H. Liu, S. Chang, J. Sun, S. Zhu, C. Pu, Y. Zhu, Z. Wang, and R. X. Xu. "Ultrasound-mediated destruction of LHRHa-targeted and paclitaxel-loaded lipid microbubbles induces proliferation inhibition and apoptosis in ovarian cancer cells", *Mol Pharm,* **11**, 40-48 (2014).

[239] F. Yan, X. Li, Q. Jin, C. Jiang, Z. Zhang, T. Ling, B. Qiu, and H. Zheng. "Therapeutic ultrasonic microbubbles carrying paclitaxel and LyP-1 peptide: preparation, characterization and application to ultrasound-assisted chemotherapy in breast cancer cells", *Ultrasound Med Biol,* **37**, 768-779 (2011).

[240] C. Pu, S. Chang, J. Sun, S. Zhu, H. Liu, Y. Zhu, Z. Wang, and R. X. Xu. "Ultrasound-mediated destruction of LHRHa-targeted and paclitaxel-loaded lipid microbubbles for the treatment of intraperitoneal ovarian cancer xenografts", *Mol Pharm,* **11**, 49-58 (2014).

[241] C. H. Fan, C. Y. Ting, H. L. Liu, C. Y. Huang, H. Y. Hsieh, T. C. Yen, K. C. Wei, and C. K. Yeh. "Antiangiogenic-targeting drug-loaded microbubbles combined with focused ultrasound for glioma treatment", *Biomaterials,* **34**, 2142-2155 (2013).

[242] Z. Fan, R. E. Kumon, J. Park, and C. X. Deng. "Intracellular delivery and calcium transients generated in sonoporation facilitated by microbubbles", *J Control Release,* **142**, 31-39 (2010).

[243] S. Kotopoulis and M. Postema. "Microfoam formation in a capillary", *Ultrasonics,* **50**, 260-268 (2010).

[244] X. W. Hu, A. Kheirolomoom, L. M. Mahakian, J. R. Beegle, D. E. Kruse, K. S. Lam, and K. W. Ferrara. "Insonation of Targeted Microbubbles Produces Regions of Reduced Blood Flow Within Tumor Vasculature", *Invest Radiol,* **47**, 398-405 (2012).

[245] A. K. W. Wood, S. M. Schultz, W. M. F. Lee, R. M. Bunte, and C. M. Sehgal. "Antivascular Ultrasound Therapy Extends Survival of Mice with Implanted Melanomas", *Ultrasound Med Biol,* **36**, 853-857 (2010).

[246] M. Rask-Andersen, J. Zhang, D. Fabbro, and H. B. Schioth. "Advances in kinase targeting: current clinical use and clinical trials", *Trends in Pharmacological Sciences,* **35**, 60-76 (2014).

[247] J. H. Hwang and L. A. Crum. "Current Status of Clinical High-Intensity Focused Ultrasound", *2009 Annual International Conference of the IEEE Engineering in Medicine and Biology Society, Vols 1-20,* 130-133 (2009).

[248] X. P. Li and L. Z. Zheng. "Advances of high intensity focused ultrasound (HIFU) for pancreatic cancer", *Int J Hyperthermia,* **29**, 678-682 (2013).

[249] Y. Zhou, Z. G. Wang, Y. Chen, H. X. Shen, Z. C. Luo, A. Li, Q. Wang, H. T. Ran, P. Li, W. X. Song, Z. Yang, H. R. Chen, Z. B. Wang, G. M. Lu, and Y. Y. Zheng. "Microbubbles from Gas-Generating Perfluorohexane Nanoemulsions for Targeted Temperature-Sensitive Ultrasonography and Synergistic HIFU Ablation of Tumors", *Adv Mater,* **25**, 4123-4130 (2013).

[250] F. M. Reid, N. A. Niemuth, S. M. Shumaker, J. D. Waugh, and J. S. Graham. "Biomechanical monitoring of cutaneous sulfur mustard-induced lesions in the weanling pig model for depth of injury", *Skin Res Technol,* **13**, 217-225 (2007).

[251] X. Yan, M. Li, Z. Chen, Y. Zhu, Y. Song, and H. Zhang. "Schlemm's Canal and Trabecular Meshwork in Eyes with Primary Open Angle Glaucoma: A Comparative Study Using High-Frequency Ultrasound Biomicroscopy", *Plos One,* **11**, e0145824 (2016).

[252] D. L. Jovanovic and Z. U. Pesic. "Preoperative skin tumours thickness determination by high-frequency ultrasound on head and neck region", *J Eur Acad Dermatol Venereol,* **27**, 251-253 (2013).

[253] S. Ghai, G. Eure, V. Fradet, M. E. Hyndman, T. McGrath, B. Wodlinger, and C. P. Pavlovich. "Assessing Cancer Risk on Novel 29 MHz Micro-Ultrasound Images of the Prostate: Creation of the Micro-Ultrasound Protocol for Prostate Risk Identification", *J Urol,* **196**, 562-569 (2016).

[254] C. L. de Korte, H. H. Hansen, and A. F. van der Steen. "Vascular ultrasound for atherosclerosis imaging", *Interface Focus,* **1**, 565-575 (2011).

[255] V. Cantisani, M. Bertolotto, H. P. Weskott, L. Romanini, H. Grazhdani, M. Passamonti, F. M. Drudi, F. Malpassini, A. Isidori, F. M. Meloni, F. Calliada, and F. D'Ambrosio. "Growing indications for CEUS: The kidney, testis, lymph nodes, thyroid, prostate, and small bowel", *Eur J Radiol,* **84**, 1675-1684 (2015).

[256] D. E. Goertz, E. Cherin, A. Needles, R. Karshafian, A. S. Brown, P. N. Burns, and F. S. Foster. "High frequency nonlinear B-scan imaging of microbubble contrast agents", *IEEE Trans Ultrason Ferroelectr Freq Control,* **52**, 65-79 (2005).

[257] V. Daeichin, J. G. Bosch, A. Needles, F. S. Foster, A. van der Steen, and N. de Jong. "Subharmonic, Non-linear Fundamental and Ultraharmonic Imaging of Microbubble Contrast at High Frequencies", *Ultrasound Med Biol,* **41**, 486-497 (2015).

[258] A. Katiyar and K. Sarkar. "Excitation threshold for subharmonic generation from contrast microbubbles", *J Acoust Soc Am,* **130**, 3137-3147 (2011).

[259] B. L. Helfield, E. Cherin, F. S. Foster, and D. E. Goertz. "Investigating the subharmonic response of individual phospholipid encapsulated microbubbles at high frequencies: a comparative study of five agents", *Ultrasound Med Biol,* **38**, 846-863 (2012).

[260] T. van Rooij, Y. Luan, G. Renaud, A. F. van der Steen, M. Versluis, N. de Jong, and K. Kooiman. "Non-linear response and viscoelastic properties of lipid-coated microbubbles: DSPC versus DPPC", *Ultrasound Med Biol,* **41**, 1432-1445 (2015).

[261] V. Inc.. "Vevo MicroMarker™ Non-Targeted Contrast Agent Kit", VisualSonics Inc., Toronto, ON, Canada2016.

[262] T. van Rooij, V. Daeichin, I. Skachkov, N. de Jong, and K. Kooiman. "Targeted ultrasound contrast agents for ultrasound molecular imaging and therapy", *Int J Hyperthermia,* **31**, 90-106 (2015).

[263] V. Daeichin, K. Kooiman, I. Skachkov, J. G. Bosch, A. F. van der Steen, and N. de Jong. "Optimization of ultrasound contrast agent for high frequency ultrasound molecular imaging using subharmonic oscillation", in *IEEE Ultrasonics Symposium Proceedings*, Chicago, Illinois, USA (2014).

[264] E. Stride and M. Edirisinghe. "Novel microbubble preparation technologies", *Soft Matter,* **4**, 2350-2359 (2008).

[265] B. Geers, I. Lentacker, N. N. Sanders, J. Demeester, S. Meairs, and S. C. De Smedt. "Self-assembled liposome-loaded microbubbles: The missing link for safe and efficient ultrasound triggered drug-delivery", *J Control Release,* **152**, 249-256 (2011).

[266] S. Sirsi, J. Feshitan, J. Kwan, S. Homma, and M. Borden. "Effect of microbubble size on fundamental mode high frequency ultrasound imaging in mice", *Ultrasound Med Biol,* **36**, 935-948 (2010).

[267] C. M. Moran, J. A. Ross, C. Cunningham, M. Butler, T. Anderson, D. Newby, K. A. A. Fox, and W. N. McDicken. "Manufacture and acoustical characterisation of a high-frequency contrast agent for targeting applications", *Ultrasound Med Biol,* **32**, 421-428 (2006).

[268] S. Wang, G. Samiotaki, O. Olumolade, J. A. Feshitan, and E. E. Konofagou. "Microbubble type and distribution dependence of focused ultrasound-induced blood-brain barrier opening", *Ultrasound Med Biol,* **40**, 130-137 (2014).

[269] M. Kaya, T. S. Gregory, and P. A. Dayton. "Changes in Lipid-Encapsulated Microbubble Population during Continuous Infusion and Methods to Maintain Consistency", *Ultrasound Med Biol,* **35**, 1748-1755 (2009).

[270] C. C. Shen and P. C. Li. "Pulse-inversion-based fundamental imaging for contrast detection", *IEEE Trans Ultrason Ferroelectr Freq Control,* **50**, 1124-1133 (2003).

[271] V. Daeichin, Z. Akkus, I. Skachkov, K. Kooiman, A. Needles, J. Sluimer, B. Janssen, M. J. Daemen, A. F. van der Steen, N. de Jong, and J. G. Bosch. "Quantification of bound microbubbles in ultrasound molecular imaging", *IEEE Trans Ultrason Ferroelectr Freq Control,* **62**, 1190-1200 (2015).

[272] A. Hoogi, Z. Akkus, S. C. van den Oord, G. L. ten Kate, A. F. Schinkel, J. G. Bosch, N. de Jong, D. Adam, and A. F. van der Steen. "Quantitative analysis of ultrasound contrast flow behavior in carotid plaque neovasculature", *Ultrasound Med Biol,* **38**, 2072-2083 (2012).

[273] J. A. Feshitan, C. C. Chen, J. J. Kwan, and M. A. Borden. "Microbubble size isolation by differential centrifugation", *J Colloid Interface Sci,* **329**, 316-324 (2009).

[274] M. Minnaert. "XVI. On musical air-bubbles and the sounds of running water", *Philos Mag,* **16**, 235-248 (1933).

[275] B. L. Helfield, B. Y. Leung, X. Huo, and D. E. Goertz. "Scaling of the viscoelastic shell properties of phospholipid encapsulated microbubbles with ultrasound frequency", *Ultrasonics,* **54**, 1419-1424 (2014).

[276] D. E. Goertz, N. de Jong, and A. F. van der Steen. "Attenuation and size distribution measurements of Definity and manipulated Definity populations", *Ultrasound Med Biol,* **33**, 1376-1388 (2007).

[277] S. A. Peyman, J. R. McLaughlan, R. H. Abou-Saleh, G. Marston, B. R. Johnson, S. Freear, P. L. Coletta, A. F. Markham, and S. D. Evans. "On-chip preparation of nanoscale contrast agents towards high-resolution ultrasound imaging", *Lab Chip,* **16**, 679-687 (2016).

[278] P. Dynarowicz-Łątka and K. Hac-Wydro. "Interactions between phosphatidylcholines and cholesterol in monolayers at the air/water interface", *Colloids and surfaces B, Biointerfaces,* **37**, 21-25 (2004).

[279] Y. Kurniawan, C. Scholz, and G. D. Bothun. "n-Butanol partitioning into phase-separated heterogeneous lipid monolayers", *Langmuir,* **29**, 10817-10823 (2013).

[280] M. M. Lozano and L. Longo. "Complex formation and other phase transformations mapped in saturated phosphatidylcholine/DSPE-PEG2000 monolayers", *Soft Matter,* **5**, 1822–1834 (2009).

[281] V. M. Kaganer, H. Mohwald, and P. Dutta. "Structure and phase transitions in Langmuir monolayers", *Reviews of Modern Physics,* **71**, 779-819 (1999).

[282] A. F. Schinkel, C. G. Krueger, A. Tellez, J. F. Granada, J. D. Reed, A. Hall, W. Zang, C. Owens, G. L. Kaluza, D. Staub, B. Coll, F. J. Ten Cate, and S. B. Feinstein. "Contrast-enhanced ultrasound for imaging vasa vasorum: comparison with histopathology in a swine model of atherosclerosis", *Eur J Echocardiogr,* **11**, 659-664 (2010).

[283] M. S. Dolan, S. S. Gala, S. Dodla, S. S. Abdelmoneim, F. Xie, D. Cloutier, M. Bierig, S. L. Mulvagh, T. R. Porter, and A. J. Labovitz. "Safety and Efficacy of Commercially Available Ultrasound Contrast Agents for Rest and Stress Echocardiography A Multicenter Experience", *J Am Coll Cardiol,* **53**, 32-38 (2009).

[284] D. W. Kitzman, M. E. Goldman, L. D. Gillam, J. L. Cohen, G. P. Aurigemma, and J. S. Gottdiener. "Efficacy and safety of the novel ultrasound contrast agent perflutren (definity) in patients with suboptimal baseline left ventricular echocardiographic images*", *Am J Cardiol,* **86**, 669-674 (2000).

[285] M. A. Borden and M. L. Longo. "Dissolution behavior of lipid monolayer-coated, air-filled microbubbles: Effect of lipid hydrophobic chain length", *Langmuir,* **18**, 9225-9233 (2002).

[286] M. A. Parrales, J. M. Fernandez, M. Perez-Saborid, J. A. Kopechek, and T. M. Porter. "Acoustic characterization of monodisperse lipid-coated microbubbles: relationship between size and shell viscoelastic properties", *J Acoust Soc Am,* **136**, 1077 (2014).

[287] S. A. Stapleton, A. Needles, E. Henderson, and F. S. Foster. "Concentration Requirements for Subharmonic Quantitative Contrast Enhanced High Frequency Ultrasound Flow Studies", in *IEEE Ultrasonics Symposium Proceedings* (2007).

[288] E. Stock, K. Vanderperren, H. Haers, L. Duchateau, M. Hesta, and J. H. Saunders. "Quantitative Differences Between the First and Second Injection of Contrast Agent in Contrast-Enhanced Ultrasonography of Feline Kidneys and Spleen", *Ultrasound Med Biol*.

[289] A. Rix, M. Palmowski, F. Gremse, K. Palmowski, W. Lederle, F. Kiessling, and J. Bzyl. "Influence of repetitive contrast agent injections on functional and molecular ultrasound measurements", *Ultrasound Med Biol,* **40**, 2468-2475 (2014).

[290] A. Dizeux, T. Payen, G. Barrois, D. Le Guillou Buffello, and S. L. Bridal. "Reproducibility of Contrast-Enhanced Ultrasound in Mice with Controlled Injection", *Mol Imaging Biol,* (2016).

[291] W. H. Organization. "WHO Good manufacturing practices for pharmaceutical products: main principles", World Health Organization2011.

[292] M.-R. Toh and G. N. C. Chiu. "Liposomes as sterile preparations and limitations of sterilisation techniques in liposomal manufacturing", *Asian J Pharm Sci,* **8**, 88-95 (2013).

[293] P. K. Hui and W. R. Diluzio. "Stabilization and terminal sterilization of phospholipid formulations", US Patent, 2002.

[294] S. B. Feinstein, J. Cheirif, F. J. Tencate, P. R. Silverman, P. A. Heidenreich, C. Dick, R. M. Desir, W. F. Armstrong, M. A. Quinones, and P. M. Shah. "Safety and Efficacy of a New Transpulmonary Ultrasound Contrast Agent - Initial Multicenter Clinical-Results", *J Am Coll Cardiol,* **16**, 316-324 (1990).

[295] A. L. Klibanov. "Ultrasound contrast agents: Development of the field and current status", *Contrast Agents Ii,* **222**, 73-106 (2002).

[296] J. T. Sutton, K. J. Haworth, G. Pyne-Geithman, and C. K. Holland. "Ultrasound-mediated drug delivery for cardiovascular disease", *Expert Opin Drug Deliv,* **10**, 573-592 (2013).

[297] J. R. Lindner. "Molecular imaging of myocardial and vascular disorders with ultrasound", *JACC Cardiovasc Imaging,* **3**, 204-211 (2010).

[298] F. Kiessling, J. Bzyl, S. Fokong, M. Siepmann, G. Schmitz, and M. Palmowski. "Targeted Ultrasound Imaging of Cancer: An Emerging Technology on its Way to Clinics", *Curr Pharm Des,* **18**, 2184-2199 (2012).

[299] ICUS. *What is CEUS? (http://www.icus-society.org/about-ceus/ ed.)* [http://www.icus-society.org/about-ceus/]. Available: http://www.icus-society.org/about-ceus/

[300] J. J. Rychak, A. L. Klibanov, K. F. Ley, and J. A. Hossack. "Enhanced targeting of ultrasound contrast agents using acoustic radiation force", *Ultrasound Med Biol,* **33**, 1132-1139 (2007).

[301] L. M. Kornmann, K. D. Reesink, R. S. Reneman, and A. P. Hoeks. "Critical appraisal of targeted ultrasound contrast agents for molecular imaging in large arteries", *Ultrasound Med Biol,* **36**, 181-191 (2010).

[302] P. A. Dayton, D. Pearson, J. Clark, S. Simon, P. A. Schumann, R. Zutshi, T. O. Matsunaga, and K. W. Ferrara. "Ultrasonic analysis of peptide- and antibody-targeted microbubble contrast agents for molecular imaging of alphavbeta3-expressing cells", *Mol Imaging,* **3**, 125-134 (2004).

[303] S. Hell and E. H. K. Stelzer. "Fundamental Improvement of Resolution with a 4pi-Confocal Fluorescence Microscope Using 2-Photon Excitation", *Optics Communications,* **93**, 277-282 (1992).

[304] S. W. Hell, M. Schrader, and H. T. M. VanderVoort. "Far-field fluorescence microscopy with three-dimensional resolution in the 100-nm range", *J Microsc,* **187**, 1-7 (1997).

[305] W. A. van Cappellen, A. Nigg, and A. B. Houtsmuller. "Enhancement of optical resolution by 4Pi single and multiphoton confocal fluorescence microscopy", in *Cellular Imaging Techniques for Neuroscience and beyond*, F. G. Wouterlood, Ed., ed Oxford: Academic Press, 2012, pp. 55-80.

[306] G. Taubin. "Estimation of planar curves, surfaces, and nonpolar space curves defined by implicit equations with applications to edge and range image segmentation", *IEEE Trans. Pattern Anal. Mach. Intell.,* **12**, 1115-1138 (1991).

[307] J. Schindelin, I. Arganda-Carreras, E. Frise, V. Kaynig, M. Longair, T. Pietzsch, S. Preibisch, C. Rueden, S. Saalfeld, B. Schmid, J. Y. Tinevez, D. J. White, V. Hartenstein, K. Eliceiri, P. Tomancak, and A. Cardona. "Fiji: an open-source platform for biological-image analysis", *Nat Methods,* **9**, 676-682 (2012).

[308] N. Emans, J. Biwersi, and A. S. Verkman. "Imaging of endosome fusion in BHK fibroblasts based on a novel fluorimetric avidin-biotin binding assay", *Biophys J,* **69**, 716-728 (1995).

[309] N. Marme, J. P. Knemeyer, M. Sauer, and J. Wolfrum. "Inter- and intramolecular fluorescence quenching of organic dyes by tryptophan", *Bioconjug Chem,* **14**, 1133-1139 (2003).

[310] J. J. Kwan and M. A. Borden. "Lipid monolayer collapse and microbubble stability", *Adv Colloid Interface Sci,* **183-184**, 82-99 (2012).

[311] I. Lentacker, B. Geers, J. Demeester, S. C. De Smedt, and N. N. Sanders. "Design and evaluation of doxorubicin-containing microbubbles for ultrasound-triggered doxorubicin delivery: cytotoxicity and mechanisms involved", *Mol Ther,* **18**, 101-108 (2010).

[312] M. Emmer, H. J. Vos, M. Versluis, and N. de Jong. "Radial modulation of single microbubbles", *IEEE Trans Ultrason Ferroelectr Freq Control,* **56**, 2370-2379 (2009).

[313] S. B. Feinstein, B. Coll, D. Staub, D. Adam, A. F. Schinkel, F. J. ten Cate, and K. Thomenius. "Contrast enhanced ultrasound imaging", *J Nucl Cardiol,* **17**, 106-115 (2010).

[314] ICUS. "CEUS Around the World", International Contrast Ultrasound Society, Chicago, USA23/07/2016 2016.

[315] N. A. Hosny, G. Mohamedi, P. Rademeyer, J. Owen, Y. Wu, M. X. Tang, R. J. Eckersley, E. Stride, and M. K. Kuimova. "Mapping microbubble viscosity using fluorescence lifetime imaging of molecular rotors", *Proc Natl Acad Sci U S A,* **110**, 9225-9230 (2013).

[316] C. H. Wang and C. K. Yeh. "Controlling the size distribution of lipid-coated bubbles via fluidity regulation", *Ultrasound Med Biol,* **39**, 882-892 (2013).

[317] Y. J. Gong, M. Cabodi, and T. M. Porter. "Acoustic investigation of pressure-dependent resonance and shell elasticity of lipid-coated monodisperse microbubbles", *Applied Physics Letters,* **104**,(2014).

[318] M. Schneider, A. Broillet, P. Bussat, N. Giessinger, J. Puginier, R. Ventrone, and F. Yan. "Gray-scale liver enhancement in VX2 tumor-bearing rabbits using BR14, a new ultrasonographic contrast agent", *Invest Radiol,* **32**, 410-417 (1997).

[319] W. Krause. "Contrast Agents II: Optical, Ultrasound, X-Ray and Radiopharmaceutical Imaging", *Topics in Current Chemistry,* **222**,(2002).

[320] E. C. Gelderblom, H. J. Vos, F. Mastik, T. Faez, Y. Luan, T. J. Kokhuis, A. F. van der Steen, D. Lohse, N. de Jong, and M. Versluis. "Brandaris 128 ultra-high-speed imaging facility: 10 years of operation, updates, and enhanced features", *Rev Sci Instrum,* **83**, 103706 (2012).

[321] N. de Jong, M. Emmer, C. T. Chin, A. Bouakaz, F. Mastik, D. Lohse, and M. Versluis. ""Compression-only" behavior of phospholipid-coated contrast bubbles", *Ultrasound Med Biol,* **33**, 653-656 (2007).

[322] H. Medwin. "Counting bubbles acoustically: A review", *Ultrasonics,* **15**, 7-13 (1977).

[323] J. Sijl, B. Dollet, M. Overvelde, V. Garbin, T. Rozendal, N. de Jong, D. Lohse, and M. Versluis. "Subharmonic behavior of phospholipid-coated ultrasound contrast agent microbubbles", *J Acoust Soc Am,* **128**, 3239-3252 (2010).

[324] T. D. Mast. "Empirical relationships between acoustic parameters in human soft tissues", *Acoustics Research Letters Online,* **1**, 37-42 (2000).

[325] P. L. van Neer, G. Matte, M. G. Danilouchkine, C. Prins, F. van den Adel, and N. de Jong. "Super-harmonic imaging: development of an interleaved phased-array transducer", *IEEE Trans Ultrason Ferroelectr Freq Control,* **57**, 455-468 (2010).

[326] J. L. Raymond, K. J. Haworth, K. B. Bader, K. Radhakrishnan, J. K. Griffin, S. L. Huang, D. D. McPherson, and C. K. Holland. "Broadband attenuation measurements of phospholipid-shelled ultrasound contrast agents", *Ultrasound Med Biol,* **40**, 410-421 (2014).

[327] S. Krishnan, J. D. Hamilton, and M. O'Donnell. "Suppression of propagating second harmonic in ultrasound contrast imaging", *IEEE Trans Ultrason Ferroelectr Freq Control,* **45**, 704-711 (1998).

[328] H. C. Starritt, F. A. Duck, A. J. Hawkins, and V. F. Humphrey. "The development of harmonic distortion in pulsed finite-amplitude ultrasound passing through liver", *Phys Med Biol,* **31**, 1401-1409 (1986).

[329] J. Sijl, M. Overvelde, B. Dollet, V. Garbin, N. de Jong, D. Lohse, and M. Versluis. ""Compression-only" behavior: a second-order nonlinear response of ultrasound contrast agent microbubbles", *J Acoust Soc Am,* **129**, 1729-1739 (2011).

[330] M. Overvelde, V. Garbin, J. Sijl, B. Dollet, N. de Jong, D. Lohse, and M. Versluis. "Nonlinear shell behavior of phospholipid-coated microbubbles", *Ultrasound Med Biol,* **36**, 2080-2092 (2010).

[331] J. Tu, J. Guan, Y. Qiu, and T. J. Matula. "Estimating the shell parameters of SonoVue microbubbles using light scattering", *J Acoust Soc Am,* **126**, 2954-2962 (2009).

[332] H. J. Vos, B. Dollet, M. Versluis, and N. de Jong. "Nonspherical shape oscillations of coated microbubbles in contact with a wall", *Ultrasound Med Biol,* **37**, 935-948 (2011).

[333] B. Dollet, S. M. van der Meer, V. Garbin, N. de Jong, D. Lohse, and M. Versluis. "Nonspherical oscillations of ultrasound contrast agent microbubbles", *Ultrasound Med Biol,* **34**, 1465-1473 (2008).

[334] B. L. Helfield, B. Y. Leung, and D. E. Goertz. "The effect of boundary proximity on the response of individual ultrasound contrast agent microbubbles", *Phys Med Biol,* **59**, 1721-1745 (2014).

[335] J. K. Willmann, Z. Cheng, C. Davis, A. M. Lutz, M. L. Schipper, C. H. Nielsen, and S. S. Gambhir. "Targeted microbubbles for imaging tumor angiogenesis: assessment of whole-body biodistribution with dynamic micro-PET in mice", *Radiology,* **249**, 212-219 (2008).

[336] K. E. Landmark, P. W. Johansen, J. A. Johnson, B. Johansen, S. Uran, and T. Skotland. "Pharmacokinetics of perfluorobutane following intravenous bolus injection and continuous infusion of sonazoid in healthy volunteers and in patients with reduced pulmonary diffusing capacity", *Ultrasound Med Biol,* **34**, 494-501 (2008).

[337] A. A. Doinikov and A. Bouakaz. "Review of shell models for contrast agent microbubbles", *IEEE Trans Ultrason Ferroelectr Freq Control,* **58**, 981-993 (2011).

[338] E. Stride. "Physical principles of microbubbles for ultrasound imaging and therapy", *Cerebrovasc Dis,* **27 Suppl 2**, 1-13 (2009).

[339] J. Castle, M. Butts, A. Healey, K. Kent, M. Marino, and S. B. Feinstein. "Ultrasound-mediated targeted drug delivery: recent success and remaining challenges", *Am J Physiol Heart Circ Physiol,* **304**, H350-357 (2013).

[340] M. Borden. "Nanostructural features on stable microbubbles", *Soft Matter,* **5**, 716-720 (2009).

[341] J. Sijl, H. J. Vos, T. Rozendal, N. de Jong, D. Lohse, and M. Versluis. "Combined optical and acoustical detection of single microbubble dynamics", *J Acoust Soc Am,* **130**, 3271-3281 (2011).

[342] T. Faez, I. Skachkov, M. Versluis, K. Kooiman, and N. de Jong. "In Vivo characterization of ultrasound contrast agents: microbubble spectroscopy in a chicken embryo", *Ultrasound Med Biol,* **38**, 1608-1617 (2012).

[343] D. H. Thomas, M. Butler, T. Anderson, M. Emmer, H. Vos, M. Borden, E. Stride, N. de Jong, and V. Sboros. "The "quasi-stable" lipid shelled microbubble in response to consecutive ultrasound pulses", *Applied Physics Letters,* **101**,(2012).

[344] S. L. Huang. "Ultrasound-responsive liposomes", *Methods Mol Biol,* **605**, 113-128 (2010).

[345] S. Paul, R. Nahire, S. Mallik, and K. Sarkar. "Encapsulated microbubbles and echogenic liposomes for contrast ultrasound imaging and targeted drug delivery", *Comput Mech,* **53**, 413-435 (2014).

[346] K. D. Buchanan, S. Huang, H. Kim, R. C. Macdonald, and D. D. McPherson. "Echogenic liposome compositions for increased retention of ultrasound reflectivity at physiologic temperature", *J Pharm Sci,* **97**, 2242-2249 (2008).

[347] S. Paul, D. Russakow, R. Nahire, T. Nandy, A. H. Ambre, K. Katti, S. Mallik, and K. Sarkar. "In vitro measurement of attenuation and nonlinear scattering from echogenic liposomes", *Ultrasonics,* **52**, 962-969 (2012).

[348] J. A. Kopechek, K. J. Haworth, J. L. Raymond, T. Douglas Mast, S. R. Perrin, M. E. Klegerman, S. Huang, T. M. Porter, D. D. McPherson, and C. K. Holland. "Acoustic characterization of echogenic liposomes: frequency-dependent attenuation and backscatter", *J Acoust Soc Am,* **130**, 3472-3481 (2011).

[349] R. Nahire, S. Paul, M. D. Scott, R. K. Singh, W. W. Muhonen, J. Shabb, K. N. Gange, D. K. Srivastava, K. Sarkar, and S. Mallik. "Ultrasound enhanced matrix metalloproteinase-9 triggered release of contents from echogenic liposomes", *Mol Pharm,* **9**, 2554-2564 (2012).

[350] M. A. Ainslie and T. G. Leighton. "Review of scattering and extinction cross-sections, damping factors, and resonance frequencies of a spherical gas bubble", *J. Acoust. Soc. Am.,* **130**, 3184-3208 (2011).

[351] J. L. Leander. "On the eigenfrequency of a gas bubble in a liquid", *J Acoust Soc Am,* **102**, 1900-1903 (1997).

[352] A. Agneni and L. Baliscrema. "Damping Measurements from Truncated Signals Via Hilbert Transform", *Mechanical Systems and Signal Processing,* **3**, 1-13 (1989).

[353] D. Chatterjee and K. Sarkar. "A Newtonian rheological model for the interface of microbubble contrast agents", *Ultrasound Med Biol,* **29**, 1749-1757 (2003).

[354] L. Hoff, P. C. Sontum, and J. M. Hovem. "Oscillations of polymeric microbubbles: Effect of the encapsulating shell", *J Acoust Soc Am,* **107**, 2272-2280 (2000).

[355] L. A. Crum. "The Polytropic Exponent of Gas Contained within Air Bubbles Pulsating in a Liquid", *J Acoust Soc Am,* **73**, 116-120 (1983).

[356] K. E. Morgan, J. S. Allen, P. A. Dayton, J. E. Chomas, A. L. Klibaov, and K. W. Ferrara. "Experimental and theoretical evaluation of microbubble behavior: effect of transmitted phase and bubble size", *IEEE Trans Ultrason Ferroelectr Freq Control,* **47**, 1494-1509 (2000).

[357] J. Tu, J. E. Swalwell, D. Giraud, W. C. Cui, W. Z. Chen, and T. J. Matula. "Microbubble Sizing and Shell Characterization Using Flow Cytometry", *IEEE Trans Ultrason Ferroelectr Freq Control,* **58**, 955-963 (2011).

[358] K. Sarkar, W. T. Shi, D. Chatterjee, and F. Forsberg. "Characterization of ultrasound contrast microbubbles using in vitro experiments and viscous and viscoelastic interface models for encapsulation", *J Acoust Soc Am,* **118**, 539-550 (2005).

[359] A. I. Malkin, *Rheology fundamentals*. Toronto-Scarborough, ON, Canada: ChemTec Pub., 1994.

[360] C. C. Church. "The Effects of an Elastic Solid-Surface Layer on the Radial Pulsations of Gas-Bubbles", *J Acoust Soc Am,* **97**, 1510-1521 (1995).

[361] Q. Li, T. J. Matula, J. Tu, X. Guo, and D. Zhang. "Modeling complicated rheological behaviors in encapsulating shells of lipid-coated microbubbles accounting for nonlinear changes of both shell viscosity and elasticity", *Phys Med Biol,* **58**, 985-998 (2013).

[362] A. A. Doinikov, J. F. Haac, and P. A. Dayton. "Modeling of nonlinear viscous stress in encapsulating shells of lipid-coated contrast agent microbubbles", *Ultrasonics,* **49**, 269-275 (2009).

[363] K. Ferrara, R. Pollard, and M. Borden. "Ultrasound microbubble contrast agents: Fundamentals and application to gene and drug delivery", *Annual Review of Biomedical Engineering,* **9**, 415-447 (2007).

[364] A. J. Mortimer, *Physical Characteristics of Ultrasound*. Clifton, NJ, USA: The Humana Press Inc., 1982.

[365] M. Azmin, Z. Harfield C Fau - Ahmad, M. Ahmad Z Fau - Edirisinghe, E. Edirisinghe M Fau - Stride, and E. Stride. "How do microbubbles and ultrasound interact? Basic physical, dynamic and engineering principles."

[366] J. R. Eisenbrey, A. Sridharan, J. B. Liu, and F. Forsberg. "Recent Experiences and Advances in Contrast-Enhanced Subharmonic Ultrasound", *Biomed Research International,* (2015).

[367] S. L. W. Denham, L. F. Alexander, and M. L. Robbin. "Contrast-Enhanced Ultrasound: Practical Review for the Assessment of Hepatic and Renal Lesions", *Ultrasound Quarterly,* **32**, 116-125 (2016).

[368] G. Renaud, J. G. Bosch, A. F. Van Der Steen, and N. De Jong. "Low-amplitude non-linear volume vibrations of single microbubbles measured with an "acoustical camera"", *Ultrasound Med Biol,* **40**, 1282-1295 (2014).

[369] J. Sijl, E. Gaud, P. J. Frinking, M. Arditi, N. de Jong, D. Lohse, and M. Versluis. "Acoustic characterization of single ultrasound contrast agent microbubbles", *J Acoust Soc Am,* **124**, 4091-4097 (2008).

[370] X. Chen, J. Wang, J. J. Pacella, and F. S. Villanueva. "Dynamic Behavior of Microbubbles during Long Ultrasound Tone-Burst Excitation: Mechanistic Insights into Ultrasound-Microbubble Mediated Therapeutics Using High-Speed Imaging and Cavitation Detection", *Ultrasound Med Biol,* (2015).

[371] J. E. Chomas, P. Dayton, D. May, and K. Ferrara. "Threshold of fragmentation for ultrasonic contrast agents", *J Biomed Opt,* **6**, 141-150 (2001).

[372] T. van Rooij, I. Skachkov, I. Beekers, K. R. Lattwein, J. D. Voorneveld, T. J. Kokhuis, D. Bera, Y. Luan, A. F. van der Steen, N. de Jong, and K. Kooiman. "Viability of endothelial cells after ultrasound-mediated sonoporation: Influence of targeting, oscillation, and displacement of microbubbles", *J Control Release,* **238**, 197-211 (2016).

[373] B. Helfield, X. C. Chen, S. C. Watkins, and F. S. Villanueva. "Biophysical insight into mechanisms of sonoporation", *Proc Natl Acad Sci U S A,* **113**, 9983-9988 (2016).

[374] M. M. Lipp, K. Y. C. Lee, D. Y. Takamoto, J. A. Zasadzinski, and A. J. Waring. "Coexistence of buckled and flat monolayers", *Physical Review Letters,* **81**, 1650-1653 (1998).

[375] S. Baoukina, L. Monticelli, H. J. Risselada, S. J. Marrink, and D. P. Tieleman. "The molecular mechanism of lipid monolayer collapse", *Proc Natl Acad Sci U S A,* **105**, 10803-10808 (2008).

[376] K. Y. Lee. "Collapse mechanisms of Langmuir monolayers", *Annu Rev Phys Chem,* **59**, 771-791 (2008).

[377] G. Pu, M. A. Borden, and M. L. Longo. "Collapse and shedding transitions in binary lipid monolayers coating microbubbles", *Langmuir,* **22**, 2993-2999 (2006).

[378] Y. Luan, G. Lajoinie, E. Gelderblom, I. Skachkov, A. F. van der Steen, H. J. Vos, M. Versluis, and N. De Jong. "Lipid shedding from single oscillating microbubbles", *Ultrasound Med Biol,* **40**, 1834-1846 (2014).

[379] S. Paul, A. Katiyar, K. Sarkar, D. Chatterjee, W. T. Shi, and F. Forsberg. "Material characterization of the encapsulation of an ultrasound contrast microbubble and its subharmonic response: Strain-softening interfacial elasticity model", *J Acoust Soc Am,* **127**, 3846-3857 (2010).

[380] H. J. Vos, B. Dollet, J. G. Bosch, M. Versluis, and N. de Jong. "Nonspherical vibrations of microbubbles in contact with a wall - A pilot study at low mechanical index", *Ultrasound Med Biol,* **34**, 685-688 (2008).

[381] A. Gopal and K. Y. C. Lee. "Morphology and collapse transitions in binary phospholipid monolayers", *J Phys Chem B,* **105**, 10348-10354 (2001).

[382] D. Y. Takamoto, M. M. Lipp, A. von Nahmen, K. Y. C. Lee, A. J. Waring, and J. A. Zasadzinski. "Interaction of lung surfactant proteins with anionic phospholipids", *Biophys J,* **81**, 153-169 (2001).

[383] J. Owen and E. Stride. "Technique for the Characterization of Phospholipid Microbubbles Coatings by Transmission Electron Microscopy", *Ultrasound Med Biol,* **41**, 3253-3258 (2015).

[384] R. Shih and A. P. Lee. "Post-Formation Shrinkage and Stabilization of Microfluidic Bubbles in Lipid Solution", *Langmuir,* (2016).

[385] E. Talu, K. Hettiarachchi, R. L. Powell, A. P. Lee, P. A. Dayton, and M. L. Longo. "Maintaining monodispersity in a microbubble population formed by flow-focusing", *Langmuir,* **24**, 1745-1749 (2008).

[386] A. L. Klibanov. "Microbubble contrast agents - Targeted ultrasound imaging and ultrasound-assisted drug-delivery applications", *Invest Radiol,* **41**, 354-362 (2006).

[387] E. Gelderblom. "Ultra-high-speed fluorescence imaging", PhD thesis, Physics of Fluids, University of Twente, Enschede, 2012.

[388] J. P. O'Brien, N. Ovenden, and E. Stride. "Accounting for the stability of microbubbles to multi-pulse excitation using a lipid-shedding model", *J Acoust Soc Am,* **130**, El180-El185 (2011).

[389] P. J. A. Frinking, E. Gaud, J. Brochot, and M. Arditi. "Subharmonic Scattering of Phospholipid-Shell Microbubbles at Low Acoustic Pressure Amplitudes", *IEEE Trans Ultrason Ferroelectr Freq Control,* **57**, 1762-1771 (2010).

[390] J. S. Yeh, C. A. Sennoga, E. McConnell, R. Eckersley, M. X. Tang, S. Nourshargh, J. M. Seddon, D. O. Haskard, and P. Nihoyannopoulos. "Quantitative Ultrasound Molecular Imaging", *Ultrasound Med Biol,* (2015).

[391] K. Kooiman, T. J. Kokhuis, I. Skachkov, J. G. Bosch, A. F. W. van der Steen, W. A. van Cappellen, and N. De Jong. "Surface contact of bound targeted microbubbles", in *IEEE Ultrasonics Symposium Proceedings*, Dresden, Germany (2012).

[392] S. Zhao, M. Borden, S. H. Bloch, D. Kruse, K. W. Ferrara, and P. A. Dayton. "Radiation-force assisted targeting facilitates ultrasonic molecular imaging", *Mol Imaging,* **3**, 135-148 (2004).

[393] P. A. Dayton, K. E. Morgan, A. L. Klibanov, G. H. Brandenburger, and K. W. Ferrara. "Optical and acoustical observations of the effects of ultrasound on contrast agents", *IEEE Trans Ultrason Ferroelectr Freq Control,* **46**, 220-232 (1999).

[394] T. van Rooij, A. F. W. van der Steen, N. de Jong, and K. Kooiman. "Influence of binding on the vibrational responses of targeted lipid-coated microbubbles", in *IEEE Ultrasonics Symposium Proceedings*, Chicago, USA (2014).

[395] P. M. Shankar, P. D. Krishna, and V. L. Newhouse. "Subharmonic backscattering from ultrasound contrast agents", *J Acoust Soc Am,* **106**, 2104-2110 (1999).

[396] K. Hettiarachchi, E. Talu, M. L. Longo, P. A. Dayton, and A. P. Lee. "On-chip generation of microbubbles as a practical technology for manufacturing contrast agents for ultrasonic imaging", *Lab Chip,* **7**, 463-468 (2007).

[397] M. Kaya, S. Feingold, K. Hettiarachchi, A. P. Lee, and P. A. Dayton. "Acoustic responses of monodisperse lipid-encapsulated microbubble contrast agents produced by flow focusing", *Bubble Sci Eng Technol,* **2**, 33-40 (2010).

[398] E. Talu, K. Hettiarachchi, S. Zhao, R. L. Powell, A. P. Lee, M. L. Longo, and P. A. Dayton. "Tailoring the size distribution of ultrasound contrast agents: possible method for improving sensitivity in molecular imaging", *Mol Imaging,* **6**, 384-392 (2007).

[399] T. Segers and M. Versluis. "Acoustic bubble sorting for ultrasound contrast agent enrichment", *Lab Chip,* **14**, 1705-1714 (2014).

[400] E. C. Pua and P. Zhong. "Ultrasound-mediated drug delivery", *IEEE Eng Med Biol Mag,* **28**, 64-75 (2009).

[401] F. E. Shamout, A. N. Pouliopoulos, P. Lee, S. Bonaccorsi, L. Towhidi, R. Krams, and J. J. Choi. "Enhancement of non-invasive trans-membrane drug delivery using ultrasound and microbubbles during physiologically relevant flow", *Ultrasound Med Biol,* **41**, 2435-2448 (2015).

[402] M. Edidin. "A rapid, quantitative fluorescence assay for cell damage by cytotoxic antibodies", *J Immunol,* **104**, 1303-1306 (1970).

[403] Z. Fan, D. Chen, and C. X. Deng. "Improving ultrasound gene transfection efficiency by controlling ultrasound excitation of microbubbles", *J Control Release,* **170**, 401-413 (2013).

[404] C. E. Shannon. "Communication in the presence of noise (Reprinted from the Proceedings of the IRE, vol 37, pg 10-21, 1949)", *Proceedings of the IEEE,* **86**, 447-457 (1998).

[405] Z. Fan, D. Chen, and C. X. Deng. "Characterization of the dynamic activities of a population of microbubbles driven by pulsed ultrasound exposure in sonoporation", *Ultrasound Med Biol,* **40**, 1260-1272 (2014).

[406] J. R. Doherty, G. E. Trahey, K. R. Nightingale, and M. L. Palmeri. "Acoustic radiation force elasticity imaging in diagnostic ultrasound", *IEEE Trans Ultrason Ferroelectr Freq Control,* **60**, 685-701 (2013).

[407] D. L. Miller and J. Song. "Tumor growth reduction and DNA transfer by cavitation-enhanced high-intensity focused ultrasound in vivo", *Ultrasound Med Biol,* **29**, 887-893 (2003).

[408] A. Ghanem, C. Steingen, F. Brenig, F. Funcke, Z. Y. Bai, C. Hall, C. T. Chin, G. Nickenig, W. Bloch, and K. Tiemann. "Focused ultrasound-induced stimulation of microbubbles augments site-targeted engraftment of mesenchymal stem cells after acute myocardial infarction", *J Mol Cell Cardiol,* **47**, 411-418 (2009).

[409] B. D. Meijering, L. J. Juffermans, A. van Wamel, R. H. Henning, I. S. Zuhorn, M. Emmer, A. M. Versteilen, W. Paulus, W. H. van Gilst, K. Kooiman, N. de Jong, R. J. Musters, L. E. Deelman, and O. Kamp. "Ultrasound and microbubble-targeted delivery of macromolecules is regulated by induction of endocytosis and pore formation", *Circ Res,* **104**, 679-687 (2009).

[410] D. Bratosin, L. Mitrofan, C. Palii, J. Estaquier, and J. Montreuil. "Novel fluorescence assay using calcein-AM for the determination of human erythrocyte viability and aging", *Cytometry A,* **66**, 78-84 (2005).

[411] K. A. Smith, S. A. Hill, A. C. Begg, and J. Denekamp. "Validation of the fluorescent dye Hoechst 33342 as a vascular space marker in tumours", *Br J Cancer,* **57**, 247-253 (1988).

[412] M. Sriram, G. A. van der Marel, H. L. Roelen, J. H. van Boom, and A. H. Wang. "Conformation of B-DNA containing O6-ethyl-G-C base pairs stabilized by minor groove binding drugs: molecular structure of d(CGC[e6G]AATTCGCG complexed with Hoechst 33258 or Hoechst 33342", *EMBO J,* **11**, 225-232 (1992).

[413] W. D. Wilson, C. R. Krishnamoorthy, Y. H. Wang, and J. C. Smith. "Mechanism of intercalation: ion effects on the equilibrium and kinetic constants for the interaction of propidium and ethidium with DNA", *Biopolymers,* **24**, 1941-1961 (1985).

[414] W. S. Rasband. "ImageJ", ed. Bethesda, Maryland, USA: U. S. National Institutes of Health, 1997-2016.

[415] N. Otsu. "Threshold Selection Method from Gray-Level Histograms", *IEEE Trans on Systems Man and Cybernetics,* **9**, 62-66 (1979).

[416] T. R. Jones, A. Carpenter, and P. Golland. "Voronoi-based segmentation of cells on image manifolds", *Computer Vision for Biomedical Image Applications, Proceedings,* **3765**, 535-543 (2005).

[417] S. Wold, K. Esbensen, and P. Geladi. "Principal Component Analysis", *Chemometrics and Intelligent Laboratory Systems,* **2**, 37-52 (1987).

[418] R. L. Tatusov, D. A. Natale, I. V. Garkavtsev, T. A. Tatusova, U. T. Shankavaram, B. S. Rao, B. Kiryutin, M. Y. Galperin, N. D. Fedorova, and E. V. Koonin. "The COG database: new developments in phylogenetic classification of proteins from complete genomes", *Nucleic Acids Res,* **29**, 22-28 (2001).

[419] Z. Zivkovic and F. van der Heijden. "Efficient adaptive density estimation per image pixel for the task of background subtraction", *Pattern Recognition Letters,* **27**, 773-780 (2006).

[420] D. Allan, N. Keim, T. Caswell, and C. van der Wel. (2015, March 9). *trackpy: Trackpy v0.3.0*. Available: http://zenodo.org/record/34028

[421] S. van der Walt, J. Schönberger, J. Nunez Iglesias, F. Boulogne, J. Warner, N. Yager, E. Gouillart, and T. Yu. (2014, March 30). *Blob detection, scikit-image: Image Processing in Python*. Available: http://scikit-image.org/docs/dev/auto_examples/plot_blob.html

[422] Y. Zhou, K. Yang, J. Cui, J. Y. Ye, and C. X. Deng. "Controlled permeation of cell membrane by single bubble acoustic cavitation", *J Control Release,* **157**, 103-111 (2012).

[423] B. Lammertink, R. Deckers, G. Storm, C. Moonen, and C. Bos. "Duration of ultrasound-mediated enhanced plasma membrane permeability", *Int J Pharm,* **482**, 92-98 (2015).

[424] A. Yudina, M. Lepetit-Coiffe, and C. T. Moonen. "Evaluation of the temporal window for drug delivery following ultrasound-mediated membrane permeability enhancement", *Mol Imaging Biol,* **13**, 239-249 (2011).

[425] P. Wu and L. Brand. "Resonance energy transfer: methods and applications", *Anal Biochem,* **218**, 1-13 (1994).

[426] T. Frey. "Detection of bromodeoxyuridine incorporation by alteration of the fluorescence emission from nucleic acid binding dyes using only an argon ion laser", *Cytometry,* **17**, 310-318 (1994).

[427] C. Mannaris and M. A. Averkiou. "Investigation of microbubble response to long pulses used in ultrasound-enhanced drug delivery", *Ultrasound Med Biol,* **38**, 681-691 (2012).

[428] H. M. DeLisser, P. J. Newman, and S. M. Albelda. "Molecular and functional aspects of PECAM-1/CD31", *Immunol Today,* **15**, 490-495 (1994).

[429] M. de Saint Victor, C. Crake, C. C. Coussios, and E. Stride. "Properties, characteristics and applications of microbubbles for sonothrombolysis", *Expert Opin Drug Deliv,* **11**, 187-209 (2014).

[430] R. Shih, D. Bardin, T. D. Martz, P. S. Sheeran, P. A. Dayton, and A. P. Lee. "Flow-focusing regimes for accelerated production of monodisperse drug-loadable microbubbles toward clinical-scale applications", *Lab Chip,* **13**, 4816-4826 (2013).

[431] J. J. Rychak and A. L. Klibanov. "Nucleic acid delivery with microbubbles and ultrasound", *Adv Drug Deliv Rev,* **72**, 82-93 (2014).

[432] Y. Morch, R. Hansen, S. Berg, A. K. O. Aslund, W. R. Glomm, S. Eggen, R. Schmid, H. Johnsen, S. Kubowicz, S. Snipstad, E. Sulheim, S. Hak, G. Singh, B. H. McDonagh, H. Blom, C. D. Davies, and P. M. Stenstad. "Nanoparticle-stabilized microbubbles for multimodal imaging and drug delivery", *Contrast Media Mol Imaging,* **10**, 356-366 (2015).

[433] T. Lammers, P. Koczera, S. Fokong, F. Gremse, J. Ehling, M. Vogt, A. Pich, G. Storm, M. van Zandvoort, and F. Kiessling. "Theranostic USPIO-Loaded Microbubbles for Mediating and Monitoring Blood-Brain Barrier Permeation", *Advanced Functional Materials,* **25**, 36-43 (2015).

[434] J. P. Kilroy, A. L. Klibanov, B. R. Wamhoff, D. K. Bowles, and J. A. Hossack. "Localized in Vivo Model Drug Delivery with Intravascular Ultrasound and Microbubbles", *Ultrasound Med Biol,* **40**, 2458-2467 (2014).

[435] H. Dewitte, S. Van Lint, C. Heirman, K. Thielemans, S. C. De Smedt, K. Breckpot, and I. Lentacker. "The potential of antigen and TriMix sonoporation using mRNA-loaded microbubbles for ultrasound-triggered cancer immunotherapy", *J Control Release,* **194**, 28-36 (2014).

[436] S. T. Laing, H. Kim, J. A. Kopechek, D. Parikh, S. L. Huang, M. E. Klegerman, C. K. Holland, and D. D. McPherson. "Ultrasound-mediated delivery of echogenic immunoliposomes to porcine vascular smooth muscle cells in vivo", *J Liposome Res,* **20**, 160-167 (2010).

[437] P. Prentice, A. Cuschierp, K. Dholakia, M. Prausnitz, and P. Campbell. "Membrane disruption by optically controlled microbubble cavitation", *Nature Physics,* **1**, 107-110 (2005).

[438] N. Kudo, K. Okada, and K. Yamamoto. "Sonoporation by Single-Shot Pulsed Ultrasound with Microbubbles Adjacent to Cells", *Biophys J,* **96**, 4866-4876 (2009).

[439] C. C. Coussios and R. A. Roy. "Applications of acoustics and cavitation to noninvasive therapy and drug delivery", *Annual Review of Fluid Mechanics,* **40**, 395-420 (2008).

[440] R. Seda, D. S. Li, J. B. Fowlkes, and J. L. Bull. "Characterization of Bioeffects on Endothelial Cells under Acoustic Droplet Vaporization", *Ultrasound Med Biol,* **41**, 3241-3252 (2015).

[441] J. J. Kwan, R. Myers, C. M. Coviello, S. M. Graham, A. R. Shah, E. Stride, R. C. Carlisle, and C. C. Coussios. "Ultrasound-Propelled Nanocups for Drug Delivery", *Small,* **11**, 5305-5314 (2015).

[442] D. Lensen, E. C. Gelderblom, D. M. Vriezema, P. Marmottant, N. Verdonschot, M. Versluis, N. de Jong, and J. C. M. van Hest. "Biodegradable polymeric microcapsules for selective ultrasound-triggered drug release", *Soft Matter,* **7**, 5417-5422 (2011).

[443] J. R. Eisenbrey, J. Hsu, and M. A. Wheatley. "Plasma sterilization of poly lactic acid ultrasound contrast agents: surface modification and implications for drug delivery", *Ultrasound Med Biol,* **35**, 1854-1862 (2009).

[444] E. Blanco, H. Shen, and M. Ferrari. "Principles of nanoparticle design for overcoming biological barriers to drug delivery", *Nature Biotechnology,* **33**, 941-951 (2015).

[445] T. M. Allen and P. R. Cullis. "Drug delivery systems: Entering the mainstream", *Science,* **303**, 1818-1822 (2004).

[446] B. Arnal, C. Perez, C. W. Wei, J. J. Xia, M. Lombardo, I. Pelivanov, T. J. Matula, L. D. Pozzo, and M. O'Donnell. "Sono-photoacoustic imaging of gold nanoemulsions: Part I. Exposure thresholds", *Photoacoustics,* **3**, 3-10 (2015).

[447] E. Kang, H. S. Min, J. Lee, M. H. Han, H. J. Ahn, I. C. Yoon, K. Choi, K. Kim, K. Park, and I. C. Kwon. "Nanobubbles from Gas-Generating Polymeric Nanoparticles: Ultrasound Imaging of Living Subjects", *Angewandte Chemie-International Edition,* **49**, 524-528 (2010).

[448] J. A. Straub, D. E. Chickering, C. C. Church, B. Shah, T. Hanlon, and H. Bernstein. "Porous PLGA microparticles: AI-700, an intravenously administered ultrasound contrast agent for use in echocardiography", *J Control Release,* **108**, 21-32 (2005).

[449] S. K. Hobbs, W. L. Monsky, F. Yuan, W. G. Roberts, L. Griffith, V. P. Torchilin, and R. K. Jain. "Regulation of transport pathways in tumor vessels: role of tumor type and microenvironment", *Proc Natl Acad Sci U S A,* **95**, 4607-4612 (1998).

[450] I. s. IEC. "Safety of laser products--Part 1: Equipment classification, requirements and user's guide", FDA/Center for Drug Evaluation and Research, Geneva, Switzerland2001.

[451] A. Loxley and B. Vincent. "Preparation of Poly(methylmethacrylate) Microcapsules with Liquid Cores", *J Colloid Interface Sci,* **208**, 49-62 (1998).

[452] R. K. Schlicher, H. Radhakrishna, T. P. Tolentino, R. P. Apkarian, V. Zarnitsyn, and M. R. Prausnitz. "Mechanism of intracellular delivery by acoustic cavitation", *Ultrasound Med Biol,* **32**, 915-924 (2006).

[453] C. Brana, C. Benham, and L. Sundstrom. "A method for characterising cell death in vitro by combining propidium iodide staining with immunohistochemistry", *Brain Res Brain Res Protoc,* **10**, 109-114 (2002).

[454] J. A. Steinkamp, B. E. Lehnert, and N. M. Lehnert. "Discrimination of damaged/dead cells by propidium iodide uptake in immunofluorescently labeled populations analyzed by phase-sensitive flow cytometry", *J Immunol Methods,* **226**, 59-70 (1999).

[455] V. C. Klema and A. J. Laub. "The Singular Value Decomposition - Its Computation and Some Applications", *IEEE Transactions on Automatic Control,* **25**, 164-176 (1980).

[456] T. Suzuki, K. Fujikura, T. Higashiyama, and K. Takata. "DNA staining for fluorescence and laser confocal microscopy", *J Histochem Cytochem,* **45**, 49-53 (1997).

[457] K. Smolders and J. Baeyens. "Thermal degradation of PMMA in fluidised beds", *Waste Management,* **24**, 849-857 (2004).

[458] X. Chen, J. M. F. Wan, and A. C. H. Yu. "Sonoporation as a Cellular Stress: Induction of Morphological Repression and Developmental Delays", *Ultrasound Med Biol,* **39**, 1075-1086 (2013).

[459] M. T. Burgess and T. M. Porter. "Acoustic Cavitation-Mediated Delivery of Small Interfering Ribonucleic Acids with Phase-Shift Nano-Emulsions."

[460] N. Reznik, O. Shpak, E. C. Gelderblom, R. Williams, N. de Jong, M. Versluis, and P. N. Burns. "The efficiency and stability of bubble formation by acoustic vaporization of submicron perfluorocarbon droplets", *Ultrasonics,* **53**, 1368-1376 (2013).

[461] E. Pisani, N. Tsapis, J. Paris, V. Nicolas, L. Cattel, and E. Fattal. "Polymeric nano/microcapsules of liquid perfluorocarbons for ultrasonic imaging: Physical characterization", *Langmuir,* **22**, 4397-4402 (2006).

[462] G. Gutierrez, H. D. Reines, and M. E. Wulf-Gutierrez. "Clinical review: hemorrhagic shock", *Crit Care,* **8**, 373-381 (2004).

[463] A. Khwaja. "KDIGO clinical practice guidelines for acute kidney injury", *Nephron Clin Pract,* **120**, c179-184 (2012).

[464] M. van Iterson, R. Bezemer, M. Heger, M. Siegemund, and C. Ince. "Microcirculation follows macrocirculation in heart and gut in the acute phase of hemorrhagic shock and isovolemic autologous whole blood resuscitation in pigs", *Transfusion,* **52**, 1552-1559 (2012).

[465] J. V. Bonventre and L. Yang. "Cellular pathophysiology of ischemic acute kidney injury", *J Clin Invest,* **121**, 4210-4221 (2011).

[466] J. Szopinski, K. Kusza, and M. Semionow. "Microcirculatory responses to hypovolemic shock", *J Trauma,* **71**, 1779-1788 (2011).

[467] A. G. Schneider, M. D. Goodwin, A. Schelleman, M. Bailey, L. Johnson, and R. Bellomo. "Contrast-enhanced ultrasound to evaluate changes in renal cortical perfusion around cardiac surgery: a pilot study", *Crit Care,* **17**, R138 (2013).

[468] A. G. Schneider, P. Calzavacca, A. Schelleman, T. Huynh, M. Bailey, C. May, and R. Bellomo. "Contrast-enhanced ultrasound evaluation of renal microcirculation in sheep", *Int Care Med Exp,* **2**,(2014).

[469] A. G. Schneider, M. D. Goodwin, A. Schelleman, M. Bailey, L. Johnson, and R. Bellomo. "Contrast-enhanced ultrasonography to evaluate changes in renal cortical microcirculation induced by noradrenaline: a pilot study", *Crit Care,* **18**, 653 (2014).

[470] F. Sui, Y. Zheng, W. X. Li, and J. L. Zhou. "Renal circulation and microcirculation during intra-abdominal hypertension in a porcine model", *Eur Rev Med Pharmacol Sci,* **20**, 452-461 (2016).

[471] C. Hoeffel, S. Mule, L. Huwart, F. Frouin, J. P. Jais, O. Helenon, and J. M. Correas. "Renal blood flow quantification in pigs using contrast-enhanced ultrasound: an ex vivo study", *Ultraschall Med,* **31**, 363-369 (2010).

[472] K. Wei, E. Le, J. P. Bin, M. Coggins, J. Thorpe, and S. Kaul. "Quantification of renal blood flow with contrast-enhanced ultrasound", *J Am Coll Cardiol,* **37**, 1135-1140 (2001).

[473] K. Kalantarinia, J. T. Belcik, J. T. Patrie, and K. Wei. "Real-time measurement of renal blood flow in healthy subjects using contrast-enhanced ultrasound", *Am J Physiol Renal Physiol,* **297**, F1129-1134 (2009).

[474] V. Daeichin, T. van Rooij, I. Skachkov, B. Ergin, P. A. C. Specht, A. Lima, C. Ince, J. G. Bosch, A. F. W. van der Steen, N. de Jong, and K. Kooiman. "Microbubble composition and preparation for high-frequency contrast-enhanced ultrasound imaging: in vitro and in vivo evaluation", *IEEE Trans Ultrason Ferroelectr Freq Control,* (2016 submitted).

[475] C. F. Dietrich, M. A. Averkiou, J. M. Correas, N. Lassau, E. Leen, and F. Piscaglia. "An EFSUMB introduction into Dynamic Contrast-Enhanced Ultrasound (DCE-US) for quantification of tumour perfusion", *Ultraschall Med,* **33**, 344-351 (2012).

[476] J. R. Lindner, J. Song, A. R. Jayaweera, J. Sklenar, and S. Kaul. "Microvascular rheology of Definity microbubbles after intra-arterial and intravenous administration", *J Am Soc Echocardiogr,* **15**, 396-403 (2002).

[477] R. L. Mehta, J. A. Kellum, S. V. Shah, B. A. Molitoris, C. Ronco, D. G. Warnock, A. Levin, and N. Acute Kidney Injury. "Acute Kidney Injury Network: report of an initiative to improve outcomes in acute kidney injury", *Crit Care,* **11**, R31 (2007).

[478] T. P. Gauthier, H. S. Wasan, A. Muhammad, D. R. Owen, and E. L. Leen. "Assessment of global liver blood flow with quantitative dynamic contrast-enhanced ultrasound", *J Ultrasound Med,* **30**, 379-385 (2011).

[479] C. Strouthos, M. Lampaskis, V. Sboros, A. McNeilly, and M. Averkiou. "Indicator dilution models for the quantification of microvascular blood flow with bolus administration of ultrasound contrast agents", *IEEE Trans Ultrason Ferroelectr Freq Control,* **57**, 1296-1310 (2010).

[480] M. Averkiou, C. P. Keravnou, M. L. Izamis, and E. Leen. "Evaluation of Perfusion Quantification Methods with Ultrasound Contrast Agents in a Machine-Perfused Pig Liver", *Ultraschall in Med,* (2016).

[481] J. D. Briers. "Laser Doppler, speckle and related techniques for blood perfusion mapping and imaging", *Physiol Meas,* **22**, R35-66 (2001).

[482] R. Bezemer, M. Legrand, E. Klijn, M. Heger, I. C. Post, T. M. van Gulik, D. Payen, and C. Ince. "Real-time assessment of renal cortical microvascular perfusion heterogeneities using near-infrared laser speckle imaging", *Opt Express,* **18**, 15054-15061 (2010).

[483] M. Gauthier, S. Pitre-Champagnat, F. Tabarout, I. Leguerney, M. Polrot, and N. Lassau. "Impact of the arterial input function on microvascularization parameter measurements using dynamic contrast-enhanced ultrasonography", *World J Radiol,* **4**, 291-301 (2012).

[484] N. de Jong. "Mechanical index", *Eur J Echocardiogr,* **3**, 73-74 (2002).

[485] J. M. Hudson, R. Williams, C. Tremblay-Darveau, P. S. Sheeran, L. Milot, G. A. Bjarnason, and P. N. Burns. "Dynamic contrast enhanced ultrasound for therapy monitoring", *Eur J Radiol,* (2015).

[486] T. L. Szabo and P. A. Lewin. "Ultrasound Transducer Selection in Clinical Imaging Practice", *J Ultrasound Med,* **32**, 573-582 (2013).

[487] L. Zafrani and C. Ince. "Microcirculation in Acute and Chronic Kidney Diseases", *Am J Kidney Dis,* **66**, 1083-1094 (2015).

[488] C. Langenberg, G. Gobe, S. Hood, C. N. May, and R. Bellomo. "Renal histopathology during experimental septic acute kidney injury and recovery", *Crit Care Med,* **42**, e58-67 (2014).

[489] B. Ergin, A. Kapucu, C. Demirci-Tansel, and C. Ince. "The renal microcirculation in sepsis", *Nephrol Dial Transplant,* **30**, 169-177 (2015).

[490] D. Schwartz, M. Mendonca, I. Schwartz, Y. Xia, J. Satriano, C. B. Wilson, and R. C. Blantz. "Inhibition of constitutive nitric oxide synthase (NOS) by nitric oxide generated by inducible NOS after lipopolysaccharide administration provokes renal dysfunction in rats", *J Clin Invest,* **100**, 439-448 (1997).

[491] K. Doi, A. Leelahavanichkul, P. S. T. Yuen, and R. A. Star. "Animal models of sepsis and sepsis-induced kidney injury", *J Clin Invest,* **119**, 2868-2878 (2009).

[492] Y. Takeda. "Velocity Profile Measurement by Ultrasound Doppler-Shift Method", *Int J Heat Fluid Fl,* **7**, 313-318 (1986).

[493] D. F. Ten Cate, J. J. Luime, M. van der Ven, J. M. Hazes, K. Kooiman, N. de Jong, and J. G. Bosch. "Very different performance of the power Doppler modalities of several ultrasound machines ascertained by a microvessel flow phantom", *Arthritis Res Ther,* **15**, R162 (2013).

[494] L. Wan, N. Yang, C. Y. Hiew, A. Schelleman, L. Johnson, C. May, and R. Bellomo. "An assessment of the accuracy of renal blood flow estimation by Doppler ultrasound", *Intensive Care Med,* **34**, 1503-1510 (2008).

[495] A. Schneider, L. Johnson, M. Goodwin, A. Schelleman, and R. Bellomo. "Bench-to-bedside review: Contrast enhanced ultrasonography - a promising technique to assess renal perfusion in the ICU", *Crit Care,* **15**,(2011).

[496] T. Schlosser, C. Pohl, C. Veltmann, S. Lohmaier, J. Goenechea, A. Ehlgen, J. Koster, D. Bimmel, S. Kuntz-Hehner, H. Becher, and K. Tiemann. "Feasibility of the flash-replenishment concept in renal tissue: which parameters affect the assessment of the contrast replenishment?", *Ultrasound Med Biol,* **27**, 937-944 (2001).

[497] P. T. Goedhart, M. Khalilzada, R. Bezemer, J. Merza, and C. Ince. "Sidestream Dark Field (SDF) imaging: a novel stroboscopic LED ring-based imaging modality for clinical assessment of the microcirculation", *Opt Express,* **15**, 15101-15114 (2007).

[498] J. Ostensen, R. Hede, Y. Myreng, T. Ege, and E. Holtz. "Intravenous injection of Albunex microspheres causes thromboxane mediated pulmonary hypertension in pigs, but not in monkeys or rabbits", *Acta Physiol Scand,* **144**, 307-315 (1992).

[499] S. E. Grauer, G. A. Pantely, J. Xu, S. Ge, G. D. Giraud, T. Shiota, and D. J. Sahn. "Myocardial imaging with a new transpulmonary lipid-fluorocarbon echo contrast agent: experimental studies in pigs", *Am Heart J,* **132**, 938-945 (1996).

[500] M. Draijer, E. Hondebrink, T. van Leeuwen, and W. Steenbergen. "Review of laser speckle contrast techniques for visualizing tissue perfusion", *Lasers in Medical Science,* **24**, 639-651 (2009).

[501] S. Hutchings, S. Watts, and E. Kirkman. "The Cytocam video microscope. A new method for visualising the microcirculation using Incident Dark Field technology", *Clin Hemorheol Microcirc,* **62**, 261-271 (2016).

[502] M. J. Massey, E. LaRochelle, G. Najarro, A. Karmacharla, R. Arnold, S. Trzeciak, D. C. Angus, and N. I. Shapiro. "The microcirculation image quality score: Development and preliminary evaluation of a proposed approach to grading quality of image acquisition for bedside videomicroscopy", *J Crit Care,* **28**, 913-917 (2013).

[503] D. De Backer, S. Hollenberg, C. Boerma, P. Goedhart, G. Buchele, G. Ospina-Tascon, I. Dobbe, and C. Ince. "How to evaluate the microcirculation: report of a round table conference", *Crit Care,* **11**,(2007).

[504] M. Sorelli, L. Bocchi, and C. Ince. "Monitoring the microcirculation at the bedside using hand-held imaging microscopes: automatic tracking of erythrocytes", *2015 37th Annual International Conference of the IEEE Engineering in Medicine and Biology Society (Embc),* 7378-7381 (2015).

[505] D. Payen, A. C. de Pont, Y. Sakr, C. Spies, K. Reinhart, and J. L. Vincent. "A positive fluid balance is associated with a worse outcome in patients with acute renal failure", *Crit Care,* **12**,(2008).

[506] M. Legrand, C. Dupuis, C. Simon, E. Gayat, J. Mateo, A. C. Lukaszewicz, and D. Payen. "Association between systemic hemodynamics and septic acute kidney injury in critically ill patients: a retrospective observational study", *Crit Care,* **17**,(2013).

[507] J. Chvojka, R. Sykora, A. Krouzecky, J. Radej, V. Varnerova, T. Karvunidis, O. Hes, I. Novak, P. Radermacher, and M. Matejovic. "Renal haemodynamic, microcirculatory, metabolic and histopathological responses to peritonitis-induced septic shock in pigs", *Crit Care,* **12**,(2008).

[508] X. Li, M. C. Liu, D. Bedja, C. Thoburn, K. Gabrielson, L. Racusen, and H. Rabb. "Acute renal venous obstruction is more detrimental to the kidney than arterial occlusion: implication for murine models of acute kidney injury", *Am J Physiol Renal Physiol,* **302**, F519-F525 (2012).

[509] S. Tanaka, A. Harrois, C. Nicolai, M. Flores, S. Hamada, E. Vicaut, and J. Duranteau. "Qualitative real-time analysis by nurses of sublingual microcirculation in intensive care unit: the MICRONURSE study", *Crit Care,* **19**,(2015).

[510] M. Cecconi, D. De Backer, M. Antonelli, R. Beale, J. Bakker, C. Hofer, R. Jaeschke, A. Mebazaa, M. R. Pinsky, J. L. Teboul, J. L. Vincent, and A. Rhodes. "Consensus on circulatory shock and hemodynamic monitoring. Task force of the European Society of Intensive Care Medicine", *Intensive Care Med,* **40**, 1795-1815 (2014).

[511] J. R. Lindner. "Microbubbles in medical imaging: current applications and future directions", *Nat Rev Drug Discov,* **3**, 527-532 (2004).

[512] B. P. Davidson, B. A. Kaufmann, J. T. Belcik, A. Xie, Y. Qi, and J. R. Lindner. "Detection of Antecedent Myocardial Ischemia With Multiselectin Molecular Imaging", *J Am Coll Cardiol,* (2012).

[513] A. Yudina, M. Lepetit-Coiffe, M. De Smet, S. Langereis, H. Grull, and C. Moonen. "In vivo temperature controlled ultrasound-mediated intracellular delivery of cell-impermeable compounds", *J Control Release,* **161**, 90-97 (2012).

[514] S. S. Abdelmoneim, M. Bernier, C. G. Scott, A. Dhoble, S. A. Ness, M. E. Hagen, S. Moir, R. B. McCully, P. A. Pellikka, and S. L. Mulvagh. "Safety of contrast agent use during stress echocardiography: a 4-

year experience from a single-center cohort study of 26,774 patients", *JACC Cardiovasc Imaging,* **2**, 1048-1056 (2009).

[515] M. L. Main, A. C. Ryan, T. E. Davis, M. P. Albano, L. L. Kusnetzky, and M. Hibberd. "Acute Mortality in Hospitalized Patients Undergoing Echocardiography With and Without an Ultrasound Contrast Agent (Multicenter Registry Results in 4,300,966 Consecutive Patients)", *Am J Cardiol,* **102**, 1742-1746 (2008).

[516] K. Wei, S. L. Mulvagh, L. Carson, R. Davidoff, R. Gabriel, R. A. Grimm, S. Wilson, L. Fane, C. A. Herzog, W. A. Zoghbi, R. Taylor, M. Farrar, F. A. Chaudhry, T. R. Porter, W. Irani, and R. M. Lang. "The safety of Definity and Optison for ultrasound image enhancement: a retrospective analysis of 78,383 administered contrast doses", *J Am Soc Echocardiogr,* **21**, 1202-1206 (2008).

[517] D. M. Hallow, A. D. Mahajan, T. E. McCutchen, and M. R. Prausnitz. "Measurement and correlation of acoustic cavitation with cellular bioeffects", *Ultrasound Med Biol,* **32**, 1111-1122 (2006).

[518] H. R. Guzman, D. X. Nguyen, S. Khan, and M. R. Prausnitz. "Ultrasound-mediated disruption of cell membranes. I. Quantification of molecular uptake and cell viability", *J Acoust Soc Am,* **110**, 588-596 (2001).

[519] W. J. Zhong, W. H. Sit, J. M. F. Wan, and A. C. H. Yu. "Sonoporation Induces Apoptosis and Cell Cycle Arrest in Human Promyelocytic Leukemia Cells", *Ultrasound Med Biol,* **37**, 2149-2159 (2011).

[520] J. Park, Z. Fan, and C. X. Deng. "Effects of shear stress cultivation on cell membrane disruption and intracellular calcium concentration in sonoporation of endothelial cells", *J Biomech,* **44**, 164-169 (2011).

[521] D. L. Miller, C. Y. Dou, and R. C. Wiggins. "Glomerular Capillary Hemorrhage Induced in Rats by Diagnostic Ultrasound with Gas-Body Contrast Agent Produces Intratubular Obstruction", *Ultrasound Med Biol,* **35**, 869-877 (2009).

[522] H. R. Guzman, A. J. McNamara, D. X. Nguyen, and M. R. Prausnitz. "Bioeffects caused by changes in acoustic cavitation bubble density and cell concentration: A unified explanation based on cell-to-bubble ratio and blast radius", *Ultrasound Med Biol,* **29**, 1211-1222 (2003).

[523] R. Karshafian, S. Samac, P. D. Bevan, and P. N. Burns. "Microbubble mediated sonoporation of cells in suspension: Clonogenic viability and influence of molecular size on uptake", *Ultrasonics,* **50**, 691-697 (2010).

[524] M. A. Hassan, P. Campbell, and T. Kondo. "The role of Ca2+ in ultrasound-elicited bioeffects: progress, perspectives and prospects", *Drug Discovery Today,* **15**, 892-906 (2010).

[525] R. S. Leow, J. M. F. Wan, and A. C. H. Yu. "Membrane blebbing as a recovery manoeuvre in site-specific sonoporation mediated by targeted microbubbles", *J R Soc Interface,* **12**,(2015).

[526] A. Delalande, S. Kotopoulis, T. Rovers, C. Pichon, and M. Postema. "Sonoporation at a low mechanical index", *Bubble Science, Engineering & Technology,* **3**, 3-12 (2011).

[527] J. D. Hutcheson, R. K. Schlicher, H. K. Hicks, and M. R. Prausnitz. "Saving Cells from Ultrasound-Induced Apoptosis: Quantification of Cell Death and Uptake Following Sonication and Effects of Targeted Calcium Chelation", *Ultrasound Med Biol,* **36**, 1008-1021 (2010).

[528] M. A. Hassan, L. B. Feril, K. Suzuki, N. Kudo, K. Tachibana, and T. Kondo. "Evaluation and comparison of three novel microbubbles: Enhancement of ultrasound-induced cell death and free radicals production", *Ultrason Sonochem,* **16**, 372-378 (2009).

[529] H. Honda, Q. L. Zhao, and T. Kondo. "Effects of dissolved gases and an echo contrast agent on apoptosis induced by ultrasound and its mechanism via the mitochondria-caspase pathway", *Ultrasound Med Biol,* **28**, 673-682 (2002).

[530] K. Yanagisawa, F. Moriyasu, T. Miyahara, M. Yuki, and H. Iijima. "Phagocytosis of ultrasound contrast agent microbubbles by Kupffer cells", *Ultrasound Med Biol,* **33**, 318-325 (2007).

[531] D. L. Miller and J. Quddus. "Lysis and sonoporation of epidermoid and phagocytic monolayer cells by diagnostic ultrasound activation of contrast agent gas bodies", *Ultrasound Med Biol,* **27**, 1107-1113 (2001).

[532] D. L. Miller and R. A. Gies. "Enhancement of ultrasonically-induced hemolysis by perfluorocarbon-based compared to air-based echo-contrast agents", *Ultrasound Med Biol,* **24**, 285-292 (1998).

[533] C. D. Ohl, M. Arora, R. Dijkink, V. Janve, and D. Lohse. "Surface cleaning from laser-induced cavitation bubbles", *Applied Physics Letters,* **89**,(2006).

[534] J. M. Escoffre, C. Mannaris, B. Geers, A. Novell, I. Lentacker, M. Averkiou, and A. Bouakaz. "Doxorubicin Liposome-Loaded Microbubbles for Contrast Imaging and Ultrasound-Triggered Drug Delivery", *IEEE Trans Ultrason Ferroelectr Freq Control,* **60**, 78-87 (2013).

[535] R. Suzuki, T. Takizawa, Y. Negishi, K. Hagisawa, K. Tanaka, K. Sawamura, N. Utoguchi, T. Nishioka, and K. Maruyama. "Gene delivery by combination of novel liposomal bubbles with perfluoropropane and ultrasound", *J Control Release,* **117**, 130-136 (2007).

[536] T. Kondo, V. Misik, and P. Riesz. "Effect of gas-containing microspheres and echo contrast agents on free radical formation by ultrasound", *Free Radical Biology and Medicine,* **25**, 605-612 (1998).

[537] W. J. Zhong, X. Chen, P. P. Jiang, J. M. F. Wan, P. Qin, and A. C. H. Yu. "Induction of Endoplasmic Reticulum Stress by Sonoporation: Linkage to Mitochondria-Mediated Apoptosis Initiation", *Ultrasound Med Biol,* **39**, 2382-2392 (2013).

[538] M. A. Hassan, Y. Furusawa, M. Minemura, N. Rapoport, T. Sugiyama, and T. Kondo. "Ultrasound-Induced New Cellular Mechanism Involved in Drug Resistance", *Plos One,* **7**,(2012).

[539] P. D. Edmonds and K. M. Sancier. "Evidence for Free-Radical Production by Ultrasonic Cavitation in Biological Media", *Ultrasound Med Biol,* **9**, 635-639 (1983).

[540] H. R. Rott. "Safety of Ultrasonic Contrast Agents", *J Acoust Soc Am,* **9**, 195-197 (1999).

[541] V. Mornstein. "Cavitation-induced risks associated with contrast agents used in ultrasonography", *J Acoust Soc Am,* **5**, 101-111 (1997).

[542] L. J. Machlin and A. Bendich. "Free-Radical Tissue-Damage - Protective Role of Antioxidant Nutrients", *Faseb Journal,* **1**, 441-445 (1987).

[543] K. K. Jain. "Nanobiotechnology-based strategies for crossing the blood-brain barrier", *Nanomedicine,* **7**, 1225-1233 (2012).

[544] H. L. Liu, M. Y. Hua, P. Y. Chen, P. C. Chu, C. H. Pan, H. W. Yang, C. Y. Huang, J. J. Wang, T. C. Yen, and K. C. Wei. "Blood-Brain Barrier Disruption with Focused Ultrasound Enhances Delivery of Chemotherapeutic Drugs for Glioblastoma Treatment", *Radiology,* **255**, 415-425 (2010).

[545] F. Y. Yang, Y. S. Lin, K. H. Kang, and T. K. Chao. "Reversible blood-brain barrier disruption by repeated transcranial focused ultrasound allows enhanced extravasation", *J Control Release,* **150**, 111-116 (2011).

[546] A. Carpentier, M. Canney, A. Vignot, V. Reina, K. Beccaria, C. Horodyckid, C. Karachi, D. Leclercq, C. Lafon, J. Y. Chapelon, L. Capelle, P. Cornu, M. Sanson, K. Hoang-Xuan, J. Y. Delattre, and A. Idbaih. "Clinical trial of blood-brain barrier disruption by pulsed ultrasound", *Sci Transl Med,* **8**, 343re342 (2016).

[547] J. H. Hwang, A. A. Brayman, M. A. Reidy, T. J. Matula, M. B. Kimmey, and L. A. Crum. "Vascular effects induced by combined 1-MHz ultrasound and microbubble contrast agent treatments in vivo", *Ultrasound Med Biol,* **31**, 553-564 (2005).

[548] H. Chen, A. A. Brayman, A. P. Evan, and T. J. Matula. "Preliminary Observations on the Spatial Correlation between Short-Burst Microbubble Oscillations and Vascular Bioeffects", *Ultrasound Med Biol,* **38**, 2151-2162 (2012).

[549] S. M. Stieger, C. F. Caskey, R. H. Adamson, S. P. Qin, F. R. E. Curry, E. R. Wisner, and K. W. Ferrara. "Enhancement of vascular permeability with low-frequency contrast-enhanced ultrasound in the chorioallantoic membrane model", *Radiology,* **243**, 112-121 (2007).

[550] J. F. Zachary, J. P. Blue, R. J. Miller, and W. D. O'Brien. "Vascular lesions and S-thrombomodulin concentrations from auricular arteries of rabbits infused with microbubble contrast agent and exposed to pulsed ultrasound", *Ultrasound Med Biol,* **32**, 1781-1791 (2006).

[551] J. M. Parker, M. W. Weller, L. M. Feinstein, R. J. Adams, M. L. Main, P. A. Grayburn, D. O. Cosgrove, B. A. Goldberg, K. Darge, P. Nihoyannopoulos, S. Wilson, M. Monaghan, F. Piscaglia, B. Fowlkes, W. Mathias, F. Moriyasu, M. C. Chammas, L. Greenbaum, and S. B. Feinstein. "Safety of Ultrasound Contrast Agents in Patients With Known or Suspected Cardiac Shunts", *Am J Cardiol,* **112**, 1039-1045 (2013).

[552] R. J. Weiss, M. Ahmad, F. Villanueva, S. Schmitz, G. Bhat, M. G. Hibberd, M. L. Main, and C. Investigators. "CaRES (Contrast Echocardiography Registry for Safety Surveillance): A Prospective Multicenter Study to Evaluate the Safety of the Ultrasound Contrast Agent Definity in Clinical Practice", *J Am Soc Echocardiogr,* **25**, 790-795 (2012).

[553] P. A. van der Wouw, A. C. Brauns, S. E. Bailey, J. E. Powers, and A. A. A. Wilde. "Premature ventricular contractions during triggered imaging with ultrasound contrast", *J Am Soc Echocardiogr,* **13**, 288-294 (2000).

[554] D. Dalecki, B. B. Keller, E. L. Carstensen, D. S. Neel, J. L. Palladino, and A. Noordergraaf. "Thresholds for Premature Ventricular Contractions in Frog Hearts Exposed to Lithotripter Fields", *Ultrasound Med Biol,* **17**, 341-346 (1991).

[555] A. G. MacRobbie, C. H. Raeman, S. Z. Child, and D. Dalecki. "Thresholds for premature contractions in murine hearts exposed to pulsed ultrasound", *Ultrasound Med Biol,* **23**, 761-765 (1997).

[556] M. Kurt, K. A. Shaikh, L. Peterson, K. M. Kurrelmeyer, G. Shah, S. F. Nagueh, R. Fromm, M. A. Quinones, and W. A. Zoghbi. "Impact of Contrast Echocardiography on Evaluation of Ventricular Function and Clinical Management in a Large Prospective Cohort", *J Am Coll Cardiol,* **53**, 802-810 (2009).

[557] M. Claudon, C. F. Dietrich, B. I. Choi, D. O. Cosgrove, M. Kudo, C. P. Nolsoe, F. Piscaglia, S. R. Wilson, R. G. Barr, M. C. Chammas, N. G. Chaubal, M. H. Chen, D. A. Clevert, J. M. Correas, H. Ding, F. Forsberg, J. B. Fowlkes, R. N. Gibson, B. B. Goldberg, N. Lassau, E. L. S. Leen, R. F. Mattrey, F. Moriyasu, L. Solbiati, H. P. Weskott, and H. X. Xu. "Guidelines and Good Clinical Practice Recommendations for Contrast Enhanced Ultrasound (CEUS) in the Liver - Update 2012 A WFUMB-EFSUMB Initiative in Cooperation With Representatives of AFSUMB, AIUM, ASUM, FLAUS and ICUS", *Ultraschall Med,* **34**, 11-29 (2013).

[558] S. B. Barnett, G. R. Ter Haar, M. C. Ziskin, H. D. Rott, F. A. Duck, and K. Maeda. "International recommendations and guidelines for the safe use of diagnostic ultrasound in medicine", *Ultrasound Med Biol,* **26**, 355-366 (2000).

[559] Definity. "Clinical Pharmacology Biopharmaceutics Review(s)", FDA/Center for Drug Evaluation and Research, Silver Spring, USA2000 2000.

[560] A. W. Appis, M. J. Tracy, and S. B. Feinstein. "Update on the safety and efficacy of commercial ultrasound contrast agents in cardiac applications", *Echo Res Pract,* **2**, R55-62 (2015).

[561] L. L. Kusnetzky, A. Khalid, T. M. Khumri, T. G. Moe, P. G. Jones, and M. L. Main. "Acute mortality in hospitalized patients undergoing echocardiography with and without an ultrasound contrast agent - Results in 18,671 consecutive studies", *J Am Coll Cardiol,* **51**, 1704-1706 (2008).

[562] E. Rosado and M. Riccabona. "Off-Label Use of Ultrasound Contrast Agents for Intravenous Applications in Children Analysis of the Existing Literature", *J Ultrasound Med,* **35**, 487-496 (2016).

[563] M. Hauben, E. Y. Hung, K. C. Hanretta, S. Bangalore, and V. Snow. "Safety of Perflutren Ultrasound Contrast Agents: A Disproportionality Analysis of the US FAERS Database", *Drug Saf*, **38**, 1127-1139 (2015).

[564] P. Soman, A. Lahiri, and R. Senior. "Safety of an intravenous second generation contrast agent in patients with severe left ventricular dysfunction", *Heart*, **84**, 634-635 (2000).

[565] R. S. Gabriel, Y. M. Smyth, V. Menon, A. L. Klein, R. A. Grimm, J. D. Thomas, and E. M. Sabik. "Safety of Ultrasound Contrast Agents in Stress Echocardiography", *Am J Cardiol*, **102**, 1269-1272 (2008).

[566] S. Kotopoulis, G. Dimcevski, O. H. Gilja, D. Hoem, and M. Postema. "Treatment of human pancreatic cancer using combined ultrasound, microbubbles, and gemcitabine: A clinical case study", *Med Phys*, **40**,(2013).

# SUMMARY

Ultrasound contrast agents have been used clinically for several decades to visualize blood flow in the heart and malignancies in the liver and kidneys. The contrast agents that are now approved for clinical use consist of microbubbles, tiny gas bubbles coated with a stabilizing layer to prevent quick dissolution into the blood and to shield them from the immune system. Because these gas bubbles are highly responsive to ultrasound and different from that of tissue, microbubbles can be clearly distinguished from surrounding tissue. Microbubbles can therefore be used for contrast enhancement of the blood. Next to that, microbubbles can also be used to target to specific biomarkers that are expressed on the inside of blood vessels by diseased tissue. **Chapter 2** gives an overview of targeting methods and the diseases that can currently be targeted. In addition, it describes how microbubbles are used for *in vitro* and *in vivo* ultrasound molecular imaging and how they can be used to enhance drug delivery by means of pore formation in the cell membrane (sonoporation) for therapeutic applications.

In order to design an ultrasound contrast agent for high-frequency contrast-enhanced ultrasound imaging, **Chapter 3** discusses different microbubble compositions and preparation techniques that can be used to manufacture ultrasound contrast agents. The performance of these contrast agents was tested *in vitro* and in an *in vivo* porcine model, and compared to Target-Ready MicroMarker, a commercially available contrast agent. Although contrast enhancement of blood can be relatively easily achieved due to the high amount of microbubbles, one of the main challenges in microbubble manufacturing is a similar response of each individual microbubble. The rationale is that for molecular imaging only a few microbubbles adhere to the biomarker of interest and you want to ensure that those few microbubbles are actually detected.

In **Chapters 4 to 7** the properties of individual non-targeted microbubbles are investigated using ultra-high-speed optical imaging. **Chapter 4** reveals that replacing the main constituent of the microbubble coating with another lipid significantly changes the microstructure, and thus the distribution of the coating components. A lipid with only two extra C-atoms changed the homogeneous distribution of lipids in the shell to a heterogeneous distribution, and also decreased the binding area. Because this is likely to also result in differences in their acoustic behavior, this was studied in **Chapter 5**. Echogenic liposomes are a slightly different type of lipid-coated contrast agent that consist of a multi-layer of lipids encapsulating a gas and an aqueous phase. Those liposomes are also promising for several therapeutic strategies, such as oxygen delivery to a tumor to enhance the effect of radiation or chemotherapy. In **Chapter 6** the shell properties of this type of contrast agent are characterized and were found to be quite similar to microbubbles. For the analysis of these agents a more sophisticated and faster experimental method was developed in cooperation with the University of Cincinnati (Cincinnati, OH, USA). The Brandaris 128 ultra-high-speed camera that was used for the research described in the previous chapters has already been in operation for over 13 years.

A similar camera has recently been built at the University of Pittsburgh (Pittsburgh, PA, USA) that is able to better capture fast oscillating fluorescently labeled microbubbles. In **Chapter 7** this camera was used to study the behavior of microbubbles that were fluorescently labeled, to gain more insights into the specific movement of the lipids and try to experimentally unravel the relation between compression-only, buckling, and the acoustic behavior of the microbubbles.

Following the chapters that discussed non-targeted microbubbles, we move on to the comparison of the acoustic properties between bound and non-bound targeted microbubbles in **Chapter 8**. The differentiation of bound microbubbles from those that are freely moving in the blood could speed up ultrasound molecular imaging acquisition and increase the specificity of the technique.

All previous chapters concerned experiments that were carried out *in vitro*, without the presence of living cells. To move more towards clinical translation, the aspect of microbubbles in contact with cells is an important hurdle that needs to be taken and better understood. Sonoporation—the increased permeability of cell membranes through pore formation mediated by ultrasound—is one of the most promising routes to enhance local uptake of therapeutic agents or to induce local cell death by means of ultrasound. In **Chapter 9** experiments were designed to fully cover the importance of microbubble displacement, oscillation, and targeting on the viability of human endothelial cells. Next to microbubbles that are driven by an acoustic pulse, one can also use other types of contrast agents. **Chapter 10** describes laser-activated polymer microcapsules that absorb the light and create a gas microbubble that interacts with nearby cells. The imaging and therapeutic windows of these types of capsules are assessed in this chapter.

The final step before clinical translation and clinical application concerns experiments on living animals. **Chapters 11 and 12** describe the *in vivo* experiments on pigs that were performed using quantitative contrast-enhanced ultrasound imaging and laser-speckle imaging of the kidney and video-microscopy on the microvasculature under the tongue. This project was initiated by the direct clinical need for new diagnostic tools to assess acute kidney injury in patients that are admitted to the intensive care unit. Two different causes of acute kidney injury were studied: hypovolemic shock induced by severe blood loss (i.e. hemorrhage, **Chapter 11**) and a systemic bloodstream infection (i.e. sepsis, **Chapter 12**). The difference between the arrival time of the contrast bolus in the cortical arteries and the cortical microcirculation was the best suitable parameter for quantifying renal cortical alterations after inducing hemorrhagic shock. For sepsis, the maximum contrast intensity and the ratio between the peak value and the final value were found to best reflect microcirculatory alterations.

**Chapter 13** discusses the use of microbubbles and the associated risks on the cellular and tissue level, clinical usage, and on long-term patient outcome. With respect to contrast-enhanced MR and CT imaging, the number of ultrasound examinations is still much lower.

From the presented overview of risks, it is clear that ultrasound contrast imaging is safer and cheaper than the other contrast-enhanced imaging modalities and also offers several therapeutic applications.

In **Chapter 14** the conclusions of all chapters are discussed and possible future directions to speed up the translation of ultrasound contrast agents for imaging and therapy to the clinic are provided.

# SAMENVATTING

Contrastmiddelen voor echografie worden al tientallen jaren gebruikt bij routineonderzoeken in het ziekenhuis om de stroming van bloed te laten zien en om onvolkomenheden in het samentrekken van de hartspier in beeld te brengen. De contrastmiddelen die nu goedgekeurd zijn voor gebruik bij patiënten bestaan allemaal uit microbellen. Dit zijn kleine gasbelletjes, die door een dun laagje vet gestabiliseerd worden. Dat vetlaagje zorgt ervoor dat de microbellen minder snel oplossen in het bloed en zorgt ook voor afscherming van het immuunsysteem. Omdat deze microbellen erg goed reageren op het ultrageluid dat gebruikt wordt voor het uitvoeren van echografie-onderzoeken en omdat ze anders reageren op dit geluid dan het omliggende weefsel, kunnen de microbellen heel specifiek in beeld worden gebracht.

Naast het gebruik van deze contrastmiddelen om de bloedstroming in beeld te brengen, kun je deze microbellen ook specifiek laten binden aan biomarkers die in de bloedbaan tot expressie komen bij bepaalde ziekteprocessen. Deze biomarkers zijn moleculen die bij een bepaalde ziekte op het oppervlak van een cel aanwezig zijn en waaraan de microbellen zich kunnen hechten. **Hoofdstuk 2** geeft een overzicht van de huidige manieren om microbellen te functionaliseren met moleculen die specifiek aan een bepaalde biomarker binden, zoals bijvoorbeeld aan een kankercel. In dit hoofdstuk wordt ook aandacht besteed aan de biomarkers die hiervoor gebruikt kunnen worden en hoe dit gebruikt kan worden voor moleculaire beeldvorming wanneer een microbel zich bindt aan de biomarker.

Wat de microbellen uniek maakt als contrastmiddel, is het feit dat ze vibreren door de inkomende ultrageluidsgolf; hierdoor kunnen ze als het ware een cel 'masseren' en hierdoor poriën creëren in een celmembraan (sonoporatie). Het laatste deel van dit hoofdstuk bespreekt de mogelijkheden van microbellen om medicijnen heel lokaal af te geven of cellen zo drastisch te behandelen dat ze dood gaan. Na deze uitgebreide introductie op het functionaliseren van microbellen en waar we deze voor kunnen gebruiken, gaan we terug naar de basis: proberen microbellen te produceren met zo goed mogelijke eigenschappen en die bij voorkeur ook nog aan specifieke eisen aangepast kunnen worden.

**Hoofdstuk 3** gaat in op de twee meest gebruikte productiemethoden voor microbellen (hard schudden of door middel van geluidsgolven) en de kwaliteit hiervan voor de beeldvorming in een gecontroleerde laboratoriumopstelling en in een levend varken (zogenaamde *in vivo* experimenten). In beide situaties worden de zelfgemaakte microbellen vergeleken met een commercieel verkrijgbaar contrastmiddel. Deze productiemethoden en kwantificaties richten zich op grote hoeveelheden microbellen bij elkaar, waardoor er al snel voldoende contrast gegenereerd wordt. Maar in het geval van moleculaire beeldvorming met gefunctionaliseerde microbellen, zullen er zich slechts enkele binden aan een biomarker, dus het signaal van een enkele microbel moet specifiek en hetzelfde zijn voor alle microbellen.

Dit is tot op heden een nog niet opgelost probleem; de grootte van een bel voorspelt het grootste deel van het gedrag, maar de eigenschappen van het stabiliserende vetlaagje spelen hierin ook een belangrijke rol. Om dit beter te begrijpen zijn individuele microbellen bekeken met een microscoop met een zeer hoge resolutie (**hoofdstuk 4**) en met de unieke Brandaris 128 hogesnelheidscamera die 25 miljoen foto's per seconde kan maken (**hoofdstuk 5**); ruim voldoende om de snelle beweging van de microbellen in de orde van 1 tot 4 miljoen vibraties per seconde in beeld te kunnen brengen. **Hoofdstuk 4** laat zien dat de verandering van één van de componenten in het stabiliserende vetlaagje de gehele ordening van de vetten verandert. Het vetmolecuul met twee koolstofatomen extra zorgt ervoor dat de homogene samenstelling verandert in een heterogene samenstelling en dat het bindingsoppervlak kleiner wordt. Omdat het logisch lijkt dat dit ook zorgt voor een verandering in de reactie op ultrageluid, is dat onderzocht met de experimenten die beschreven staan in **hoofdstuk 5**.

Met diezelfde hogesnelheidscamera bestuderen we in **hoofdstuk 6** niet de klassieke microbellen, maar echogene liposomen. Deze contrastmiddelen hebben een dikkere vetlaag en kunnen bijvoorbeeld gevuld worden met zuurstof, wat afgeleverd kan worden in een tumor om het effect van bestraling of chemotherapie te versterken. Voor de analyse van het gedrag van deze liposomen hebben we een geavanceerdere en snellere methode ontwikkeld. Deze methode laat zien dat de eigenschappen van het vetlaagje vrij sterk lijken op die van de microbellen.

De Brandaris 128 hogesnelheidscamera die gebruikt is in de vorige hoofdstukken, is ondertussen al 13 jaar in gebruik en recent is aan de Universiteit van Pittsburgh (Pittsburgh, Pennsylvania, Verenigde Staten) een vergelijkbare camera ontwikkeld. Deze camera heeft een hogere lichtgevoeligheid, waardoor op hogere snelheden ook beelden gemaakt kunnen worden van fluorescent gelabelde microbellen. Deze camera is gebruikt in **hoofdstuk 7** om beter te begrijpen hoe de vetmoleculen bewegen gedurende de snelle vibraties van de microbel. Tevens proberen we hiermee voor het eerst experimenteel de relatie inzichtelijk te maken tussen zogenaamd compressiegedrag, waarbij de bel meer compressie dan expansie vertoont, de frequentie waarmee de bel beweegt en het indeuken van het vetlaagje ('buckling').

In de **hoofdstukken 5 – 7** worden de echogene eigenschappen bestudeerd van microbellen die niet vastzitten aan een biomarker, maar vrij kunnen bewegen. Omdat het waarschijnlijk is dat deze eigenschappen veranderen zodra de microbel bindt aan een biomarker vergelijken we in **hoofdstuk 8** hetzelfde type bellen in deze twee situaties: gebonden en niet gebonden. Het onderscheid van het akoestisch signaal van microbellen die vrij in de bloedbaan kunnen bewegen en de microbellen die vastzitten aan een biomarker kan de specificiteit van moleculaire beeldvorming verhogen. Tevens kan dit de opnametijd die nodig is om hiervan een beeld te maken significant verkorten.

De experimenten in de vorige hoofdstukken zijn allemaal *in vitro* (in een laboratoriumomgeving) uitgevoerd zonder de aanwezigheid van levende cellen. Op de weg

naar de toepassing in het ziekenhuis is het belangrijk om hier ook aandacht aan te besteden, omdat een celmembraan zich anders gedraagt dan een kunstmatig membraan van plastic. Zoals eerder gezegd is sonoporatie een van de meest veelbelovende therapieën die we met ultrageluid naar het ziekenhuis kunnen brengen om lokale medicijnafgifte en celdood beter te kunnen controleren. In **hoofdstuk 9** wordt besproken wat de invloed van het functionaliseren van microbellen en de verplaatsing en oscillatie ervan voor invloed hebben op humane endotheelcellen.

Tot nu toe ging het over microbellen die onder invloed van ultrageluid beginnen met oscilleren, maar er zijn ook andere mogelijkheden waar je aan kunt denken bij contrastmiddelen voor echografie. **Hoofdstuk 10** beschrijft laser-geactiveerde microcapsules met een licht-absorberende kleurstof in het polymere omhulsel. Door gebruik te maken van een polymeer, in plaats van een vetlaagje, creëer je een contrastmiddel met een langere levensduur in de bloedbaan van de patiënt. De laser verdampt de olie in de kern van de microcapsule, wat een gasbel veroorzaakt. Door deze verdamping van de olie in een gas wordt een ultrageluidssignaal gegenereerd. Uit het onderzoek naar het effect van de verdamping van deze microcapsules in de nabijheid van humane endotheelcellen, blijkt dat ze erg effectief zijn in het doden van cellen, wat bijvoorbeeld gebruikt zou kunnen worden bij de behandeling van tumoren.

De stap van cellen naar een patiënt blijft nog steeds erg groot. Daarom is er als tussenstap gekozen voor het uitvoeren van experimenten op levende dieren. **Hoofdstuk 11 en 12** beschrijven de *in vivo* experimenten op varkens, waarbij acuut nierfalen is opgewekt via het simuleren van een grote bloeding of een bacteriële infectie. Behalve contrastechografie van de nier hebben we in deze experimenten ook gebruik gemaakt van laser speckle beeldvorming van de nier en videomicroscopie van de microcirculatie onder de tong. We laten hier zien dat we veranderingen in de fysiologie van de falende nier kunnen kwantificeren met behulp van echografie van de nier en met behulp van videomicroscopie onder de tong. Dit project is direct geïnitieerd door de intensive care afdeling van het Erasmus MC om nieuwe manieren te vinden voor de identificatie van acuut nierfalen en deze methoden hebben daarom een grote kans om snel in de praktijk toegepast te kunnen worden.

Aan elke injectie in de bloedbaan zijn risico's verbonden, zo ook bij het gebruik van microbellen. In **hoofdstuk 13** geven we een overzicht van de risico's waar rekening mee gehouden moet worden op verschillende niveaus: op celniveau, weefselniveau en langetermijneffecten voor de patiënt. Ondanks dat contrastechografie veiliger en goedkoper is dan bijvoorbeeld contrastmiddelen voor MRI of CT, is het belangrijk om stil te staan bij de mogelijke risico's. Tenslotte geeft **hoofdstuk 14** een overzicht van de belangrijkste conclusies, implicaties voor de translatie naar het ziekenhuis en richtingen voor toekomstig onderzoek.

# DANKWOORD

Op het heerlijk avondje in december zit ik aan tafel en ben ik bezig met het schrijven van het meest gelezen deel van mijn proefschrift: het dankwoord. Ik kan me nog goed herinneren hoe het allemaal begon in maart 2012 tijdens mijn sollicitatiegesprek met Hans, Nico en Ton. Toen ik binnenkwam was het eerste wat ik zag een lelijk betonnen gebouw wat ervoor zorgde dat ik me meteen thuis voelde omdat het zoveel lijkt op W-Hoog op de TU/e. De 'opgeruimde' kantoren waren ook niet helemaal wat ik verwacht had. Gelukkig was het een goed gesprek en was het een afdeling met erg leuke mensen. Ton en Nico, bedankt voor het vertrouwen dat jullie in mij hadden, en wat ik hoop en denk ook waar te hebben kunnen maken. Toen jullie me belden dat ik kon beginnen, moesten jullie wel nog even geduld hebben, omdat ik diezelfde ochtend mijn contract op de TU/e, bij Klaas Nicolay, had ondertekend. Door de goede connecties met Klaas was het ook totaal geen probleem dat ik daar nog even bleef werken, maar dit bood ook een goede kans om hem te gebruiken als referentie om navraag naar me te doen. Klaas werd door Nico gebeld tijdens een college, en hij nam zonder aarzelen de telefoon op en vertelde aan alle aanwezige studenten dat er gebeld werd naar aanleiding van een sollicitatie van mij (ik was mede-docent bij dit vak). Klaas, ik weet zeker dat ik dankzij jouw positieve woorden zonder een tweede sollicitatieronde aangenomen ben voor dit project. Ook tijdens mijn promotie, binnen het NanoNextNL consortium, was je nog betrokken bij mijn onderzoek en was je elke keer dat we elkaar spraken oprecht geïnteresseerd in mijn werk. Ik ben je heel erg dankbaar voor je hulp en de samenwerking en ik hoop dat je nog kunt genieten van het lezen van mijn proefschrift.

Het onderzoek dat beschreven staat in mijn proefschrift had nooit tot stand kunnen komen zonder de geweldige hulp en begeleiding van Nico, Ton en Klazina. Ik heb deze vier jaar fijn met jullie samengewerkt en vind het jammer dat daar nu een einde aan gaat komen. Ik heb veel van jullie kunnen leren op wetenschappelijk gebied en door de samenwerking met Nico kan ik nu ook uitstekend omgaan met mensen bij wie afspraken nakomen niet echt hun sterkste punt is.

Naar goed voorbeeld van een van mijn stellingen (nummer 8) was er regelmatig afleiding te vinden door de hoeveelheid vrouwen binnen een straal van 3 meter van mijn bureau: Inés, Kirby en Sara thank you for making it fun to go to work! I enjoyed your company and help and I hope you won't miss me too much. Kirby, my work-sister, thanks for constantly picking on me and making Klazina worry whether we would scare off Inés when she started her internship. Next to picking on me, I really appreciated your help in proofreading my English and helping me out with the first draft of chapter 9. Inés, zonder jouw hulp had ik de artikelen waarbij je betrokken was niet zo efficiënt en goed af kunnen ronden als nu het geval is. Heel veel succes als de nieuwe hoeder van Brandaris, ik weet dat je er goed voor zult zorgen. Oh, and Inés and Kirby, while fighting over my chair: don't forget that you still have to share an office for a few years.

I also want to thank the old inhabitants of my office: Tom, Ying and Jason. Tom, ik heb fijn met je samengewerkt en vooral in de beginperiode van mijn promotie was het erg prettig iemand vlakbij te hebben die me wegwijs kon maken in het lab en op de afdeling. Het was alleen niet altijd even praktisch om naast elkaar te zitten en dezelfde voornaam en hetzelfde telefoonnummer te hebben. Ying, you were always an easy victim to pick on together with Tom or Robert. You helped me a lot with my first paper and we've had some good discussions. Jason, you were nice to work with, which resulted in a nice paper. Although you were only there for a year, you taught me some things regarding Brandaris I did not know before.

All the people of the BME family who helped me during my research, Ilya, Verya, Jason, Rik, Guillaume Renaud, Hans, Deep, Geert and Michiel, thank you for your contributions. Frits en Robert, zonder jullie kennis van de Brandaris zouden diverse experimenten waarschijnlijk uitgelopen zijn op een fiasco. Jullie jarenlange ervaring en creativiteit om de Brandaris draaiende te houden zijn van onschatbare waarde geweest voor mij, maar zeker ook voor de rest van de afdeling.

Het labuitje dat ik twee jaar achter elkaar heb georganiseerd heb ik met plezier neergezet. In het eerste jaar leerde ik iedereens wensen en kwaliteiten kennen: Tom Kokhuis houdt van boten, Pieter van out-of-the-box activiteiten en familieactiveiten en Jelle en ik waren goede quizmakers en -masters. Bedankt voor het samen organiseren van dit uitje. The year after the new recruits Ayla and Jovana joined as junior organizers. Since Jelle and I were the seniors, the two of you took care of most of the work that year, including taking caring of Jacopo when he tried to chop off his thumb. I still regret that we didn't organize the sheep herding workshop, but hopefully someone of the new committee will read this and put it into action.

Zonder de kwaliteiten van onze secretaresses Mieke, Gracia en Sharon zou de afdeling nooit zo goed draaien en zouden de promovendi veel meer zelf moeten regelen. Bedankt voor het regelen van alle zaken wat betreft de hoofdpijnafdeling P&O en het afhandelen van de papierwinkel omtrent mijn verdediging.

Next to the people mentioned above, I want to thank all the BME family members who made our department a nice working environment: Jan, Gerard, Charles, Krista, Jacopo, Alex, Zeynettin, Hans Verdoes, Gracia, Lambert, David, Harm, Merih, Leah, Jolanda, Gijs, Frank, Kim, Kim, Ali, Tianshi, Ruoyu, Muthu, Eric, Eline, Sophinese, Mirjam, Min, Reza, Erik-Jan, Leonardo, Lana, Annette, Kristina, and all the interns.

Zoals het een bellenonderzoeker betaamt in onze groep was er een sterke samenwerking met de Physics of Fluids groep van de Universiteit Twente. Als eerste wil ik Michel bedanken voor de nuttige input bij het schrijven van mijn allereerste artikel en de rest van de samenwerking de afgelopen jaren. Daarnaast was het ook altijd weer gezellig om samen met je de lokale brouwerijen of restaurants op te zoeken. Ik weet nu dat ik jou moet bellen als ik in een stad ben waar ik nooit eerder geweest ben en op zoek ben naar een brouwerij of een goed lokaal biertje. Tim, ik heb prettig met je samengewerkt, maar helaas hebben we het niet

voor elkaar kunnen krijgen om het onderzoek om te zetten in een artikel. And of course a special thanks to Guillaume, with whom I spent two weeks fulltime in the Brandaris lab and at least four times that amount of time on Skype. Your knowledge on physics is impressive and we were a great team. I enjoyed working with you and wish you all the luck with your future career in bubbles. Elk jaar in Leeds en in Rotterdam was de coalitie tussen Enschede en Rotterdam weer snel gevormd. We vormden een vast clubje dat elke avond (vaak tot iets te laat) de kroeg opzocht om samen speciaalbier te drinken en soms ook nog wel wat inhoudelijks te bediscussiëren. Deze coalitie was echter niet compleet zonder vrouwelijk tegenwicht in de vorm van de dames uit Gent. Ine, Ine, Heleen en Silke, jullie ook bedankt voor deze gezellige congresdagen, maar vooral ook de gezelligheid in de avonduren.

Vanaf december 2014 heb ik erg intensief samengewerkt met de afdelingen Anesthesiologie en de Intensive Care van het Erasmus MC en Translationele Fysiologie van het AMC in ons onderzoek naar acuut nierfalen. Deze varkensexperimenten duurden de hele dag (en vaak ook nog ver in de avond), maar gelukkig hadden we een team wat er altijd de moed inhield. Yasin, jij zorgde altijd voor de vrolijke noot, nutteloze filmpjes of je verhalen over Thailand. Patricia zorgde voor het vrouwelijke tegenwicht, maar veel belangrijker nog voor de kennis en ervaring van het doen van onderzoek met grote proefdieren. Zonder jouw hulp hadden we de experimenten niet zo succesvol uit kunnen voeren. Bulent, you quickly got familiar with the surgical procedure and calmly handled our energetic talks about nothing, and additional experiments we wanted to perform. Alex, you were nice to work with and I'm proud of the paper we wrote. En Can, zonder jouw inzet was deze studie nooit tot stand gekomen. Het was een gouden idee om jouw kennis van de fysiologie en microcirculatie te combineren met de ultrasoundkennis van onze afdeling. Onze samenwerking ging allesbehalve van een leien dakje en we hebben heftige discussies gehad. Soms wist ik echt niet meer wat ik met je aan moest als ik je voor de twintigste keer probeerde te overtuigen van mijn gelijk. Uiteindelijk wist ik je vertrouwen te winnen en zijn we tot erg mooie resultaten gekomen met methodes die jullie nu gaan testen bij patiënten op de IC. Ik ben er trots op dat ik aan de voorbereiding hiervoor heb mee kunnen werken. Voor onze experimenten waren we te gast bij Anesthesiologie waar Harold, Sam en Nathalie altijd in waren voor een praatje en om ons even af te leiden tijdens het wachten tussen de verschillende metingen. Voor een paar van onze experimenten zijn we uitgeweken naar de operatiekamer van Experimentele Cardiologie, waarvoor ik Dirk-Jan en Maaike wil bedanken.

Als je samen een verdieping deelt kom je elkaar regelmatig tegen op de gang, in de lift of bij de koffieautomaat en sommige mensen kom je daar vaker tegen dan anderen. Ihsan, ik kon altijd bij je terecht voor een kwartier slap ouwehoeren over niks tijdens je vele koffiepauzes. Succes met jouw laatste loodjes!

Ik ben tijdens mijn promotie naar erg veel congressen geweest en heb daar veel mensen leren kennen. Met de groepen uit Nijmegen en Eindhoven maakten we elke stad waar IEEE Ultrasonics gehouden werd onveilig. Anne, Stein, Chris, Kai, Rik, Renate, Gijs, Richard, Emiel

en Niels, bedankt voor deze Nederlandse onderonsjes. The other usual suspects at the international conferences, Brandon, Ryan, and Marianne were always good to hang out with. Ryan, we hung out together for some time in Providence, Boston and Chicago which I really enjoyed. Marianne, thank you for showing me around in Chicago with your friends. Marjolein, ik vond het leuk je op de ISTU in Utrecht weer tegen te komen en bedankt voor je leuke afscheidsfeestje. Succes nog in de VS en met de afronding van jouw promotie!

Ongeveer wekelijks probeerden we wel samen een keertje thee te gaan drinken (stelling 11 moest in ere gehouden worden) en verder waren we er goed in om via Facebook over onze dagelijkse PhD-sleur te klagen. Ayla, bedankt voor al die uren die we bij een kop thee hebben doorgebracht, die afleiding hadden we allebei vaak wel even nodig. Dat ga ik wel missen, maar ik hoop dat we dat gewoon voort kunnen zetten als je straks half of helemaal in Eindhoven woont. Behalve een collega ben je ook een goede vriendin geworden en daarom ben ik ook blij dat je mij als paranimf bij wil staan tijdens mijn verdediging. Ondanks dat ik mezelf altijd zag als iemand die dingen op regelt, heb ik mijn beide paranimfen pas vrij laat gevraagd. Rick, ik ben blij dat je op korte termijn tijd kon maken zodat ik jullie nieuwe huis kon bekijken en mezelf een handige gelegenheid gaf jou te vragen om mijn paranimf te zijn. We hebben sinds ons eerste jaar op de TU/e veel samen gedaan en gedeeld en ik ben dan ook blij dat jij toezegde om mijn paranimf te zijn.

Stiekem heb ik de laatste 3 maanden van de afronding nog erg veel moeten doen. Behalve mijn proefschrift zat ik ook nog in mijn maag met het zoeken naar een baan en opeens alles thuis alleen moeten regelen. Gelukkig stond ik daar niet helemaal alleen in en kon ik altijd bij jou terecht, Lianne. Voor gezelschap, een sarcastische opmerking of gewoon om even te klagen. In de laatste maanden fungeerde je als eerste klankbord wat betreft mijn stellingen, lay-out, cover en als proofreader van stukken tekst. Ondanks dat we het qua stijl bijna standaard met elkaar oneens waren, hebben je hulp en commentaar me erg geholpen. Ik hoop dat ik je tijdens de afronding van jouw proefschrift op dezelfde manier kan helpen.

Flip, jou wil ik heel erg bedanken voor het helpen met het ontwerp van de kaft en de uitnodiging van dit proefschrift, hij is erg mooi geworden! Het einde van dit dankwoord en daarmee toch ook wel een beetje mijn promotietijd, komt nu in zicht. Maar niet zonder dat ik vrienden, familie, papa, mama, Evie en Flip bedankt heb. Jullie begrepen vaak niet waar ik nou vier jaar mee bezig was, waarom ik 's avonds of in het weekend aan het werk was en wat ik er nou zo leuk aan vond. Als ik weer eens druk was en weinig tijd had om te koken, afleiding nodig had of wat dan ook, kon ik altijd bij jullie terecht. Hopelijk snappen jullie bij het zien van dit proefschrift waar ik het allemaal voor gedaan heb.

## PEER-REVIEWED PAPERS

**Tom van Rooij***, Guillaume Lajoinie*, Ilya Skachkov, Emilie Blazejewski, Gert Veldhuis, Nico de Jong, Klazina Kooiman, Michel Versluis. "Laser-activated polymer microcapsules for acoustic imaging and therapy: an *in vitro* feasibility study", *Biophysical Journal* (2016) – *submitted*

**Tom van Rooij**, Inés Beekers, Kirby R. Lattwein, Antonius F.W. van der Steen, Nico de Jong, Klazina Kooiman. "Vibrational responses of targeted lipid-coated single microbubbles", *IEEE Transactions on Ultrasound, Ferroelectrics and Frequency Control* (2016) – *submitted*

Verya Daeichin, **Tom van Rooij**, Ilya Skachkov, Bulent Ergin, Patricia A.C. Specht, Alexandre Lima, Can Ince, Johan G. Bosch, Antonius F.W. van der Steen, Nico de Jong, Klazina Kooiman. "Microbubble composition and preparation for high-frequency contrast-enhanced ultrasound imaging: *in vitro* and *in vivo* evaluation", *IEEE Transactions on Ultrasound, Ferroelectrics and Frequency Control* (2016) – *submitted*

**Tom van Rooij**, Ilya Skachkov, Inés Beekers, Kirby R. Lattwein, Jason D. Voorneveld, Tom J.A. Kokhuis, Deep Bera, Ying Luan, Antonius F.W. van der Steen, Nico de Jong, Klazina Kooiman. "Viability of endothelial cells after ultrasound-mediated sonoporation: influence of targeting, oscillation, and displacement of microbubbles", *Journal of Controlled Release,* **238**, 197–211 (2016)

Jason L. Raymond, Ying Luan, **Tom van Rooij**, Klazina Kooiman, Shao-Ling Huang, David D. McPherson, Michel Versluis, Nico de Jong, Christy K. Holland. "Impulse response method for characterization of echogenic liposomes", *Journal of the Acoustical Society of America,* **137**, 1693–1703 (2015)

**Tom van Rooij**, Ying Luan, Guillaume Renaud, Antonius F.W. van der Steen, Michel Versluis, Nico de Jong, Klazina Kooiman. "Non-linear response and viscoelastic properties of lipid-coated microbubbles: DSPC versus DPPC", *Ultrasound in Medicine & Biology*, **41**, 1432–1445 (2015)

**Tom van Rooij***, Verya Daeichin*, Ilya Skachkov, Nico de Jong, Klazina Kooiman. "Targeted ultrasound contrast agents for ultrasound molecular imaging and therapy", *International Journal of Hyperthermia*, **31**, 90–106 (2015)

Klazina Kooiman, Tom J.A. Kokhuis, **Tom van Rooij**, Ilya Skachkov, Alex Nigg, Johannes G. Bosch, Antonius F.W. van der Steen, Wiggert A. van Cappellen, and Nico de Jong. "DSPC or DPPC as main shell component influences ligand distribution and binding area of lipid-coated targeted microbubbles", *European Journal of Lipid Science and Technology*, **116**, 1217–1227 (2014)

Eline P.M. Cardinaels*, Alma M.A. Mingels*, **Tom van Rooij**, Paul O. Collinson, Frits W. Prinzen, and Marja P. van Dieijen-Visser. "Time-dependent Degradation Pattern of Cardiac Troponin T Following Myocardial Infarction", *Clinical Chemistry*, **59**, 1083-90 (2013)

## PAPERS IN PREPARATION

**Tom van Rooij***, Alexandre Lima*, Bulent Ergin, Michele Sorelli, Yasin Ince, Patricia A.C. Specht, Egbert G. Mik, Leonardo Bocchi, Klazina Kooiman, Nico de Jong, Can Ince, "Renal contrast-enhanced ultrasound and sublingual video-microscopy identify microcirculatory dysfunction in acute kidney injury"

Klazina Kooiman, **Tom van Rooij**, Bin Qin, Frits Mastik, Hendrik J. Vos, Michel Versluis, Alexander L. Klibanov, Nico de Jong, Flordeliza S. Villanueva, Xucai Chen "Focal areas of increased lipid concentration on the coating of microbubbles during short tone-burst ultrasound insonification"

## CONFERENCE PROCEEDINGS

**Tom van Rooij**, Alexandre Lima, Verya Daeichin, Patricia A.C. Specht, Bulent Ergin, Yasin Ince, Nico de Jong, Can Ince, Klazina Kooiman. "Feasibility of in vivo contrast-enhanced ultrasound imaging of the renal cortex during hemorrhagic shock", *Proceedings IEEE International Ultrasonics Symposium 2015, Taipei, Taiwan, 21-24 Oct 2015*

**Tom van Rooij**, Antonius F.W. van der Steen, Nico de Jong, Klazina Kooiman. "Influence of binding on the vibrational responses of targeted lipid-coated microbubbles", *Proceedings IEEE International Ultrasonics Symposium 2014, Chicago, Illinois, USA, 3-6 Sept 2014*

**Tom van Rooij**, Ying Luan, Guillaume Renaud, Antonius F.W. van der Steen, Nico de Jong, Klazina Kooiman. "Acoustical response of DSPC versus DPPC lipid-coated microbubbles", *Proceedings IEEE International Ultrasonics Symposium 2013, Prague, Czech Republic, 21-25 July 2013*

Ying Luan, Guillaume Lajoinie, Erik Gelderblom, Ilya Skachkov, Heleen Dewitte, Ine Lentacker, **Tom van Rooij**, Hendrik Vos, Antonius F.W. van der Steen, Michel Versluis, Nico de Jong. "Liposome shedding from a vibrating microbubble on nanoseconds timescale", *Proceedings IEEE International Ultrasonics Symposium 2013, Prague, Czech Republic, 21-25 July 2013*

(* both first authors contributed equally)

# CONFERENCE PRESENTATIONS

(presenter underlined)

Inés Beekers, **Tom van Rooij,** Martin D. Verweij, Michel Versluis, Nico de Jong, Sebastiaan J. Trietsch, Klazina Kooiman. "A novel microfluidics system for in vitro ultrasound-enhanced drug delivery: acoustic characterization", *Dutch Biomedical Engineering Conference 2017, Egmond aan Zee, the Netherlands, 26-27 Jan (oral)*

**Tom van Rooij**, Ilya Skachkov, Inés Beekers, Kirby R. Lattwein, Jason D. Voorneveld, Tom J.A. Kokhuis, Deep Bera, Ying Luan, Antonius F.W. van der Steen, Nico de Jong, Klazina Kooiman. "Bubble-cell interactions for endothelial sonoporation at long pulses using targeted and non-targeted microbubbles", *IEEE International Ultrasonics Symposium 2016, Tours, France, 18-21 Sept 2016 (oral)*

Inés Beekers, Shreyas B. Raghunathan, **Tom van Rooij,** Verya Daeichin, Nico de Jong, Klazina Kooiman, Sebastiaan J. Trietsch. **"**Wave propagation in a novel microfluidics system for in vitro ultrasound-enhanced drug delivery", *IEEE International Ultrasonics Symposium 2016, Tours, France, 18-21 Sept 2016 (poster)*

**Tom van Rooij**, Ilya Skachkov, Inés Beekers, Kirby R. Lattwein, Jason D. Voorneveld, Tom J.A. Kokhuis, Deep Bera, Ying Luan, Antonius F.W. van der Steen, Nico de Jong, Klazina Kooiman. "Viability of endothelial cells after ultrasound-mediated sonoporation", *31st Bubble Conference 2016, Chicago, Illinois, USA, 10-12 Sept (oral)*

Verya Daeichin, **Tom van Rooij**, Ilya Skachkov, Bulent Ergin, Patricia A.C. Specht, Alexandre Lima, Can Ince, Johan G. Bosch, Antonius F.W. van der Steen, Nico de Jong, Klazina Kooiman. "Microbubbles for high-frequency contrast ultrasound imaging", *6th Microbubble Symposium 2016, Leeds, UK, 18-19 July 2016 (oral)*

Inés Beekers, Shreyas B. Raghunathan, **Tom van Rooij**, Verya Daeichin, Nico de Jong, Klazina Kooiman, Sebastiaan J. Trietsch. "Acoustic characterization of a novel microfluidics system for in vitro ultrasound-mediated drug delivery", *NanoCity 2016, Amsterdam, the Netherlands, 21 June 2016 (oral & poster)*

**Tom van Rooij**, Guillaume Lajoinie, Ilya Skachkov, Nico de Jong, Klazina Kooiman, Michel Versluis. "Interaction of laser-activated polymeric microcapsules with cells", *NanoCity 2016, Amsterdam, the Netherlands, 21 June 2016 (poster)*

**Tom van Rooij**, Guillaume Lajoinie, Ilya Skachkov, Nico de Jong, Klazina Kooiman, Michel Versluis. Interaction of laser-activated polymeric microcapsules with cells", *21st European symposium on Ultrasound Contrast Imaging, Rotterdam, the Netherlands, 21-22 Jan 2016 (poster)*

Inés Beekers, Shreyas B. Raghunathan, **Tom van Rooij**, Verya Daeichin, Nico de Jong, Klazina Kooiman, Sebastiaan J. Trietsch. "Acoustic characterization of a novel cell culture platform for ultrasound-mediated drug delivery", *21st European symposium on Ultrasound Contrast Imaging, Rotterdam, the Netherlands, 21-22 Jan 2016 (poster)*

**Tom van Rooij**, Alexandre Lima, Verya Daeichin, Patricia A.C. Specht, Bulent Ergin, Yasin Ince, Can Ince, Nico de Jong, Klazina Kooiman. "Contrast-enhanced ultrasound imaging of the renal cortex of pigs during hemorrhagic shock", *21st European symposium on Ultrasound Contrast Imaging, Rotterdam, the Netherlands, 21-22 Jan 2016 (oral)*

Guillaume Lajoinie, Ine De Cock, Heleen Dewitte, Ying Luan, **Tom van Rooij**, Erik Gelderblom, Mirjam Visscher, Klazina Kooiman, Benjamin Dollet, Ine Lentacker, Michel Versluis. "Multiscale high-speed imaging to study complex behavior of ultrasound contrast agents", *31st International Congress on High-Speed Imaging and Photonics, Osaka, Japan, 7-10 Nov 2015 (oral)*

**Tom van Rooij**, Alexandre Lima, Verya Daeichin, Patricia A.C. Specht, Bulent Ergin, Yasin Ince, Nico de Jong, Can Ince, Klazina Kooiman. "Feasibility of in vivo contrast-enhanced ultrasound imaging of the renal cortex during hemorrhagic shock", *IEEE International Ultrasonics Symposium 2015, Taipei, Taiwan, 21-24 Oct 2015 (poster)*

Klazina Kooiman, **Tom van Rooij**, Bin Qin, Frits Mastik, Hendrik J. Vos, Alexander L. Klibanov, Nico de Jong, Flordeliza S. Villanueva, Xucai Chen. "Fluorescence high-speed microscopy reveals dynamic behavior of lipid coating on ultrasound contrast agents in an ultrasound field", *3rd Phospholipids in Pharmaceutical Research Symposium 2015, Heidelberg, Germany, 21-22 Sept 2015 (poster)*

**Tom van Rooij**, Alexandre Lima, Verya Daeichin, Patricia A.C. Specht, Bulent Ergin, Yasin Ince, Nico de Jong, Can Ince, Klazina Kooiman. "In vivo contrast enhanced ultrasound imaging of the renal cortex during hemorrhagic shock", *30th Bubble Conference 2015, Chicago, Illinois, USA, 10-12 Sept (oral)*

**Tom van Rooij**, Alexandre Lima, Verya Daeichin, Patricia A.C. Specht, Bulent Ergin, Yasin Ince, Nico de Jong, Can Ince, Klazina Kooiman. "In vivo contrast-enhanced ultrasound imaging of the renal cortex during hemorrhagic shock", *5th Microbubble Symposium 2015, Leeds, UK, 29-30 June 2015 (oral)*

Klazina Kooiman, **Tom van Rooij**, Flordeliza S. Villanueva, Bin Qin, Frits Mastik, Hendrik J. Vos, Alexander L. Klibanov, Nico de Jong, Xucai Chen. "Lipid shell buckling during microbubble compression – a fluorescence high-speed camera study", *5th Microbubble Symposium 2015, Leeds, UK, 29-30 June 2015 (oral)*

**Tom van Rooij**, Antonius F.W. van der Steen, Nico de Jong, Klazina Kooiman. "Radial excursions of bound and non-bound targeted lipid-coated single microbubbles", *169th meeting of the Acoustical Society of America, Pittsburgh, Pennsylvania, US, 18-22 May 2015 (oral & poster)*

**Tom van Rooij**, Antonius F.W. van der Steen, Nico de Jong, Klazina Kooiman. "The influence of binding on the acoustical response of targeted microbubbles", *15th International Symposium of Therapeutic Ultrasound, Utrecht, the Netherlands, 15-18 April 2015 (oral)*

**Tom van Rooij**, Antonius F.W. van der Steen, Nico de Jong, Klazina Kooiman. "The influence of binding on the radial excursions of lipid-coated microbubbles", *20th European symposium on Ultrasound Contrast Imaging, Rotterdam, the Netherlands, 22-23 Jan 2015 (poster)*

Klazina Kooiman, **Tom van Rooij**, Flordeliza S. Villanueva, Bin Qin, Frits Mastik, Hendrik J. Vos, Alexander L. Klibanov, Nico de Jong, Xucai Chen. "To buckle or not to buckle, that is the question – a fluorescence high-speed camera study", *20th European symposium on Ultrasound Contrast Imaging, Rotterdam, the Netherlands, 22-23 Jan 2015 (oral)*

Ilya Skachkov, Tom J.A. Kokhuis, **Tom van Rooij**, Ying Luan, Antonius F.W. van der Steen, Nico de Jong, Klazina Kooiman. "Correlating sonoporation dynamics to reversible and irreversible sonoporation", *20th European symposium on Ultrasound Contrast Imaging, Rotterdam, the Netherlands, 22-23 Jan 2015 (poster)*

Klazina Kooiman, Flordeliza S. Villanueva, Bin Qin, **Tom van Rooij**, Frits Mastik, Alexander L. Klibanov, Nico de Jong, Xucai Chen. "Unraveling lipid-coating movements of oscillating microbubbles - a fluorescence high-speed optical study", *IEEE International Ultrasonics Symposium 2014, Chicago, Illinois, USA, 3-6 Sept 2014 (oral)*

**Tom van Rooij**, Antonius F.W. van der Steen, Nico de Jong, Klazina Kooiman. "Influence of binding on the vibrational responses of targeted lipid-coated microbubbles", *IEEE International Ultrasonics Symposium 2014, Chicago, Illinois, USA, 3-6 Sept 2014 (oral)*

**Tom van Rooij**, Antonius F.W. van der Steen, Nico de Jong, Klazina Kooiman. "Effects of binding on the acoustical dynamics of targeted lipid-coated microbubbles", *4th Microbubble Symposium 2014, Leeds, UK, 14-15 July 2014 (poster)*

Klazina Kooiman, Flordeliza S. Villanueva, Bin Qin, **Tom van Rooij**, Frits Mastik, Alexander L. Klibanov, Nico de Jong, Xucai Chen. "Resolving lipid coating behavior using high-speed fluorescence imaging", *4th Microbubble Symposium 2014, Leeds, UK, 14-15 July 2014 (oral)*

**Tom van Rooij**, Ying Luan, Guillaume Renaud, Antonius F.W. van der Steen, Nico de Jong, Klazina Kooiman. "Response to ultrasound of two types of lipid-coated microbubbles observed with a high-speed optical camera", *167th meeting of the Acoustical Society of America, Providence, Rhode Island, US, 5-9 May 2014 (oral & poster)*

Jason L. Raymond, Ying Luan, **Tom van Rooij**, Shao-Ling Huang, David D. McPherson, Nico de Jong, Christy K. Holland. "Estimation of damping coefficient based on the impulse response of Echogenic Liposomes", *167th meeting of the Acoustical Society of America, Providence, Rhode Island, US, 5-9 May 2014 (oral & poster)*

**Tom van Rooij**, Ying Luan, Guillaume Renaud, Antonius F.W. van der Steen, Nico de Jong, Klazina Kooiman. "Influence of DSPC versus DPPC on acoustical responses of lipid-coated microbubbles", *19th European symposium on Ultrasound Contrast Imaging, Rotterdam, the Netherlands, 23-24 Jan 2014 (poster)*

Klazina Kooiman, Flordeliza S. Villanueva, Bin Qin, **Tom van Rooij**, Frits Mastik, Alexander L. Klibanov, Nico de Jong, Xucai Chen. "Ultra-fast lipid movement in the microbubble coating during oscillation – a fluorescence high-speed camera study", *19th European symposium on Ultrasound Contrast Imaging, Rotterdam, the Netherlands, 23-24 Jan 2014 (oral)*

Jason L. Raymond, Ying Luan, **Tom van Rooij**, Shao-Ling Huang, David D. McPherson, Christy K. Holland, Nico de Jong. "Impulse response of Echogenic Liposomes", *19th European symposium on Ultrasound Contrast Imaging, Rotterdam, the Netherlands, 23-24 Jan 2014 (poster)*

**Tom van Rooij**, Ying Luan, Guillaume Renaud, Antonius F.W. van der Steen, Nico de Jong and Klazina Kooiman, "Influence of streptavidin functionalization on the acoustical response of DSPC and DPPC based ultrasound contrast agents", *NanoNextNL NanoMedicine day, Amsterdam, The Netherlands, 22 Nov 2013 (poster)*

Klazina Kooiman, **Tom van Rooij**, Tom J.A. Kokhuis, Ying Luan, Ilya Skachkov, Johannes G. Bosch, Antonius F.W. van der Steen, Wiggert A. van Cappellen, Nico de Jong. "DSPC versus DPPC lipid as coating for ultrasound contrast agents", *3rd Phospholipids in Pharmaceutical Research Symposium 2013, Heidelberg, Germany, 16-17 Sept 2013 (poster)*

Ying Luan, Guillaume Lajoinie, Erik Gelderblom, Ilya Skachkov, Heleen Dewitte, Ine Lentacker, **Tom van Rooij**, Hendrik Vos, Antonius F.W. van der Steen, Michel Versluis, Nico de Jong. "Liposome Shedding from a Vibrating Microbubble on Nanoseconds Timescale", *IEEE International Ultrasonics Symposium 2013, Prague, Czech Republic, 21-25 July 2013 (oral)*

**Tom van Rooij**, Ying Luan, Guillaume Renaud, Antonius F.W. van der Steen, Nico de Jong, Klazina Kooiman. "Influence of streptavidin functionalization on the acoustical response of DSPC versus DPPC lipid-coated microbubbles**",** *3rd Microbubble symposium 2013, Leeds, UK, 17-18 July 2013 (poster)*

Klazina Kooiman, Tom J.A. Kokhuis, **Tom van Rooij**, Ying Luan, Ilya Skachkov, Johannes G. Bosch, Antonius F.W. van der Steen, Wiggert A. van Cappellen, Nico de Jong. "The optimal lipid coating for therapeutic bubbles", *18th European symposium on Ultrasound Contrast Imaging, Rotterdam, the Netherlands, 17-18 Jan 2013 (oral)*

Alma M.A. Mingels, **Tom van Rooij**, Will K.W.H. Wodzig, Marja P. van Dieijen-Visser. "What you see is not what you get: cardiac troponin T is completely degraded in serum of AMI patients", *Nationale Wetenschapsdag Klinische Chemie NVKC, Amersfoort, the Netherlands, 19 April 2012 (poster)*

# PhD PORTFOLIO

| **Courses:** | **Year** | **ECTS** |
|---|---|---|
| Cardiovascular imaging and diagnostics (COEUR) | 2013 | 1.5 |
| Medical ultrasound transducers (IEEE IUS, Prague) | 2013 | 0.15 |
| Biomedical photoacoustics: From bench to bedside (IEEE IUS, Prague) | 2013 | 0.15 |
| Risk Analysis and Technology Assessment (NanoNextNL, Amersfoort) | 2013 | 0.5 |
| Biomedical English Writing and Communication (Erasmus MC) | 2014 | 3.0 |
| Media contacts for researchers (Erasmus MC) | 2015 | 0.15 |
| Scientific Integrity (Erasmus MC) | 2015 | 0.3 |
| | | |
| **COEUR Research Seminars:** | | |
| Biomarkers in cardiovascular disease | 2012 | 0.4 |
| Glucose metabolism and vascular disease | 2012 | 0.4 |
| Current cardiac and vascular aging research at EMC | 2014 | 0.4 |
| Arterial thrombosis in acute ischemic stroke | 2014 | 0.2 |
| Secondary prevention with anti-thrombotics: unravelling the conundrum of bleeding vs efficacy | 2015 | 0.1 |
| Translational research | 2016 | 0.2 |
| | | |
| **COEUR Lectures:** | | |
| HDL's Protein Cargo: Friend or Foe in Cardioprotection? *Prof Jay W. Heinecke, MD, PhD* | 2013 | 0.1 |
| Biomechanics of Atherosclerotic Plaque: Site, Stability and in vivo Modeling *Prof Jaques Ohayon, PhD* | 2013 | 0.1 |
| Monitoring of biological processes: identification of biomarkers in renal diseases and new inhibitor of renin angiotensin system *Prof Dulce E. Casarini, PhD* | 2015 | 0.1 |
| | | |
| **Scientific meetings:** | | |
| NVMU Radboudumc (Nijmegen) | 2012 | 0.4 |
| NVMU Erasmus MC (Rotterdam) | 2013 | 0.4 |
| NVMU Maastricht University (Maastricht) | 2013 | 0.4 |
| NVMU Erasmus MC (Rotterdam) | 2016 | 0.4 |

| | | |
|---|---|---|
| NanoNextNL Program meeting Molecular Imaging (Eindhoven) | 2013 | 0.4 |
| NanoNextNL NanoMedicine Day (Amsterdam) | 2013 | 0.5 |
| NanoNextNL Program meeting Molecular Imaging (Utrecht) | 2014 | 0.4 |
| MedTechWest (Delft) | 2014 | 0.4 |
| NanoNextNL workshop Bubbles, Droplets, and Spheres (Wageningen) | 2014 | 0.4 |

**Teaching activities:**

| | | |
|---|---|---|
| Translational Imaging Workshop AMIE - From mouse to man | 2015 | 0.2 |
| Co-supervision MSc student Infection and Immunity (Erasmus MC) | 2015 | 2.5 |
| Co-supervision MSc student Applied Sciences (TU Delft) | 2015 | 0.3 |

**Attended symposia and conferences:**

| | | |
|---|---|---|
| 18th European Symposium on Ultrasound Contrast Imaging<br>*Rotterdam, the Netherlands* | 2013 | 0.6 |
| 3rd Microbubble Symposium<br>*Leeds, UK* | 2013 | 1.1 |
| IEEE International Ultrasonics Symposium<br>*Prague, Czech Republic* | 2013 | 1.7 |
| 19th European Symposium on Ultrasound Contrast Imaging<br>*Rotterdam, the Netherlands* | 2014 | 1.1 |
| 167th Meeting of the Acoustical Society of America<br>*Providence, Rhode Island, USA* | 2014 | 3.0 |
| 4th Microbubble Symposium<br>*Leeds, UK* | 2014 | 1.1 |
| IEEE International Ultrasonics Symposium<br>*Chicago, Illinois, USA* | 2014 | 1.9 |
| NanoCity<br>*Utrecht, the Netherlands* | 2014 | 0.3 |
| 20th European Symposium on Ultrasound Contrast Imaging<br>*Rotterdam, the Netherlands* | 2015 | 1.1 |
| 15th International Symposium on Therapeutic Ultrasound<br>*Utrecht, the Netherlands* | 2015 | 2.0 |
| 169th Meeting of the Acoustical Society of America<br>*Pittsburgh, Pennsylvania, USA* | 2015 | 3.0 |
| 5th Microbubble Symposium<br>*Leeds, UK* | 2015 | 1.6 |

| | | |
|---|---|---|
| NanoCity<br>*Amersfoort, the Netherlands* | 2015 | 0.5 |
| IEEE International Ultrasonics Symposium<br>*Taipei, Taiwan* | 2015 | 2.3 |
| 21st European Symposium on Ultrasound Contrast Imaging<br>*Rotterdam, the Netherlands* | 2016 | 2.1 |

# CURRICULUM VITAE

Tom van Rooij was born in Eindhoven, the Netherlands, in 1987. In 2005 he started his academic training at the Eindhoven University of Technology (TU/e) and earned his BSc degree in Biomedical Engineering in 2008. During his master Medical Engineering (2009-2012) at the same university he was an intern at the Division of Imaging Sciences & Biomedical Engineering at St Thomas' Hospital in London, United Kingdom and performed his thesis at the department of Clinical Chemistry of the Maastricht University Medical Center (Maastricht, the Netherlands). Before starting his PhD he held a teaching position at the Biomedical NMR group, department of Biomedical Engineering at the TU/e. In July 2012 he started a PhD project at the department of Biomedical Engineering of the Thorax Center, Erasmus MC, Rotterdam, the Netherlands. This project focused on ultrasound imaging and therapy and characterization of ultrasound contrast agents using ultra-high-speed optical imaging techniques.

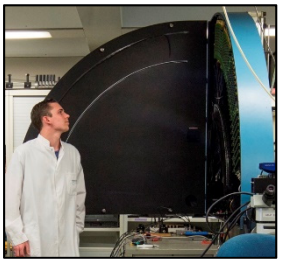

Tom van Rooij is in 1987 geboren te Eindhoven. Na het afronden van de middelbare school is hij in 2005 begonnen met de bacheloropleiding Biomedische Technologie aan de Technische Universiteit Eindhoven (TU/e) en heeft daarvoor in 2008 zijn diploma behaald. Na een fulltime bestuursjaar van Studievereniging der BioMedische Technologie "Protagoras" is hij in 2009 gestart met de opleiding Medical Engineering aan dezelfde universiteit. Na een stage op de afdeling Imaging Sciences & Biomedical Engineering van het St Thomas' Hospital in Londen (Verenigd Koninkrijk) is hij begonnen met zijn afstudeeronderzoek in het Klinisch Chemisch Laboratorium van het Maastricht Universitair Medisch Centrum. In 2012 heeft hij de opleiding Medical Engineering succesvol afgerond. Na zijn afstuderen heeft hij drie maanden als assistent-docent gewerkt voor de vakgroep Biomedical NMR van de TU/e om in juli 2012 te starten met zijn promotieonderzoek in het Erasmus MC in Rotterdam, op de afdeling Biomedische Technologie. Dit onderzoek richtte zich op ultrasound contrastmiddelen voor beeldvorming en therapie van *in vitro* tot *in vivo* toepassingen, waarvan u hier het resultaat voor u ziet.